A record of transpression-related brittle-ductile deformation and associated alteration within granitoid plutons of the Wabigoon subprovince, Superior Province

Bailey Drover

Thesis submitted to the
Department of Geology
Faculty of Science and Environmental Studies
at Lakehead University
in partial fulfillment of the
requirements for a
Master of Science Degree in Geology
at Lakehead University
2022

ABSTRACT

The Wabigoon subprovince is a 900 km long by 150 km wide Archean-aged granite greenstone belt. Large, synvolcanic batholiths with smaller late to post-tectonic stocks cut the numerous greenstone belts of the subprovince. One of the post-tectonic stocks is the Taylor Lake Stock, located within the western Wabigoon subprovince with a late Archean crystallization age that has been interpreted to infer the cessation of regional tectonics in the area. However, granitoids are highly competent and dry rocks that are difficult to deform, leading them to appear undeformed/unmetamorphosed in the field even though they may have undergone ductile deformation, brittle deformation and associated hydrothermal/metasomatic alteration. In this study, field mapping and sampling, petrographic analysis, mineralogical compositional analysis, stable isotope geochemistry and cathodoluminescence imaging of twelve granitoid plutons (including the Taylor Lake Stock) across the subprovince are used to constrain the relationship between the brittle deformation, ductile deformation and alteration of the plutons to provide insight into the tectonic history of the Wabigoon subprovince.

The twelve plutons record chlorite and/or epidote infilled steeply dipping shear fractures with sub-horizontal lineations that indicate an oblique strike-slip displacement, characteristic of transpression. The strike of the infilled shear fractures varies across the individual plutons, possibly as a result of non-coaxial strain in which the rigid and competent granitoid bodies have undergone a component of rigid body rotation, resulting in a shifting trend of the maximum elongation direction. Evidence for this stems from the shape of the Ottertail pluton in the western Wabigoon subprovince that resembles a porphyroclast entrained within a dextral shear zone. Adjacent to the chlorite and/or epidote infilled shear fractures, wall-rock alteration common to all plutons includes white mica (mostly phengite) ± epidote alteration of the feldspar and chloritization of biotite. Epidote, chlorite and sphene are also commonly seen along microfractures within the host rock. Alteration of the plutons is noted to be lesser in the low strain areas of the plutons where brittle deformation is not as pervasive. Cathodoluminescence imaging of the feldspars from the various strain zones supports lower degrees of alteration in lower strain zones, as feldspars are more consistent with their color hues in the lowest strain samples.

Each of the twelve plutons also record solid-state deformation microstructures within quartz and feldspar, demonstrating dislocation creep was active in both mineral phases. As dislocation creep does not become an effective process within feldspar until temperatures reach

~450°C, these solid-state deformation microstructures provide evidence for amphibolite facies metamorphism of the plutons. Ductilely overprinted quartz veins and the presence of chlorite and/or epidote shear fractures within shear zones demonstrates brittle deformation during regional ductile deformation and associated alteration, which is seen in six of the plutons studied (Sabaskong batholith, Dryberry batholith, Revell batholith, Ottertail pluton, Irene-Eltrut batholithic complex and the Croll Lake Stock), providing evidence that regional-scale transpression consisted of coeval brittle-ductile deformation and associated alteration within the granitoid plutons. The δD_{fluid} and $\delta^{18}O_{fluid}$ values of the hydrothermal fluid calculated from measured δD and $\delta^{18}O$ values of chlorite infilled shear fractures from six samples in two plutons range from -30 to -45‰ and 5.6 to 7.1‰, respectively, recording a metamorphic water signature that likely stems from the devolatilization of the surrounding host greenstone during regional Archean metamorphism.

XRD qualitative mineral phase analysis of two chlorite infilled shear fractures also shows the presence of the illite 2M1 polytype associated with the vein, suggesting that some of the hydrothermal fluid circulation occurred at temperatures within the realm of the illite 2M1 stability field (lower than roughly 300°C). This coupled with the presence of a chlorite infilled cataclasite, which represents a lower temperature brittle feature, suggests that at least a component of the brittle deformation and associated hydrothermal fluid flow occurred post peak metamorphism, likely into exhumation of the granitoid plutons.

Furthermore, the alteration and deformation of the twelve plutons studied demonstrates evidence for coeval brittle-ductile deformation and associated hydrothermal fluid flow in the amphibolite facies of metamorphism, with brittle fracturing and alteration continuing into exhumation. The late Archean crystallization age date from the Taylor Lake Stock should not be used to mark the cessation of regional tectonics within the western Wabigoon subprovince.

ACKNOWLEDGMENTS

Many people are to thank for bringing this project together. I would first like to thank my two supervisors, Dr. Shannon Zurevinski and Dr. Mary Louise Hill, for their support and guidance throughout this project. Their varying expertise were essential to the outcome of this research. I would also like to thank the Nuclear Waste Management Organization for funding this project and providing me the opportunity to be a part of it. I'd also like to thank my external reviewer, Dr. Dyanna Czeck, who provided very insightful comments to this research.

Thanks goes out to Kristi Tavener and Jonas Valiunas of the Lakehead University's Lapidary facility for their timely effort in making my many polished thin sections. Thanks to Dorothy Campbell and Craig Ravnaas of the Ministry of Northern Development, Mines, Natural Resources and Forestry (NDMNRF) who assisted in obtaining chlorite infilled shear fracture samples from drill core for stable isotope analysis. Agnico Eagle is also thanked for providing drill core samples of their Hammond Reef project for stable isotope analysis.

My field assistants Megan Landman, Maddison Hodder, Dana Campbell and Ettore Colaiacovo all deserve a round of applause for their help smashing rocks and taking notes in the field. Thanks goes out to Panseok Yang in the microprobe lab at the University of Manitoba for taking my cathodoluminescence images as well as to the team at the Queens Facility for Isotope Research for conducting my XRD analysis and stable isotope analysis of the chlorite shear fractures.

This project, as well as my personal growth, greatly benefited from the weekly structure group meetings held throughout the school terms – thanks goes out to Dr. Mary Louise Hill, Conway, Louis, Khalid, Daniel, Blaize, Sara, Megan and Rebecca. And of course, I would like to thank my family, Andrew and Brittany for their support throughout this project.

Contents

Table of Figures

Table of Tables

Chapter 1: Introduction

The timing of pluton emplacement within greenstone belts can be complex to analyze with traditional field mapping approaches, as the higher competency of the granitic suite plutons when compared to the surrounding hydrous greenstone belt results in different styles of strain accommodation. To further complicate the assessment of pluton emplacement, the main mineral constituents of granitic suite plutons are quartz and feldspars, which are stable over wide temperature ranges and do not alter to form metamorphic index minerals. The lack of a characteristic metamorphic mineral assemblage within the plutons is also driven by the dry nature of granitoids, as fluids are a necessity for metamorphic reactions to occur. For these reasons, the deformation history of the granitoid plutons across the Wabigoon subprovince is not well understood – leading to the interpretation of some smaller stocks being emplaced post-tectonism. The high competency of the plutons coupled with the lack of a characteristic metamorphic mineral assemblage means that other techniques must be used to constrain the relative timing of emplacement. The quantification of solid-state deformation microstructures exhibited in the quartz and feldspar mineral phases is a particularly useful tool in assessing the deformation conditions of quartzofeldspathic rocks where metamorphic mineral assemblages are not present (Faleiros et al., 2010; Cavalcante et al., 2018; Hunter et al., 2018; Ribeiro et al., 2019).

The timing, conditions and presence of brittle deformation may also provide insight into the tectonic history of the granitoid plutons as quartzofeldspathic rocks are quite competent and may deform via brittle fracturing when other rock types exposed to the same conditions might undergo purely ductile deformation. Brittle deformation also provides pathways for hydrothermal/metasomatic fluid flow, so any alteration experienced within the plutons can in part be understood with an understanding of the brittle deformation. Studying the brittle deformation and alteration of the plutons is essential to understanding fluid-rock interactions.

This research assesses the relationship between brittle deformation, ductile deformation, and alteration of several granitoid plutons across the Wabigoon subprovince of the Archean Superior Province in order to assess the timing of emplacement of the plutons and to provide insight into Archean regional tectonics. Techniques used in this work include macro- and microscale structural analysis, SEM-EDX quantitative analysis of the alteration minerals, stable isotope (δD and $\delta^{18}O$) analysis of chlorite infilled shear fractures and cathodoluminescence imaging of quartz and feldspars.

Chapter 2: Regional Geology

The Wabigoon subprovince is a 900km long by 150km wide Archean-aged granite-greenstone belt that makes up one of the several roughly east-west trending subprovinces comprising the Archean Superior Province. The subprovinces of the Superior Province are divided on the basis of lithological and structural contrasts and are commonly separated by subparallel boundary faults (Card and Ciesielski, 1986). To the north-west, the Wabigoon subprovince is bounded by the metaplutonic Winnipeg River subprovince, to the north-east by the migmatitic English River subprovince, and to the south by the metasedimentary Quetico subprovince (Blackburn et al., 1991). The amalgamation of the subprovinces to form the Superior Province occurred during the late stages of the Kenoran Orogeny – which consisted of a northwest-directed horizontal compression oblique to the trend of the subprovinces (Schwerdtner et al. 1979; Park 1981) that occurred over the time interval of 2.72-2.68 Ga (Percival et al., 2006). Historically, the Wabigoon subprovince has been sub-divided into the greenstone dominated western and eastern regions with a 200 km wide central region that is primarily made up of granitoid plutons (Blackburn et al., 1991) (Figure 1). The western Wabigoon region is the youngest with interpreted crystallization ages of 2.78 – 2.66 Ga while the eastern and central regions have interpreted crystallization ages of 3.08 – 2.67 Ga (Tomlinson et al., 2004). More recent work reframes the Wabigoon subprovince in terms of discrete tectonic terranes including the western Wabigoon terrane, the eastern Wabigoon terrane, the central Marmion terrane and the southwestern Winnipeg River terrane (Percival et al., 2006). Terranes represent the building blocks of the Superior Province with boundaries defined based on isotopic and zircon inheritance studies (Percival et al., 2006). These terranes have tectono-stratigraphic histories that are independent of their neighbouring terranes prior to amalgamation, but subsequent amalgamation of the terranes to form the Wabigoon subprovince has led to overprinting by Neoarchean magmatism, metamorphism and deformation (Percival et al., 2006). This study uses the older terminology of Card and Ciesielski (1986) when discussing the regional geology of the region as the focus of this work is on the deformation and alteration of the granitoid plutons of the Wabigoon subprovince during and post amalgamation.

The Wabigoon subprovince is interpreted to be a volcanic arc with mafic and felsic lava flows from 2.75 to 2.72 Ga, followed by plutonism until roughly 2.69 Ga (Stone, 2010). As for the metamorphism of the region, Blackburn et al. (1991) note that the highest grade of metamorphism within the subprovince is seen in volcanic rock that records middle amphibolite metamorphic

mineral assemblages. The highest metamorphic grades (middle amphibolite facies) are seen in the greenstone within proximity to the granitoid batholiths and along the subprovince boundaries.

This chapter will focus on the regional geology of the Wabigoon subprovince with a specific emphasis on the granitoid plutons – as these are the focus of this thesis.

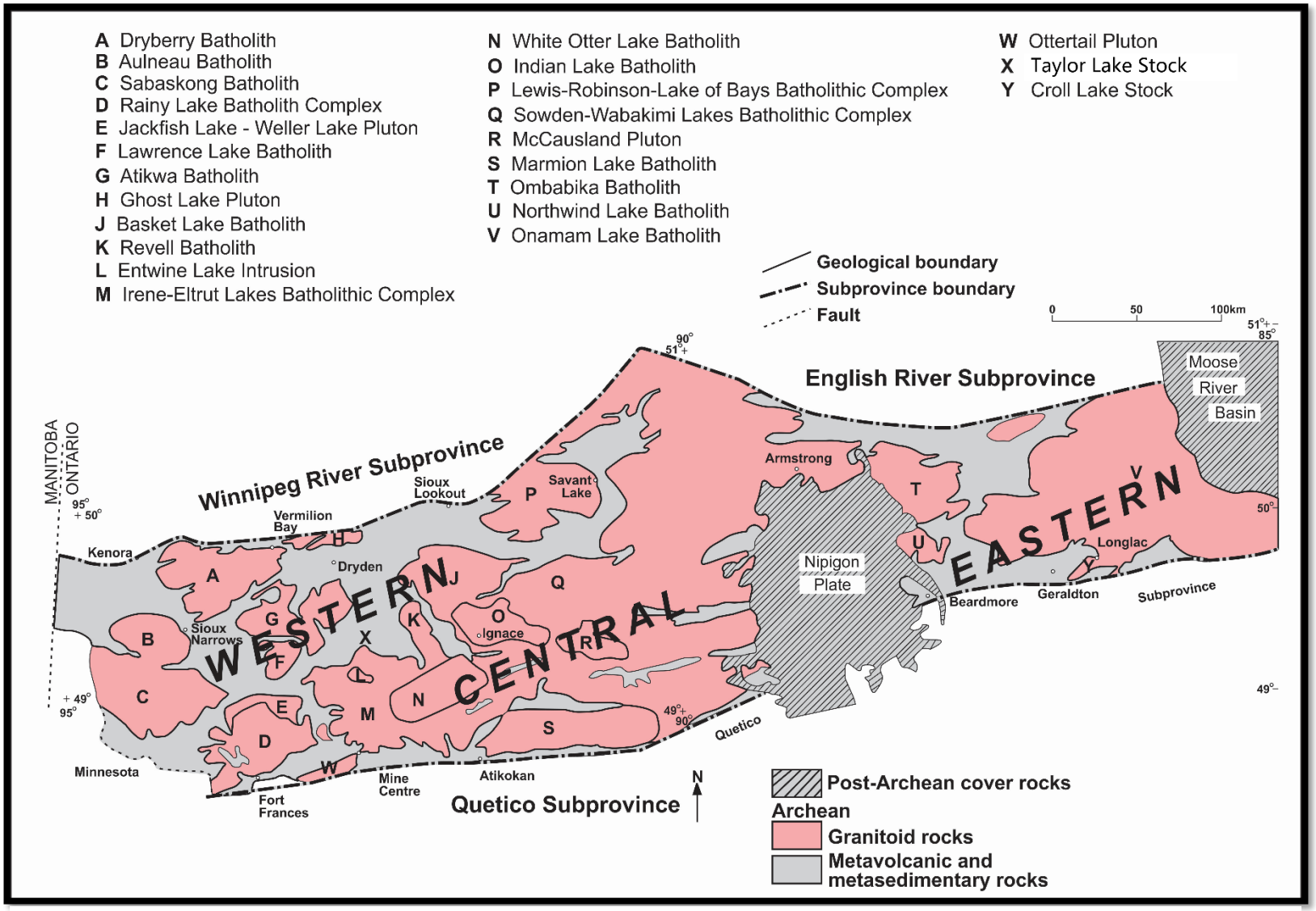

Figure 1. Map of the Wabigoon subprovince. Grey units indicate the host 'greenstone' and pink units represent the granitoid plutons. Letters within the plutons corresponds to the legend. Note that the Taylor Lake Stock is not outlined on the map. Modified from Blackburn et al. (1991).

2.1 Western Wabigoon subprovince

The western Wabigoon subprovince is described as a region characterized by metavolcanic dominated greenstone belts surrounding large elliptical batholiths such as the Sabaskong batholith, Dryberry batholith, Atikwa batholith and the Aulneau batholith (Blackburn et al., 1991). Beakhouse et al. (1995) noted that most of the large batholiths (including the Aulneau, Atikwa and Sabaskong) range compositionally from ultramafic to granitic with dominant tonalitic to granodioritic compositions and are closely associated petrogenetically and temporally with the metavolcanics of the surrounding greenstone belts. Two U-Pb ages from tonalitic phases of the Sabaskong batholith are 2724 ± 2 Ma and 2723 ± 2 Ma, which is only slightly younger than a gabbro into which the batholith was emplaced (2731 ± 4 Ma) and the overlying Phinney-Dash Lakes complex (2728 ± 1 Ma), leading to the interpretation of the Sabaskong batholith being emplaced syn-volcanically (Davis and Edwards 1982; Davis and Edwards 1986).

Beakhouse et al. (1995) note that the smaller stocks are predominately late- to post-tectonic with varying compositions from diorite to granite and syenite. These small, post-tectonic plutons were emplaced over a 15 My interval roughly commencing at 2699 Ma (Beakhouse et al., 1995). One of the interpreted post-tectonic stocks is the Taylor Lake stock that outcrops along Highway 502 just north of the western contact of the Irene-Eltrut batholithic complex. Davis et al. (1982) used U-Pb zircon dating to provide a crystallization age of 2695.0 ± 3.6 Ma. They note that since the Taylor Lake stock is post-tectonic in emplacement, this date indicates that major tectonic activity in the area had terminated before this time. Another late to post tectonic stock is the Ottertail pluton, located in the Rainy Lake region just north of the Quetico fault. Some have noted that this 'post-tectonic' pluton has fabrics parallel to the fabrics seen in the region (Borradaile and Kehlenbeck 1996; Melynk et al., 1999; Scott 1999), which has been interpreted by some to indicate syntectonic emplacement. Although some believe that the pluton was emplaced syn-tectonically, others have used the age of the pluton to represent the cessation of regional deformation (Davis et al., 1989; Poulsen, 2000). To resolve the issue of emplacement timing, Czeck et al (2006) studied the microstructures present within the quartz and feldspars of the pluton and completed both a magnetic and gravity studies of the Ottertail pluton. Their findings, which consist of ductile deformation in the quartz and brittle fracturing in the feldspars, suggest solid-state deformation of the pluton with peak temperatures less than 550°C. Also of interest is the presence of a well-defined and steep magnetic fabric that is roughly coincident with the regional steep tectonic foliations measured in the surrounding rocks. The gravity profile indicates that the Ottertail pluton

is quite shallow, supporting the idea that the steep fabrics seen within the pluton are not the result of magmatic flow from a feeder zone, but are more likely to be the result of regional strain. Finally, Czeck et al. (2006) suggest that the shallow nature of the pluton is consistent with syntectonic emplacement into a transpressional setting – possibly along en echelon P shears. These findings are important as they suggest that the age of ~ 2686 Ma for the Ottertail pluton as found by Davis et al. (1989) should not be used to constrain the cessation of regional tectonics in the area. This hypothesis of syn-tectonic emplacement for the Ottertail pluton is also in part supported by the shape of the pluton (Figure 2), which resembles a porphyroclast entrained within a dextral shear zone as noted by Czeck et al. (2006).

The western Wabigoon subprovince is transected and bounded by regional-scale faults that are typically steeply dipping with shear-sense indicators suggesting transcurrent movement and less commonly, dip-slip movement (Beakhouse, 2013). Beakhouse (2013) also notes that these shear-sense indicators likely record a very late component of the regional deformation with these faults originally having formed with different orientations and kinematics – such as thrust and detachment faults.

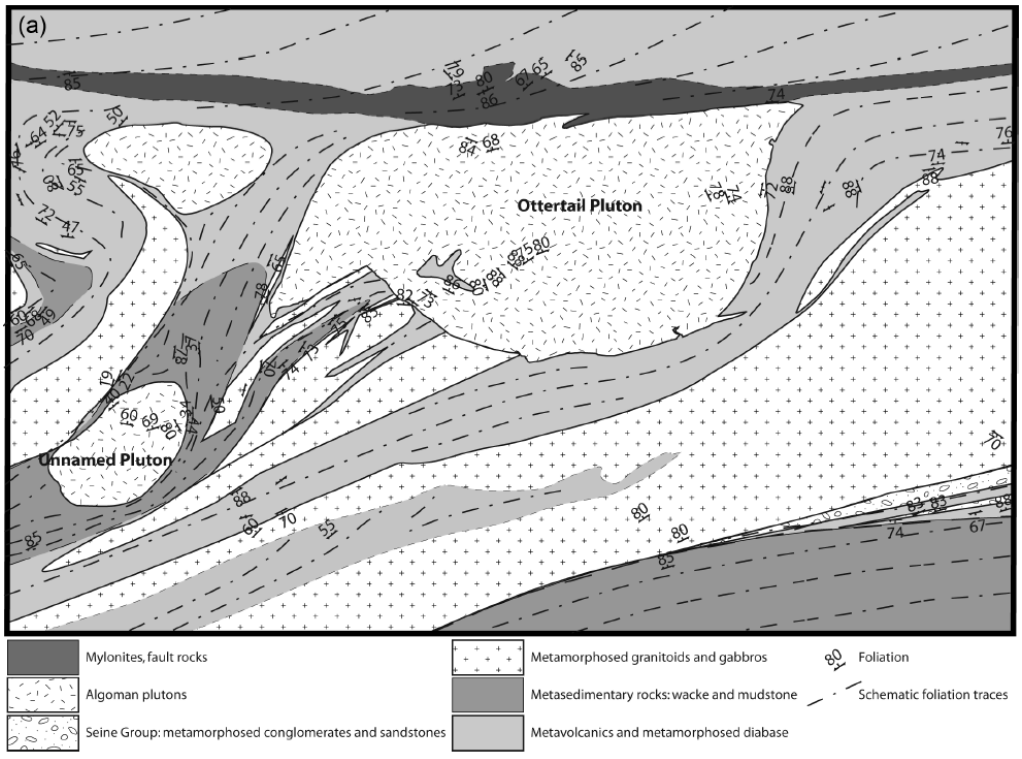

Figure 2. A map of the Ottertail Pluton in the Rainy Lake region of the western Wabigoon subprovince. The pluton is noted to resemble a porphyroclast caught within a dextral shear zone with the foliation of the surrounding less competent greenstone belt wrapping around the more competent granitoid pluton. From Czeck et al. (2006).

2.2 Central Wabigoon subprovince

The central Wabigoon subprovince is an approximately 200 km wide corridor dominated by granitoid plutons with lesser greenstone lenses. Geochronological and stratigraphic evidence (Davis and Jackson, 1988; Wilks and Nisbet, 1988, respectively) suggests this region of the Wabigoon subprovince includes an area with a granitoid basement to the greenstones (Blackburn et al., 1991), as the Marmion batholith records crystallization ages of 3.00 Ga and is overlain by volcanic sequences with ages of 3.00-2.90, 2.83 and 2.73-2.72 Ga (Tomlinson et al., 2003; Tomlinson et al., 2004). Metamorphism within the small greenstone belts in the region are noted to display greenschist to amphibolite facies index minerals. Zircon, titanite and monazite have been used to estimate the age of metamorphism within the region, providing ages that range from 2722 to 2657 Ma (Stone, 2010 and references therein). A titanite date from the White Otter Lake batholith gives a metamorphic age of 2667 Ma (Davis, 1993).

Stone (2010) notes that the late, massive and mainly post-tectonic intrusive rocks include the biotite granitoid, sanukitoid and Lac de Iles suites, with examples of the biotite granite bodies including the White Otter Lake, Cecil (Indian Lake) and Muskeg batholiths. Stone (2010) also notes that there are two major sets of Neoarchean faults that are subvertical and transcurrent in nature that transect the area. Of these two major sets, one includes the dextral Quetico and Shelby Lake faults seen along the Quetico-Wabigoon subprovince boundary while the other set strikes northeast to north-northeast and includes the Entwine, Marmion, Pakashkan and Gull River faults. The northeast to eastward striking orientations suggests a conjugate strike-slip relationship between the two sets.

2.3 Eastern Wabigoon subprovince

East of Lake Nipigon is the greenstone dominated eastern Wabigoon subprovince. Similar to the western Wabigoon subprovince, this region consists of greenstone belts surrounding large, elliptical batholithic complexes. Batholiths range from pre- to post-tectonic in nature with dates that range from 2764 – 2702 Ma (Davis et al., 1982; 1988). The Croll Lake stock, which outcrops around Longlac, Ontario, is interpreted as a syn-tectonic body that ranges compositionally from ultramafic to granodioritic (Corfu, 2000). Two zircon U-Pb ages for two phases within the stock (one quartz-feldspar porphyry and the other a dioritic component) record identical age dates of 2690 ± 1 Ma (Corfu, 2000). The Croll Lake stock is the only pluton studied as part of this research within the eastern Wabigoon subprovince.

Chapter 3: Methods

This study employed a variety of methods including a field study, petrographic analysis, SEM-EDX analysis, stable isotope analysis and cathodoluminescence imaging.

3.1 Field study

A field study conducted on twelve plutons of the Wabigoon subprovince focused on measuring fracture orientations associated with hydrothermal/metasomatic alteration and collecting hand samples for petrographic and SEM-EDX analysis. Appendix I lists the location GPS coordinates of all outcrops studied. Appendix II lists all collected orientations across the plutons. Fracture orientations were taken using a Brunton compass and recorded using the notation of the right-hand rule. Some hand samples were oriented in the field for the purpose of making oriented thin sections. Field investigations focused on Highway roadside outcrops for two primary reasons. The first reason is that the blasting associated with the building of the highways results in a vertical rock cut with numerous natural fracture planes exposed – ideal for taking structural orientations. The second benefit is that the highways themselves tend to weave in and out of the margins of the plutons – as the granitoid rocks are much harder to blast than the surrounding less competent greenstone. From a structural perspective (and therefore an alteration perspective), outcrops located along the margins of the plutons are ideal as strain is likely to be concentrated where the competency contrast of the plutons with the host greenstone is present. These outcrops allow for a more in-depth characterization of the structural orientations and accompanying alteration.

3.2 Macrostructural analysis

After structural orientations were collected in the field, orientation data for each of the plutons were plotted on stereonets using the software 'Stereonet v. 11' (Allmendinger et al., 2012; Cardozo and Allmendinger., 2013). Rose diagrams were plotted using the software 'Georose' which was downloaded from http://www.yongtechnology.com/download/georose (Young Technology Inc., 2014).

3.3 Petrography and microstructural analysis

Petrographic and microstructural analyses were completed using standard transmitted light petrography. Polished thin sections (some oriented, most not) were made in the Lakehead University Lapidary Facility from hand samples collected in the field. Petrographic analysis focused on assessing mineralogy (magmatic and alteration) while microstructural analysis focused

on assessing brittle deformation features and solid-state dislocation creep textures. The microstructural analysis focused only on the solid-state ductile deformation and brittle deformation of the plutons as opposed to pluton emplacement microstructures corresponding to magmatic and/or magma mush microstructures. Magmatic to sub-magmatic microstructures include a lack of or rare undulatory extinction in quartz, imbricate structures of minerals with random orientation, and euhedral plagioclase with growth zoning. The work of Passchier and Trouw (2005) was used to identify solid-state ductile deformation microstructures such as undulatory extinction, serrated grain boundaries, recrystallization and grain size reduction that are the product of solid-state dislocation creep through crystalline lattices.

Microstructural analysis was also used to assess the degree of strain exhibited in each sample. Within the context of Chapter 4, high strain samples are those that exhibit at least a few of the following criteria: grain size reduction of quartz and/or feldspar, prominent dynamic recrystallization as evidenced through bulging recrystallization within quartz and feldspar, a moderate dimensional preferred orientation, evidence for coeval brittle-ductile deformation in the form of ductilely deformed quartz veins, moderate to strong presence of brittle fracturing (both veining and fracturing of feldspar) and strong subgrains in quartz and/or feldspar. Low strain samples never exhibit grain size reduction, typically only have weak to borderline moderate undulose extinction in quartz and feldspar and display weakly serrated to semi-smooth grain boundaries of quartz and feldspar. Low strain samples also exhibit little amounts of brittle fracturing (such as veining or fracturing of feldspars).

3.4 SEM-EDX analysis

Twenty-four samples were chosen for detailed analysis by standard petrographic methods, and back-scattered electron (BSE) imagery and energy dispersive X-ray spectrometry using a Hitachi SU-70 scanning electron microscope. The Hitachi SU-70 Schottky Field Emission SEM was used to conduct quantitative analyses of the minerals, with a 15mm working distance and an accelerating voltage of 20kV via the Oxford Aztec 80mm/124 ev electron dispersive X-ray spectrometer (EDX) equipped on the SEM. The following well characterized mineral and synthetic standards were used: jadeite (Na, Al); wollastonite (Ca, Si); orthoclase (K); ilmenite (Fe, Ti); periclase (Mg); Mn-hortonolite (Mn); apatite (F, P); barite (Ba and S); $SrTiO_3$ (Sr); and KCl (Cl). Acquisition time was 30 seconds. SEM-EDX point analyses were used to construct mineral formulas for chlorite, epidote, white mica, biotite and feldspars on the basis of fourteen, twelve,

eleven, eleven and eight oxygens, respectively. Raw SEM-EDX point analysis data (weight % oxides) were converted to stoichiometric coefficients using the method of Deer at al. (1992). Since the point analyses calculated all iron as FeO, the Droop (1987) equation was used to convert FeO to Fe_2O_3 when constructing epidote mineral formulas. Raw SEM-EDX data can be found in Appendix III.

3.5 Stable Isotope Analysis

The δD and $\delta^{18}O$ values of hydrothermal/metasomatic chlorite in shear fractures were assessed for seven veins across six drill core samples taken from three plutons. Obtaining pure chlorite powders proved difficult due to the thin and anastomosing nature of the infilled shear fractures. Chlorite was liberated from the drill core using dental tools, and powders were checked for impurities using a binocular microscope. Subsequent XRD phase analyses completed at Queen's University for each of the samples show trace impurities of the powders, discussed in more depth in Chapter 6. The samples were analyzed for their isotopic compositions. Oxygen was analyzed using a Thermo-Finnigan Delta^{plus} XP Isotope Ratio Mass Spectrometer (IRMS). Oxygen extraction was completed on 20 mg of sample at 550-600°C according to the conventional BrF_5 procedure of Clayton and Mayeda (1963). $\delta^{18}O$ values are reported using the delta (δ) notation in units of permil (‰) relative to the Vienna Standard Mean Ocean Water (VSMOW) international standard with a precision of 0.4‰ (2σ). δD was measured on 10 mg of powder using a Thermo-Finnigan MAT 253 Continuous-Flow Isotope-Ratio Mass Spectrometer (CF-IRMS). Samples were weighed into silver capsules, degassed for 1 hour at 100°C then crushed and loaded into a zero-blank auto sampler. δD values are reported using delta (δ) notation in permil (‰), relative to the Vienna Standard Mean Ocean Water (VSMOW) international standard, with a precision of 3‰ (2σ).

3.6 XRD Analysis

Phase analysis of chlorite powders for stable isotope analysis was completed at Queen's University's Facility for Isotope Research (QFIR) to check for impurities within the samples. The data was collected on a PANalytical X-ray diffractometer (spinning stage), using the X'Pert Data Collector, and analyses using X'Pert HighScore Plus software. Data was collected over a range of 5-80°2θ with CuKα radiation. XRD peaks for each sample analyzed are shown in Appendix IV.

3.7 Cathodoluminescence Imaging

Cathodoluminescence (CL) imaging was completed on 18 polished thin sections using a Reliotron Cathodoluminescent system attached to an optical microscope. Images were taken at 4 second exposure times and 2x gain. A 9 kV accelerating voltage and 480 μA beam current was used. These conditions resulted in nice feldspar images, but quartz only showed very weak to non-existent CL colors. Cathodoluminescence imaging was completed at the University of Manitoba.

Chapter 4: The macrostructure, microstructure and alteration of the granitoid plutons across the subprovince

4.1 - Overview

This chapter documents the brittle deformation, ductile deformation, and alteration for each of the plutons studied. Table 1 summarizes the features present in each pluton.

Each of the twelve plutons studied within the Wabigoon subprovince record brittle deformation that consists of epidote and/or chlorite infilled shear fractures with shallowly plunging slickenlines, indicative of an oblique strike-slip displacement. In total, four hundred and two structural measurements were taken within the plutons across the subprovince. These orientations span thirty-one outcrops of twelve plutons and include chlorite and/or epidote infilled shear fractures, quartz veins, shear zones, foliation orientations and unfilled fractures. Note that although chlorite and/or epidote infilled shear fractures with sub-horizontal slickenlines are recognized in the Croll Lake Stock, slickenline orientations were not measure in the field. Additionally, a total of thirty-nine outcrops were visited, however structural orientations were not measured in all outcrops.

Of particular interest to this study are the chlorite and/or epidote infilled shear fractures – which will be the focus when discussing brittle deformation as these are the structures most likely to be representative of Archean tectonics, hydrothermal fluid flow and the associated alteration of the granitoid plutons. Strikes of the shear fractures are variable across the plutons and the sub-province, potentially as a results on non-coaxial strain in which the granitoid bodies have undergone rigid body rotation. This would result in a shifting trend to the maximum elongation direction. It is important to note that since the infilled shear fractures have metasomatic chlorite and/or epidote along them, it can be concluded that the fractures formed at depth and not at surface – somewhere within the broad stability field of epidote and chlorite.

Quartz veins are also commonly seen within the plutons of the Wabigoon subprovince. Quartz veins are typically 1 to 3 cm thick and represent extensional (tensile) veins that likely formed during Archean transpression based on their ductile overprint and presence within shear zones. Quartz veins are seen boudinaged within shear zones and are sometimes offset by infilled shear fractures. These extensional quartz veins form perpendicular to the maximum direction of elongation.

Every pluton shows microscopic solid state deformation textures indicative of dislocation creep with the quartz and feldspar mineral phases, revealing that peak metamorphic conditions

reached at least 450°C, the temperature at which dislocation creep becomes effective within the crystal lattice of feldspars (Passchier and Trouw, 2005). Undulose extinction, serrated grain boundaries and subgrains within feldspars are consistently observed across all plutons. Within quartz, common deformation microstructures include undulose extinction, subgrains, serrated grain boundaries and recrystallization along grain boundaries. Strain in the form of ductile deformation is pervasive through all outcrops studied – even towards the centers of the plutons.

The hydrothermal alteration/metasomatism of the plutons is also remarkably similar in all plutons studied. Alteration minerals occur in their highest intensity within close proximity to the chlorite and/or epidote infilled shear fractures and include chlorite, epidote group minerals, white mica (mostly phengite) and sphene with lesser amounts of calcite and hematite. The brittle deformation of the plutons is greatest near the margins where strain is concentrated due to the contrasting competencies of the granitoids and the surrounding weaker greenstone. Since the alteration is directly associated with brittle deformation, the intensity of the alteration minerals is also greatest near the margins of the plutons. Thin sections taken in lower strain zones where brittle fracturing is not abundant display very little alteration mineral assemblages.

Six of the twelve plutons (Sabaskong batholith, Dryberry batholith, Revell batholith, Ottertail pluton, Irene-Eltrut batholithic complex and the Croll Lake Stock) host evidence for coeval brittle-ductile deformation during Archean tectonics in the form of ductilely deformed quartz veins and/or the presence of chlorite and/or epidote infilled shear fractures within shear zones. This is important as it highlights that brittle deformation was ongoing during peak metamorphism associated with Archean tectonics.

Figure 3 shows the approximate outcrop locations where the brittle and/or ductile deformation were studied. Note that due to the scale of the map, some stars represent clusters of outcrops. GPS coordinates of all outcrops studied are shown in Appendix I.

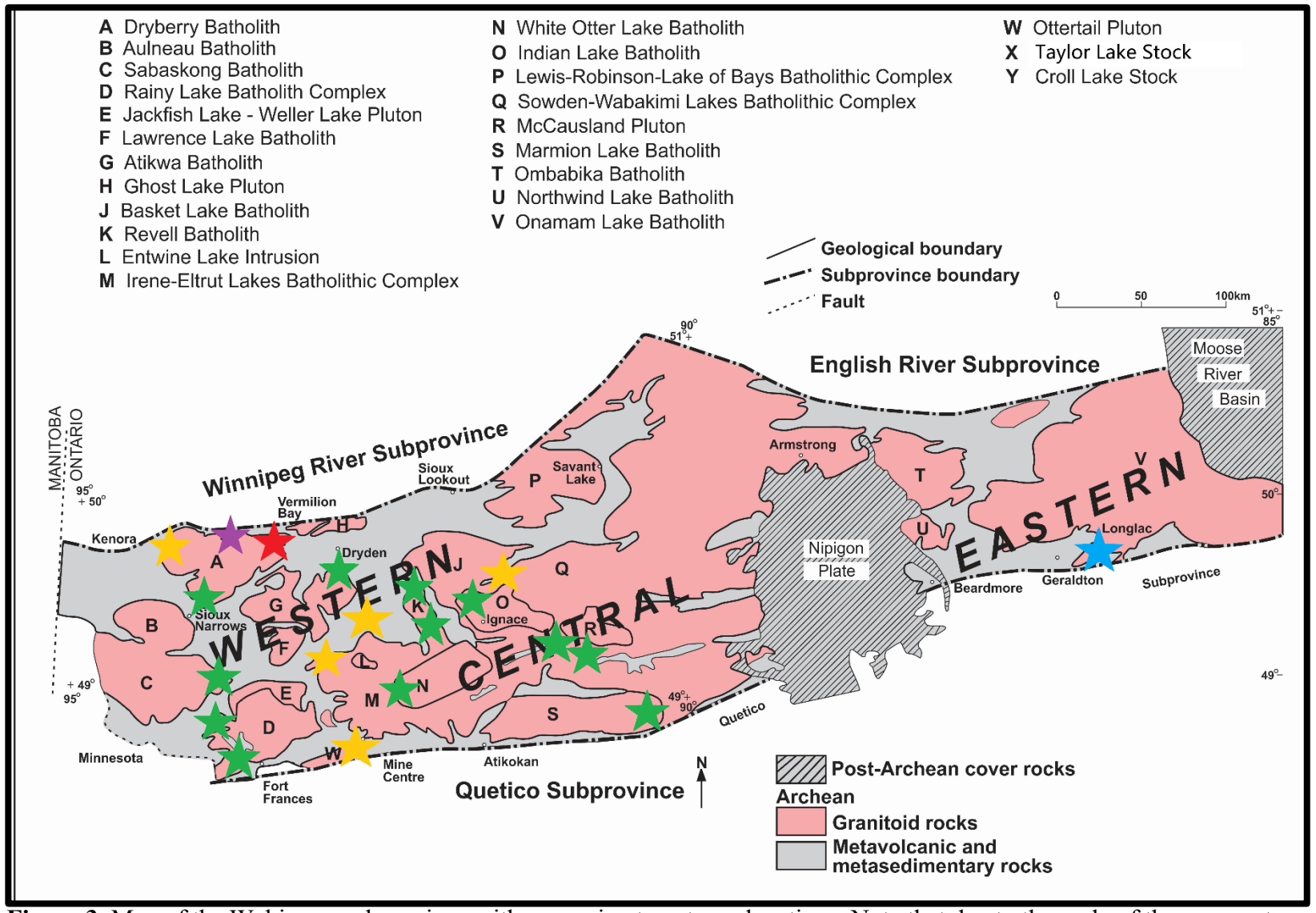

Figure 3. Map of the Wabigoon subprovince with approximate outcrop locations. Note that due to the scale of the map, not all individual outcrops can be shown. Green stars represent 1 outcrop, red 2 outcrops, yellow 3 outcrops, blue 4 outcrops and purple 5 outcrops. Modified from Blackburn et al. (1991).

Table 1. General features of Wabigoon subprovince plutons from this study.

Pluton	Region	Shear fractures with sub-horizontal slickenlines?	Dislocation creep in quartz and feldspar?	Alteration mineral assemblage	Shear Zones	Presence of dykes in outcrops studied?	Evidence for coeval brittle-ductile deformation?
Ottertail	Western	Yes (plunging 10 to 33 with an outlier of 65)	Yes	Epidote, chlorite, white mica, sphene, carbonate	Yes	No	Yes
Sabaskong	Western	Yes (plunging from 00 to 22)	Yes	Epidote, chlorite, white mica, biotite	Yes	No	Yes
Dryberry	Western	Yes (plunging 12 to 27)	Yes	Epidote, chlorite, white mica, sphene	Yes	No	Yes
Taylor Lake	Western	Yes (plunging 04 to 16 with an outlier of 45)	Yes	Epidote, chlorite, biotite, white mica, sphene, calcite	No	Yes- Partially metamorphosed to amphibolite	No
Atikwa	Western	Yes (plunging 02 to 08)	Yes	Epidote, chlorite, white mica, sphene, calcite	No	No	No
Irene-Eltrut	Western	Yes (plunging 10 to 22)	Yes	Epidote, chlorite, white mica, sphene, biotite, calcite	Yes	No	Yes
Revell	Central	Yes (plunging 8 to 10)	Yes	White mica, epidote, chlorite, sphene	No	No	Yes
Indian Lake	Central	Yes (plunging 02 to 15)	Yes	White mica, epidote, chlorite, sphene	No	No	No
White Otter	Central	Yes – plunging 08	Yes	White mica, epidote, chlorite, hematite	No	No	No
Sowden-Wabakimi	Central	Yes (plunging 10 to 21)	Yes	Epidote, chlorite, sphene, white mica	Yes	Yes - amphibolite	No
Marmion	Central	Yes (plunging 21)	Yes	White mica, epidote, chlorite, biotite	No	No	No
Croll Lake	Eastern	Yes- not measured	Yes	Chlorite, epidote, white mica, biotite, sphene	Yes	No	Yes

4.2 Western Wabigoon subprovince

4.2.1 Ottertail Pluton

The Ottertail pluton outcrops near Mine Center, Ontario. Twenty-nine structural orientations were collected from three outcrops – one located near the western margin of the pluton, another near the eastern margin and the last from the center of the pluton (Figure 4). Hand samples from each outcrop were collected for thin sections. Strain is pervasive throughout the pluton, and the intensity of strain varies from its highest degree in the marginal outcrops and its lowest degree in the middle outcrop. All outcrops lack a penetrative foliation and/or lineation.

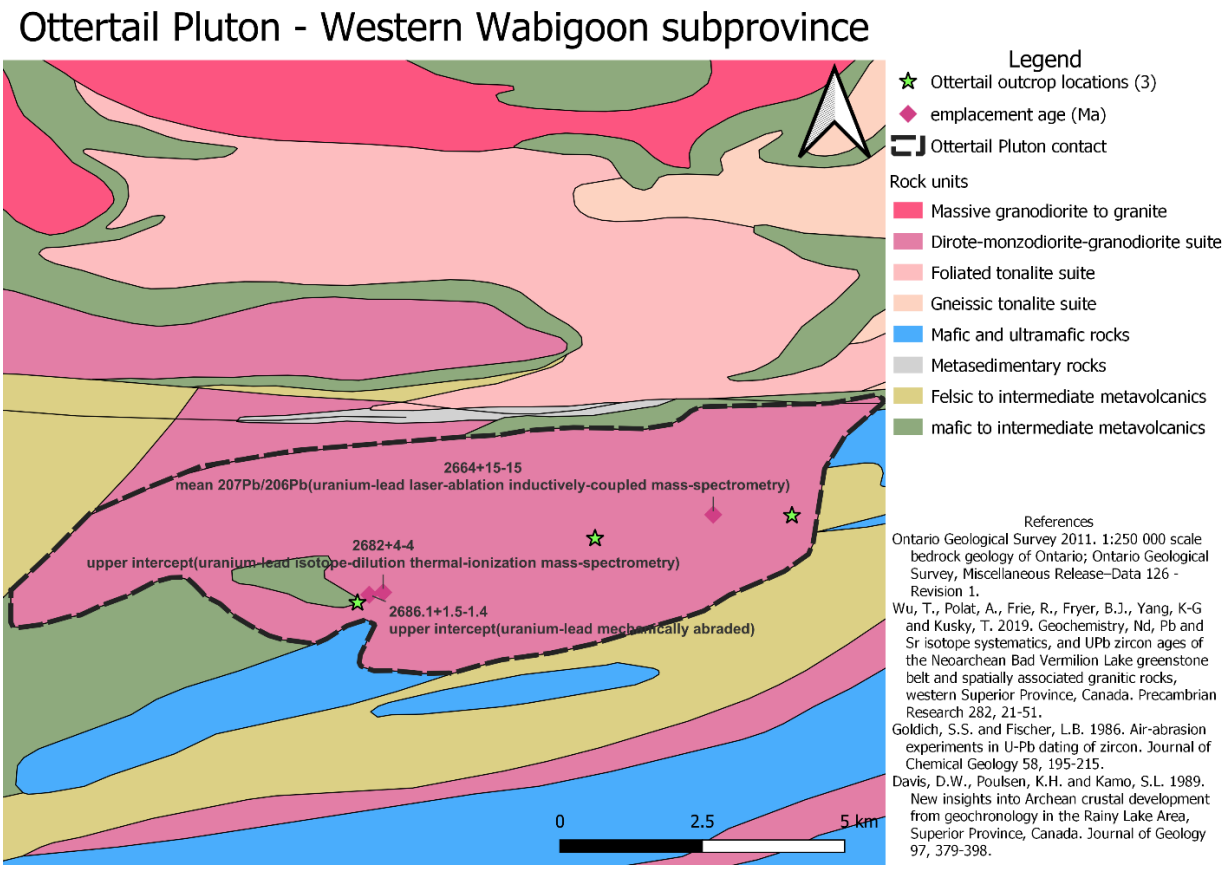

Figure 4. Geologic map of the Ottertail pluton (pink unit in center of map) with the locations of the 3 outcrops visited. Also shown are the available pluton emplacement ages of the Ottertail pluton.

Mineralogy and alteration

The mineralogy of the Ottertail pluton is comprised of quartz, plagioclase feldspar and potassic feldspar with accessory minerals hornblende, biotite and metasomatic/hydrothermal sphene, epidote, chlorite, white mica (phengite and sericite), calcite and opaques (Figure 5). Although the mineral percentages vary across the three outcrops, the magmatic quartz and feldspars make up the bulk of the rock (~85%) while the accessory minerals make up the remaining 15%. The degree of alteration minerals (epidote, chlorite, white mica, sphene and carbonate) is highest in the marginal two outcrops where brittle fracturing is most abundant. Epidote occurs as a replacement of feldspars, along microfracture terminations within the rocks, and along shear fractures. Some feldspars show a strong degree of sericite/white mica alteration while others show only a minor 'dusting'. Chlorite appears infilling shear fractures, microfractures and as a replacement of magmatic biotite. Calcite occurs predominately with epidote within shear fractures but may also occur along microfractures. Epidote and chlorite are the most abundant alteration minerals within the host rock. A representative photomicrograph of the chlorite-epidote alteration is shown in Figure 5.

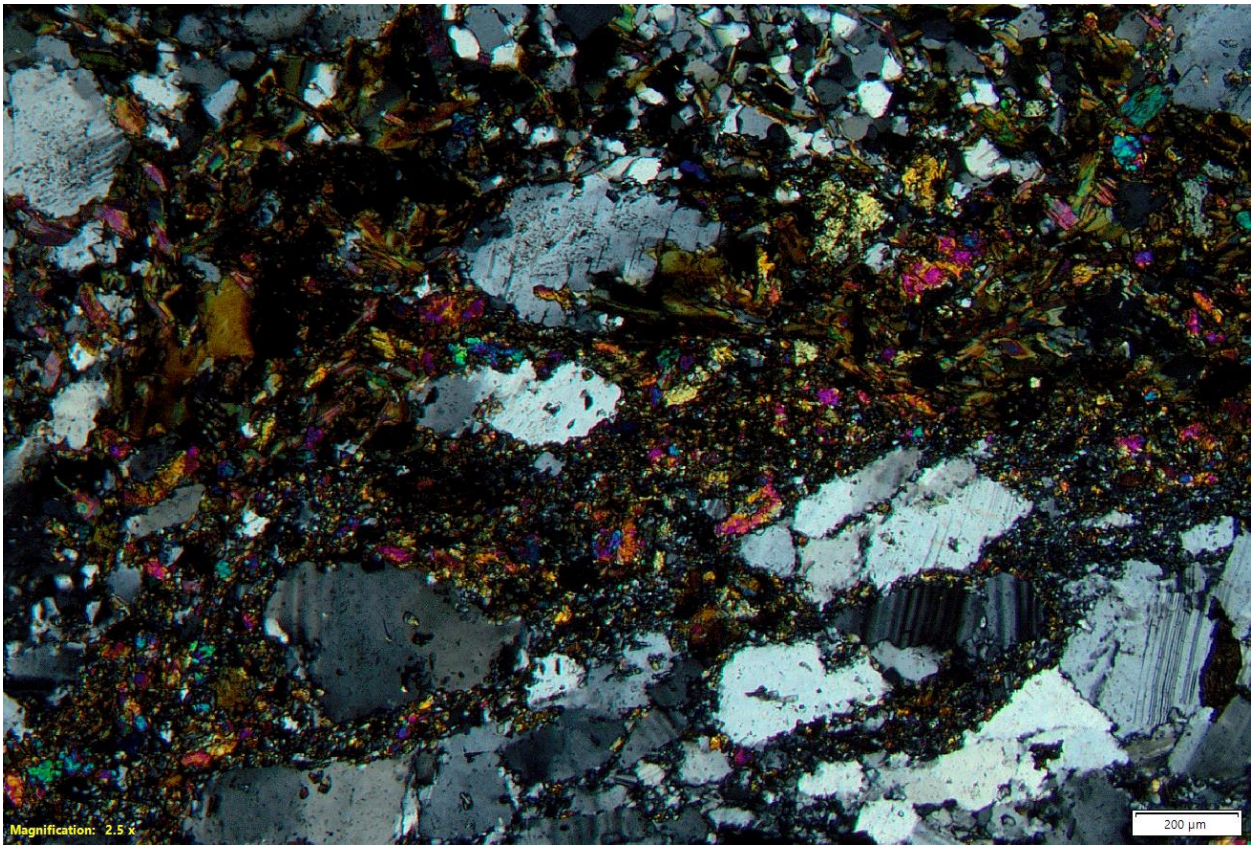

Figure 5. Photomicrograph of epidote-chlorite alteration along microfractures and grain boundaries. Cross Polarized Light (XPL). Scale bar is 200 µm.

Macrostructural analysis

The most abundant macroscopic brittle deformation features within the Ottertail pluton consists of chlorite and/or epidote infilled shear fractures with sub-horizontal slickenlines that have plunges ranging between 10° and 33°, with the exception of one slickenline plunge of 65°. These infilled shear fractures (seventeen measured in total) have dips ranging between 62° and 90° and show a conjugate strike-slip relationship in the field (Figure 6). Although a conjugate strike-slip relationship is noted in the field, the strike of the chlorite and/or epidote shear fractures vary across the pluton (Figure 7, Figure 8).

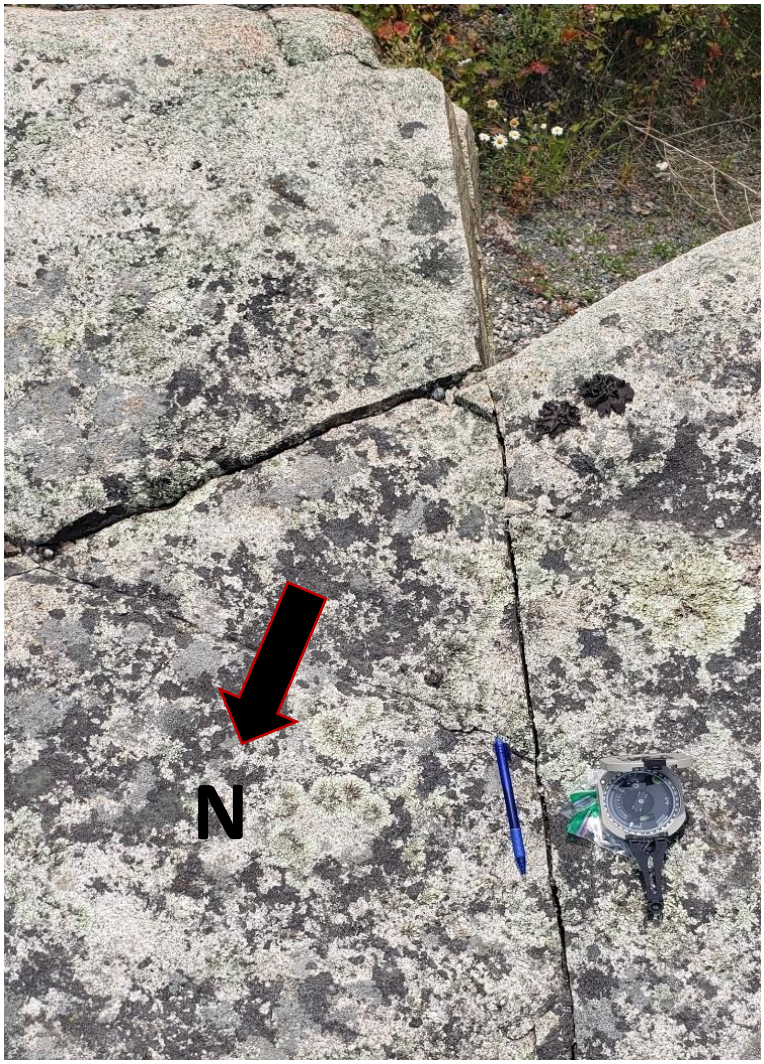

Figure 6. Two infilled shear fractures displaying a conjugate strike-slip relationship within the Ottertail Pluton of the western Wabigoon subprovince. Plan view.

Other measured macroscopic deformation features include mixed infilled veins (chlorite, epidote, and quartz accounting for two orientation measurements), quartz veins (one), a brittle-ductile shear zone (one), and unfilled fractures (eight). The orientations of the various brittle deformation features are shown with a stereonet (Figure 7). Figure 8 breaks down individual stereonets for the two major populations (chlorite infilled shear fractures and unfilled fractures) along with their accompanying rose diagrams. It is possible that the steeply dipping unfilled fracture population may be weathered out infilled shear fractures – although no conclusions can be made.

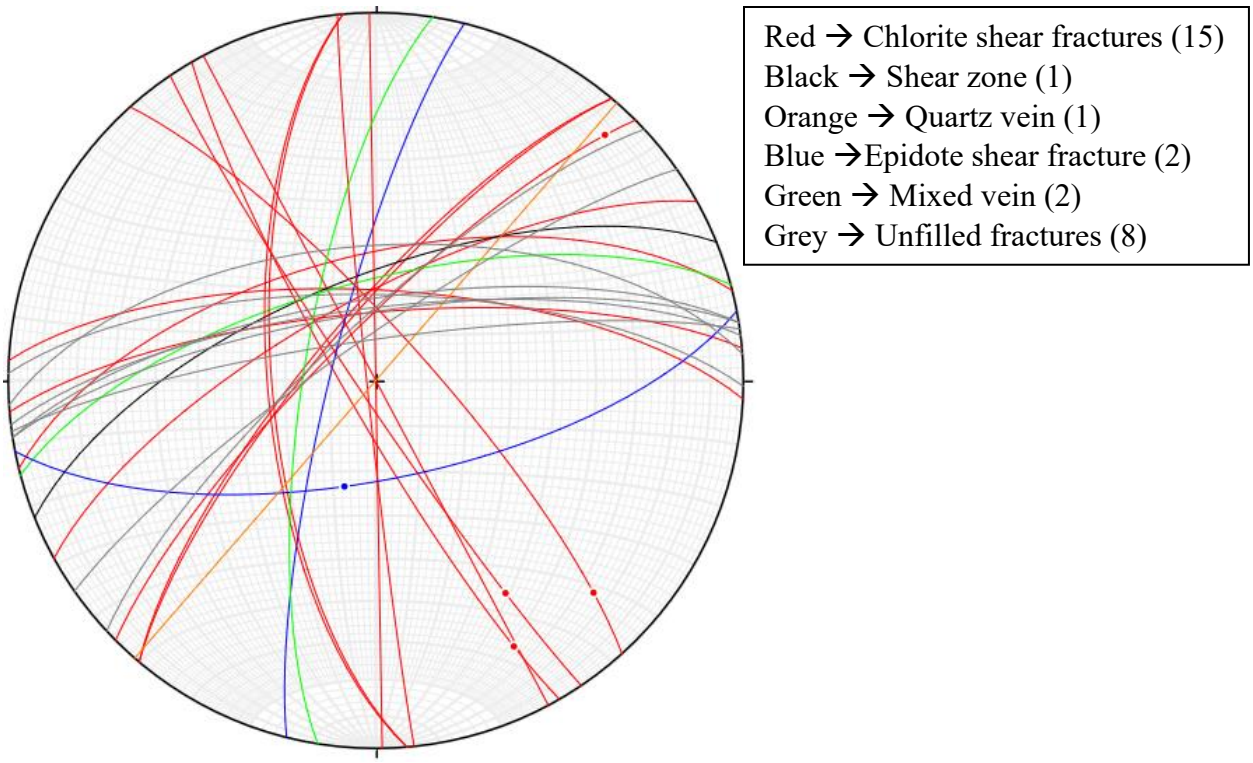

Figure 7. Stereonet displaying the macro-scale brittle deformation orientations recorded within the Ottertail Pluton.

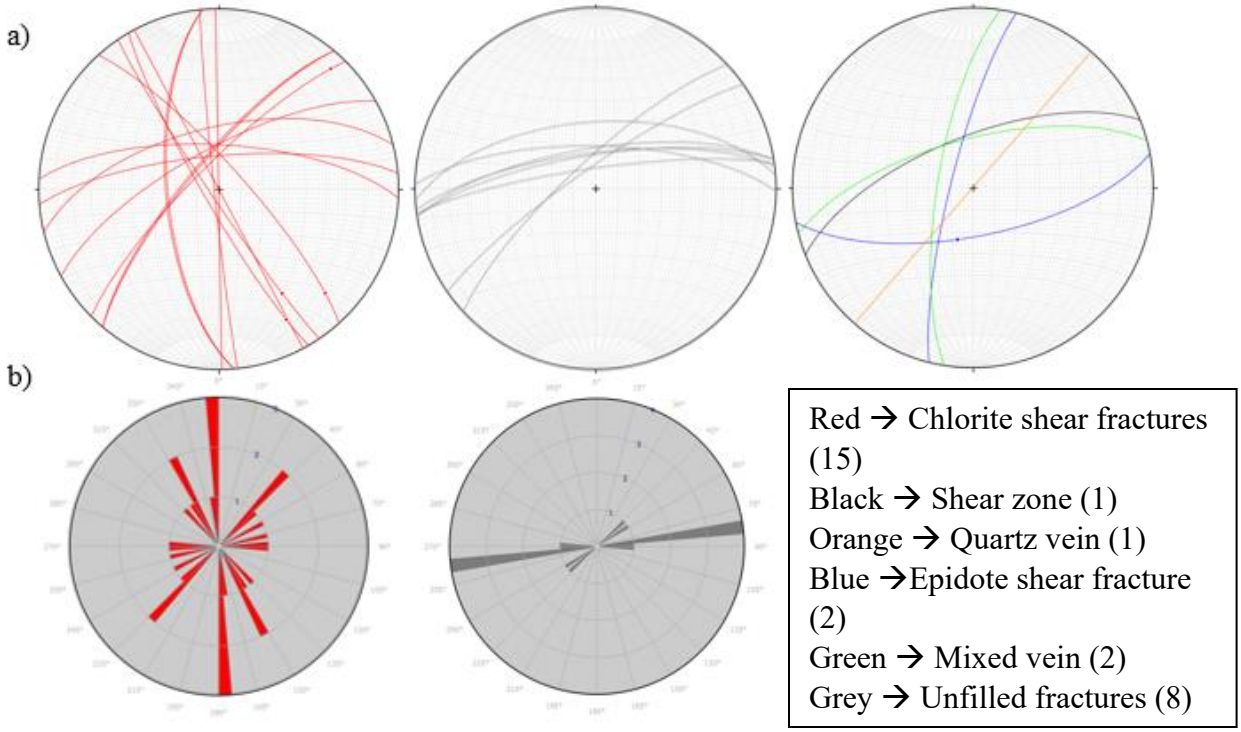

Figure 8. Individual stereonets and rose diagrams for the macro-scale deformation features within the Ottertail pluton.

Microstructural analysis

Samples taken from the Ottertail pluton can be divided into low strain and high strain samples. Low strain samples are those that lack a penetrative grain size reduction associated with shear zones. Within the low strain population of samples, deformation microstructures within the feldspar phases include strong undulatory extinction, serrated grain boundaries, deformation twins (when twinning is present), subgrains and intragranular microcracks that are sometimes infilled with epidote group minerals. Some of the largest plagioclase feldspars have intragranular deformation bands composed of very fine grained (<0.1 mm) feldspars with undulose extinction and serrated grain boundaries. The presence and abundance of these deformation bands decrease with increasing distance from high strain zones. Myrmekyte and perthite are also preserved in the lowest strain samples of the western Ottertail pluton. Quartz within the western Ottertail pluton is typically very fine to fine grained (<0.5 mm) but can also reach diameters of up to 3 mm. The coarsest quartz population have deformation microstructures including serrated grain boundaries with bulging of crystals into adjacent quartz, strong checkered undulose extinction, subgrains and minor recrystallized quartz along grain boundaries. The finer grained quartz has weak (or lack of) undulose extinction with smooth to semi-serrated grain boundaries, likely due to recrystallization. These low strain samples lack foliation or lineation. Accessory minerals within the western Ottertail pluton also show some evidence of ductile deformation. Relict hornblende laths commonly display undulose extinction and minor subgrains. Biotite laths (including the ones that have been partially replaced by chlorite) also display undulose extinction and bending of laths. Epidote group minerals commonly have minor undulose extinction with minor subgrains. The low strain samples in the eastern portion of the Ottertail pluton are very similar to those in the western region, although samples taken from the eastern portion of the Ottertail are slightly higher strain as evidenced by the presence of epidote-carbonate infilled shear fractures and slightly finer grain sizes. Deformation microstructures remain the same within the quartz and feldspars.

In the center of the pluton, thin section analysis shows a lower degree of alteration when compared to the marginal outcrops. This is likely due to less brittle fracturing in the center of the pluton (as noted during field work). The central outcrop has roughly the same grain size distribution within the quartz and feldspar phases as the other two outcrops, but the presence of a single feldspar reaching up to 10 cm in length is also noted. This coarse feldspar has moderate undulose extinction, serrated grain boundaries and subgrains. Deformation microstructures within the remaining feldspars include undulose extinction of various degrees (some feldspars exhibit

minor undulatory extinction while others display strong checkered undulatory extinction), semi-serrated grain boundaries, subgrains and deformation twins. There is a notable decrease in the degree of feldspar fracturing in the central outcrop and a complete lack of intragranular deformation bands. Although recrystallization is still present in the form of subgrains and finely recrystallized feldspars around grain boundaries of coarser feldspar, the degree of recrystallization is less than what is seen in the marginal outcrops. Quartz within the central outcrop displays a strong undulatory extinction, serrated grain boundaries, subgrains and a moderate dimensional preferred orientation (DPO) not seen within either of the marginal outcrops. Accessory minerals in the central outcrop include all minerals seen in the marginal outcrops – but only account for less than 10 % of the bulk rock volume. Figure 9 shows a photomicrograph of a representative low strain sample in the Ottertail pluton.

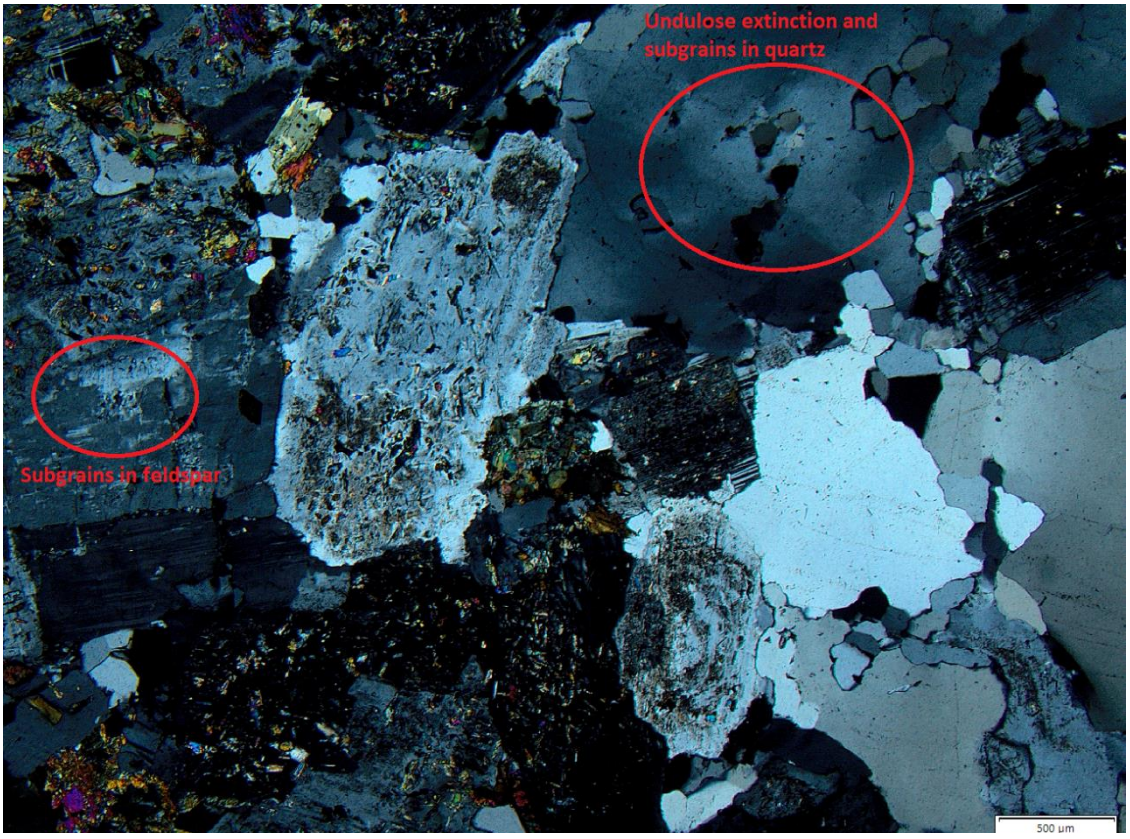

Figure 9. Photomicrograph of a representative low strain sample within the Ottertail pluton (XPL). Scale bar is 500 µm.

Evidence for coeval brittle-ductile deformation

Thin section analysis of the Ottertail pluton demonstrates evidence for coeval brittle-ductile deformation. A quartz vein sampled within the Ottertail pluton shows a strong ductile deformation overprint in cross-polarized light – indicative of ongoing ductile deformation during accompanying brittle deformation (Figure 10). Evidence for the ductile deformation of the quartz vein consists of dislocation creep textures such as strong undulose extinction, subgrains and recrystallization.

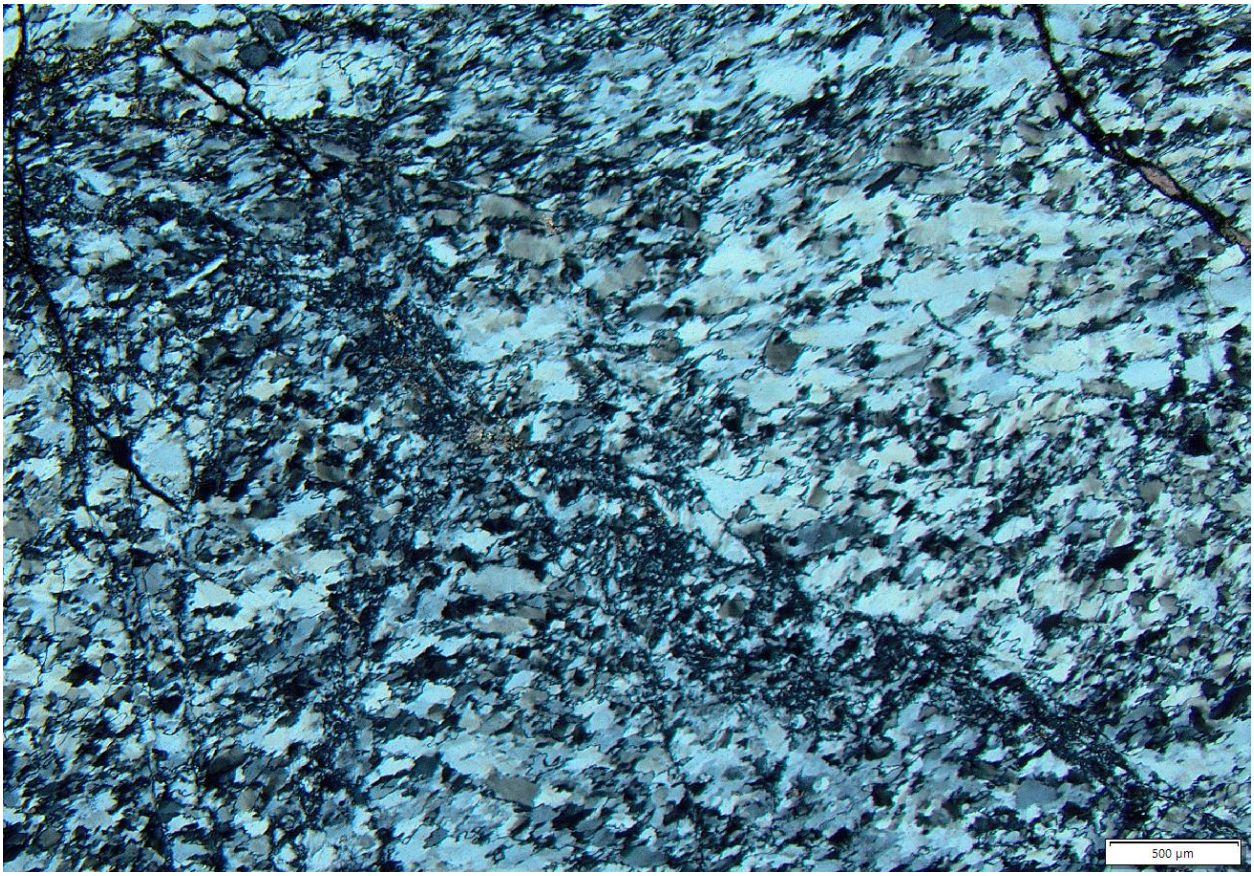

Figure 10. Photomicrograph of a quartz vein with a strong ductile overprint, evidence for coeval brittle-ductile deformation (XPL). Scale bar is 500 µm.

Another indicator of high-temperature brittle deformation stems from the presence of an ultracataclasite/potential recrystallized pseudotachylyte within the eastern outcrop of the Ottertail pluton. Representative photomicrographs of the ultracataclasite or possibly recrystallized pseudotachylyte are shown in Figure 11. In thin section in plane polarized light (PPL), the pseudotachylyte and ultracataclastite units are aphanitic and light brown to dark brown in color. There are also several parallel trending dark bands that anastomose around some feldspar and quartz porphyroclasts that range from rounded to angular in shape, depending on the location of

the porphyroclasts within the high strain zone. In XPL, both units appear ‘glassy’ in the sense that the unit seems isotropic and mineral phases are difficult to identify. The relationship between the angular/circular habit of the porphyroclasts with respect to their location in the high strain zone is difficult to assess with regular petrographic approaches but becomes much clearer with SEM-BSE imaging (Figure 11C). In Figure 11C, the bottom half of the image shows the high strain area of interest. Feldspar and quartz porphyroclasts along the margins of the high strain zone are semi-angular to circular in geometry while the porphyroclasts near the center of the high strain zone are sharply angular. The ultracataclasite / pseudotachylyte vein is also noted to have several injection veins extending out from the main vein at varying angles – most often at low to moderate angles with occasional high angle veins. These injection veins are common features of both pseudotachylyte and ultracataclasite. Also of importance is the notable increase in muscovite alteration close to the high strain zone that is not noted elsewhere in the Ottertail pluton. Since muscovite alteration is directly related to hydrothermal fluid flow in crystalline rocks, it follows that the increase in muscovite corresponds to an increase in brittle deformation that can be associated with both pseudotachylyte and ultracataclasite formation.

The most reliable way to identify pseudotachylyte is to demonstrate that the fault rock has undergone melting at some point – which largely relies on a combination of optical and scanning-electron microscope techniques (Kirkpatrick and Rowe, 2013). Textures indicative of a solidified melt phase include (from Kirkpatrick and Rowe, 2013):

1. Quenched margins defined by cryptocrystalline or glassy material at the edges of veins.
2. The presence of microcrystallites within the matrix that have a lath-shaped habit, a prismatic/dendritic habit or display spinifex texture.
3. Survivor clasts with partial melting textures.
4. Euhedral micro-crystals that quench from the melt and display oscillatory or irregular zoning.

The above textures are predominately found in ‘pristine’ pseudotachylyte as pseudotachylyte is much more susceptible to deformation, alteration and overprinting than its surrounding host rock after solidification – largely due to the presence of meta-stable glass, very fine grain sizes and competency contrasts with the surrounding host rock which favors localization of deformation along the rheologically weaker pseudotachylyte (Kirkpatrick and Rowe, 2013). Melt origin pseudotachylyte can commonly be seen with sharp edges and concentric color banding indicative of quenched margins (Kirkpatrick and Rowe, 2013). Kirkpatrick and Rowe (2013) also

note that pseudotachylyte vein material is typically composed of a brown to black aphanitic matrix that contains rounded clasts of feldspars and quartz (which are more competent mineral phases resistant to melting during frictional sliding). It should also be noted that relict clasts in pseudotachylyte tend to be rounded whereas cataclasite rock types that lack melting tend to be composed of more angular clasts (Lin, 1999; Kirkpatrick and Rowe, 2013).

Using SEM-BSE imaging, no textures of solidified melt were identified in the potential pseudotachylyte. This may be due to one factor or a combination of the following: 1) the unit is not a pseudotachylyte, 2) subsequent recrystallization and deformation has overwritten the evidence for a solidified melt phase, or 3) the scale used on the SEM was too low to successfully identify the textures. The apparent isotropic nature of the light to dark brown matrix coupled with the increase in muscovite alteration and the presence of rounded feldspar and quartz porphyroclasts is enough to conclude the possibility of a pseudotachylyte, but not enough to prove undoubtably its existence.

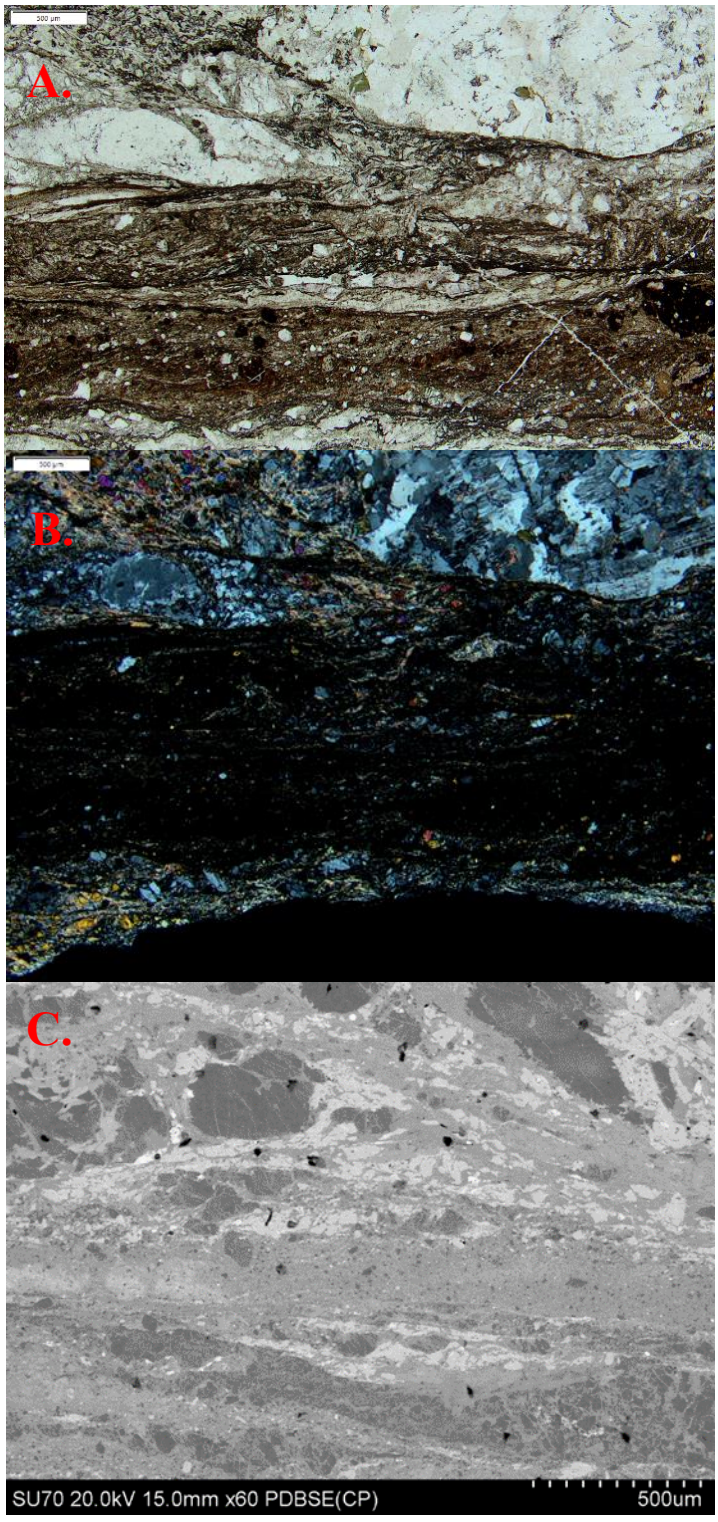

Figure 11. a) Photomicrograph of potential pseudotachylyte and ultracataclasite (PPL). Scale bar is 500 µm.
b) Potential pseudotachylyte and ultracataclasite (XPL). Scale bar is 500 µm.
c) SEM-BSE image of potential pseudotachylyte and ultracataclasite showing rounded and angular clasts.

4.2.2 Sabaskong batholith

Seven thin sections and thirty-five orientations of fractures and faults were taken from one outcrop of the Sabaskong batholith that outcrops along Highway 71, north of Fort Frances (Figure 12, Figure 13). The outcrop is characterized by lack of penetrative foliation and fine to medium grained quartz and feldspars.

Figure 12. The Sabaskong batholith outcrop located along Highway 71. The steeply dipping fractures are chlorite and/or epidote infilled shear fractures while most of the sub-horizontal fractures are unfilled.

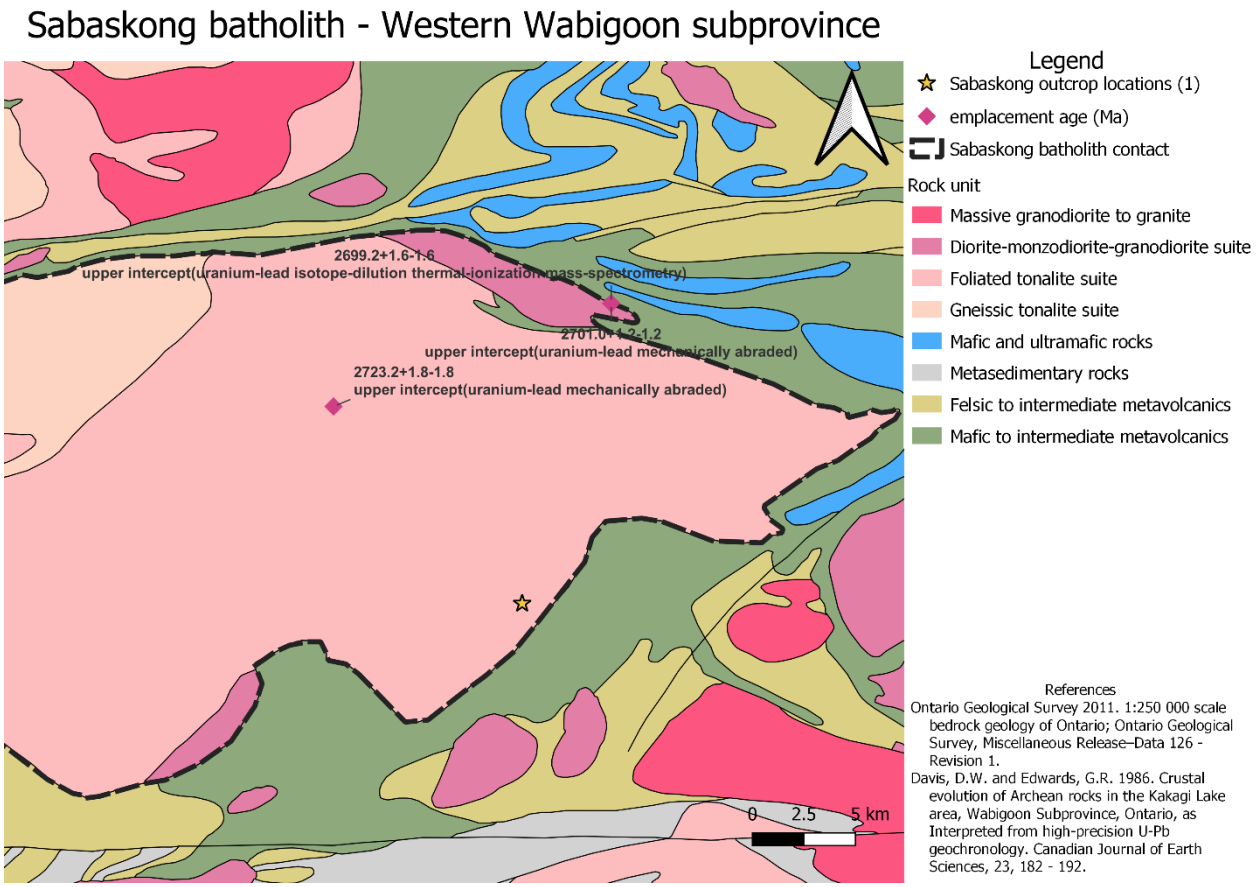

Figure 13. Map of the Sabaskong batholith showing the location of the one outcrop studied. Also shown are interpreted batholith emplacement ages.

Mineralogy and alteration

The Sabaskong batholith is composed of roughly 50% feldspar group minerals and 20% quartz with magmatic biotite (5%) and alteration minerals such as white mica (10%), biotite (5%) epidote (5%), chlorite (<5%), sphene (<5%) and opaques (<5%) (Figure 13). Quartz and feldspars are fine to medium grained with quartz roughly 1 – 1.5 mm on average and feldspars roughly 1 – 3.5 mm. White mica is typically very fine to fine grained and occurs exclusively as a replacement of feldspars, though is not always present. Epidote occurs infilling shear fractures, along microcracks within the host rock and along grain boundaries. Chlorite occurs as shear fracture infilling, along microfractures and replacing biotite in some areas. Sphene is associated with epidote and biotite. A representative photomicrograph of the alteration is shown in Figure 14.

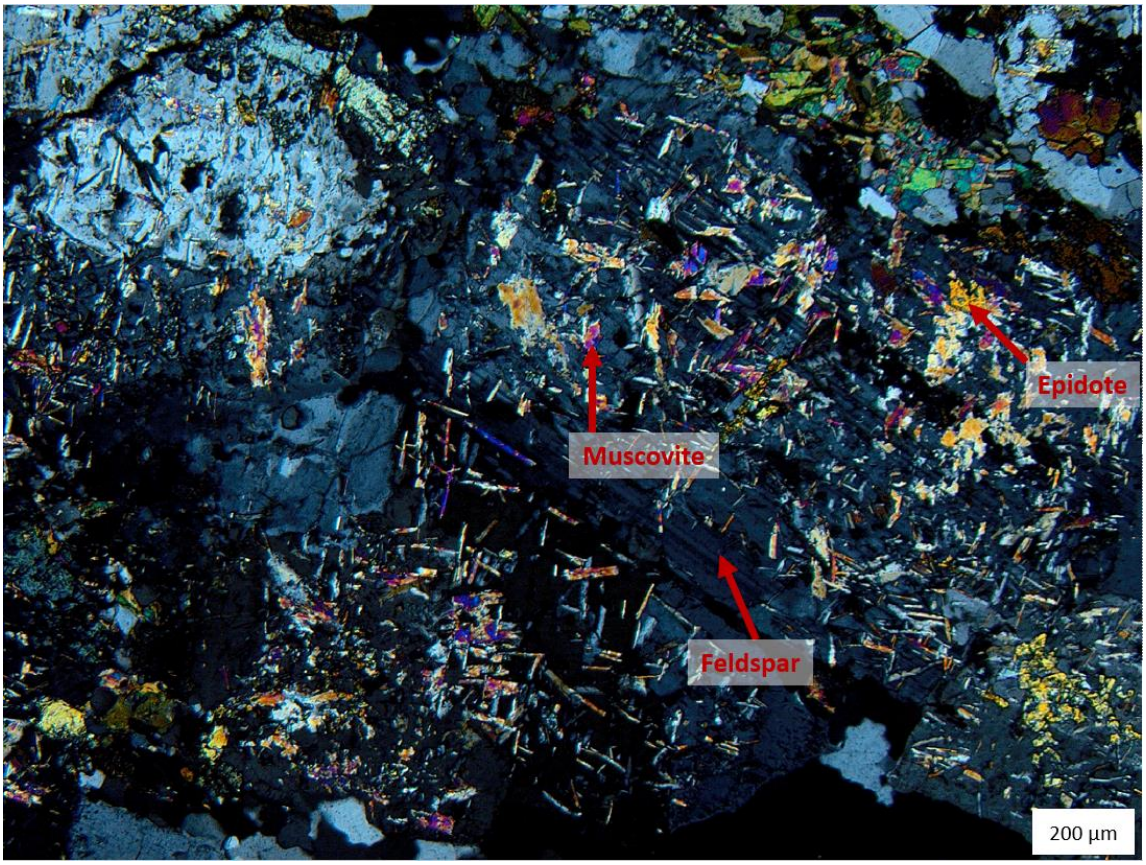

Figure 14. Photomicrograph of white mica-epidote alteration within feldspar (XPL). Scale bar is 200 µm.

Macrostructural analysis

Of the thirty-five structural orientations taken in the Sabaskong batholith, twenty-four are chlorite and/or epidote infilled shear fractures, two are shear zone contacts, one is a quartz vein, and eight are unfilled fractures. Of the chlorite and/or epidote infilled shear fractures, seven of them have slickenlines with plunges that range between 0° and 22°, indicative of an oblique strike-slip displacement along the shear surfaces. Dips of these infilled shear fractures range from 15° to 90°, with an average of 71° and a mean of 80°. A stereonet showing the structural orientations measured in the Sabaskong batholith can be seen in Figure 15. Figure 16 shows the individual stereonets for each type of structure measured as well as rose diagrams for the two major structures measured (infilled shear fractures and unfilled fractures).

Figures 15 and 16 show two major orientations of the infilled shear fractures – one population striking south and the other striking south-east, conforming to a conjugate strike-slip relationship expected for oblique strike-slip shear fractures.

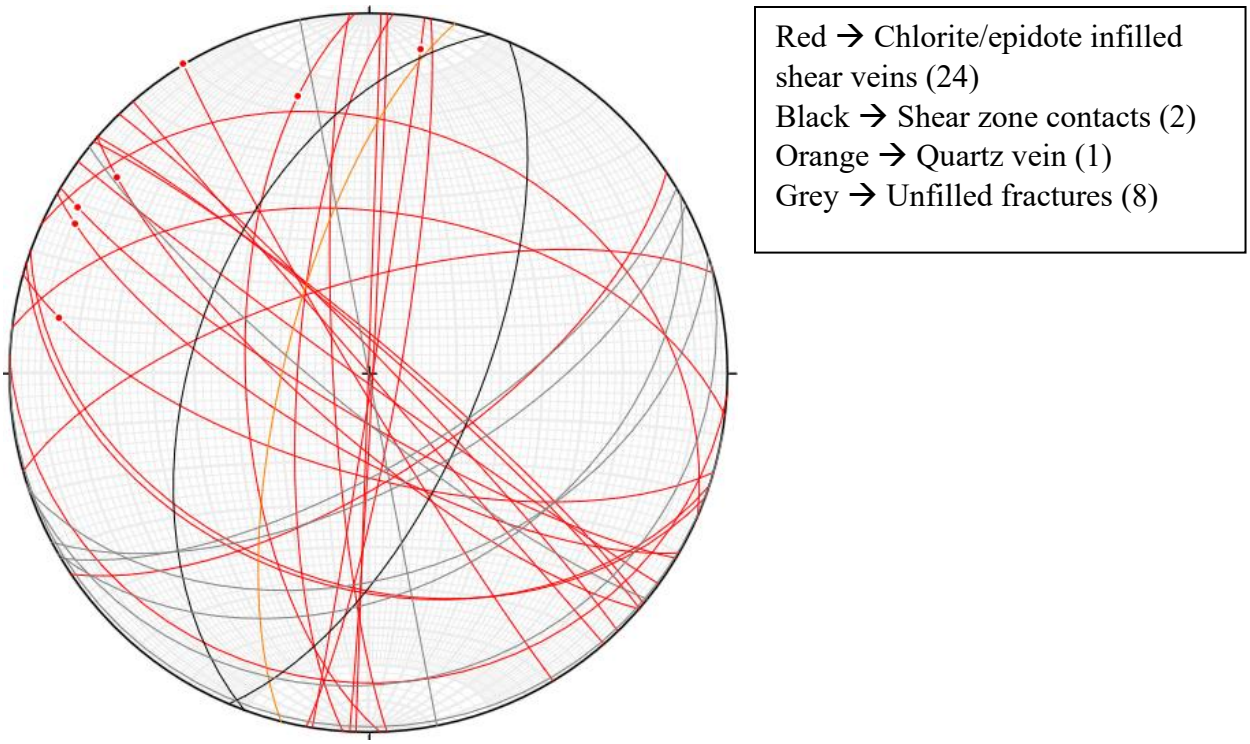

Figure 15. Stereonet of all orientation measurements taken in the Sabaskong Batholith outcrop. 35 measurements in total. Legend shown in upper right corner.

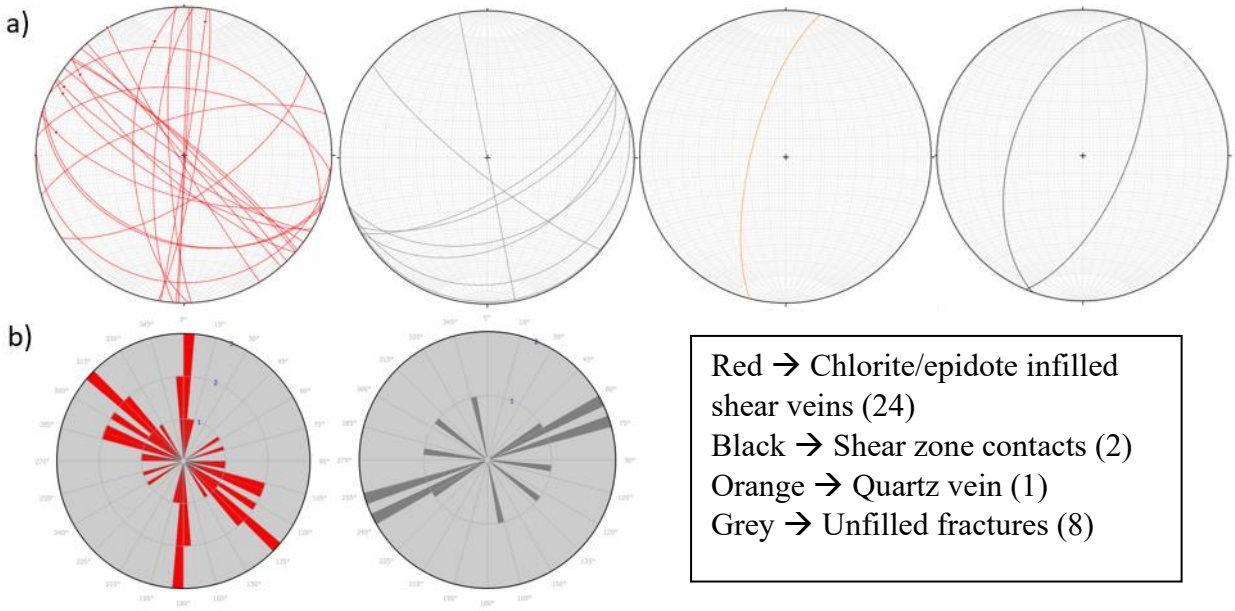

Figure 16. Stereonets of all measurements taken from Sabaskong Batholith outcrop. **b)** Rose diagrams for the infilled shear fractures and unfilled fractures.

Microstructural analysis

The low strain samples of the Sabaskong batholith display deformation microstructures within the quartz that include strong undulatory extinction, heavily serrated grain boundaries and subgrains. Localized patches of quartz have a moderate to strong dimensional preferred orientation (DPO) but lack a crystallographic/lattice preferred orientation (CPO/LPO). Feldspars are altered to muscovite and epidote group minerals which masks some of the deformation microstructures present. Through the alteration, undulatory extinction and subgrains are commonly seen. Grain boundaries are serrated, and deformation twins can be seen when twinning is visible. Minor recrystallization of the feldspars can be seen along grain boundaries. Although strain is pervasive, perthite, myrmekyte and primary zoning can also still be observed in some of the feldspar crystals. Kinked biotite laths with coronas of very fine-grained biotite are also present within the Sabaskong batholith. These biotite laths have undulose extinction and minor subgrains. Overall, there is no penetrative microscopic foliation or lineation within any of the low strain samples of the Sabaskong batholith. A representative photomicrograph of a low strain sample is shown in Figure 17.

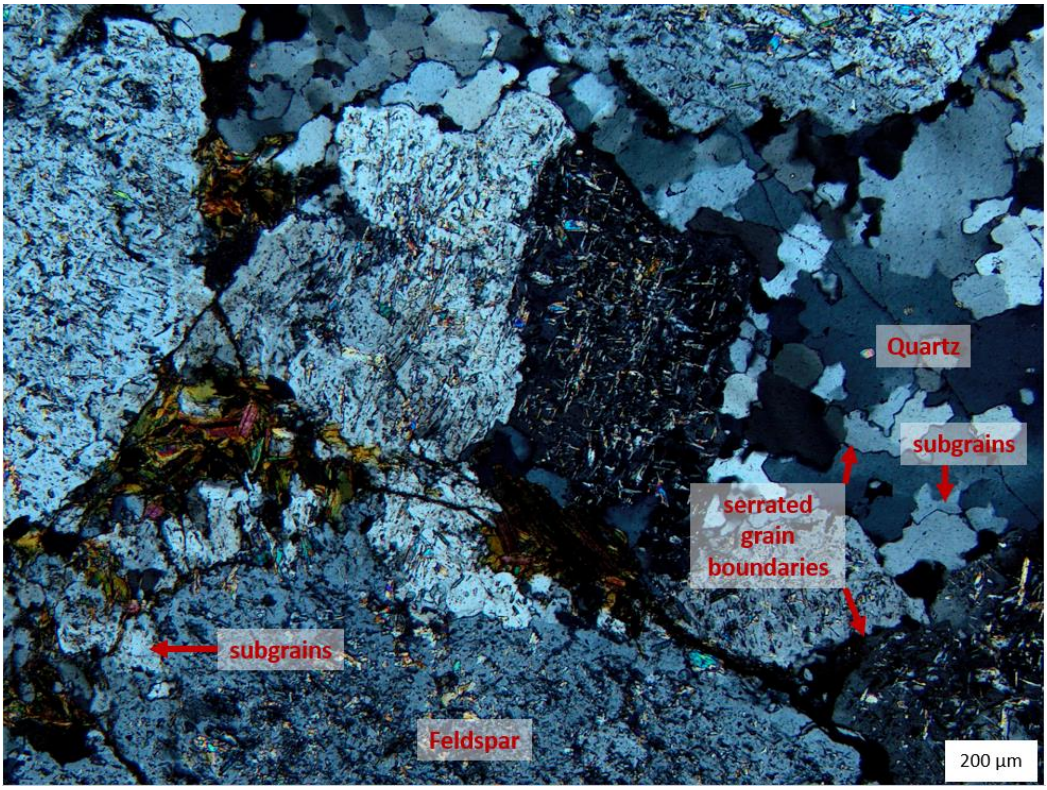

Figure 17. Photomicrograph of a representative low strain sample within the Sabaskong batholith. Quartz and feldspar have irregular grain boundaries, subgrains and undulose extinction (XPL). Scale bar is 200 µm.

Three thin sections taken from the Sabaskong batholith represent high strain zones (shear zones). Two of the shear zones are characterized as brittle-ductile shear zones while the third is a ductile shear zone. In outcrop, the brittle-ductile shear zone has a strong penetrative fabric defined by the parallel alignment of several mm-wide chlorite infilled shear fractures (Figure 18). Boudinaged quartz veins run parallel to the chlorite shear fractures and the shear zone walls. The shear zone has sharp contacts with the surrounding lower strain host granitoid and is roughly 15 cm thick. In thin section, this brittle-ductile shear zone consists of a grain size reduced quartz and feldspar matrix that is extremely fine grained (<0.1 mm). There is a notable lack of porphyroclasts indicating that ductile grain size reduction was very prominent during shearing. Deformation microstructures in the grain size reduced quartz and feldspar include undulose extinction, serrated grain boundaries and subgrains (Figure 19).

Figure 18. A brittle-ductile shear zone within the Sabaskong batholith. Fabric is defined by the parallel alignment of chlorite infilled shear fractures and boudinaged quartz veins.

The second brittle-ductile shear zone differs from the first as it has the presence of feldspar porphyroclasts wrapped by chlorite infilled shear fractures (Figure 20). An extensional quartz vein within the shear zone has strong ductile overprint and displays deformation microstructures such as undulose extinction and serrated grain boundaries (Figure 21). Deformation microstructures within the grain size reduced matrix material are the same in both brittle-ductile shear zones.

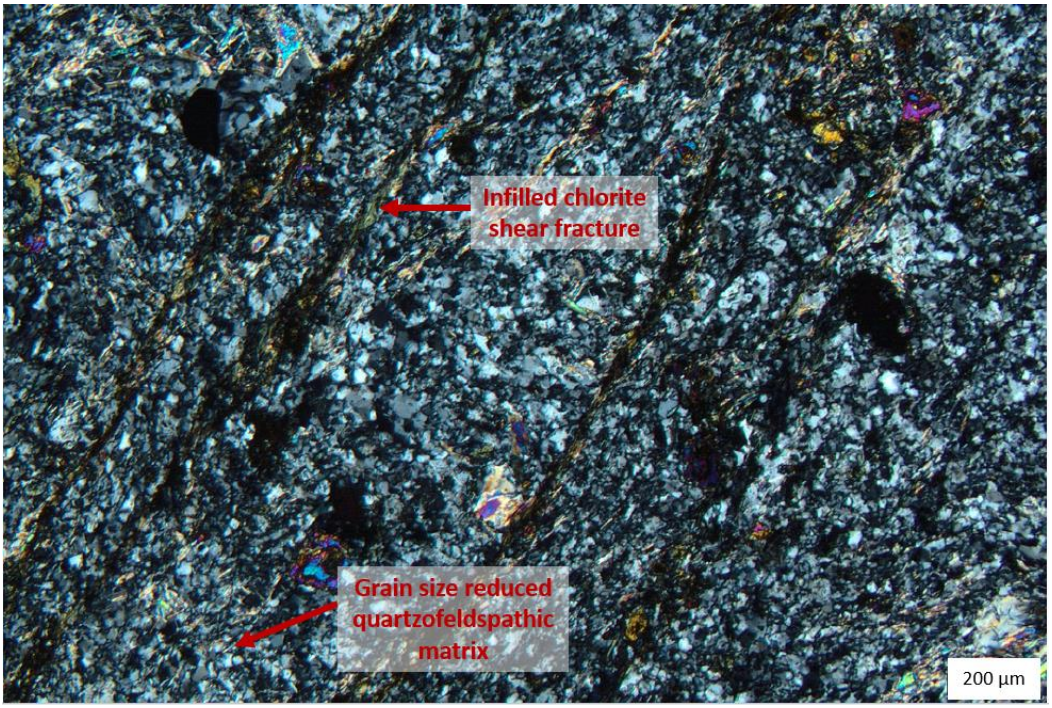

Figure 19. Photomicrograph of a brittle-ductile shear zone. Parallel striking chlorite-infilled shear fractures. Weak epidote-muscovite alteration can be seen in the grain-size reduced matrix (XPL). Scale bar is 200 µm.

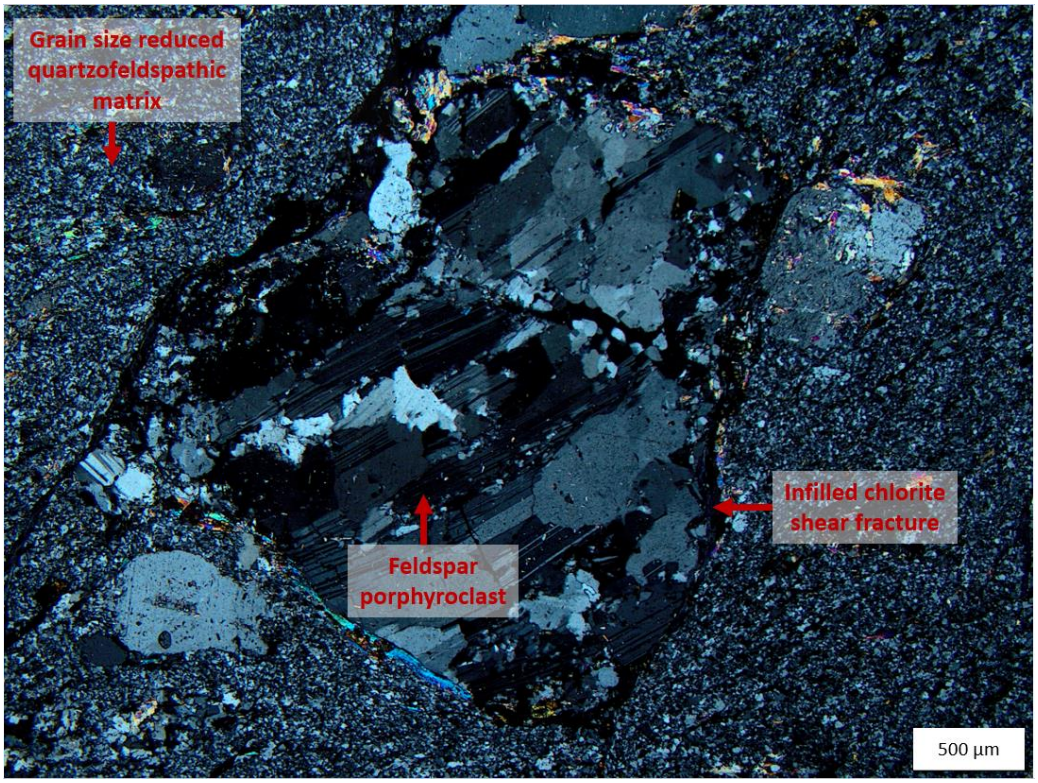

Figure 20. Photomicrograph of a feldspar porphyroclast with a chlorite-infilled shear fracture bounding it (XPL). Scale bar is 500 µm.

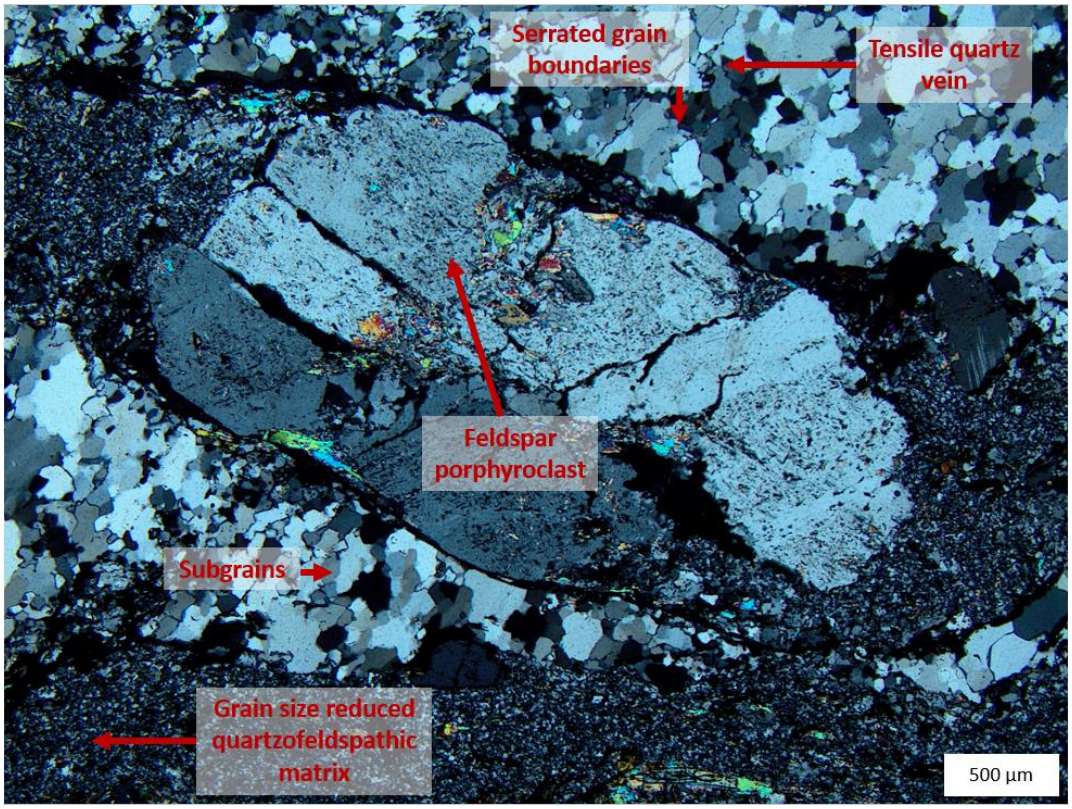

Figure 21. Photomicrograph of a brittle-ductile shear zone displaying a feldspar porphyroclast surrounded by grain size reduced quartz and feldspar. A ductiley deformed quartz vein with serrated grain boundaries, subgrains and undulose extinction is present (XPL). Scale bar is 500 µm.

The ductile shear zone differs from the brittle-ductile shear zone as it lacks shear fractures and quartz boudins. Feldspar porphyroclasts comprise roughly 10% of the rock volume and are commonly seen with serrated grain boundaries, deformation twins, primary magmatic zoning, undulose extinction and minor subgrains (Figure 22). Deformation microstructures within the grain size reduced quartz and feldspar include serrated grain boundaries, undulose extinction and subgrains. Note that the extent of grain-size reduction within the ductile shear zone is not as intense as in the brittle-ductile shear zone. The lower degree of grain-size reduction and the lack of brittle fractures in the ductile shear zone signifies that it is likely lower strain than the brittle ductile shear zone.

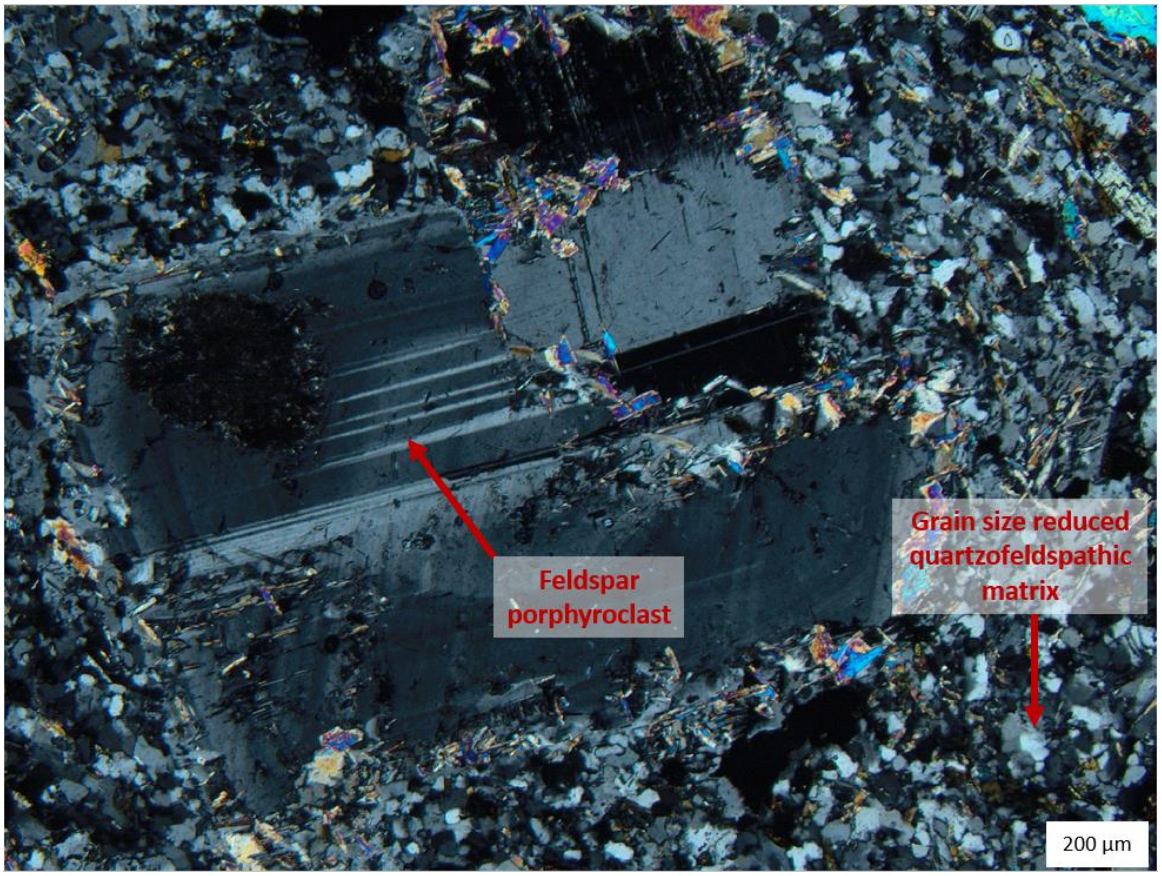

Figure 22. Photomicrograph of a feldspar porphyroclast within a grain size reduces matrix of quartz and feldspars from a ductile shear zone (XPL). Scale bar is 200 µm.

4.2.3 Dryberry Batholith

Eighty-seven structural orientations were measured across six outcrops of the Dryberry batholith and nineteen thin sections were made from hand samples collected at twelve outcrops. Figure 23 shows the approximate outcrop locations where the brittle and/or ductile deformation were studied.

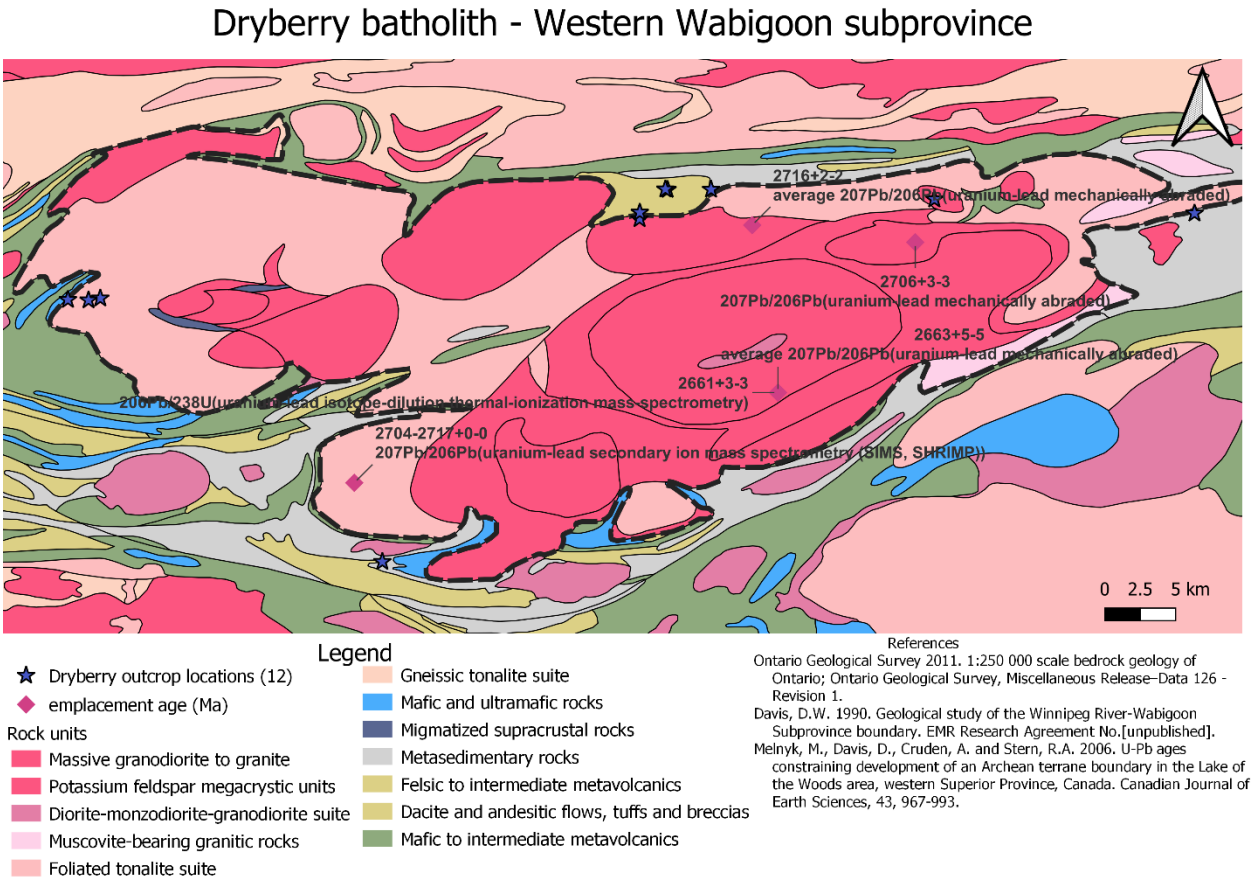

Figure 23. Geologic map of the Dryberry batholith. Blue stars show approximate outcrop locations where the brittle and/or ductile deformation were studied. Dark pink: massive granodiorite, light pink: tonalite, green: mafic metavolcanics, yellow: felsic metavolcanics, blue: mafic and ultramafic rocks.

Mineralogy and alteration

The mineralogy of the Dryberry batholith is primarily composed of quartz (20-25%), plagioclase feldspars (30-35%) and potassic feldspars (20-25%) with lesser amount of biotite (5%) and metasomatic/hydrothermal white mica, epidote, sphene and chlorite (Figure 24). The intensity of the alteration minerals is highest in the western outcrops of the batholith, with the central and eastern outcrops along Experimental Lakes Road and towards Vermillion Bay displaying the weakest alteration. Within the western outcrops, chlorite appears infilling shear fractures, along microfractures within the host rock and as a replacement of biotite. Epidote occurs infilling shear fractures, along microfractures, within shear zones and as a replacement of plagioclase feldspars along with white mica (saussuritization). White mica occurs predominately as a replacement of feldspars but is not always present. A representative photomicrograph of the alteration within the western outcrops of the Dryberry batholith is shown in Figure 24. In the central and eastern portion of the batholith, both epidote and chlorite are present as fracture infilling. Within the host rock itself, white mica and epidote are the most abundant alteration minerals but appear only as a weak replacement of feldspars along microfractures and grain boundaries. Some chlorite can also be found along microcracks and within feldspar. A representative photomicrograph of the alteration in the central and eastern outcrops is shown in Figure 25.

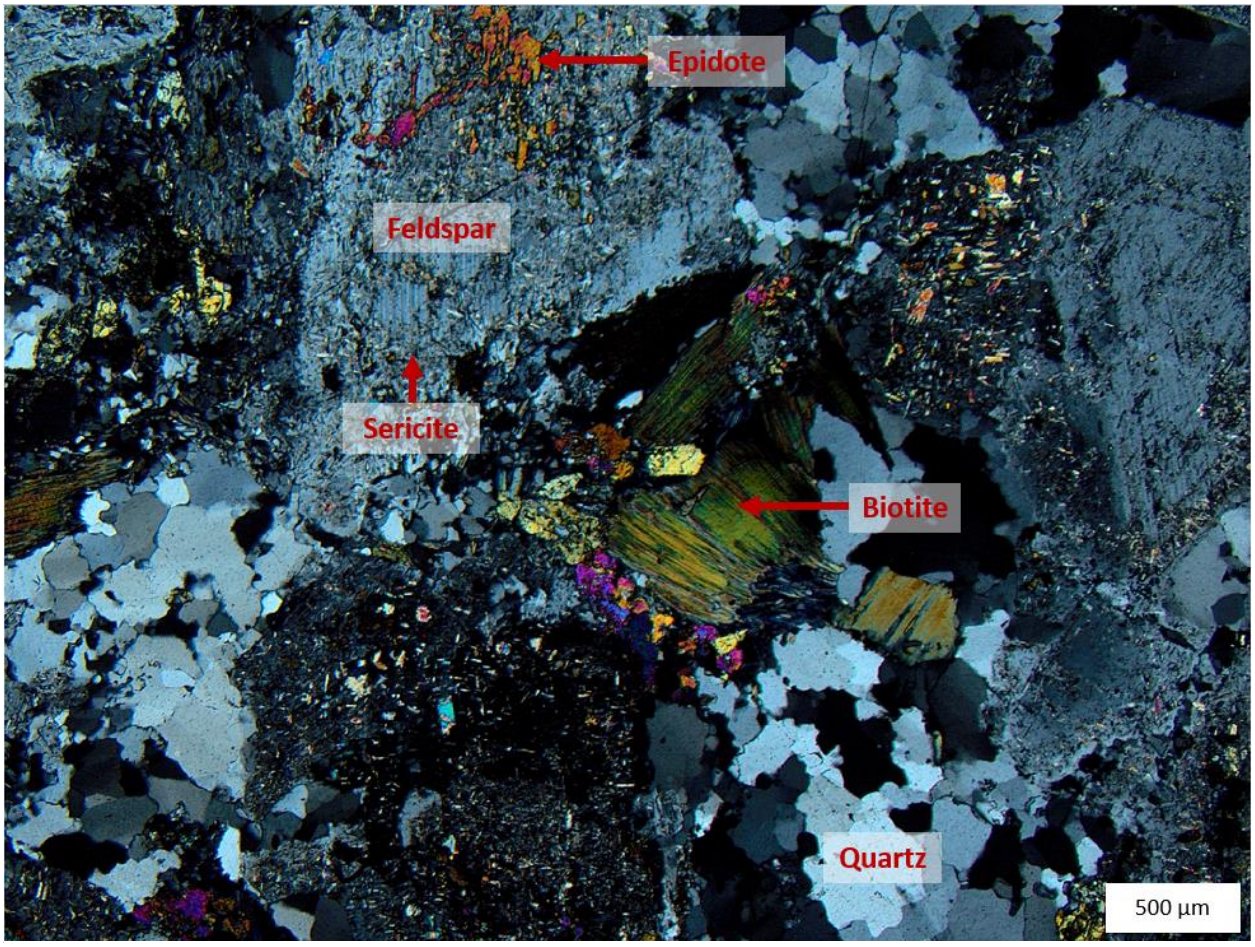

Figure 24. Photomicrograph of the typical alteration seen in the western and eastern margins of the Dryberry batholith. White mica-epidote alteration of the feldspars can be seen. Biotite with weak chlorite replacement is present. Epidote and biotite are typically clustered together in the host rock (XPL). Scale bar is 500 µm.

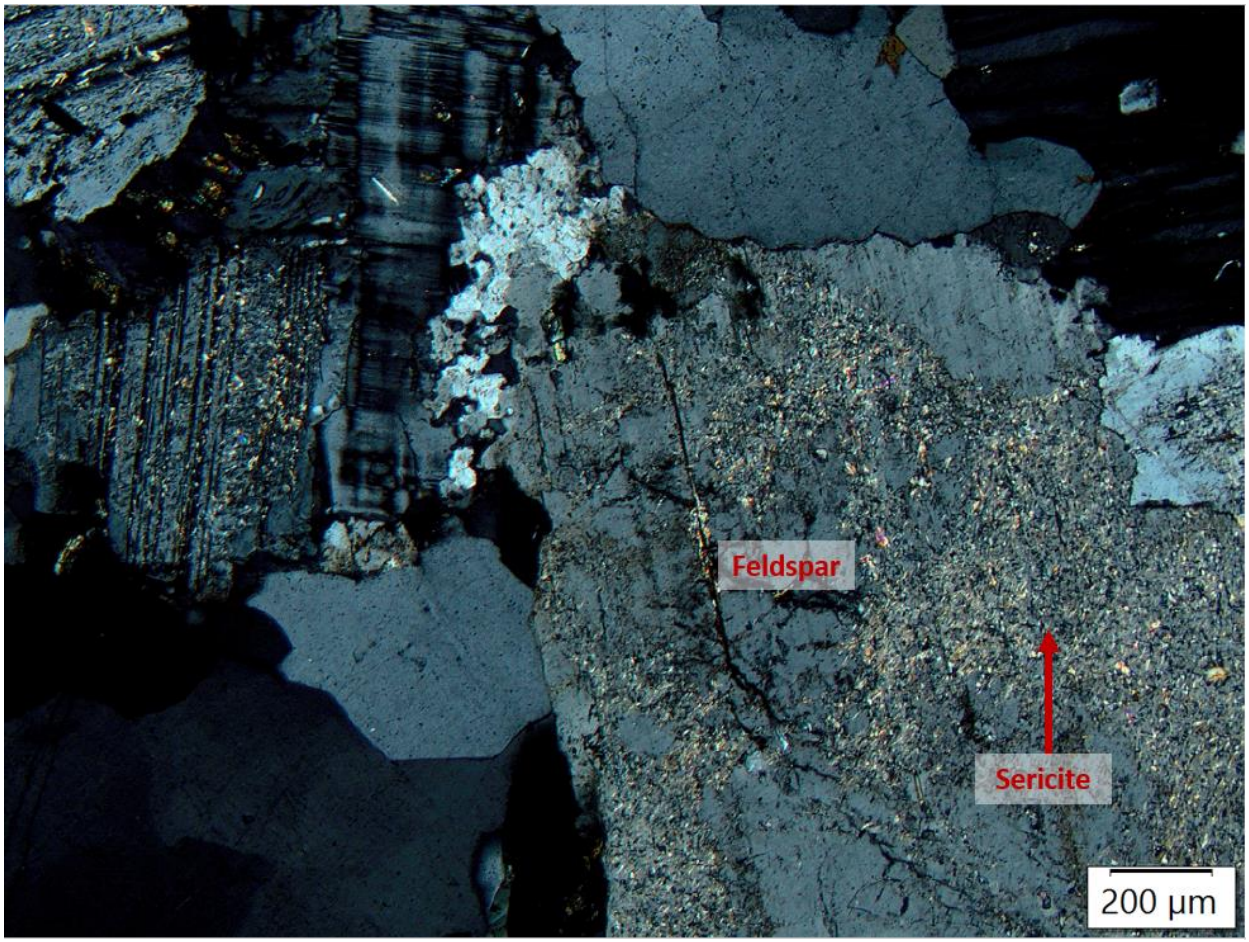

Figure 25. Photomicrograph of the typical alteration style (weak sericitization) seen in the central and eastern outcrops of the Dryberry batholith (XPL). Scale bar is 200 µm.

Macrostructural analysis

Eighty-seven structural orientations including chlorite and/or epidote infilled shear fractures (55), quartz veins (2), unfilled fractures (26), mixed infilled shear fractures (2), foliation (1) and a shear zone (1) were measured from six outcrops of the batholith. Figure 26 shows the stereonet for all collected structural data. Figure 27 shows individual stereonets and accompanying rose diagrams for the major orientation sets. The average dip of the fifty-five epidote and/or chlorite infilled shear fractures is 76° while the median is 80°, highlighting a fairly steep dip to the fractures. Slickenlines measured on nine of the shear fractures have plunges that range from 12° to 26°, again indicating a sub-horizontal displacement along the shear fractures. Although there is some consistency to the dip and slickenline orientation on the shear fractures, the strike of the

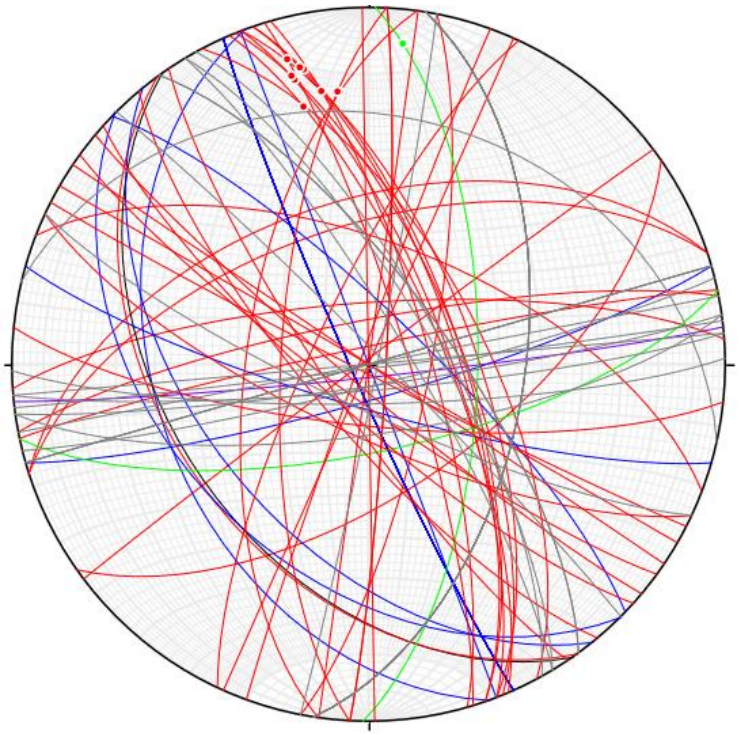

Red → Chlorite infilled shear fractures (38)
Orange → Quartz vein (2)
Grey → Unfilled fractures (26)
Green → Mixed veins (2)
Blue → Epidote infilled shear fractures (17)
Purple → Foliation (1)
Black → Shear zone (1)

Figure 26. A stereonet displaying all orientation measurements taken in the Dryberry batholith. Legend shown in the upper right-hand corner.

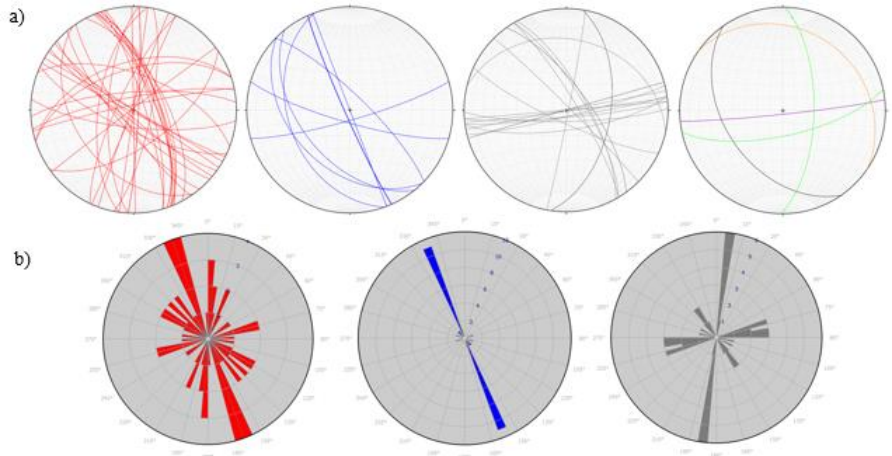

Red → Chlorite infilled shear fractures (38)
Orange → Quartz vein (2)
Grey → Unfilled fractures (26)
Green → Mixed veins (2)
Blue → Epidote infilled shear fractures (17)
Purple → Foliation (1)
Black → Shear zone (1)

Figure 27. a). Stereonets of all measurements taken in the Dryberry Batholith. **b)** Rose diagrams for the chlorite infilled shear fractures, epidote infilled shear fractures and the unfilled fracture population set.

shear fractures varies widely across the pluton. The unfilled fracture population is likely to represent weathered shear fractures, as the average dip for these fractures is 74° while the mean is 80°, remarkably similar to the dips of the infilled shear fractures. It's possible that the variation in strike of the shear fractures could be a function of non-coaxial strain in which the rigid and competent pluton itself has undergone a component of rigid body rotation during regional transpression, similar to the concept of a rigid garnet porphyroclast entrained within a shear zone. A component of rotation would result in a shifting trend of the maximum elongation direction, explaining the varying orientations of the infilled shear fractures. Some of the outcrops have more consistency to the orientation of the shear fractures, although the limited amount of orientation data available for each individual outcrop means that no conclusions should be made about the orientations of the shear fractures on an outcrop scale versus on a pluton scale.

Microstructural analysis

Microstructures that provide evidence for solid state deformation by dislocation creep within quartz and feldspars are seen across all twelve outcrops of the pluton. Both quartz and feldspars display subgrains, serrated grain boundaries, undulatory extinction and recrystallization along grain boundaries. Figure 28 shows a photomicrograph of recrystallization within the feldspars – seen in the central Dryberry outcrops. Feldspars also record micro-fracturing and deformation twins when twinning is present. Dislocation creep does not become an effective process within feldspar until temperatures reach 450°C (Passchier and Trouw, 2005), indicating that peak metamorphic temperatures within the Dryberry batholith must have reached at least the lower amphibolite facies of metamorphism. Dislocation creep is pervasive throughout all samples studied but is most notable within shear zones that record dislocation creep assisted grain-size reduction within the quartz and feldspar mineral phases.

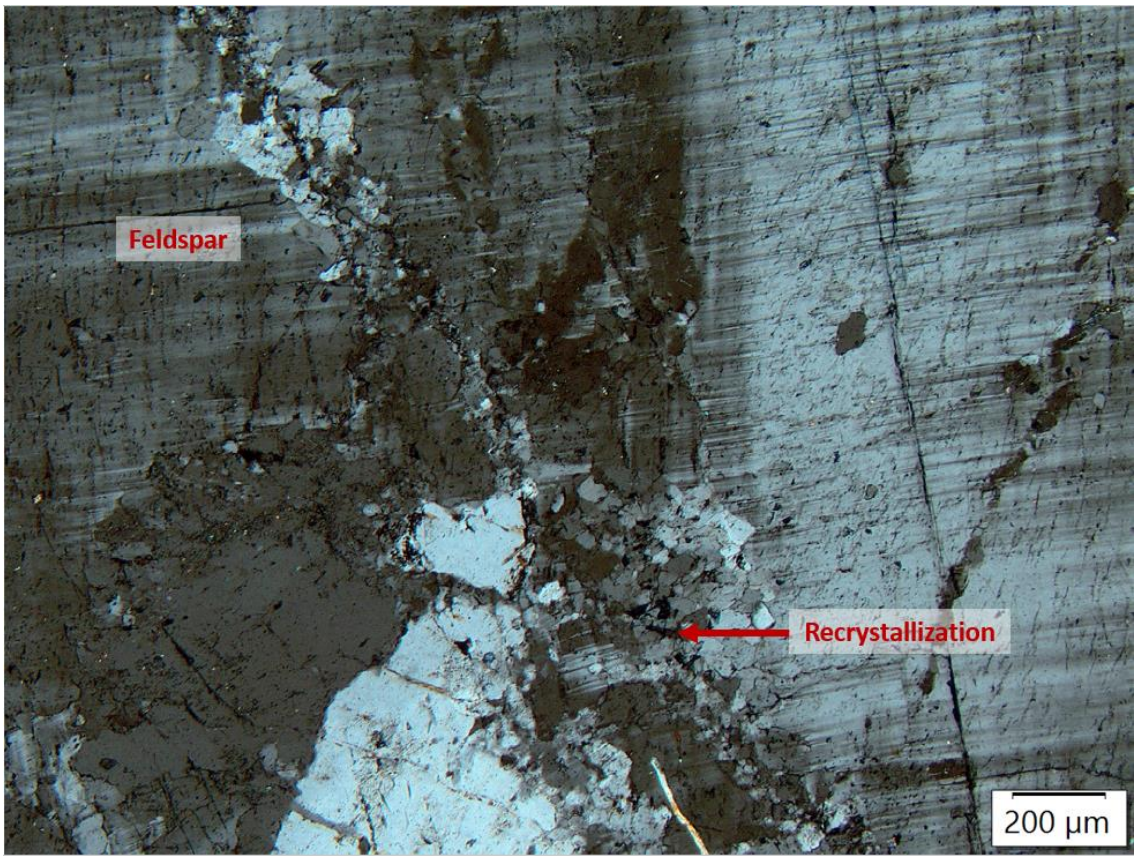

Figure 28. Photomicrograph of feldspar displaying recrystallization within one of the central outcrops of the Dryberry batholith (XPL). Scale bar is 200 µm.

Evidence for coeval brittle-ductile deformation

Although deformation is clear in thin section, outcrops of the Dryberry batholith typically lack a penetrative foliation. In an outcrop located along highway 71 (just south of the turn off to highway 17), a penetrative fabric is defined by the parallel alignment of quartz 'eyes' ranging in size from 1 mm x 1 mm to roughly 7 mm x 1 mm (Figure 29). The quartz eyes are composed of fine grained (~1 mm) quartz that has a ductile overprint shown by the presence of serrated grain boundaries, strong undulose extinction and minor subgrains (Figure 29). Quartz eyes are surrounded by grain-size reduced quartz (<0.5mm) and feldspars (<0.5 mm to 1.5 mm) and could potentially represent rotated and boudinaged extensional quartz veins. This zone of quartz eyes within a grain-size reduced matrix of quartz and feldspars likely represents a brittle-ductile shear zone within the Dryberry Batholith. Accessory minerals within the shear zone include epidote, biotite, chlorite and white mica. Deformation microstructures within the shear zone include undulatory extinction, grain size reduction and serrated grain boundaries of the quartz and feldspar.

The presence of these interpreted boudinaged quartz veins indicates ongoing brittle deformation during ductile deformation of the pluton.

Further evidence for coeval brittle-ductile deformation within the Dryberry batholith stems from a brittle-ductile shear zone that contains several parallel aligned epidote infilled shear fractures (Figure 30). This shear zone displays strong grain size reduction of the quartz and feldspar mineral phases and epidote alteration in the host rock.

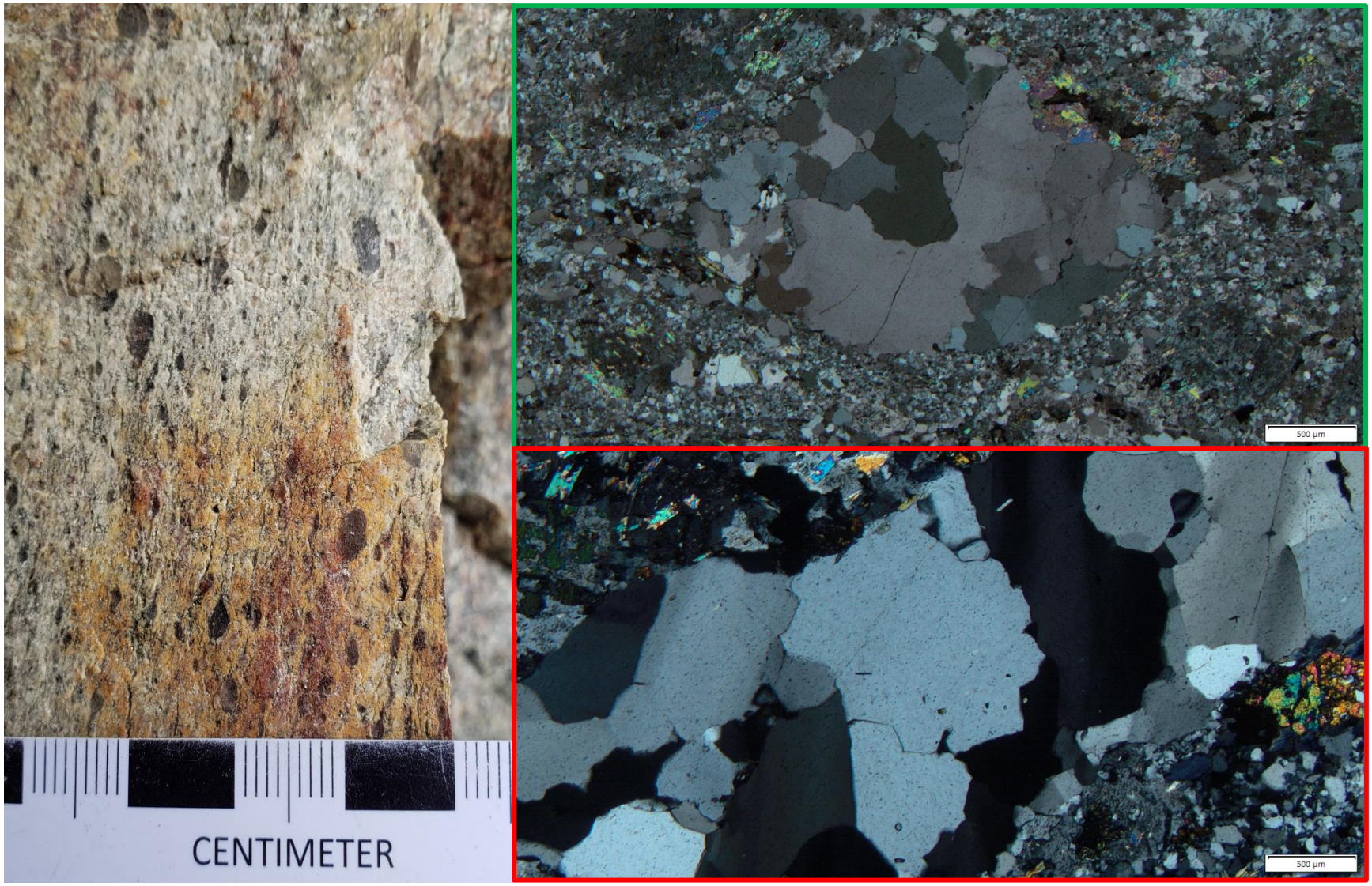

Figure 29. Left - Quartz eyes defining fabric in an outcrop of the Dryberry batholith located along Highway 71. Quartz eyes range from 1 mm x 1mm pods to 7mm x 1mm pods. Right – Photomicrograph showing undulatory extinction, subgrains and serrated grain boundaries within the quartz eyes (XPL). Scale is the same for both photomicrographs (500 µm).

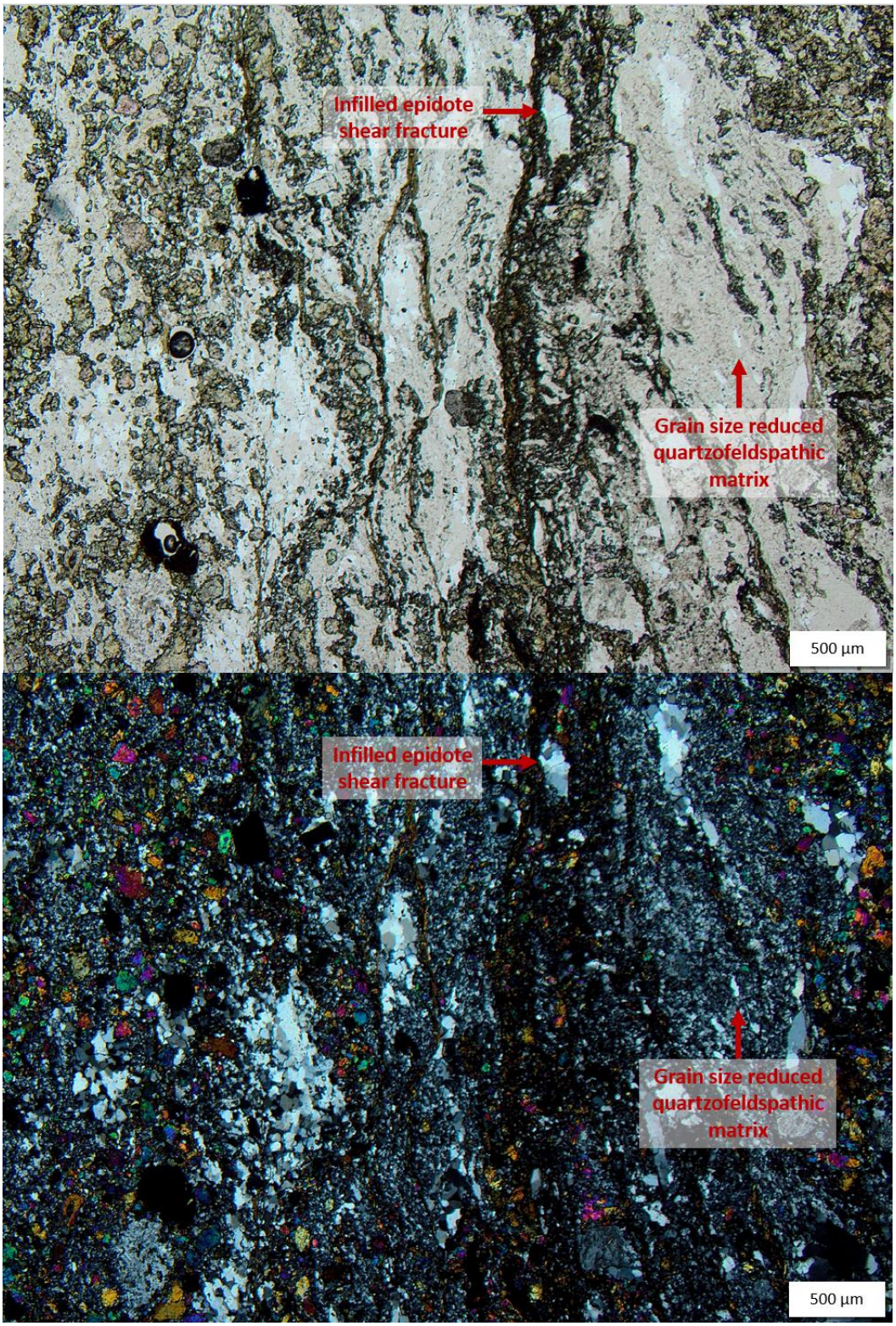

Figure 30. Photomicrograph of a brittle-ductile shear zone within the Dryberry batholith. Epidote infilled shear veins along with epidote alteration of the host rock occurred coeval with ductile grain size reduction of quartz and feldspar mineral phases (top, PPL and bottom, XPL). Scale bar is 500 µm.

4.2.4 Taylor Lake Stock

The Taylor Lake Stock is a small stock located just north of the western contact of the Irene-Eltrut batholithic complex (Figure 31). Four samples taken from three outcrops located along highway 502 were collected, and eleven structural orientations were taken from two of the outcrops. Of particular interest within the Taylor Lake Stock is the presence of a dyke – the mineralogy of which can be used to help constrain regional metamorphic conditions.

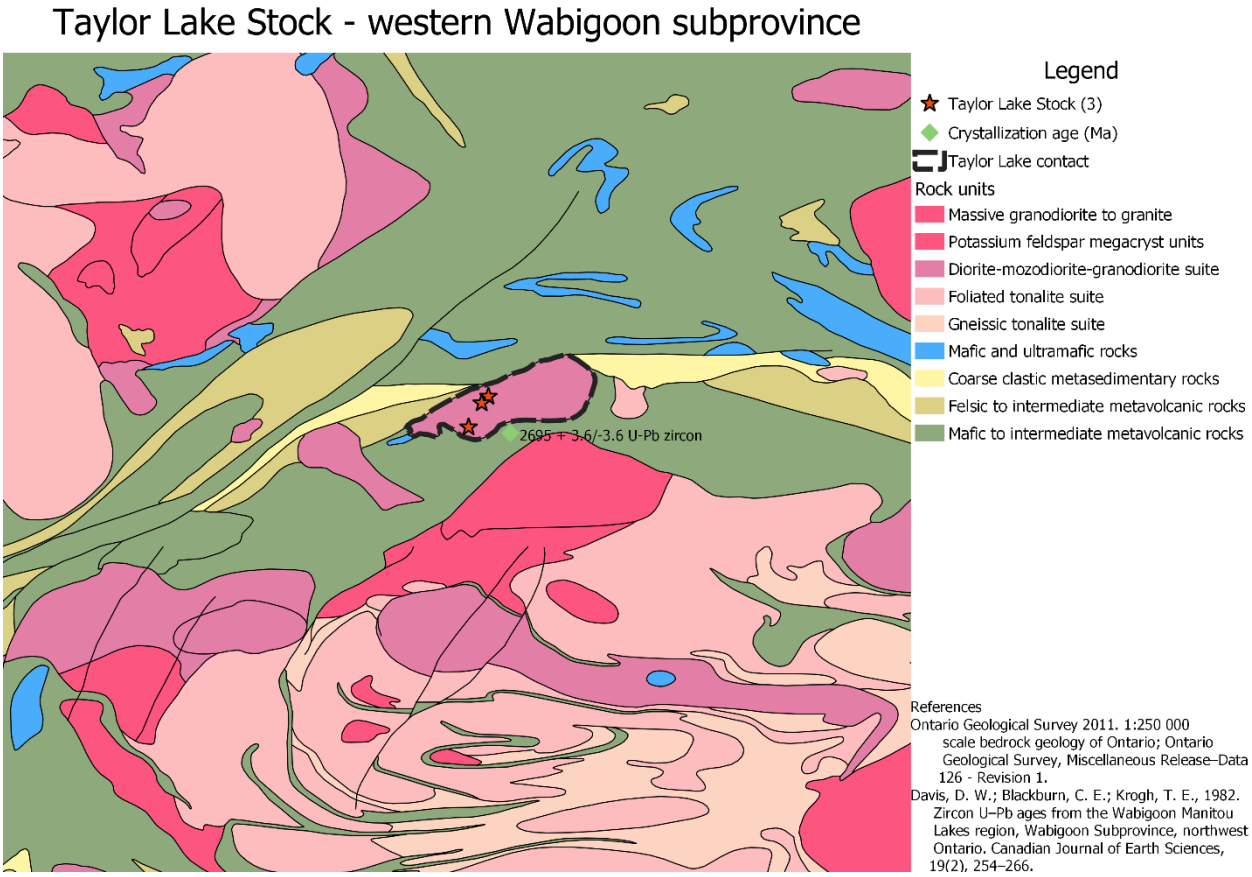

Figure 31. Map of the Taylor Lake Stock in the western Wabigoon subprovince. The crystallization age just south of the Taylor Lake stock is from the Taylor Lake stock, not the greenstone.

Dyke Mineralogy

The dyke appears dark green in outcrop. In thin section, its mineralogy is comprised of coarse-grained amphibole, plagioclase, clinopyroxene (CPX), apatite and biotite. Hornblende is poikilitic with fine grained inclusions of CPX. CPX is also present outside of the hornblende and is in contact with all other mineral phases – indicating that it is part of the stable metamorphic mineral assemblage. Plagioclase within the dyke is fine to medium grained and exhibits a moderate to strong undulatory extinction, strong subgrains and semi-serrated to moderately serrated grain boundaries. Polysynthetic and deformation twins are noted where twinning is present. Hornblende also displays undulatory extinction and minor subgrains. The mineralogy of this dyke is consistent with a mafic igneous protolith partially metamorphosed to the amphibolite facies of metamorphism. Figure 32 shows a representative photomicrograph of the amphibolite dyke.

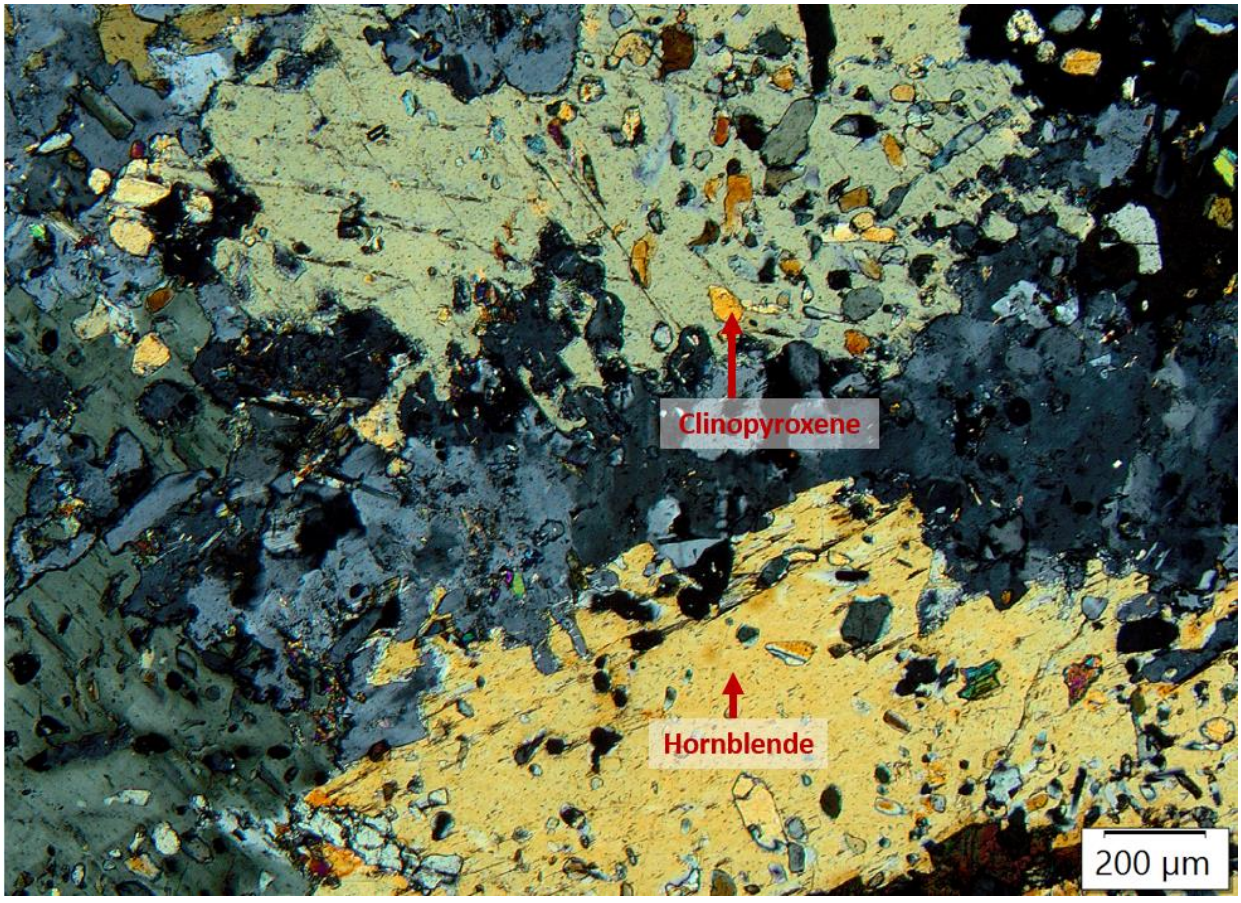

Figure 32. Photomicrograph of a dyke within the Taylor Lake Stock. The metamorphic mineral assemblage consists of amphibole + CPX + plagioclase + apatite + biotite (XPL). Scale bar is 200 µm.

Pluton mineralogy and alteration

The mineralogy of the Taylor Lake Stock consists of potassic feldspar, plagioclase feldspar and quartz with minor (< 10% bulk rock volume) hornblende, chlorite, biotite, sphene, calcite, white mica and epidote. White mica, epidote and calcite occur as replacements of feldspars (saussuritization) which is a common alteration feature seen in the pluton (Figure 33). Calcite and epidote (with some chlorite) occur clustered together along microfractures. Biotite can occur as primary laths or as laths with chlorite replacement. Chlorite and epidote are also seen infilling shear fractures.

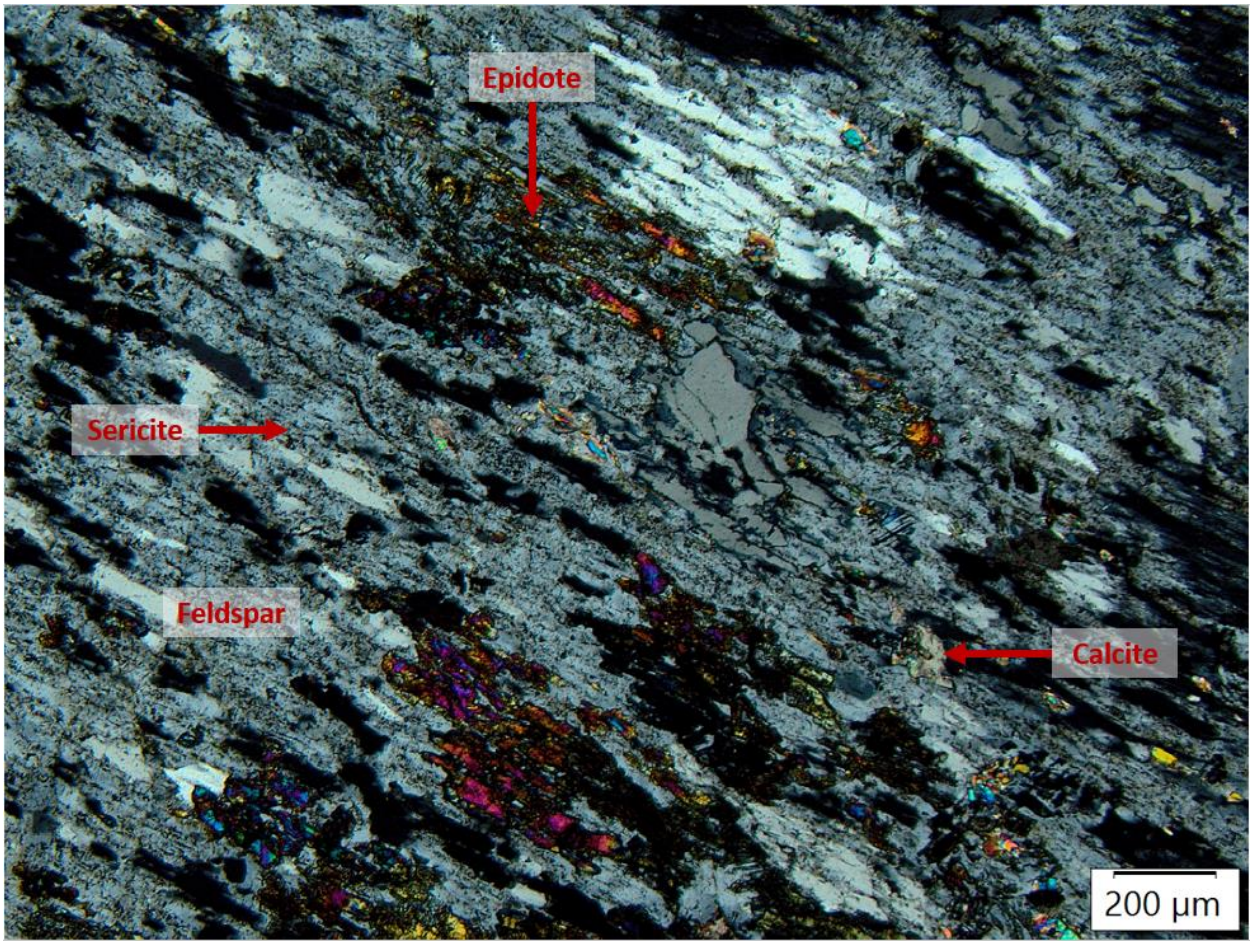

Figure 33. Saussuritization (epidote, calcite and white mica alteration) of a ductilely deformed feldspar crystal (XPL). Scale bar is 200 µm.

Macrostructural analysis

Eleven structural orientations were taken from two outcrops of the Taylor Lake Stock. Of these orientations, six are chlorite infilled shear fractures, four are mixed infilled shear fractures and one is an epidote infilled shear fracture. The average dip of the eleven shear fractures is 75° while the median is 79°. Eight slickenlines along the shear surfaces have plunges that range from 4° to 16° and one plunge of 45°, highlighting an oblique strike-slip displacement along the steeply dipping shear surfaces. Figure 34 shows a stereonet for the structural orientations taken within the Taylor Lake Stock, while Figure 35 shows the individual stereonets and rose diagrams for the major structural populations.

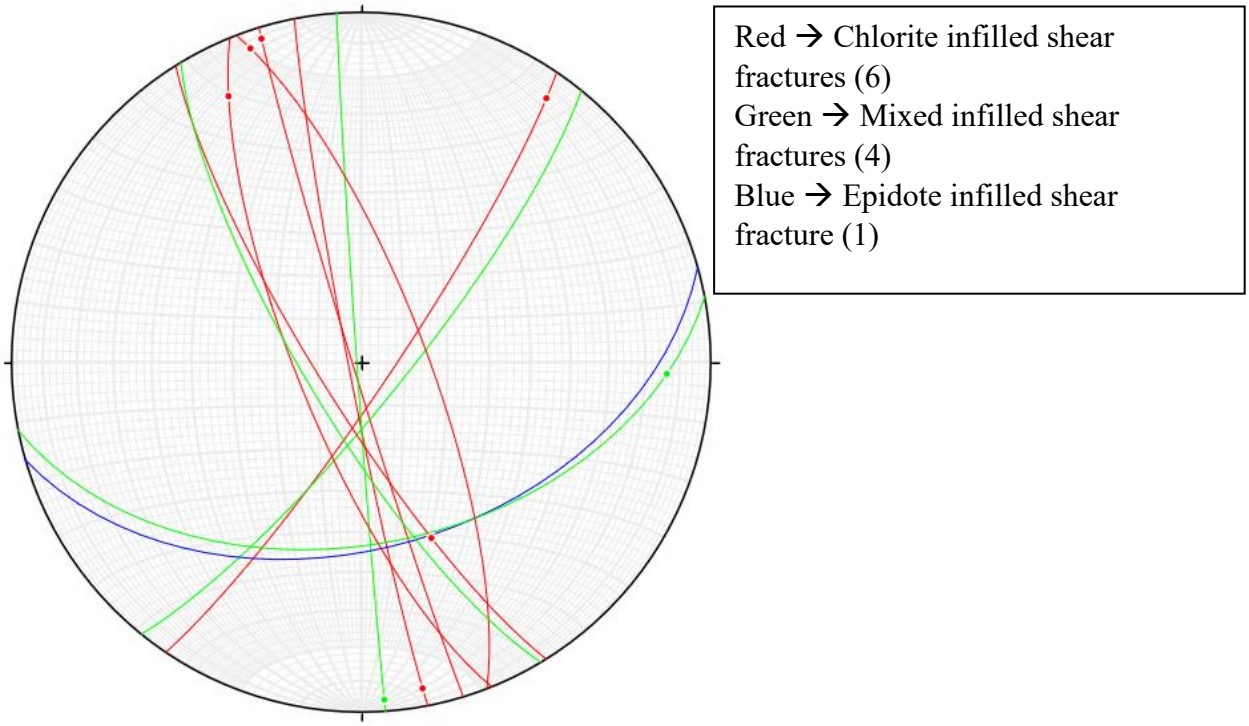

Figure 34. Stereonet of the eleven infilled shear fracture orientations taken in the Taylor Lake Stock.

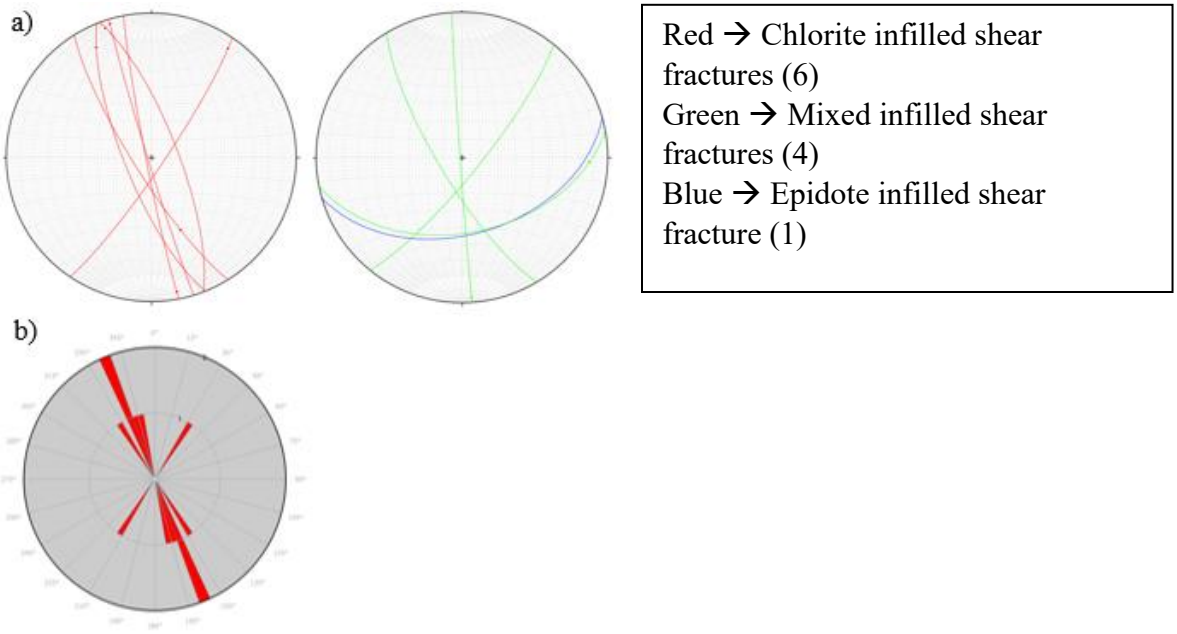

Figure 35. a) Stereonets of all measurements taken from the Taylor Lake Stock outcrops. **b)** Accompanying rose diagram.

Microstructural analysis

Within the Taylor Lake Stock, feldspar has deformation microstructures such as intragranular microcracks, smooth to serrated grain boundaries, deformation twins when twinning is present, subgrains, undulose extinction and minor recrystallization along grain boundaries. Although strain is pervasive, rare instances of myrmekyte within the plagioclase feldspar has been preserved. Quartz displays deformation textures such as semi-serrated grain boundaries, undulose extinction (sometimes strong checkered extinction) and subgrains. Minor intragranular fractures are also noted in a few of the quartz grains. No macroscopic or microscopic fabric is noted. A representative photomicrograph of the micro-scale deformation is shown in Figure 36.

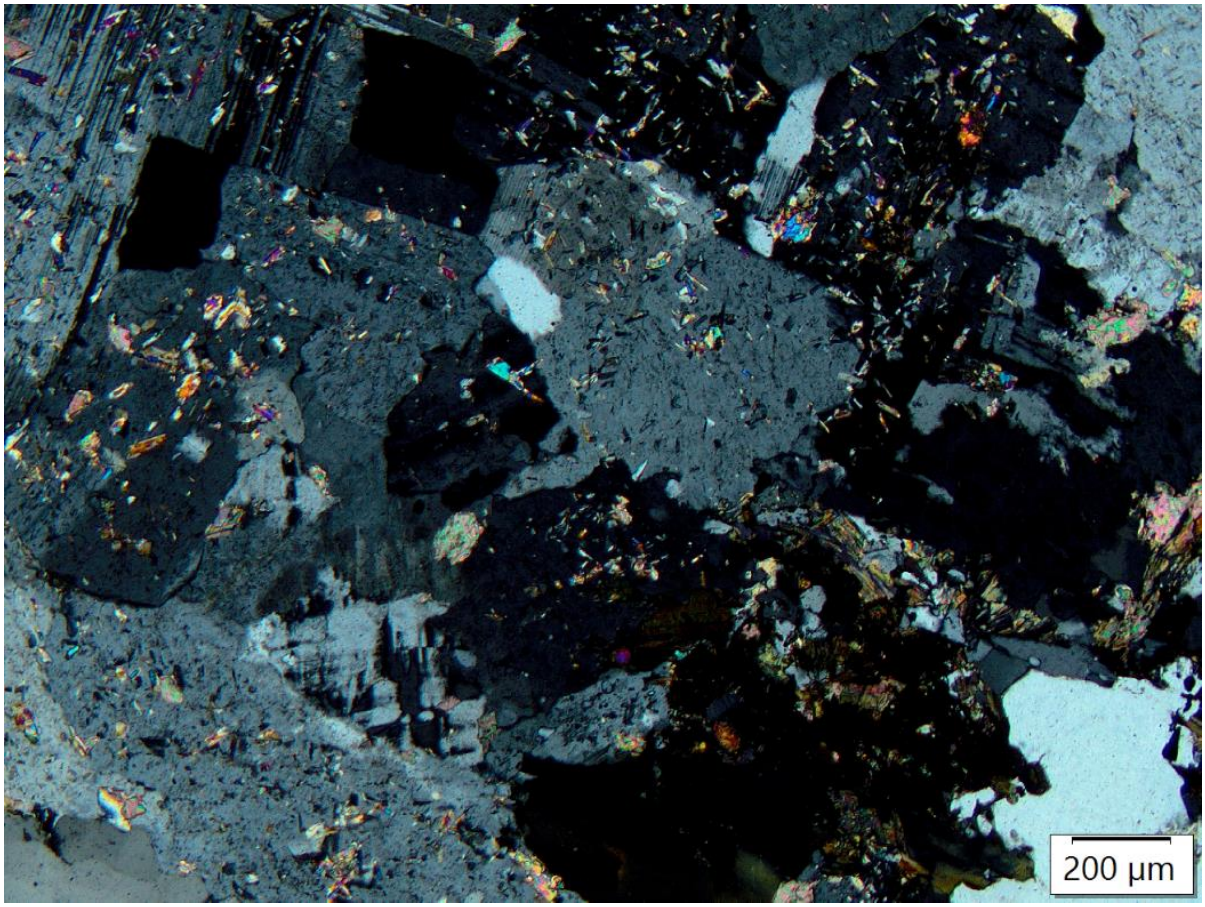

Figure 36. Photomicrograph showing deformation twinning, serrated grain boundaries and subgrains within feldspar (XPL). Scale bar is 200 µm.

4.2.5 Atikwa Batholith

Two hand samples and twenty-nine structural orientations were taken from one outcrop located on highway 502 just south of Dryden (Figure 37). One of the hand samples is low strain while the other is a higher strain sample. The outcrop lacks a penetrative foliation and or lineation and is white to light pink in color.

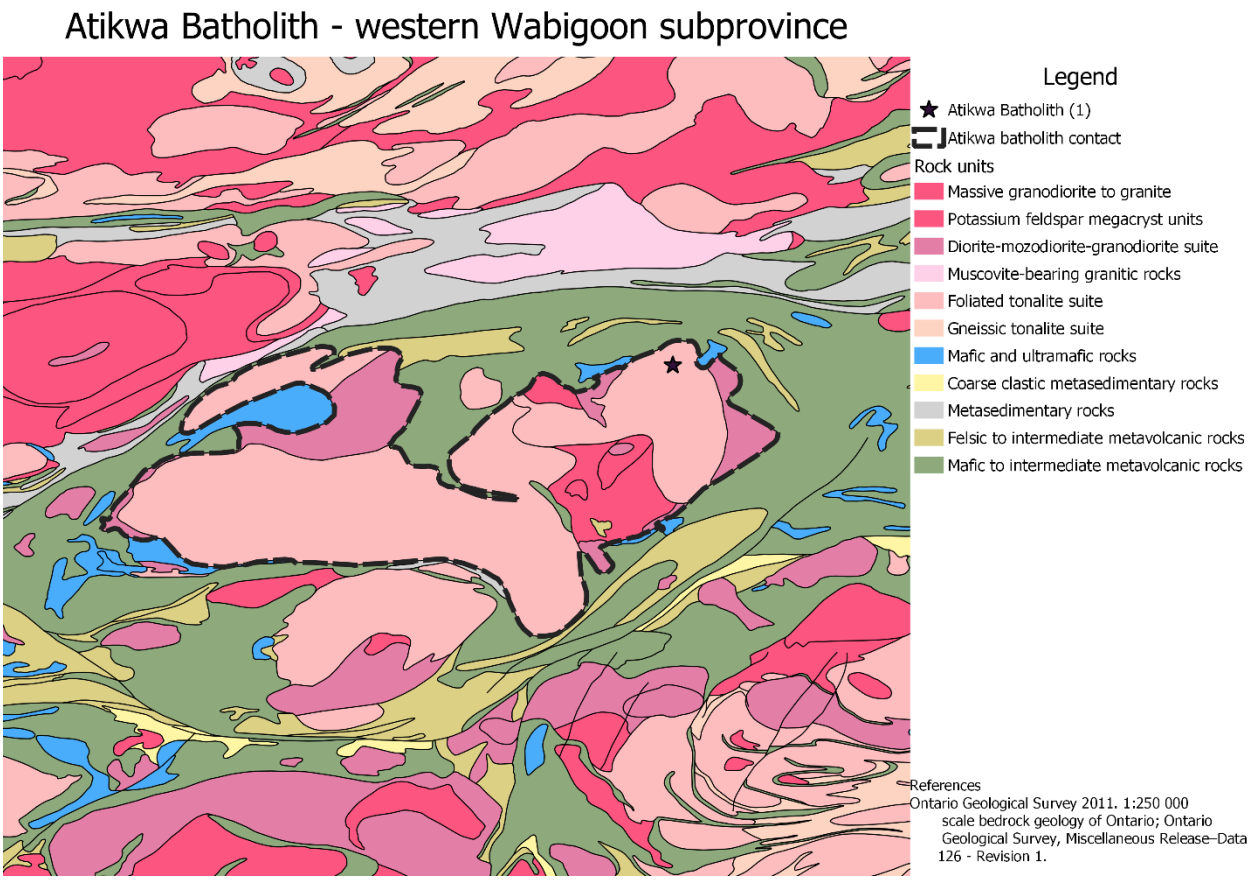

Figure 37. Map of the Atikwa batholith in the western Wabigoon subprovince showing the 1 outcrop location studied. Note: no age dates are available for this batholith.

Mineralogy and alteration

The Atikwa batholith is comprised pre-dominantly of quartz, plagioclase feldspar and potassic feldspar that accounts for roughly 85% of the bulk rock composition. Alteration minerals include white mica, epidote group minerals, calcite, sphene and chlorite, with increasing alteration mineral intensity within and proximal to the high strain sample (Figures 38, 39). Plagioclase has a weak sericite alteration with minor occurrences of sericite + epidote alteration. Chlorite tends to be localized to infilling shear fractures while epidote group minerals and white mica make up the major alteration mineral assemblage within the host rock. Minor occurrences of calcite and sphene are associated with the host rock white-mica + epidote alteration. Figure 38 shows a representative photomicrograph of the alteration mineral assemblage (white mica + epidote) within the low strain sample while Figure 39 shows the characteristic white mica + epidote alteration within the high strain sample. Alteration minerals are finer grained in the higher strain sample.

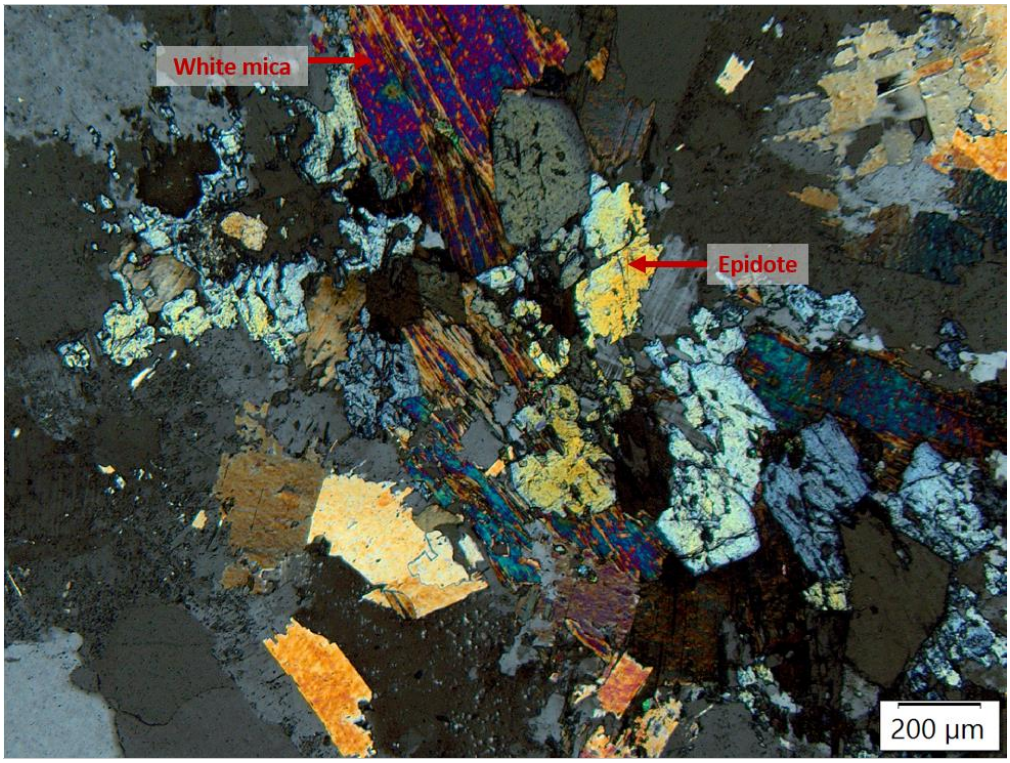

Figure 38. Photomicrograph of white mica + epidote alteration within the low strain sample of the Atikwa Batholith (XPL). Scale bar is 200 µm.

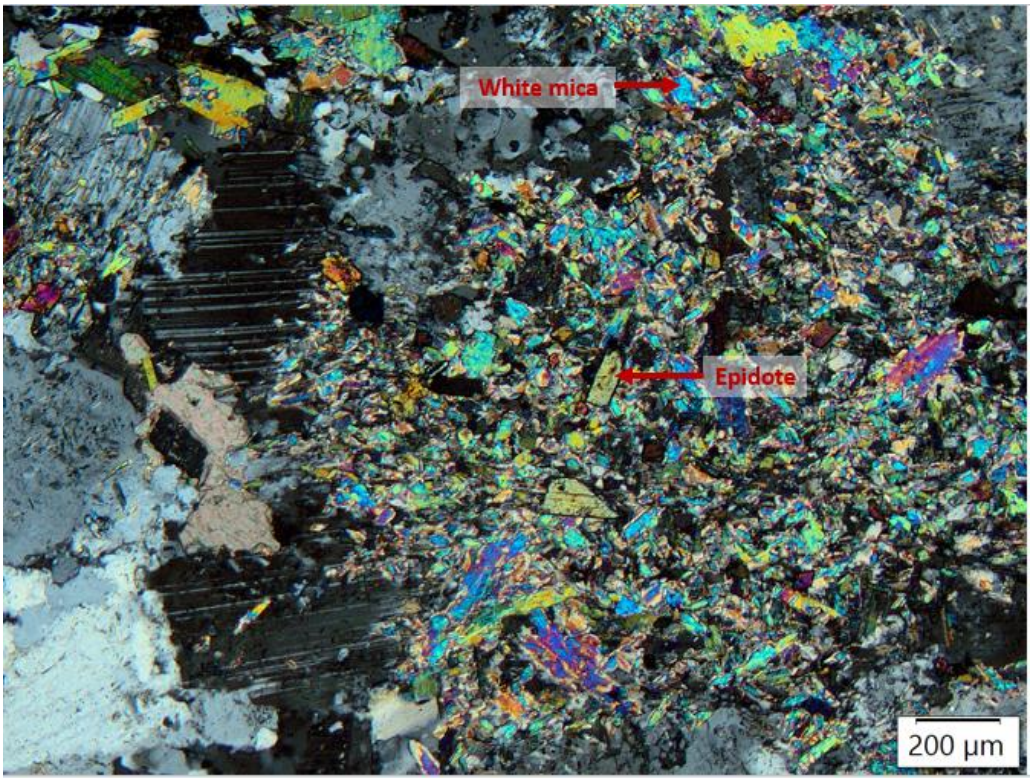

Figure 39. Photomicrograph of the characteristic white mica + epidote alteration within the high strain sample of the Atikwa batholith. Alteration minerals are finer grained in the high strain sample than the lower stain sample seen in Figure 35 (XPL). Scale bar is 200 µm.

Macrostructural analysis

Of the twenty-nine structural orientations measured within one outcrop, fifteen are unfilled fractures, ten are chlorite infilled shear fractures, two are extensional quartz veins, one is a mixed infilled shear fracture, and one is a shear zone contact (Figure 40). Of the ten shear fractures, only two had measurable slickenlines with plunges of 3° and 8°. Average and median dips of the shear fractures is 65°. The strike of the shear fractures and the shear zone are consistent across the outcrop with a north to north-north-west orientation. The sub-horizontal nature of the slickenlines again indicates an oblique strike-slip displacement along the shear fractures. Figure 41 shows the individual stereonets for the major fracture populations.

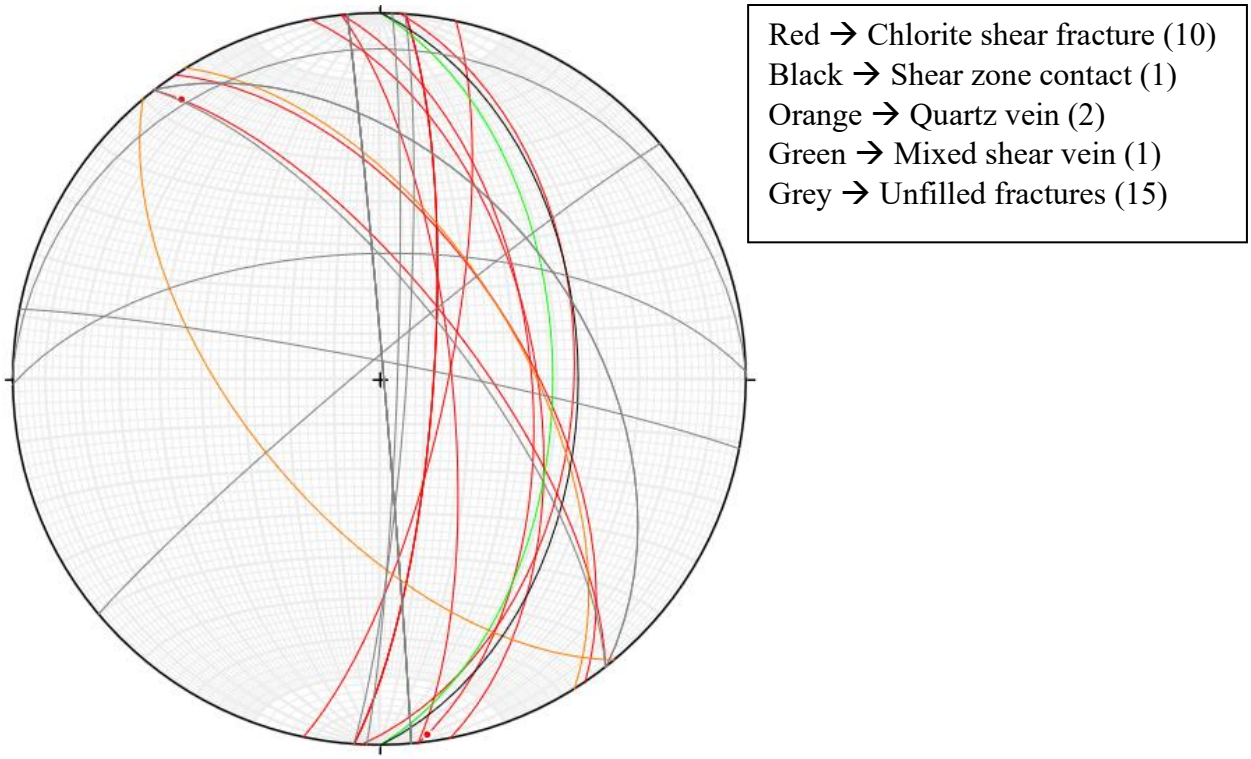

Figure 40. Stereonet displaying all structural features measured in the Atikwa Batholith. Legend shown in upper right-hand corner.

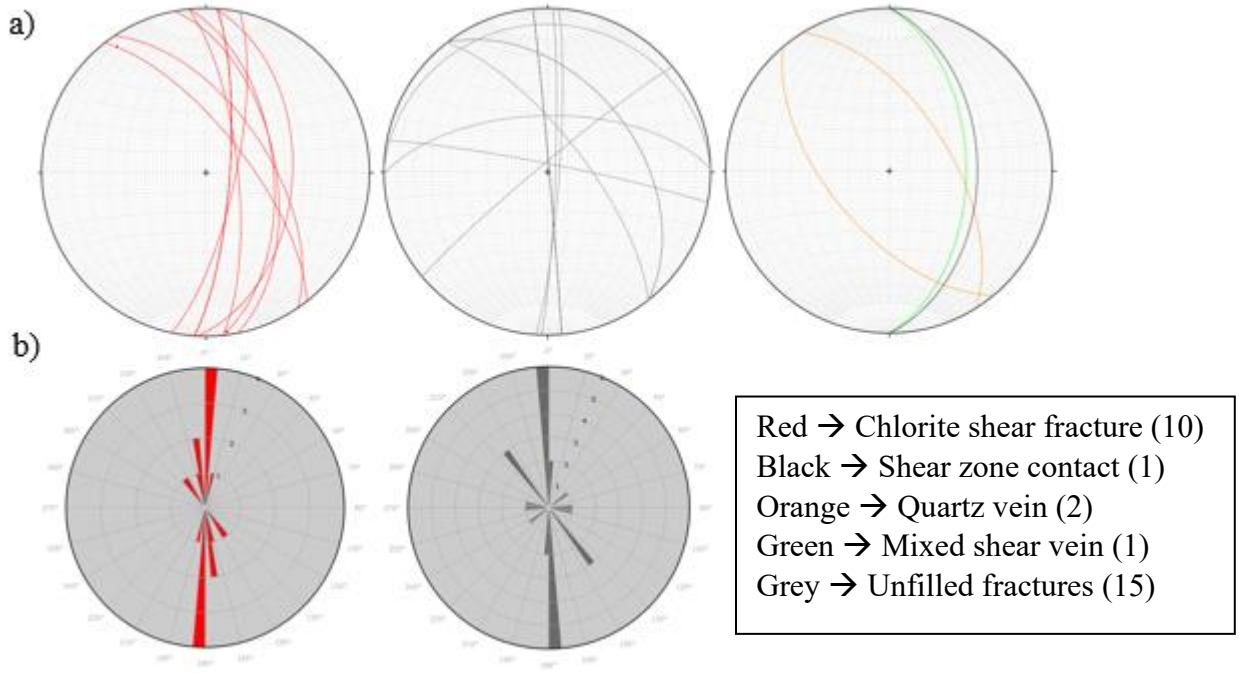

Figure 41. a) Individual stereonets for each major structural feature population. **b)** Rose diagrams for the chlorite shear fractures and the unfilled fractures.

Microstructural analysis

Of the two thin sections from the Atikwa batholith, one is a low strain granitoid sample and the other a higher strain sample. The higher strain sample has a weak to moderate fabric defined by the DPO of quartz that is not observed in the lower strain sample. Quartz within the less strained granitoid sample displays semi-serrated to straight grain boundaries with weak undulatory extinction, minor subgrains and minor bulging of grain boundaries into adjacent grains. Although deformation microstructures are minor in quartz, feldspars display moderately to heavily serrated grain boundaries, strong undulose extinction, patches of recrystallized feldspars along grain boundaries of coarser grained feldspars, deformation twins and subgrains (Figure 42).

Quartz lithons that are nearly circular in shape are observed in the lower strain sample. In the higher strain samples, these lithons appear flattened and are suggestive of boudinaged quartz veins (Figure 43), indicating coeval brittle-ductile deformation. Textural evidence for this pluton suggests recrystallization was dominant in quartz while dislocation creep was active in feldspars, highlighting a deformation temperature of 450°C or higher.

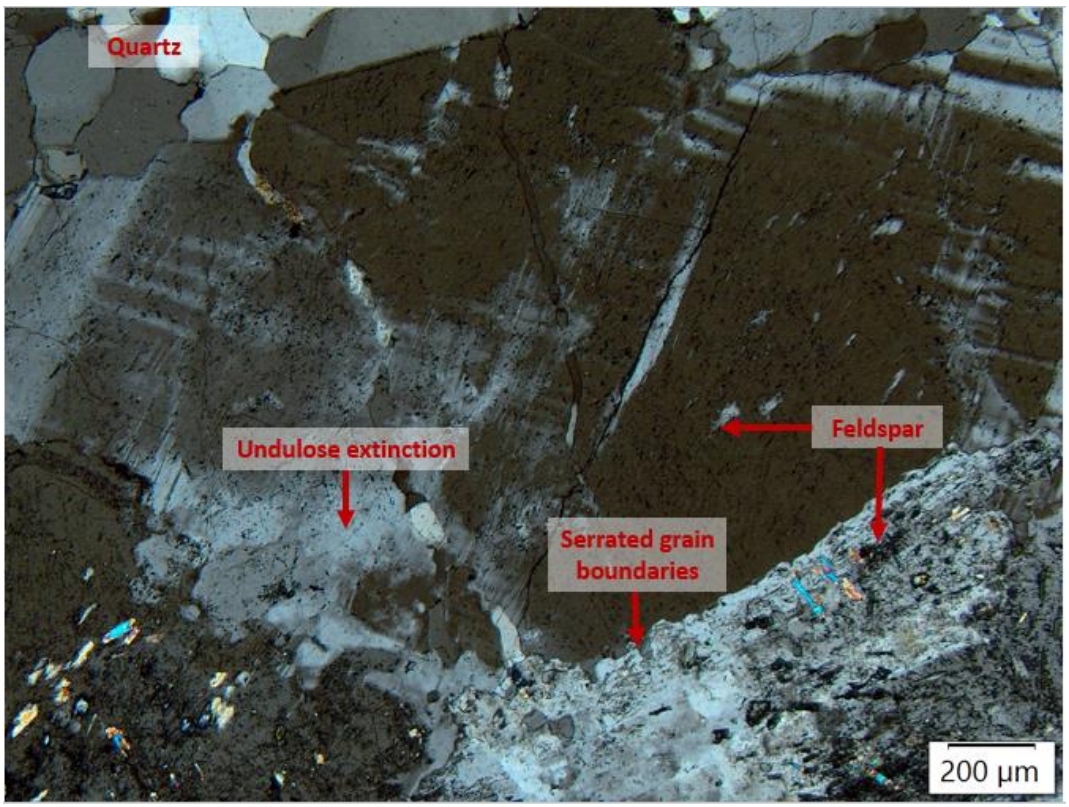

Figure 42. Photomicrograph showing undulose extinction in potassic feldspars (center) and serrated grain boundaries with undulose extinction in plagioclase feldspar (lower right corner). Quartz displays fairly smooth grain boundaries with minor undulose extinction and subgrains (upper left corner) (XPL). Scale bar is 200 µm.

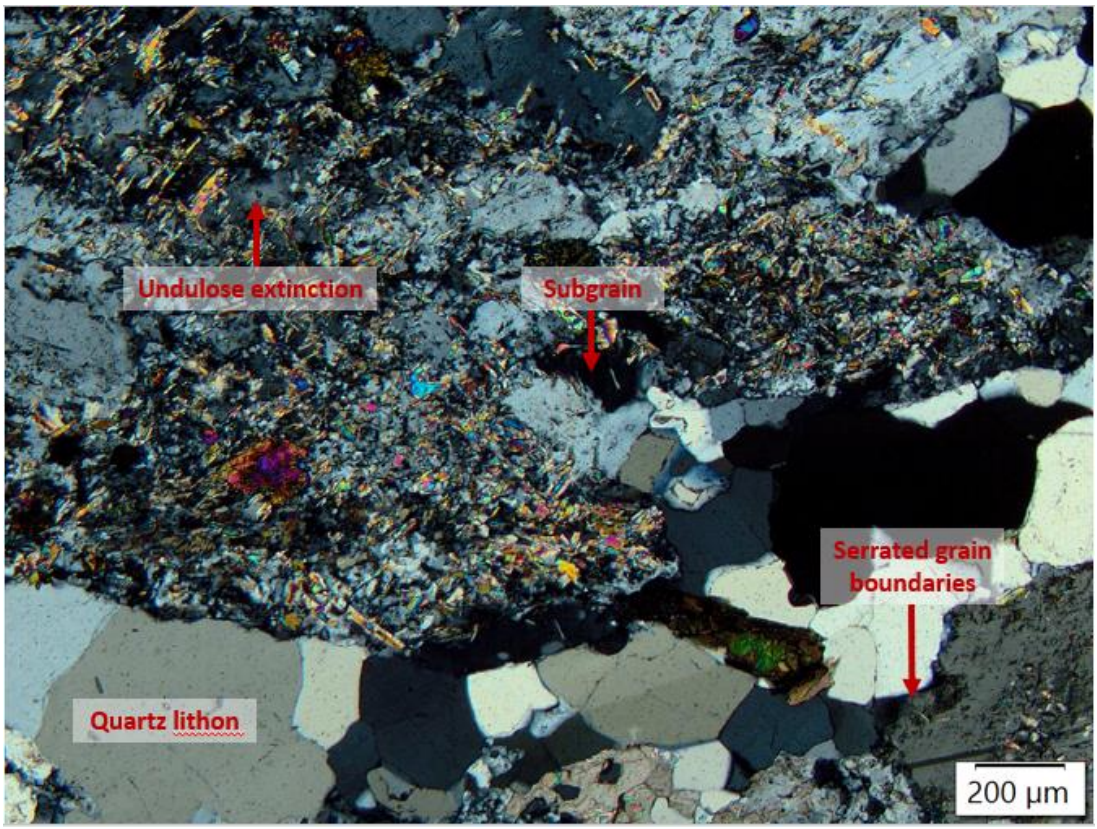

Figure 43. Photomicrograph of the higher strain sample within the Atikwa batholith (XPL). Feldspars have serrated grain boundaries, undulose extinction and subgrains. Quartz lithons are elongated within the higher strain sample with quartz displaying weak undulose extinction and subgrains. Scale bar is 200 µm.

4.2.6 Irene-Eltrut Batholithic complex – western contact

Three outcrops of the western contact of the Irene-Eltrut batholithic complex along highway 502 were studied (Figure 44). All outcrops lack a penetrative foliation and/or lineation. Thirteen structural orientations were taken from one of the outcrops, which include six epidote infilled shear fractures, four mixed infilled shear fractures, two shear zones and one chlorite infilled shear fracture. Six thin sections were made from the three outcrops – four low strain, one intermediate strain and one high-strain shear zone.

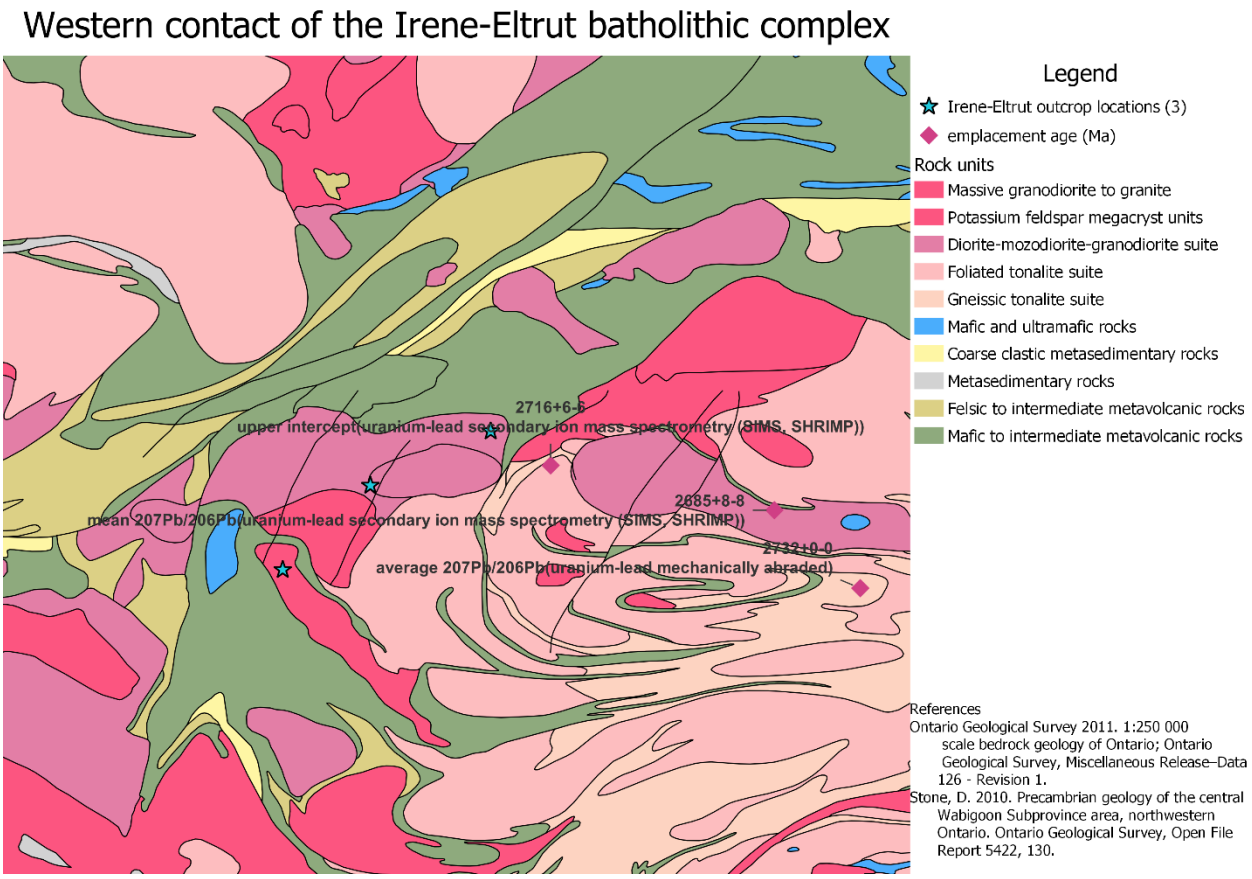

Figure 44. Locations of the 3 outcrops along the western contact of the Irene-Eltrut batholithic complex in the western Wabigoon subprovince with available emplacement ages.

Mineralogy and alteration

Potassic feldspar, plagioclase feldspar and quartz make up the bulk mineralogy (85%) with minor magmatic hornblende and alteration minerals calcite, epidote, biotite, sphene and chlorite. Chlorite occurs mostly within shear fractures but may also appear as an alteration of biotite and along microfractures within the host rock. Epidote and calcite are mostly found occurring together within shear fractures (Figure 45) but also occur as alteration products of feldspar along with white mica (Figure 46). Biotite occurs within rectangular aggregates associated with a localized grain size reduction.

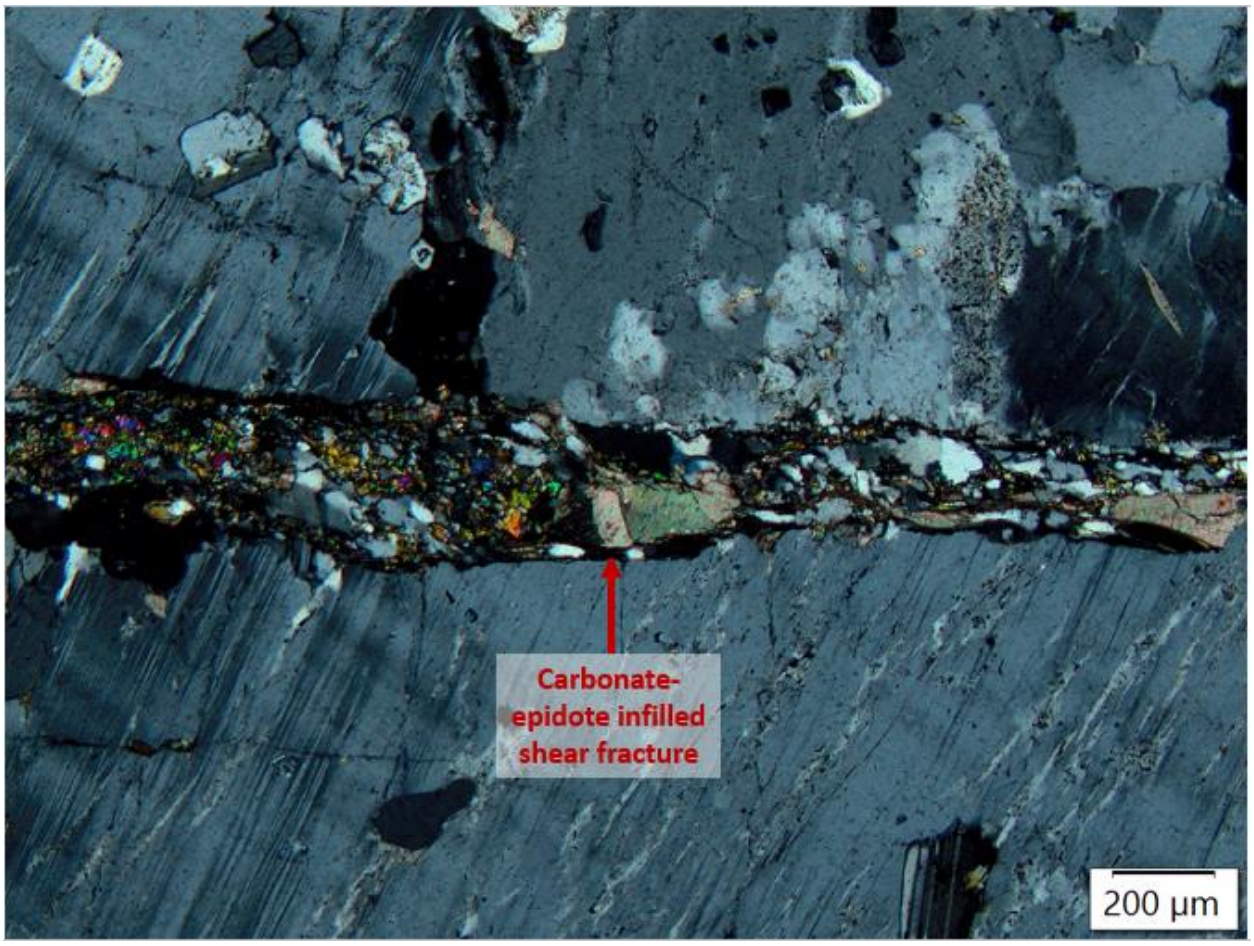

Figure 45. Photomicrograph showing an epidote-calcite infilled shear fracture within the western portion of the Irene-Eltrut batholithic complex (XPL). The anastomosing nature of the shear vein is a common feature among the plutons throughout the subprovince. Scale bar is 200 µm.

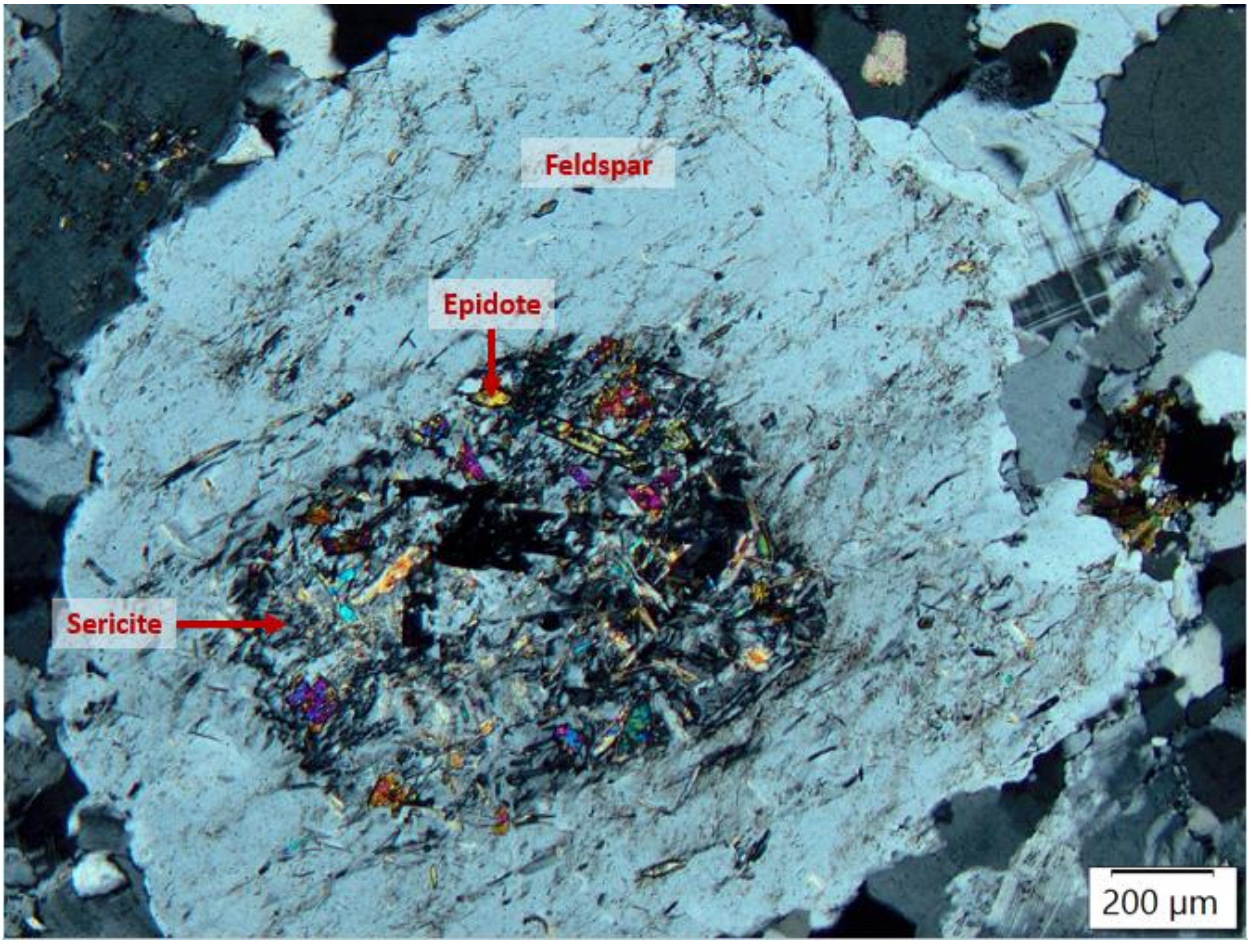

Figure 46. Photomicrograph of epidote - white mica alteration within the core of a feldspar crystal (XPL). Scale bar is 200 µm.

Macrostructural analysis

Within the infilled shear fracture population, five occurrences of slickenlines were noted. Slickenline plunges range from 10° to 22° indicating an oblique strike-slip displacement. Average and median dips of the eleven infilled shear fracture population are 64° and 61°, respectively. Figure 47 shows the stereonet for all structural orientations measured while Figure 48 shows the individual stereonet for the major populations as well as a rose diagram displaying the strike variations within the epidote infilled shear fractures. Consistent will all other plutons studied within the western Wabigoon subprovince, the western region of the Irene-Eltrut batholithic complex displays structural features (fairly steep shear surfaces with shallowly plunging slickenlines) consistent with a shallow oblique sense of movement.

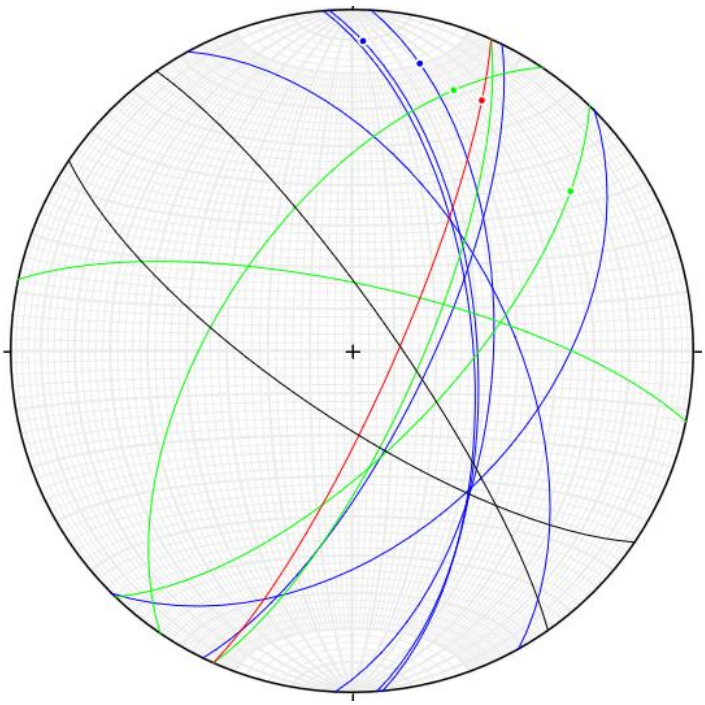

Red → Chlorite shear fractures (1)
Black → Shear zone contacts (2)
Green → Mixed infilled shear fractures (4)
Blue → Epidote shear fractures (6)

Figure 47. Stereonet displaying the thirteen structural orientations taken in the western region of the Irene-Eltrut batholithic complex. Legend shown in upper right corner.

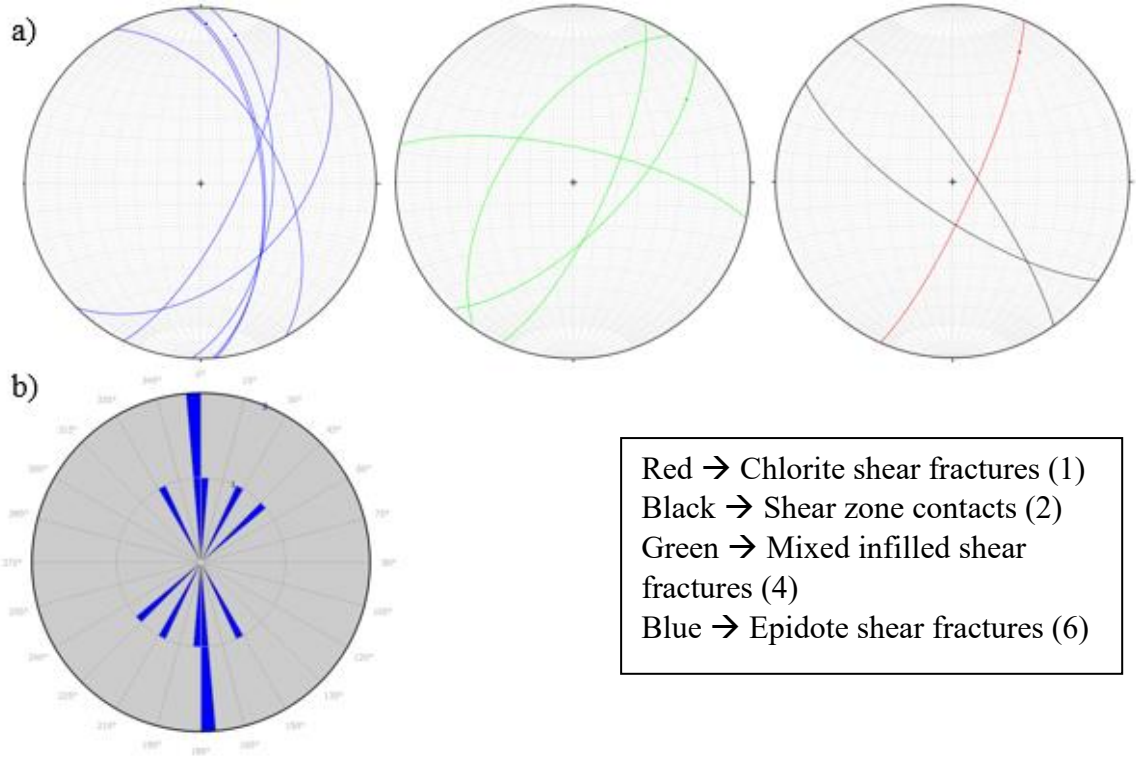

Figure 48. a) Individual stereonets for the major population of structural orientations. **b)** rose diagram displaying the variations in strike of the epidote shear veins.

Microstructural analysis

Thin sections range from low strain (four), intermediate strain (one) to high strain (one). In the lower strain samples, deformation microstructures within the quartz primarily consists of serrated grain boundaries, subgrains and undulose extinction that varies from moderate to strong checkered extinction. Feldspars commonly have moderately serrated grain boundaries with patchy undulatory extinction, subgrains, deformation twins, minor intragranular microcracks and minor recrystallization along grain boundaries. Some of the feldspar also have primary relict zoning while plagioclase feldspars also some myrmekite. Hornblende within the lower strain samples also displays evidence for dislocation creep in the form of minor undulatory extinction and subgrains. Hornblende is the only mineral to display a DPO.

The intermediate strain sample has an epidote-carbonate shear fracture (Figure 45) along with an interesting texture not documented in any of the other samples or plutons studied. This texture is described as rectangular aggregates of very fine-grained biotite ± calcite that occurs with grain-size reduced quartz and feldspars. Immediately outside of these rectangular aggregates are the coarser-grained counter parts of the grain-size reduced quartz and feldspars (Figure 49). There are three possible genetic origins of this texture. The first option is that localized ductile grain-size reduction occurred during deformation near the shear vein. This grain-size reduction led to a greater surface area for reactions to occur on, leading to the replacement by biotite ± calcite of primary grain-size reduced minerals. This leaves behind the biotite (± calcite) with grain-size reduced quartz and feldspar that did not alter. The second option is that the grain-size reduction is a result of later stage localized cataclasis which would also result in the formation of new mineral species due to the surface area increase of the minerals. The last option is that the biotite-carbonate rectangular pods represent fragments of dismembered veins. Since the quartz and feldspar within the pods are not angular as would be expected with cataclasis, the first or third genetic origin discussed are the most likely scenarios. Aside from the presence of this texture, deformation microstructures within feldspar and quartz remain the same across the low and intermediate strain samples.

The high strain sample is characterized as a brittle-ductile shear zone with a few mm-scale chlorite infilled shear fractures aligned parallel (or slightly oblique to) the dimensional preferred orientation defined by the quartz and alteration minerals (chlorite, epidote, white mica, biotite and calcite). The intensity of alteration within the shear zone is much greater than the alteration seen within the low strain and intermediate strain sample. Quartz within the shear zone is bimodal with

grain sizes that range from <0.1 mm in one population and around 0.5 mm in the other. The coarser population of quartz is seen in lithons that are not grain-size reduced as significantly as the quartz surrounding it. Quartz within the lithons displays deformation microstructures such as serrated grain boundaries that bulge into adjacent grains, subgrains, moderate to strong undulose extinction and penetrative dimensional preferred orientation. Quartz outside of the lithons displays strong grain size reduction, subgrains and undulose extinction. Feldspar occurs as both grain size reduced matrix material and as slightly coarser grained porphyroclasts – but are most commonly seen as porphyroclasts. Matrix material feldspar is seen with undulose extinction, serrated grain boundaries, subgrains and deformation twins. Figure 50 shows a representative photomicrograph of the brittle-ductile shear zone.

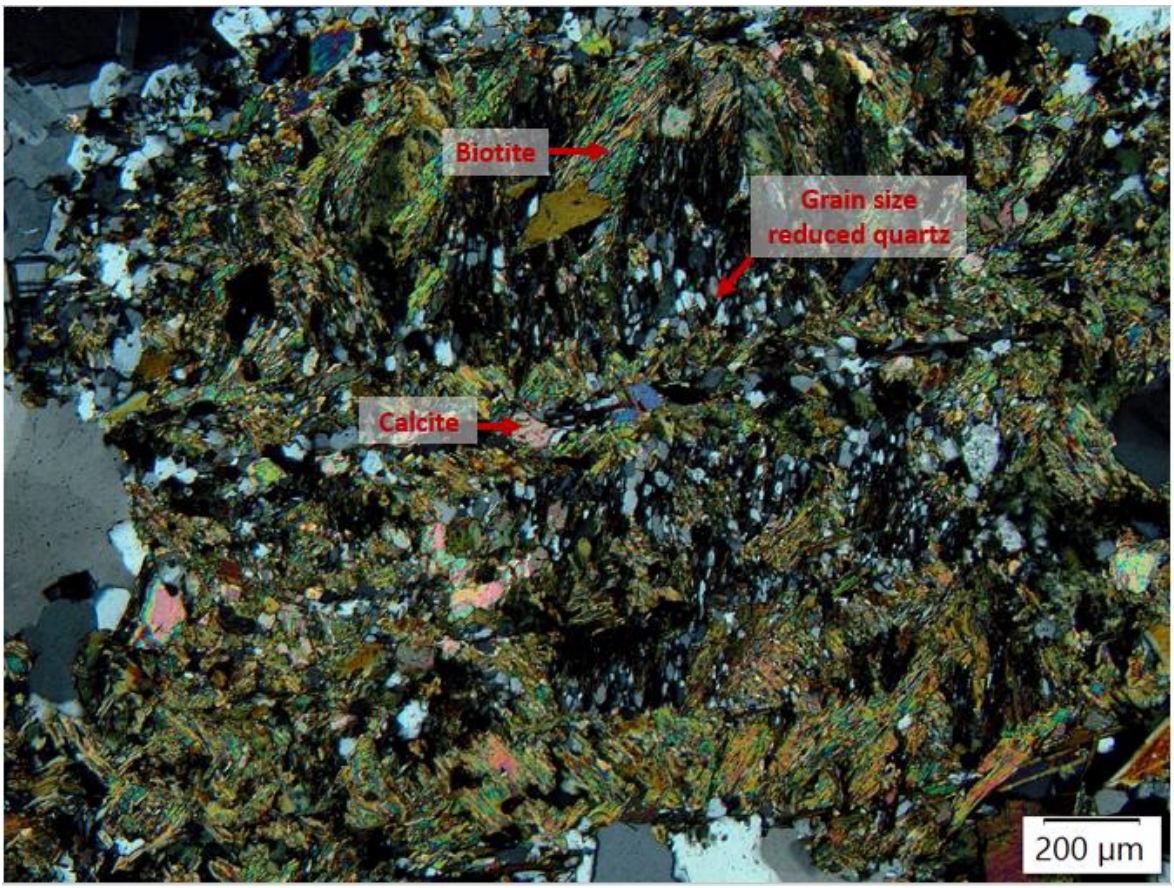

Figure 49. Photomicrograph displaying a complex texture within the western region of the Irene-Eltrut batholithic complex (XPL). Rectangular aggregates of biotite ± calcite with grain size reduced quartz and feldspar are surrounded by non-grain size reduced quartz and feldspar. Scale bar is 200 µm.

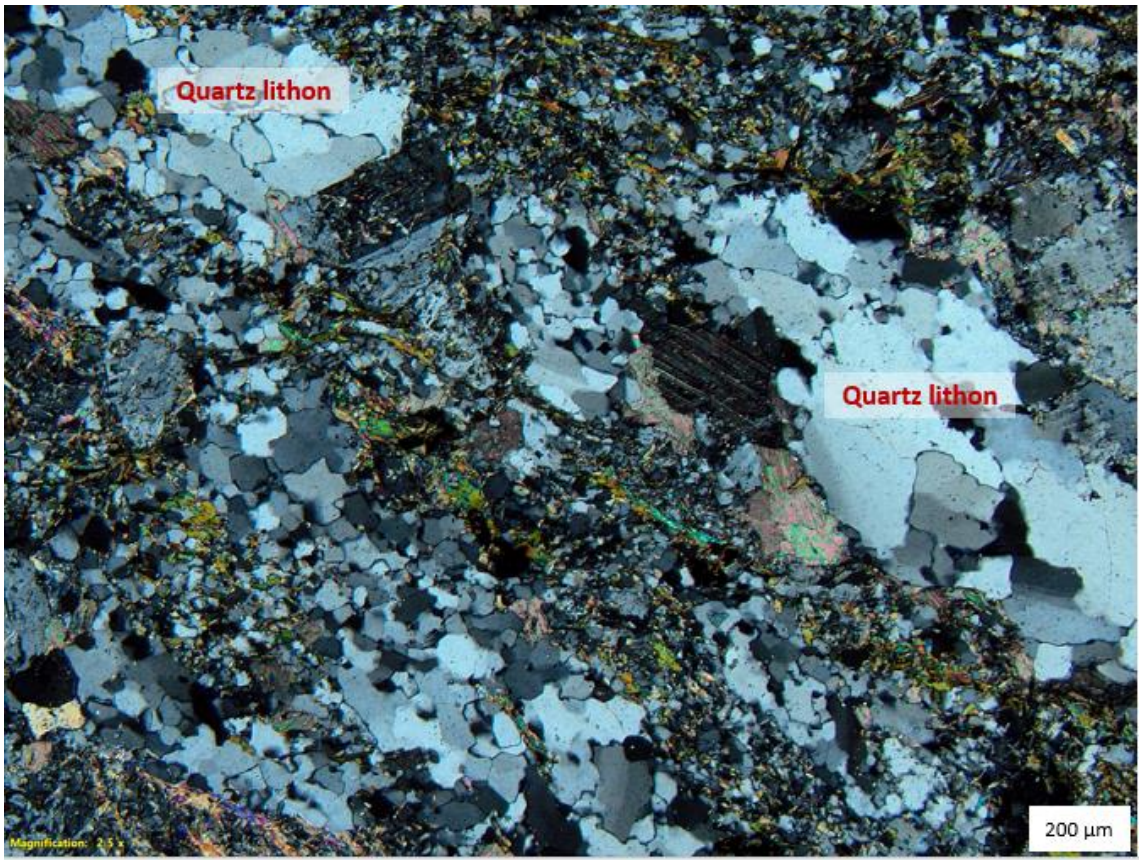

Figure 50. Photomicrograph of a brittle-ductile shear zone within the western region of the Irene-Eltrut batholithic complex (XPL). Scale bar is 200 µm.

4.3 Central Wabigoon subprovince

4.3.1 Revell Batholith

Eight hand samples and forty-two structural orientations were collected from two outcrops in the northern portion of the Revell batholith (Figure 51). One outcrop is located along highway 17 just east of the highway 622 intersection. In this outcrop, the contact between the Revell batholith and the surrounding host greenstone is present. The other outcrop is located along highway 622. Both outcrops are considered low strain – no shear zones were seen or sampled within this batholith. All outcrops lack a penetrative foliation and/or lineation.

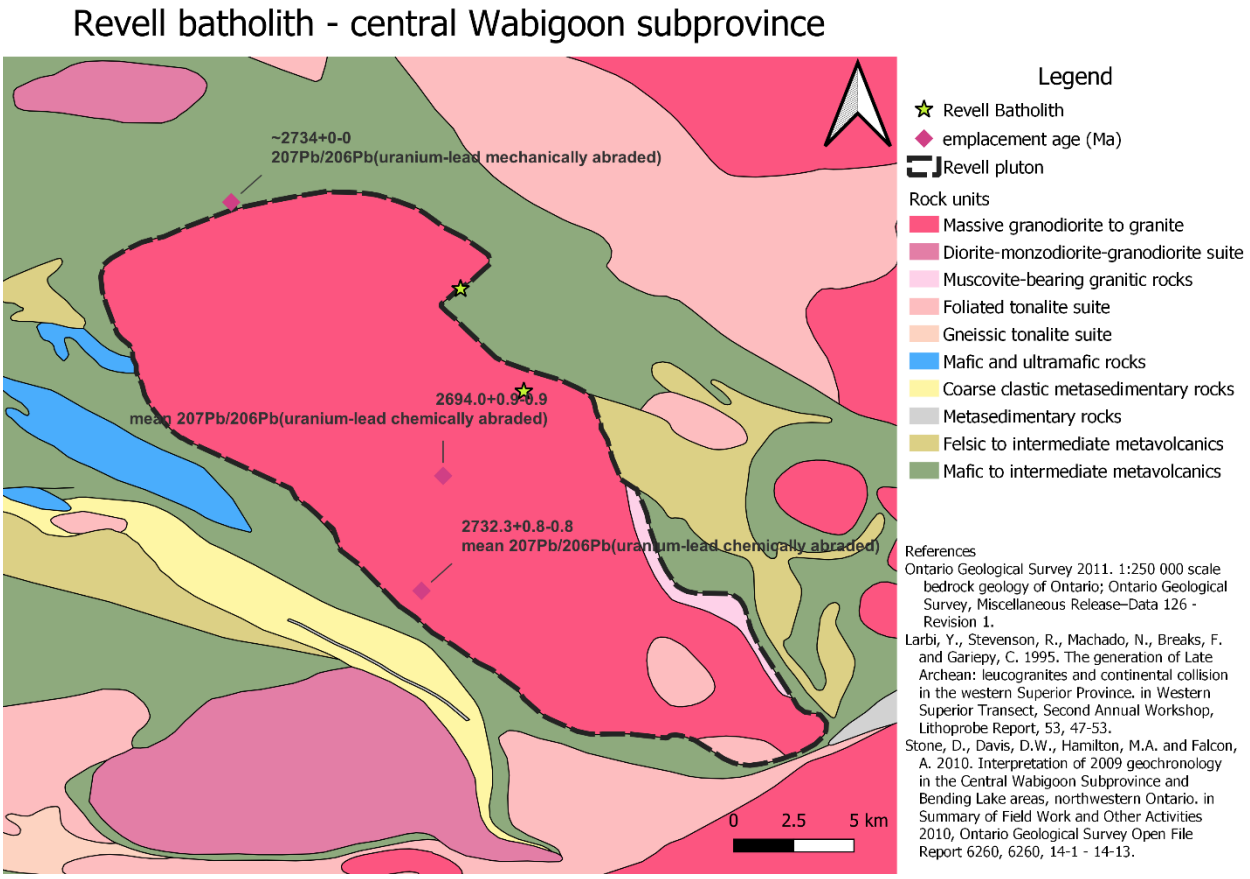

Figure 51. Map of the Revell batholith in the central Wabigoon subprovince showing outcrop locations and emplacement ages dates.

Mineralogy and alteration

The mineralogy of the Revell batholith is composed of quartz, plagioclase feldspar and potassic feldspar in varying amounts that account for roughly 90% of the bulk rock composition. Minor amounts (~10%) of alteration is present which includes white mica, epidote, sphene and chlorite. Chlorite, epidote and sphene can each be found along microfractures within the host rock, and chlorite and epidote are also seen infilling shear fractures. White mica occurs as a weak replacement of feldspar that is not always present. Overall, the alteration in these outcrops of the Revell batholith is weak, with a representative photomicrograph of the alteration shown in Figure 52.

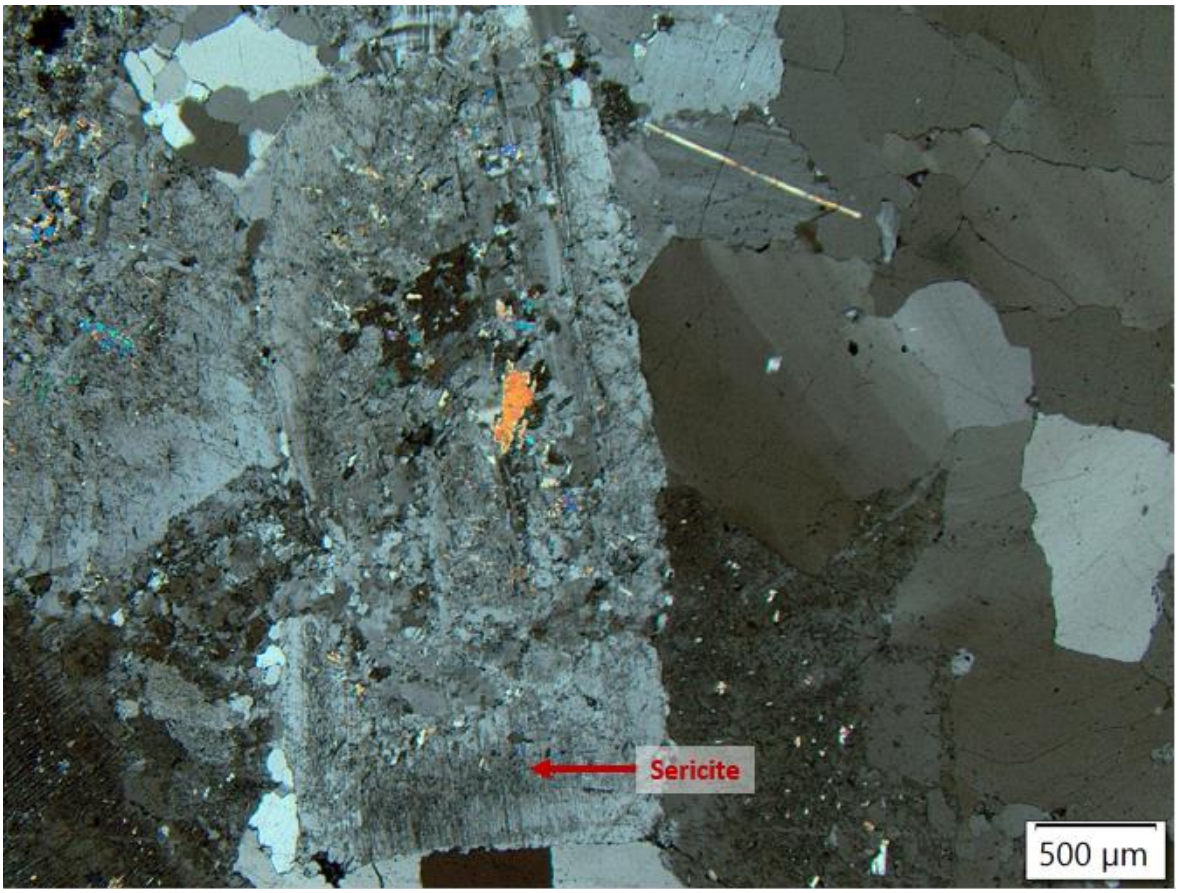

Figure 52. Photomicrograph showing typical white mica alteration of feldspar within the Revell batholith (XPL).

Macrostructural analysis

Of the forty-two structural orientations collected, twenty-six are unfilled fractures, fourteen are chlorite infilled shear fractures and two are mixed infilled shear fractures. Figure 53 shows the stereonet with all structural orientations plotted and Figure 54 shows the individual stereonets for each population and accompanying rose diagrams displaying strike variations for the two major populations (chlorite infilled shear fractures and unfilled fractures). The chlorite infilled shear fractures are steeply dipping with an average and median dip of 82° and 81°, respectively. Only two slickenline orientations were observed and measured in the field, with plunges of 8° and 10°, again indicating a sub-horizontal (oblique strike-slip) displacement along the shear surfaces. The strike of the chlorite infilled shear fractures is remarkably consistent across the two outcrops with a dominant north-west strike. A minor north-east striking population is also seen, possibly representing a conjugate set to the major striking population. Many of the unfilled fractures measured show consistency in orientation to the chlorite infilled shear fractures – apart from a few sub-horizontal fracture planes. The steeply dipping unfilled fractures could represent weathered shear fractures while the sub-horizontal population could represent exfoliation joints formed during the retreat of glaciation. The two mixed infilled shear veins have slightly shallower dips than the non-mixed infilled shear fractures but strike in the same general direction. Overall, the Revell batholith records oblique strike-slip shear fractures.

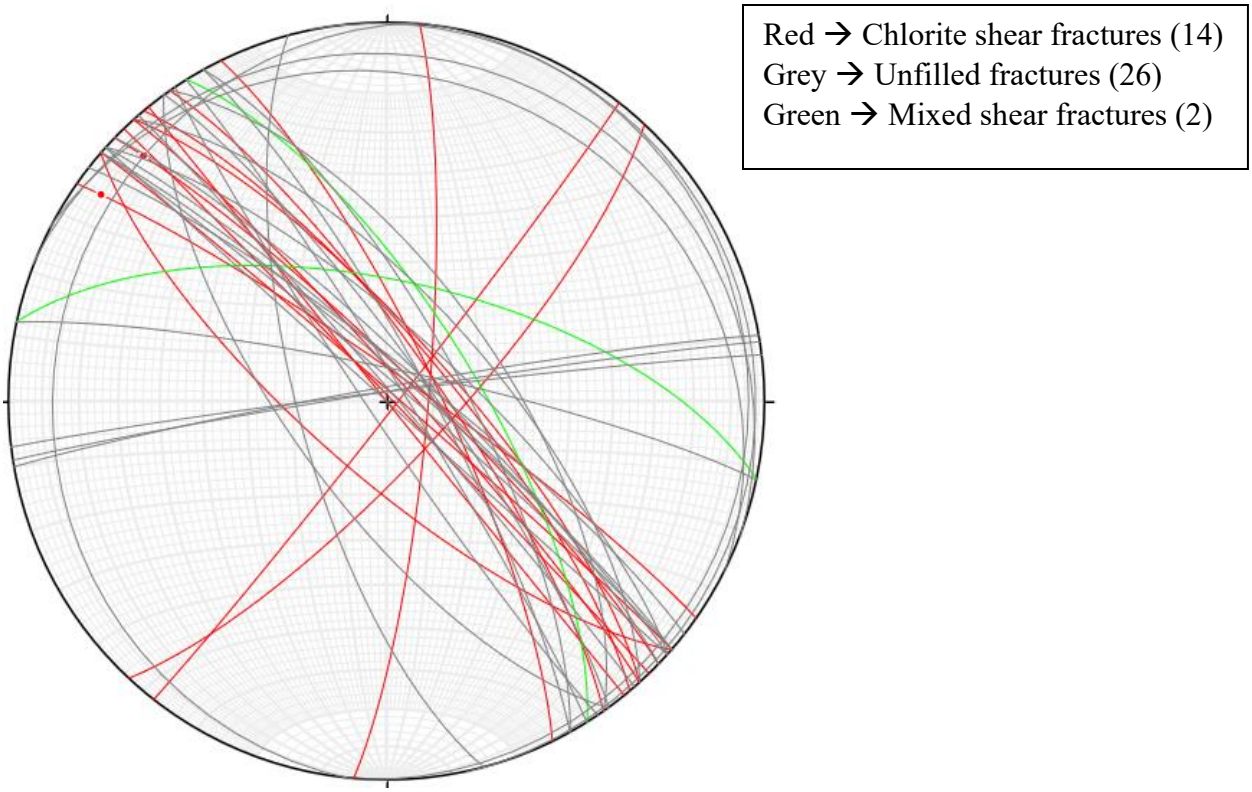

Figure 53. Stereonet display all forty-two structural orientations measured in the Revell batholith.

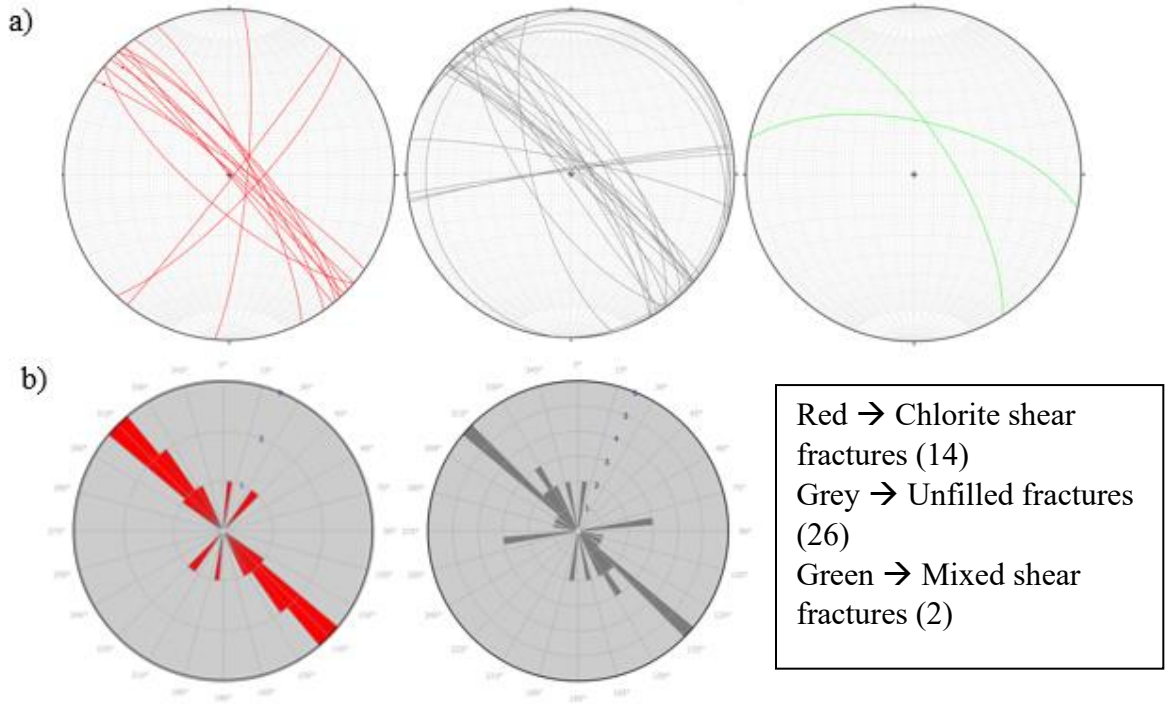

Figure 54. a) Individual stereonets for each fracture type. **b)** Rose diagrams of strikes for the chlorite infilled shear fractures and unfilled fractures.

Microstructural analysis

Strain is pervasive through-out all samples. Common microstructures of the feldspar phases include serrated grain boundaries, undulatory extinction, subgrains, deformation twins, intracrystalline microfractures, deformation bands, and minor recrystallization along grain boundaries (Figure 52). Quartz is commonly seen with serrated grain boundaries, undulose extinction and subgrains (Figure 52). Like the majority of the granitoid plutons discussed, there is no pervasive lattice preferred orientation or dimensional preferred orientation within the feldspars or quartz. Rare myrmekite is seen within the plagioclase feldspars indicating low strain rates (a requirement to preserving the delicate texture).

A quartz vein within the Revell batholith shows a ductile overprint, indicative of coeval brittle-ductile deformation. The quartz within the vein is fine grained with strong dimensional preferred orientation, heavily serrated grain boundaries that bulge into adjacent grains (bulging recrystallization), a moderate to strong undulose extinction and numerous subgrains (Figure 55).

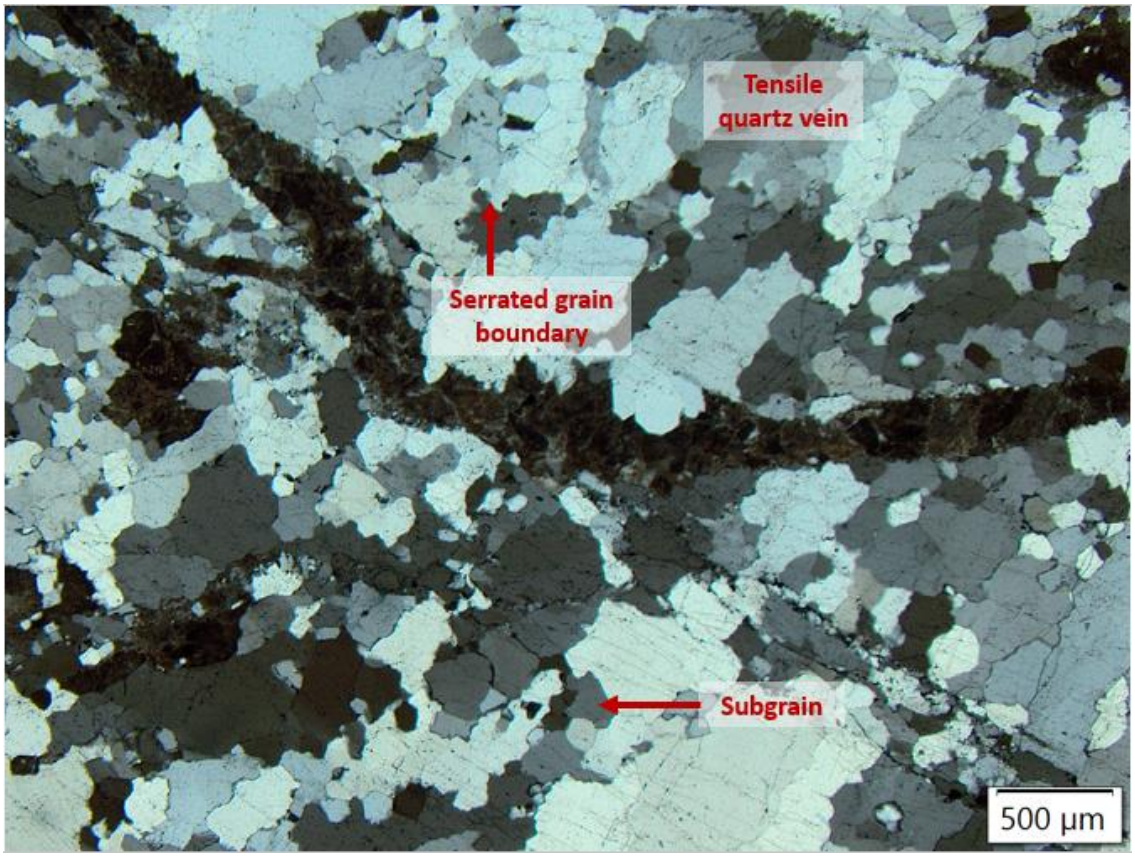

Figure 55. Photomicrograph of a quartz vein with a ductile overprint seen in the Revell batholith (XPL). Quartz has serrated grain boundaries, subgrains and undulose extinction. Scale bar is 500 µm.

4.3.2 Indian Lake Batholith

Fifty-eight structural orientations along with five hand samples were collected from four outcrops of the Indian Lake batholith (Figure 56). Each of the outcrops are exposed along highway 599 north of Ignace, Ontario. Each outcrop appears bright pink with no penetrative foliation and/or lineation. The outcrops also have a large population of sub-horizontally dipping unfilled fractures which were not measured – this fracture population likely represents exfoliation joints formed by retreating glaciers. All outcrops are considered low strain. No shear zones were documented.

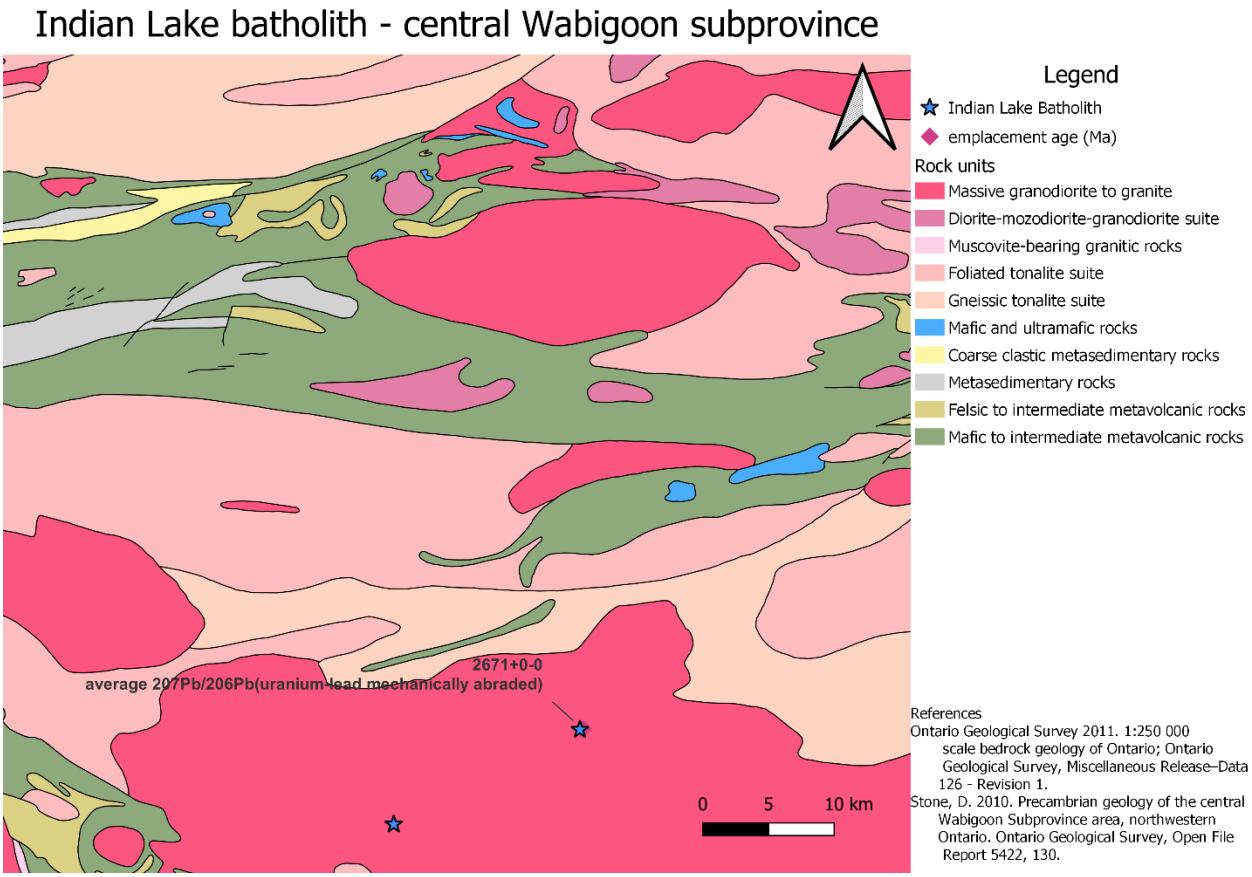

Figure 56. Map of the Indian Lake batholith outcrops with one available emplacement age. Note that although there are 4 outcrops, they overlap at this scale (2 outcrops in the northern area and 2 outcrops in the southern area).

Mineralogy and alteration

The mineralogy of the Indian Lake batholith consists of quartz, potassic feldspar and plagioclase feldspar that make up roughly 90% of the rock in varying amounts. The remaining 10% is comprised of alteration minerals white mica, epidote, sphene, hematite and chlorite with minor magmatic hornblende. The alteration of this pluton is very weak compared to other plutons. Most commonly, the alteration comprises a weak white mica alteration of feldspar. Epidote, sphene, and chlorite are seen along some microfractures within the host rock. Hematite is also seen along microfractures within feldspar and quartz. Epidote and chlorite are also present as fracture infill. A representative photomicrograph of white mica alteration and myrmekite preservation seen in the plagioclase feldspar is shown in Figure 57.

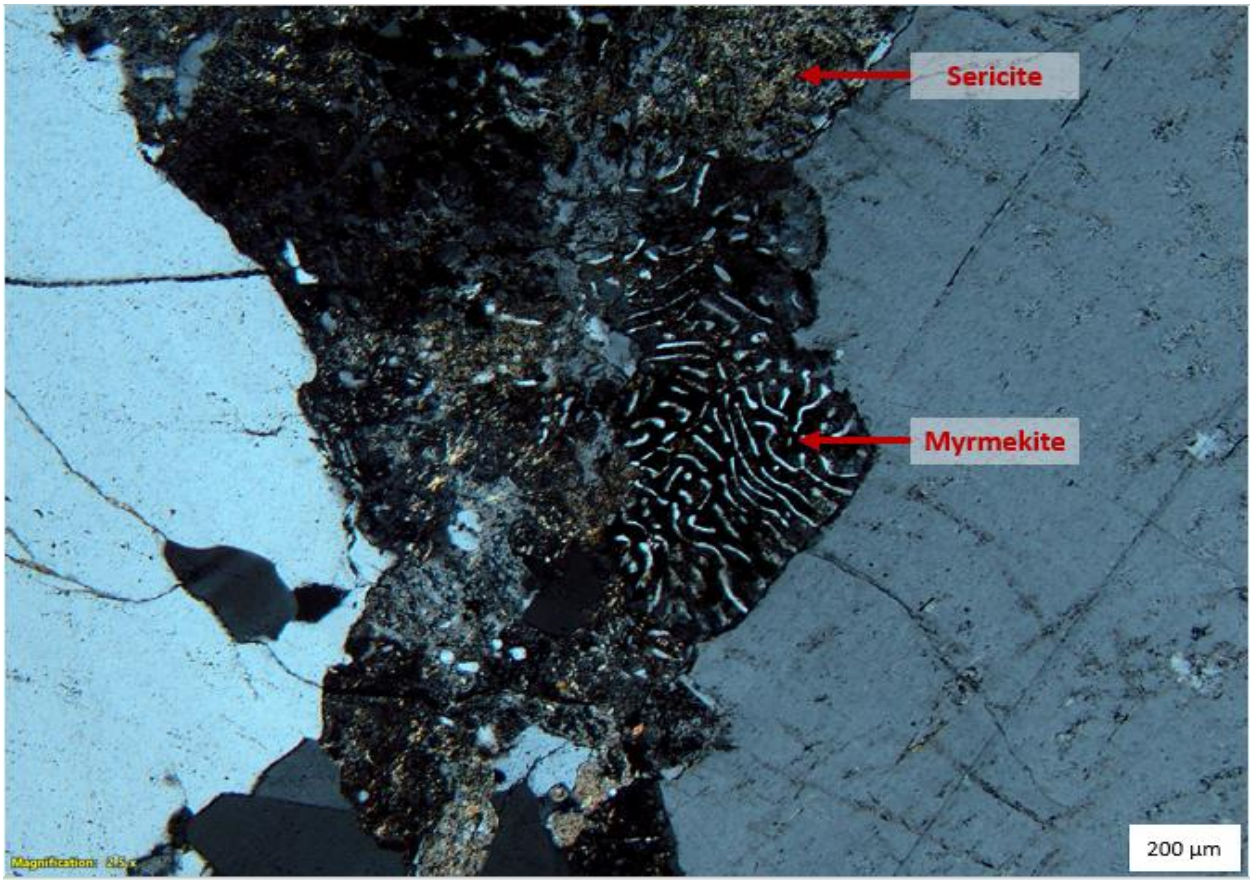

Figure 57. Photomicrograph showing weak white-mica alteration of plagioclase feldspar with myrmekite preservation (XPL). Scale bar is 200 µm.

Macrostructural analysis

Twenty chlorite infilled shear fractures and thirty-eight unfilled fracture orientations were collected across the four outcrops of the Indian Lake batholith. Of the twenty chlorite infilled shear fractures, the average dip is 73° while the median is 72°. Nine of the shear fractures have slickenlines with plunges ranging between 1° and 15°, indicative of an oblique strike-slip displacement. A dominant strike of south-east is noted within the chlorite infilled shear fracture population. Of the thirty-eight unfilled fractures measured, only five of them have dips shallower than 66°. Of the thirty-three unfilled fractures with steep dips, half of them have strikes consistent with the shear fractures while the remaining half strike north – presenting as a possible oblique strike-slip conjugate set to the infilled shear fractures. For these reasons, it is likely that the majority of the steeply dipping unfilled fractures measured within the Indian Lake batholith are weathered out shear fractures. Figure 58 shows a stereonet with all fifty-eight orientations while Figure 59 shows the individual stereonets and corresponding rose diagrams for the chlorite shear fractures and unfilled fractures.

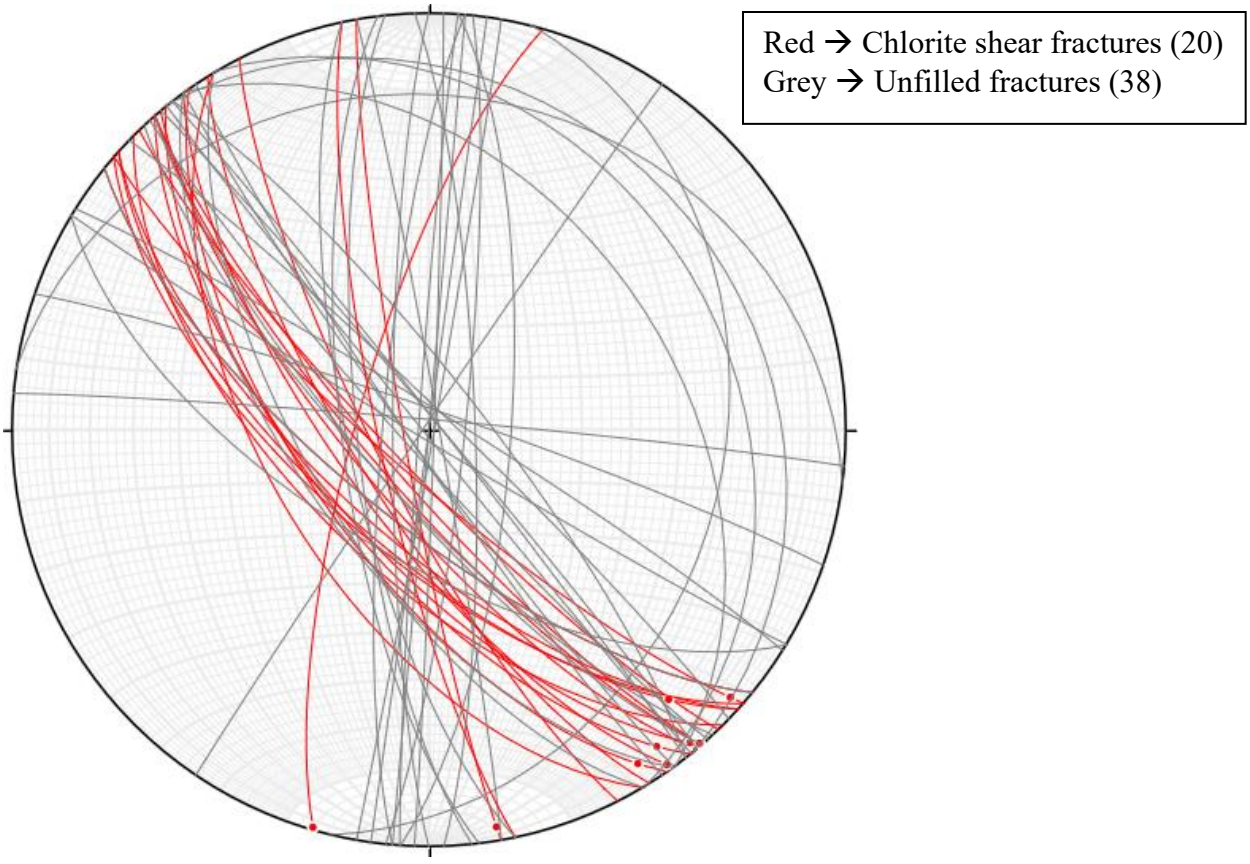

Figure 58. Stereonet of all measurements taken at the Indian Lake Batholith outcrops. 58 measurements in total. Legend shown in the upper right-hand corner.

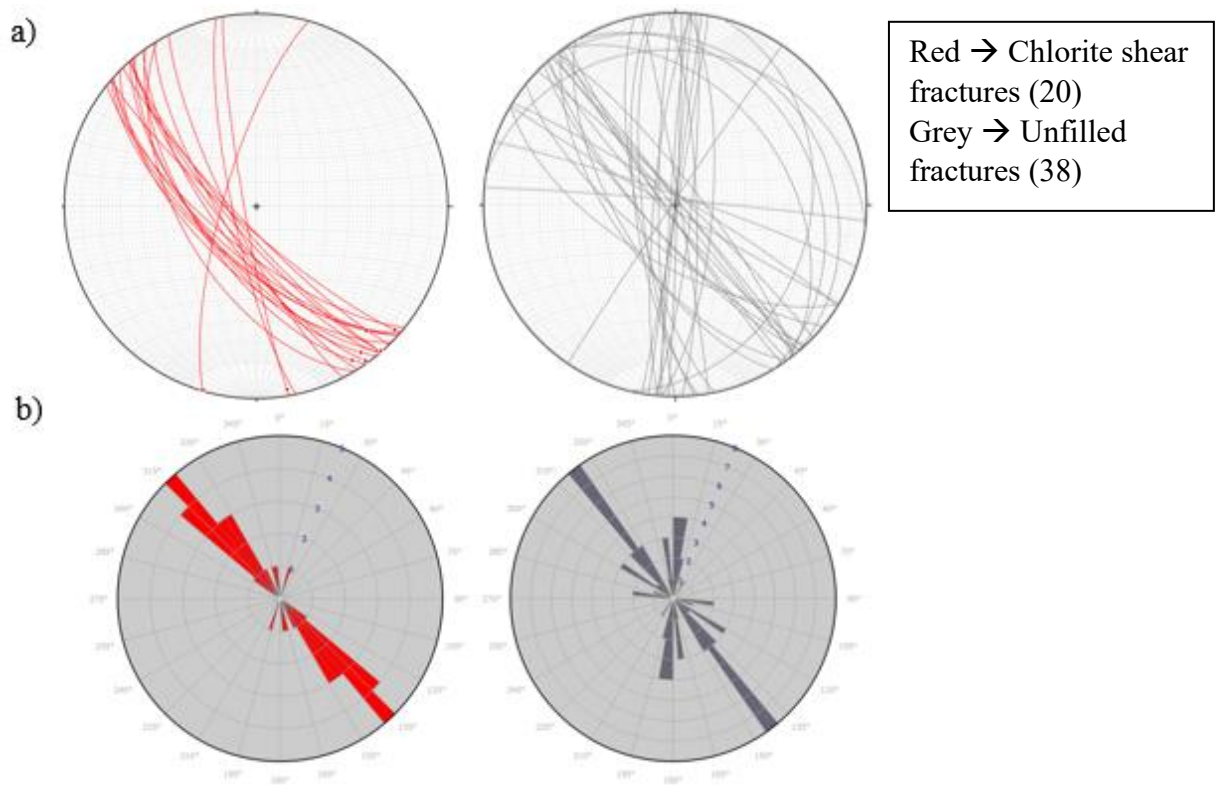

Figure 59. a) Stereonets for the chlorite-coated shear fractures and unfilled fractures. **b)** Rose diagrams for the chlorite-coated shear fractures and unfilled fractures.

Microstructural analysis

Quartz is fine-grained with undulose extinction, subgrains and serrated grain boundaries that commonly bulge into adjacent grains (bulging recrystallization). Feldspar is seen with undulose extinction, serrated grain boundaries, subgrains and intracrystalline microcracks. Some samples show minor foliation defined by the parallel alignment of muscovite, biotite and epidote. Recrystallization of the feldspar is minor and when present is typically seen along grain boundaries (Figure 60). Although alteration is minimal in the collected samples, strain is pervasive.

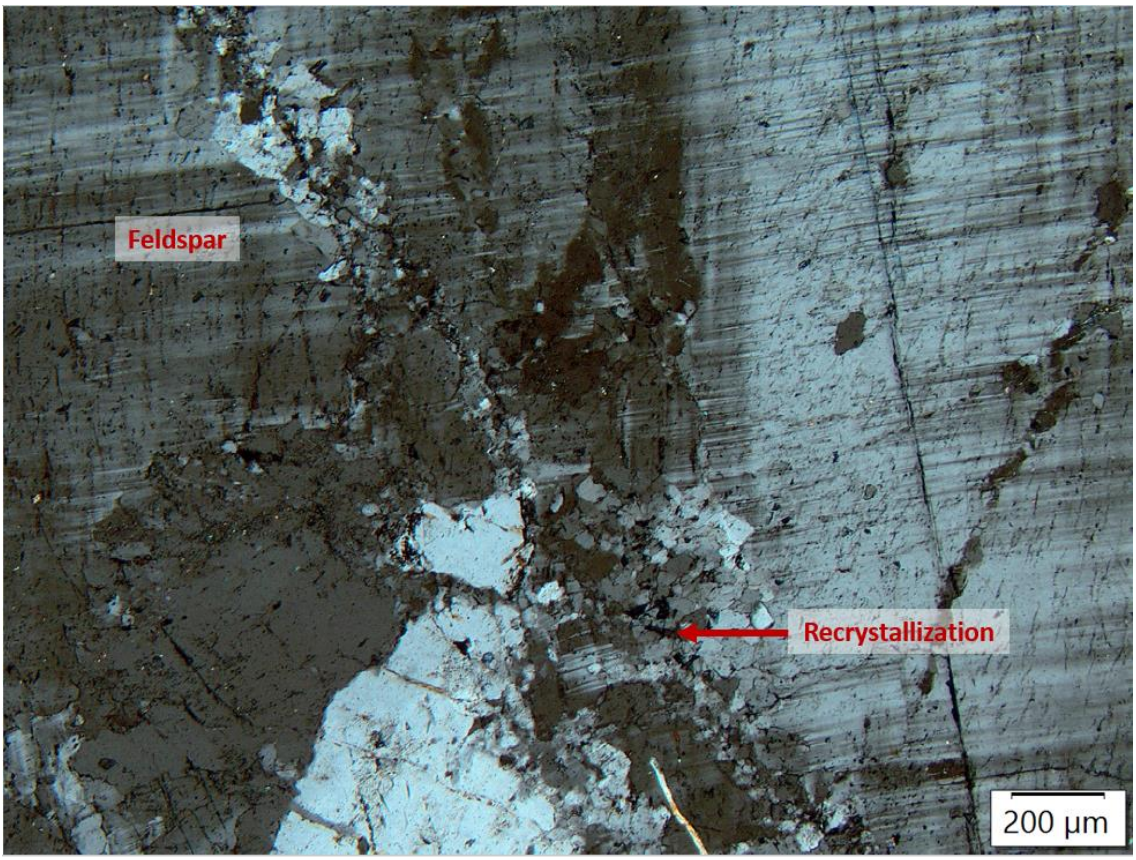

Figure 60. Photomicrograph of recrystallization along feldspar grain boundaries (XPL). Scale bar is 200 µm.

4.3.3 White Otter Lake Pluton

One outcrop of the White Otter Lake pluton was studied during this research (Figure 61). Three hand samples and seventeen structural orientations of mixed infilled shear fractures and unfilled fractures were collected.

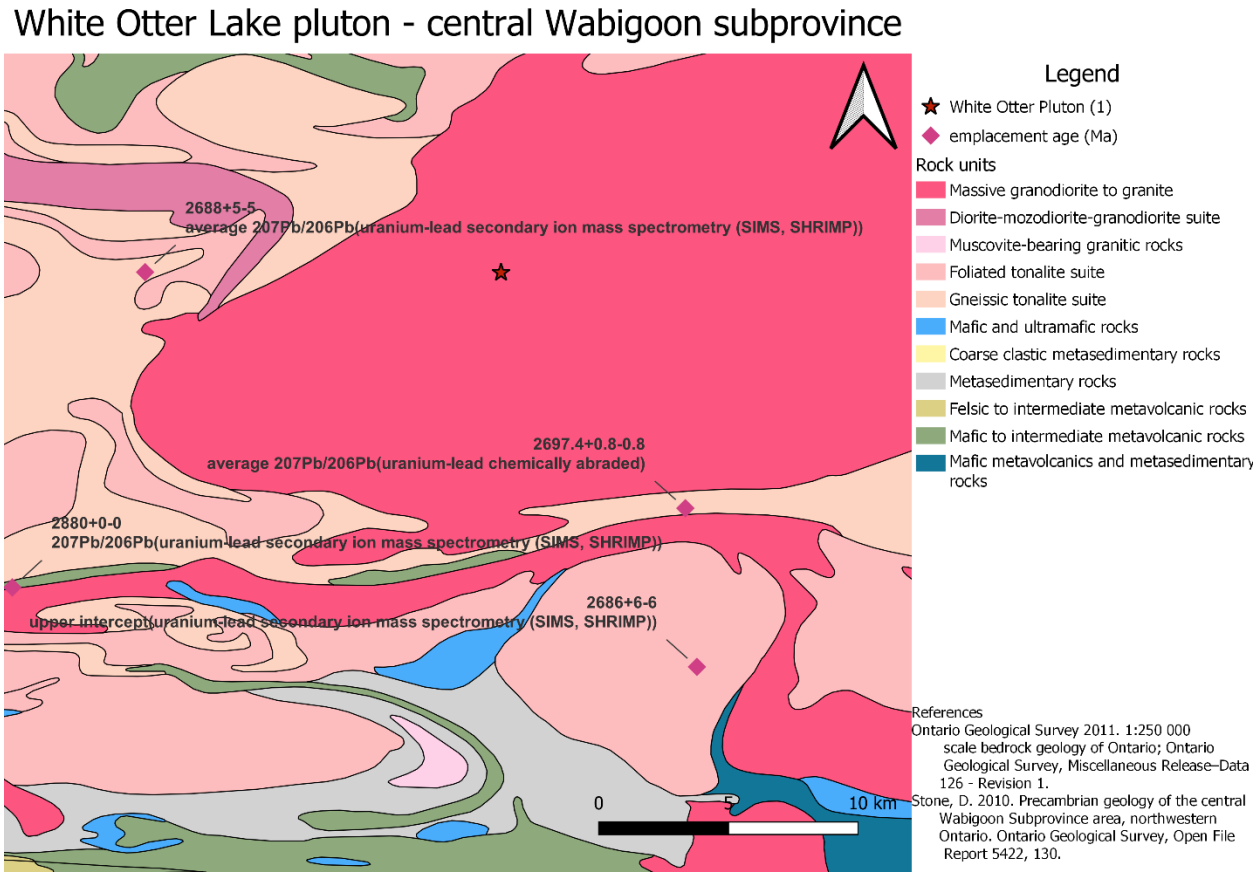

Figure 61. Map of the White Otter Lake pluton showing the 1 outcrop studied.

Mineralogy and alteration

Ninety-five percent of the bulk rock composition consists of quartz, plagioclase feldspar and potassic feldspars. The remaining 5% consists of alteration minerals including hematite, chlorite, white mica and epidote. Alteration is weak and sporadic in the samples collected. White mica replacement of feldspar occurs as a faint 'dusting' in thin section. Epidote is sometimes seen in association with the white mica or may occur on its own along fracture planes. Chlorite is seen infilling shear fractures, along microfractures within the host rock as well as forming the matrix in a cataclasite. Figure 62 shows chlorite along microfractures within feldspar along with weak sericite 'dusting'.

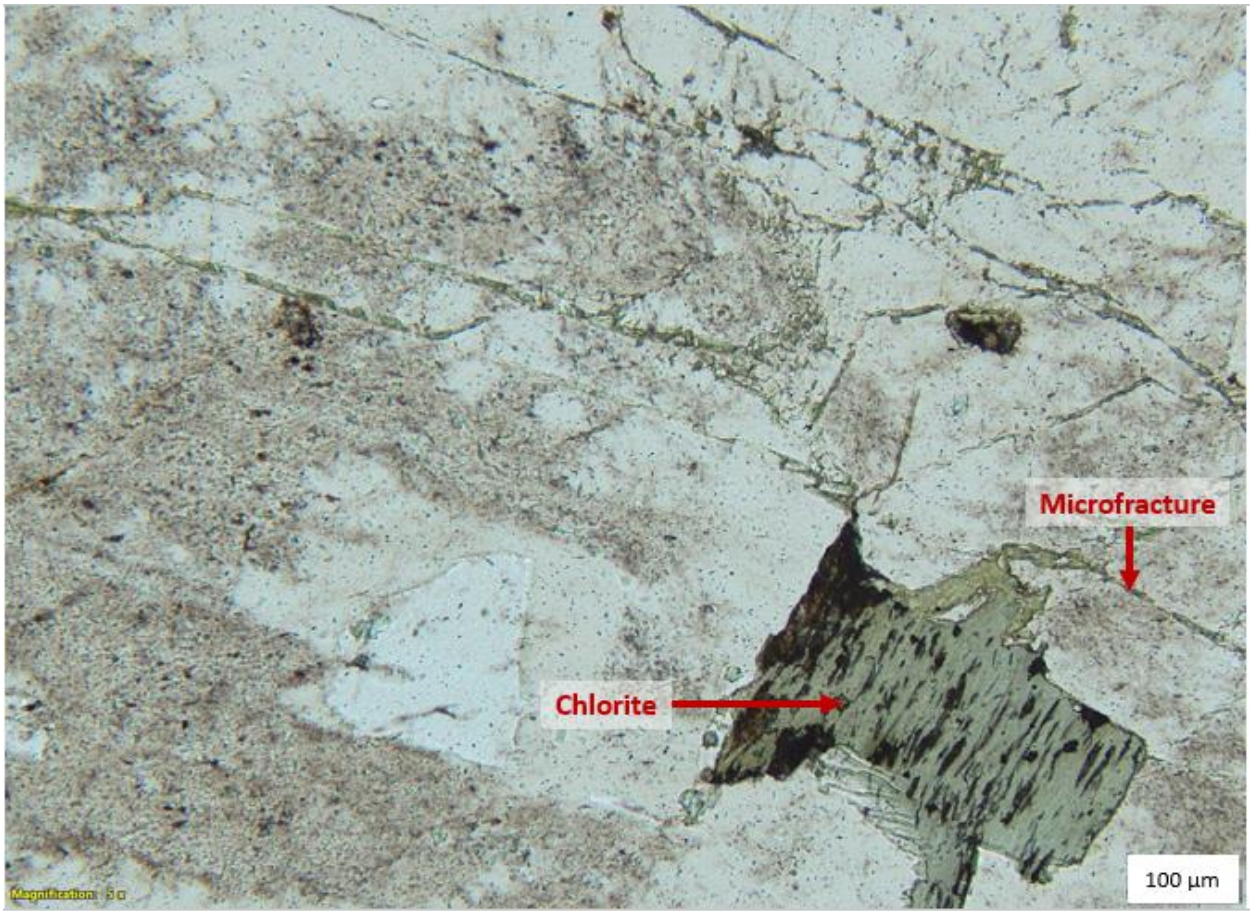

Figure 62. Photomicrograph of chlorite along microfractures within the White Otter Lake Pluton (PPL). Scale bar is 100 µm.

Macrostructural analysis

Seventeen structural orientations were taken from the White Otter Lake pluton – ten mixed infilled shear fractures (biotite ± chlorite ± epidote) and seven unfilled fracture plans. Some of the unfilled fracture plans appeared to have dark red staining on the fracture surfaces, potentially corresponding to hematite. All seventeen fractures are steeply dipping with an average and median dip of 86° and 88.5°, respectively. Only one slickenline was measured with a plunge of 12°, consistent with oblique strike-slip displacement. Figure 63 shows the stereonet for the seventeen fracture orientations. Figure 64 shows the individual stereonets and accompanying rose diagrams for the mixed infilled shear fractures and their accompanying rose diagrams. Both populations of fractures have a dominant south-west to north-west strike.

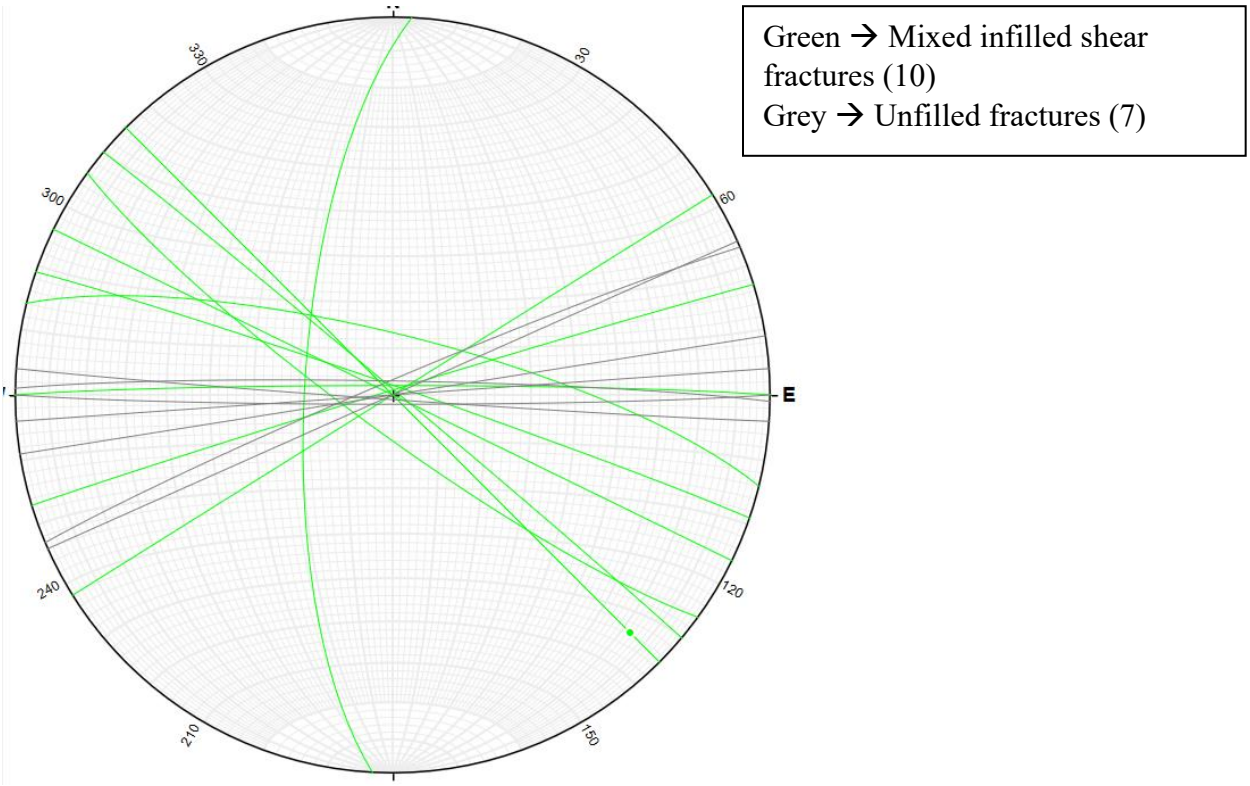

Figure 63. Stereonet displaying the seventeen fracture orientations measured in the White Otter Lake pluton. Legend in upper right-hand corner.

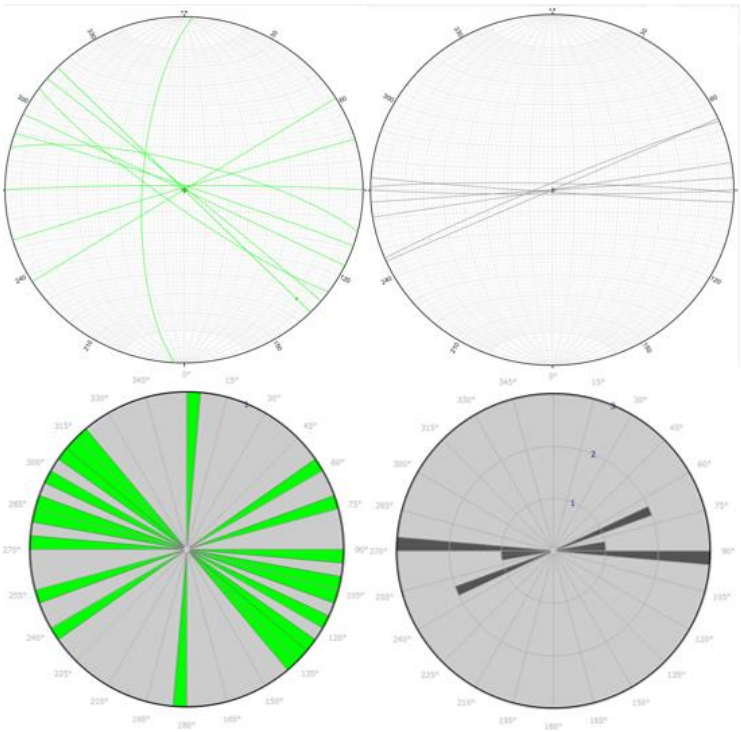

Figure 64. a) Individual stereonets for the mixed infilled shear fractures and the unfilled fractures. **b)** Rose diagrams for the mixed infilled shear fractures and the unfilled fractures.

Microstructural analysis

Deformation microstructures within quartz include strong undulose extinction, subgrains and serrated grain boundaries. Feldspars commonly have microfractures infilled with muscovite ± hematite, serrated grain boundaries, subgrains, minor evidence of dynamically recrystallized feldspars along grain boundaries, deformation twins and minor amounts of myrmekite.

One of the thin sections of the White Otter Lake batholithic complex shows a small three mm wide cataclasite infilled with a chlorite matrix. This cataclasite is host to angular fragmented pieces of feldspars and quartz ranging from < 0.05 mm to roughly 1 mm maximum. Narrow damage zones < 1 mm in width radiate outwards from the cataclasite which caused a localized grain-size reduction of host mineral phases through comminution. This brittle feature requires space to operate and likely corresponds to a later and lower temperature deformation event than the shear fractures and shear zones noted in the other plutons. Figure 65 shows the photomicrographs of the chlorite infilled cataclasite.

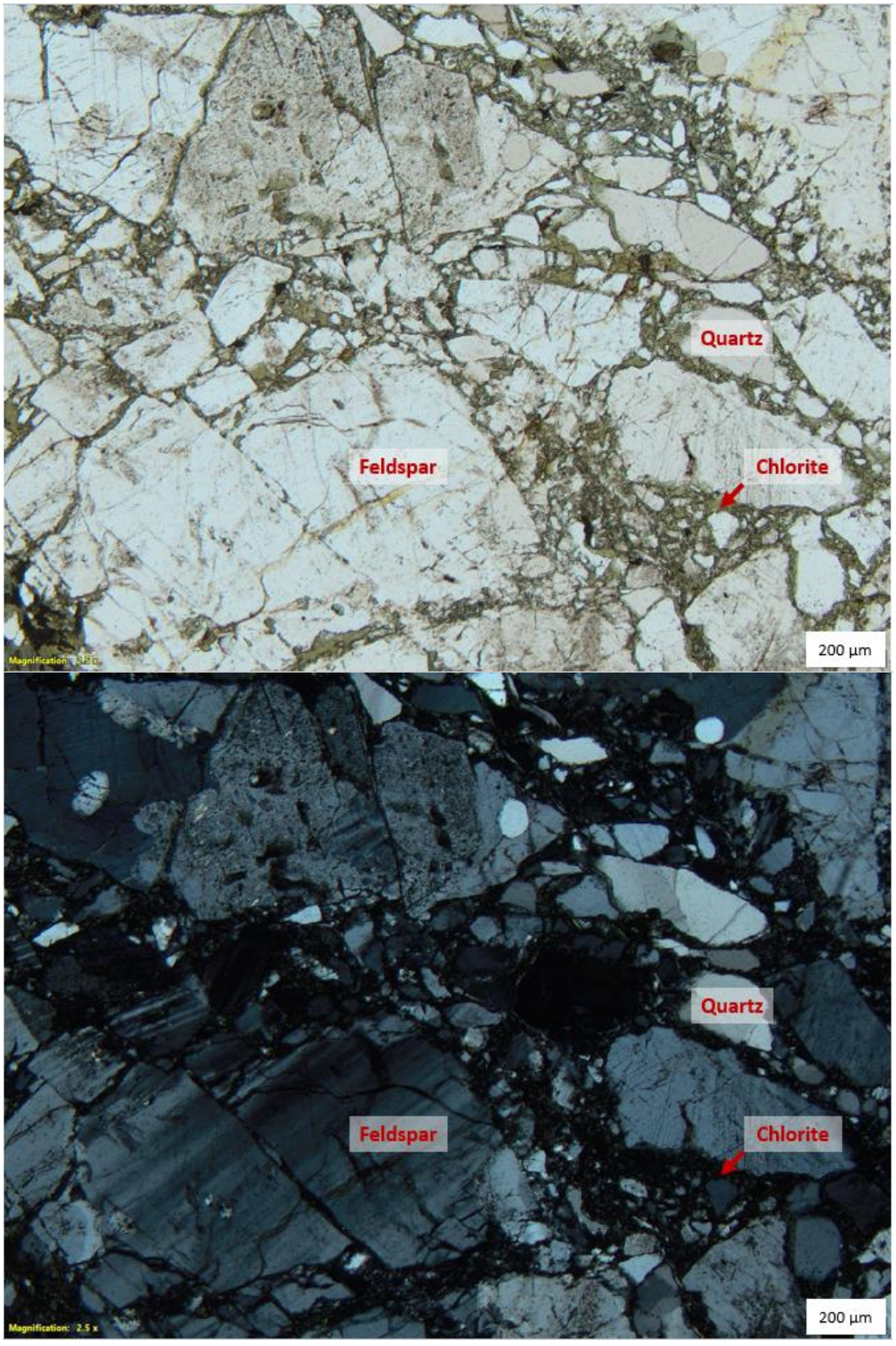

Figure 65. Top – PPL, **Bottom** – XPL. A chlorite infilled cataclasite seen in the White Otter Lake batholithic complex. Angular clasts of feldspars and quartz are seen displaying undulose extinction and subgrains. Scale bar is 500 µm for both images.

4.3.4 Sowden-Wabakimi Lakes batholithic complex

Seven hand samples and forty-four structural orientations were taken from four outcrops of the Sowden-Wabakimi Lakes batholithic complex exposed along Highway 11/17 (Figure 66). Of particular interest is the presence of mafic dikes within one of the outcrops (Figure 67) – the mineralogy of which can be used to help constrain the metamorphic grade of the pluton.

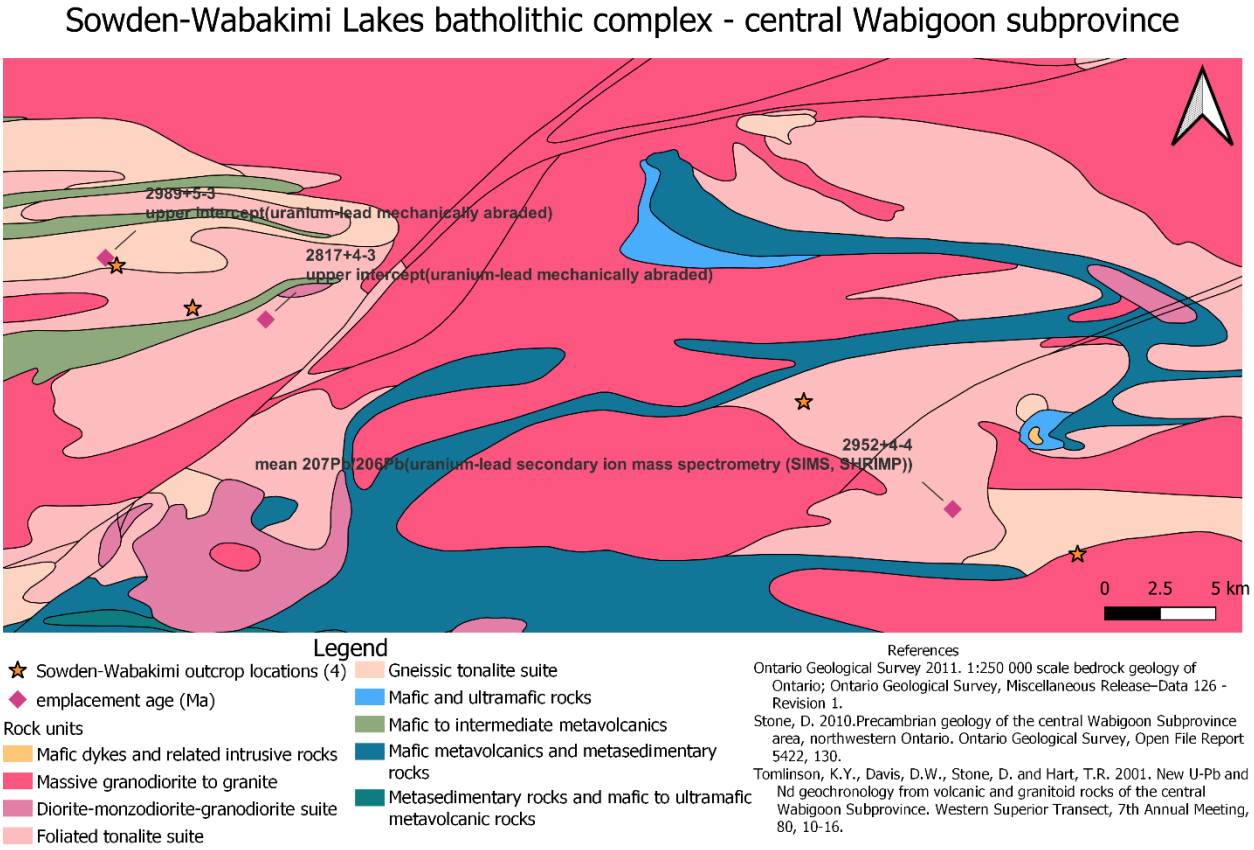

Figure 66. Map of the Sowden-Wabakimi Lakes batholithic complex showing the 4 outcrops studied and available emplacement ages of various granitoid rocks.

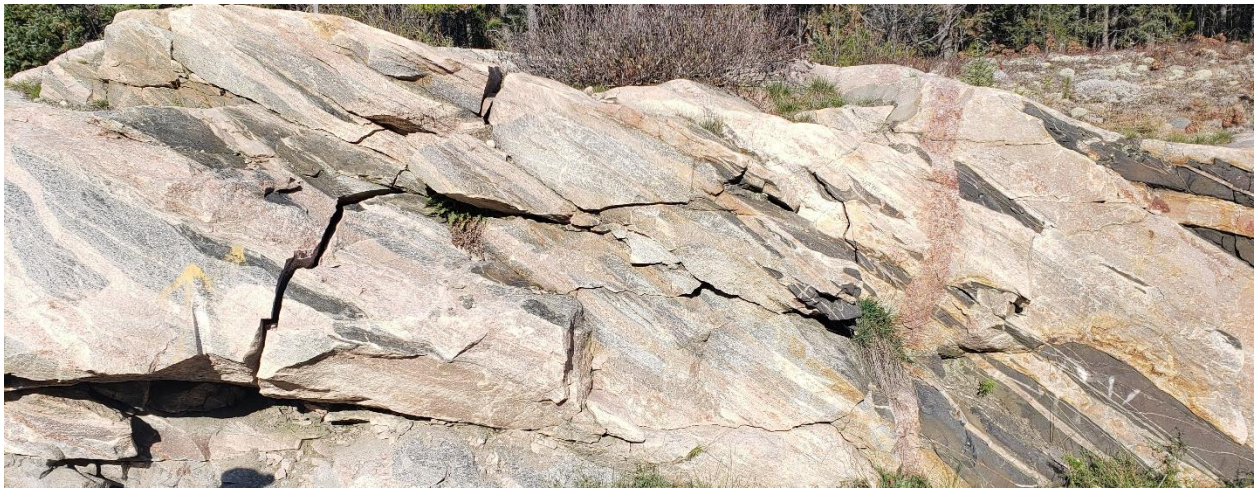

Figure 67. Outcrop photo of dykes within the Sowden-Wabakimi Lakes batholithic complex.

Dike mineralogy

Fine-grained hornblende (ranging from 0.5 mm to 2 mm), fine-grained quartz and fine-grained plagioclase are the main mineral constituents of the dikes. Trace amounts of biotite, sphene, epidote and chlorite can also be seen. Chlorite occurs exclusively as a replacement of biotite. A representative photomicrograph of the dike sampled is shown in Figure 68. This mineral assemblage is typical of a metamorphosed mafic dike to the amphibolite facies of metamorphism which agrees with the peak metamorphic mineral assemblage recorded by the deformation microstructures within the pluton and the other plutons studied.

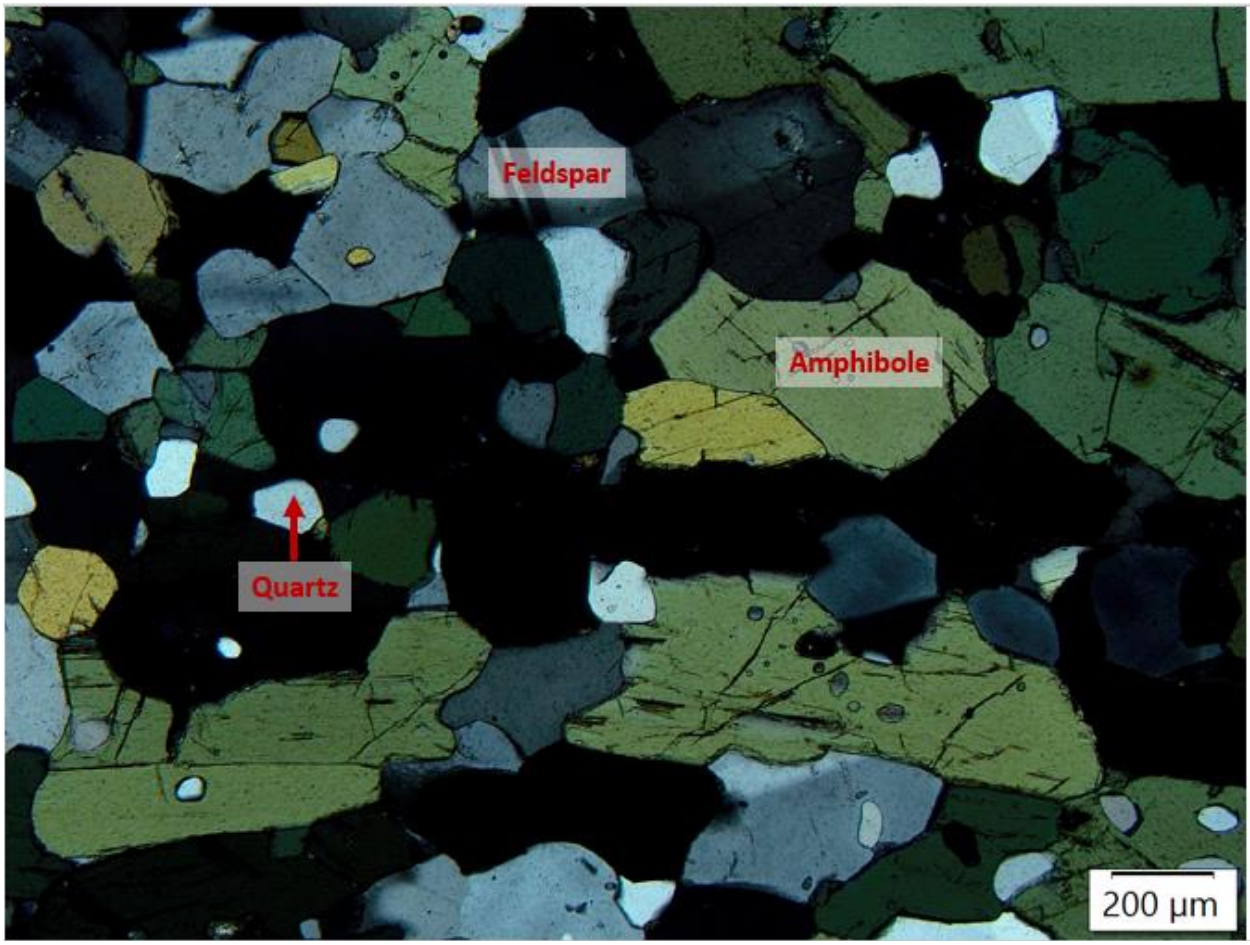

Figure 68. Photomicrograph of a dike within the Sowden-Wabakimi Lakes batholithic complex (XPL). The dike is characterized as an amphibolite with a metamorphic mineral assemblage of amphibole + plagioclase + quartz with accessory biotite, sphene, chlorite and epidote.

Pluton mineralogy and alteration

The mineralogy of the Sowden Wabakimi Lakes batholithic complex is comprised of fine-grained quartz, fine- to medium-grained plagioclase feldspar and fine to medium grained potassic feldspar. Minor amounts (< 15% of bulk rock) of hornblende, white mica, biotite, sphene and chlorite are present. White mica is the dominant alteration mineral present within the collected thin sections and appears as a weak to strong alteration product of plagioclase feldspars. Some epidote is seen with the white mica. Chlorite and epidote occur primarily along shear fractures, and both are also present within the host rock, typically along microfractures or grain boundaries. When present, sphene tends to be associated with epidote. Sericitization of feldspars is shown in Figure 69.

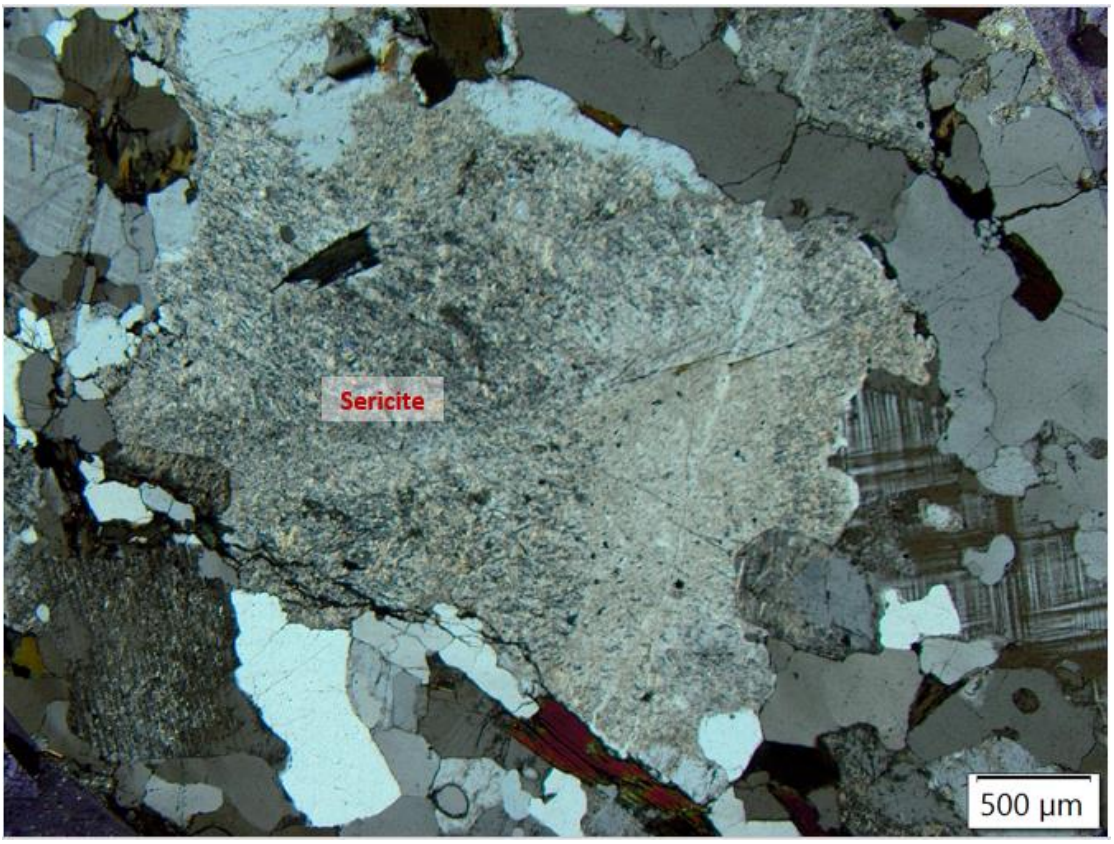

Figure 69. Photomicrograph of sericitization in feldspars within the Sowden-Wabakimi Lakes batholithic complex (XPL). Scale bar is 500 µm.

Macrostructural analysis

Of the forty-four structural orientations measured, eighteen are chlorite infilled shear fractures, twenty-three are unfilled fractures, two are foliation measurements and one is a shear zone. Figure 70 shows the stereonet with all structural orientations plotted while Figure 71 shows the individual orientations and rose diagrams for the major populations. The average and median dips of the chlorite infilled shear fractures are 74.5° and 78°, respectively. Only two slickenline orientations were measured, which plunge 21° and 10°. Most of the measured unfilled fractures fit the general dips and strikes of the shear fracture population and are likely representative of weathered out shear surfaces. The strikes of both populations (Figure 71b) vary quite a bit across the three outcrops studied, possibly due to non-coaxial strain in which the trend of the maximum elongation direction shifts in response to the rigid body rotation of the competent granitoid plutons.

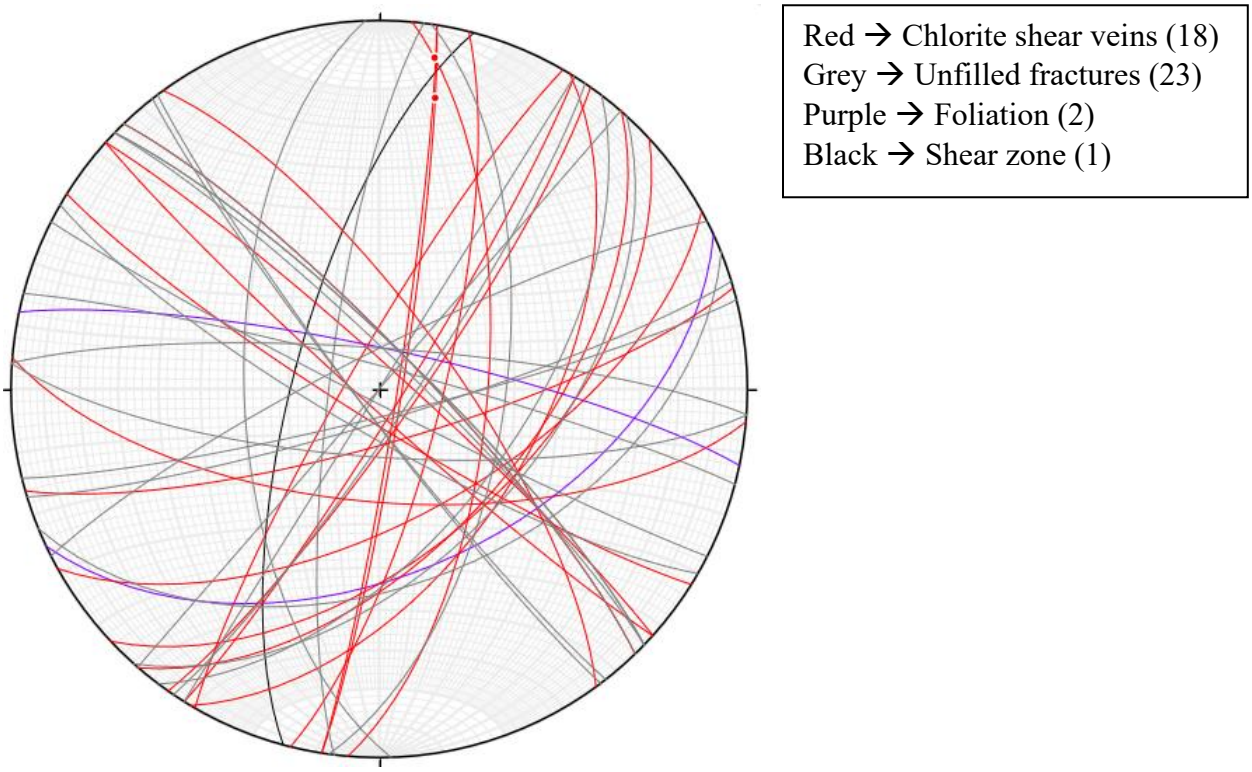

Figure 70. Stereonet of all measurements taken at the Sowden Wabakimi batholithic outcrops. 44 measurements in total. Legend shown in upper right-hand corner.

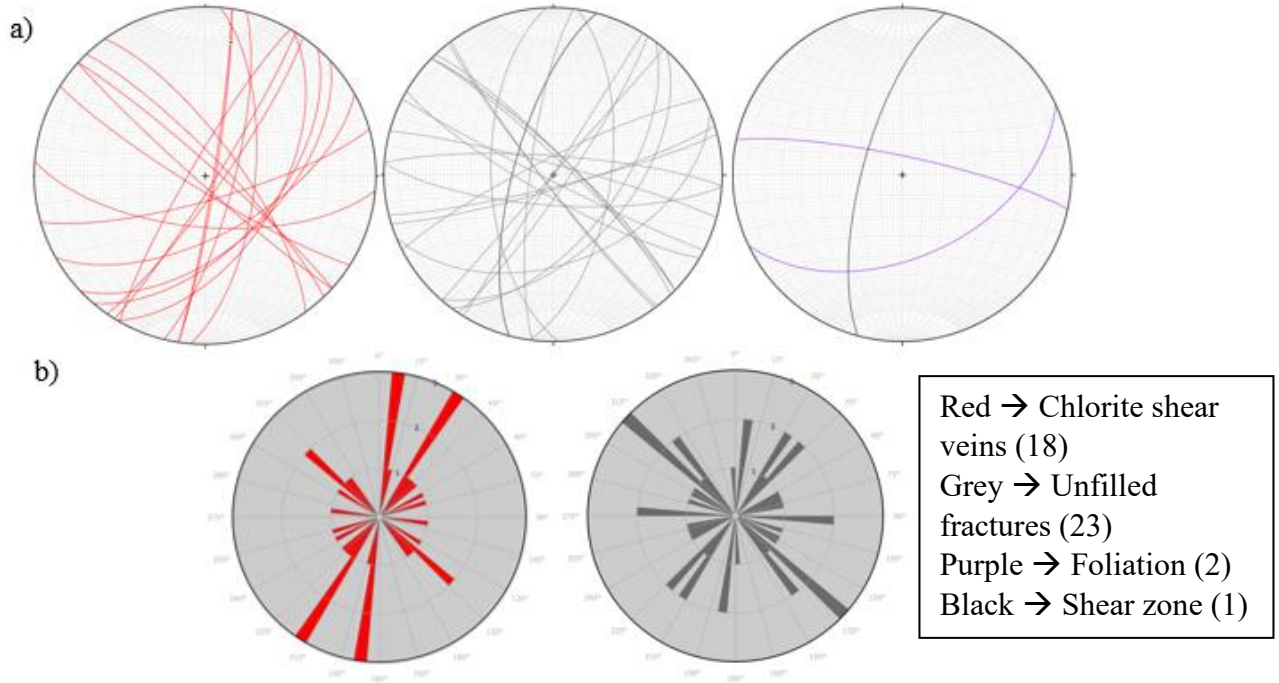

Figure 71. a) Stereonets of all measurements taken from the Sowden-Wabakimi batholithic complex outcrops. **b)** Rose diagrams for the Sowden-Wabakimi batholithic complex outcrops.

Microstructural analysis

Most samples represent low strain zones in which quartz is commonly seen with weakly serrated grain boundaries, strong undulose extinction and subgrains. Feldspar is commonly seen with weakly to moderately serrated grain boundaries, minor undulose extinction, subgrains, deformation twins, polysynthetic twins and intracrystalline microfractures. Some of the microfractures are infilled with hematite. Occasional occurrences of myrmekite are identified within the plagioclase, typically near grain boundaries.

One sample is characterized as a shear zone in which quartz and feldspar are grain-size reduced compared to the surrounding host rock. A moderate foliation defined by biotite and feldspar is seen within the shear zone. Quartz and feldspar have deformation microstructures such as undulose extinction, subgrains and semi-serrated grain boundaries. A lack of shear fractures or other brittle features within the shear zone classifies it as a ductile shear zone. Figure 72 shows the ductile shear zone on the left half of the photomicrograph while the right half is the non-sheared portion of the pluton.

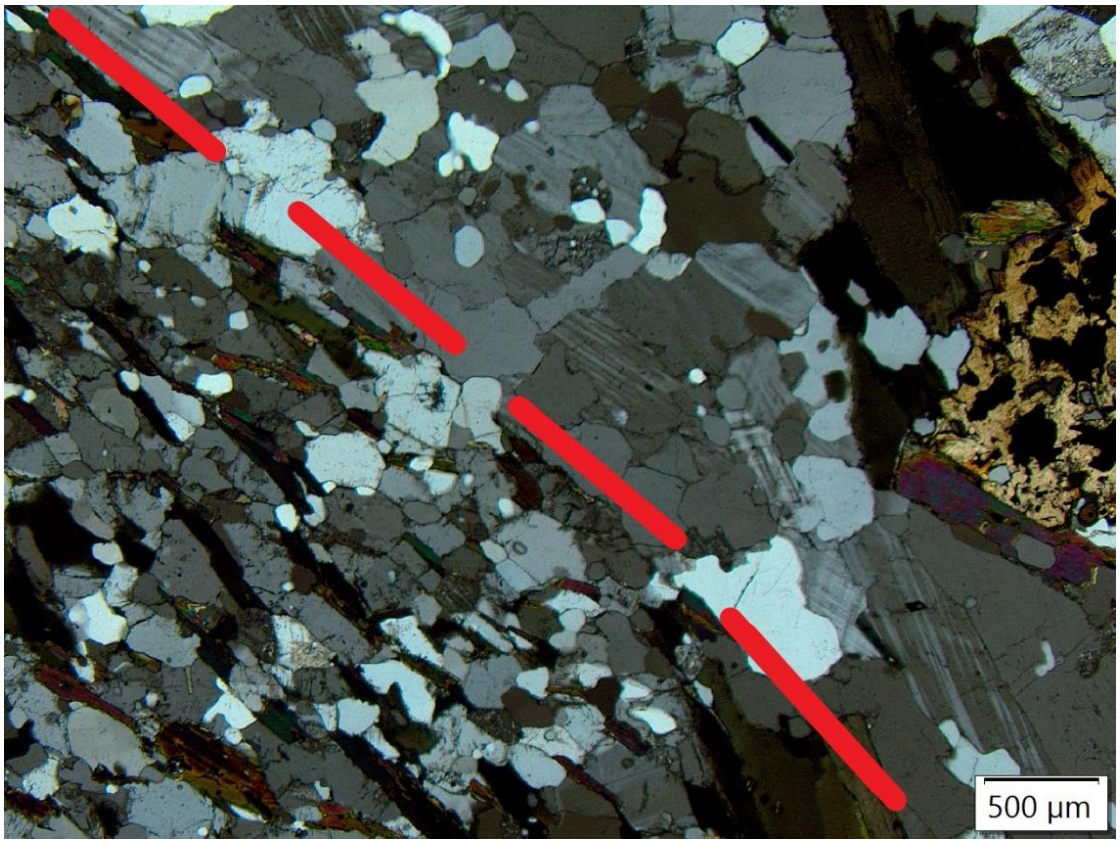

Figure 72. Photomicrograph of the contact (dashed red line) between a ductile shear zone and the host Sowden Wabakimi Lakes batholithic complex granitoid (XPL). Scale bar is 500 µm.

4.3.5 Marmion batholith

Nine structural orientations and seven hand samples were collected from one outcrop of the Marmion batholith (Figure 73). An additional three samples were collected from three drill core samples provided by Agnico Eagle. Each of the drill core samples have chlorite-coated shear fractures that were assessed for stable isotopic analysis (see Chapter 6).

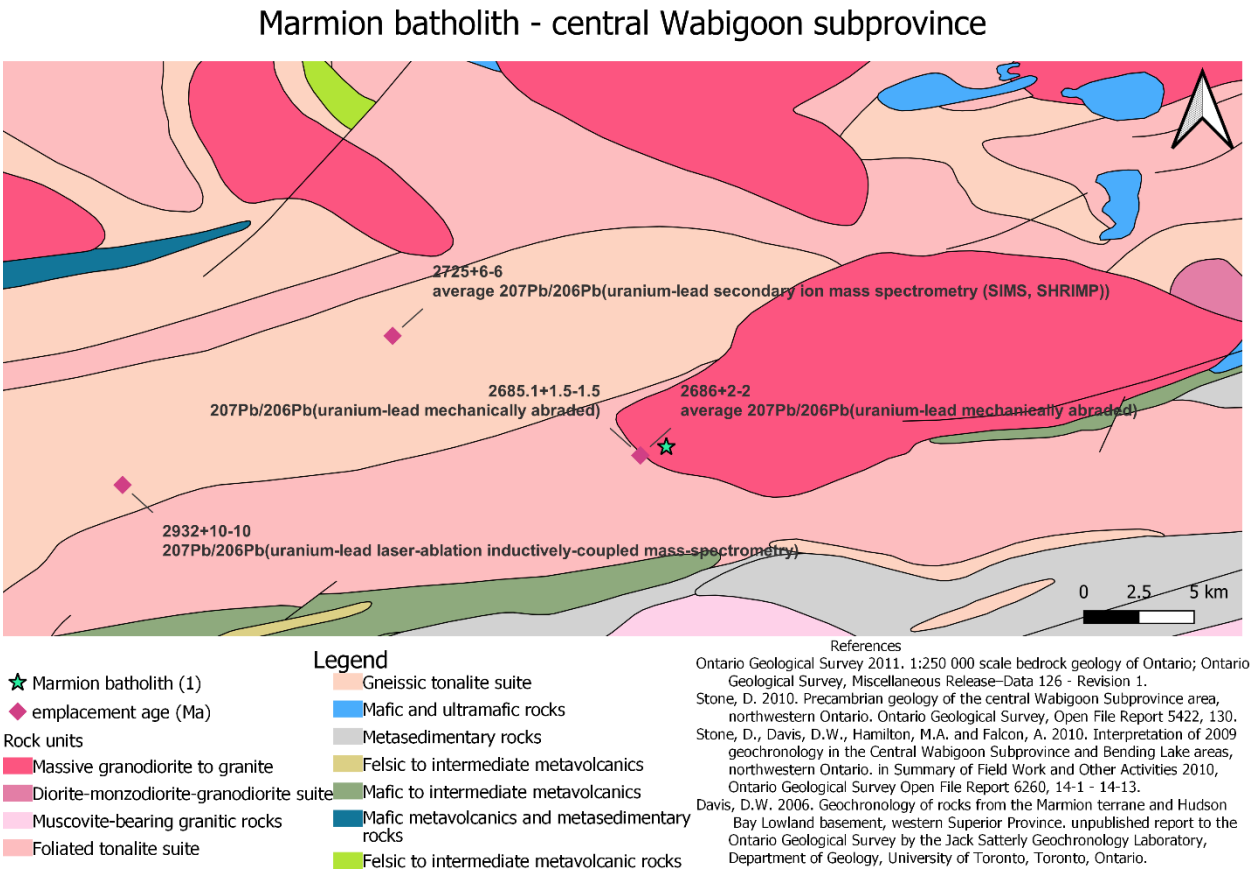

Figure 73. Map of the Marmion batholith area with the 1 outcrop location studied. Available emplacement ages are also shown.

Mineralogy and alteration

Roughly 90% of the bulk mineralogy is composed of quartz, plagioclase feldspar and potassic feldspar while the remaining 10% represents varying amounts of white mica, epidote group minerals, biotite and chlorite. Chlorite occurs predominately as infillings to shear fractures but is also seen within the host rock along grain boundaries and microfractures. White mica is commonly seen replacing feldspar, occasionally with epidote group minerals. Epidote occurs as an alteration mineral replacing feldspar but is also thought to be present as a magmatic phase. The potential magmatic epidote (classified as zoisite – see Chapter 5) has strong fan-like undulose extinction and is completely encased in chlorite (Figure 74), meaning that it is not part of the stable metamorphic mineral assemblage.

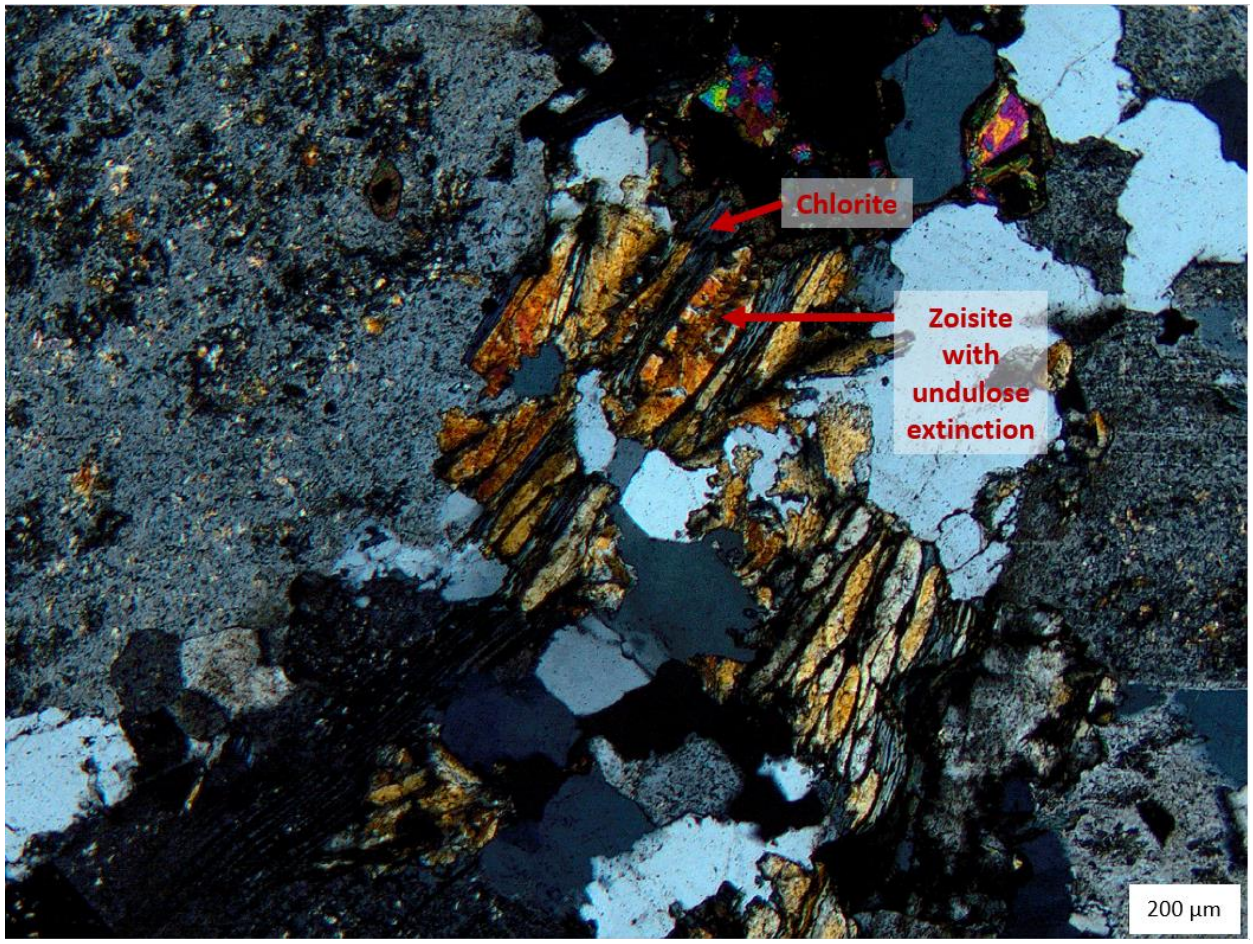

Figure 74. Photomicrograph of potential magmatic epidote (zoisite) with undulatory extinction (XPL). Zoisite is completely encased in chlorite - indicating that the zoisite is not part of the stable metamorphic mineral assemblage. Scale bar is 200 µm.

Macrostructural analysis

Although only nine structural orientations were taken in the outcrop. The four chlorite infilled shear fractures measured in the field have dips ranging from 65° to 84°, with one of the fractures recording slickenlines with a plunge of 21°. The foliation measured within the outcrop dips 72°. Figure 75 shows the stereonet for the Marmion batholith structures. Note that no rose diagrams were produced since not many orientations were measured.

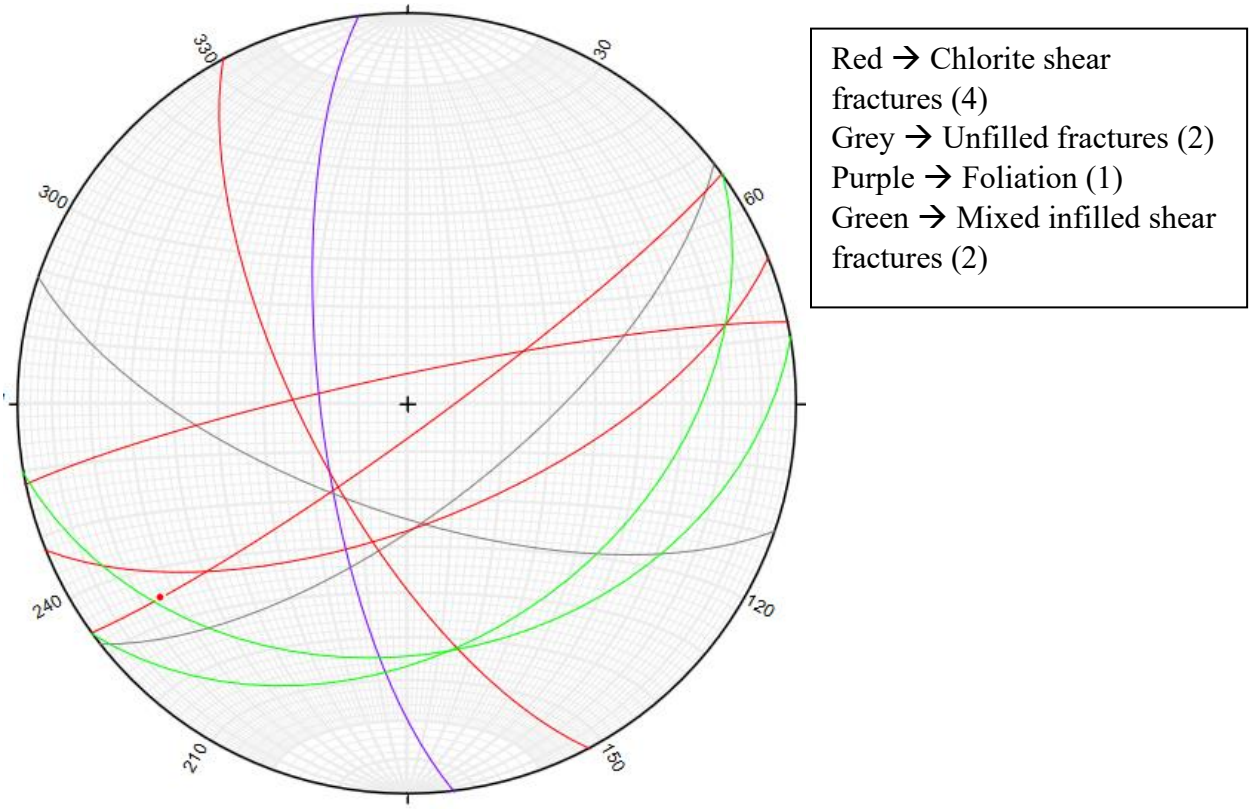

Figure 75. Stereonet of the nine structural orientations taken in the Marmion batholith.

Microstructural analysis

Deformation microstructures are consistent across the outcrop. Quartz displays serrated grain boundaries, undulose extinction, subgrains and bulging of crystals into adjacent crystals (bulging recrystallization). Feldspar is commonly identified with serrated grain boundaries, undulose extinction, subgrains, deformation twins and minor recrystallization along grain boundaries. The drill core samples are higher strain than the outcrop samples. Drill core samples have chlorite-coated and muscovite-coated infilled shear fractures, a higher degree of subgrains, undulose extinction and subgrains within all mineral phases and a strong muscovite alteration overprint. A representative photomicrograph is shown in Figure 76. The higher degree of muscovite alteration within the drill core samples is likely due to the presence of the chlorite infilled shear fractures within proximity to the increased alteration. There is also the possibility of sampling bias as altered rocks near surface would weather more rapidly – so alteration is most likely to be preserved in samples taken at depth where weathering doesn't occur.

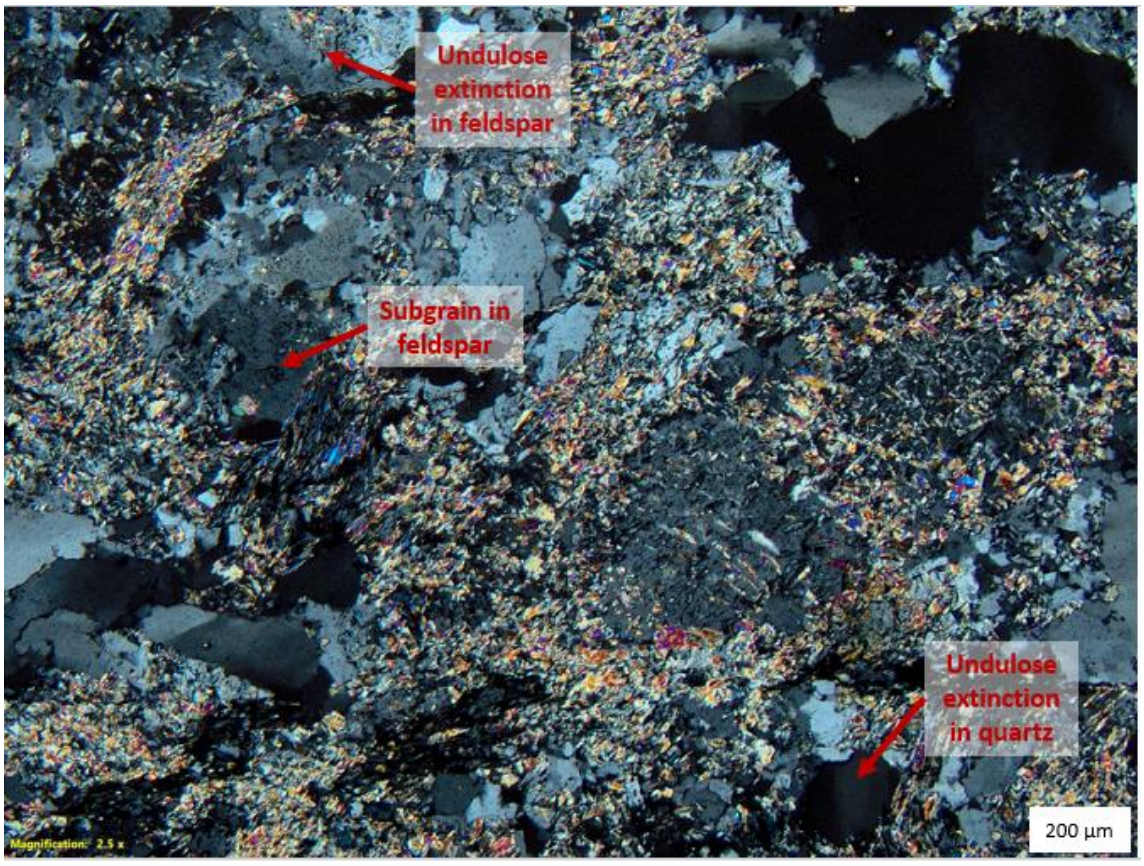

Figure 76. Photomicrograph of the Marmion batholith drill core showing strong undulose extinction in quartz and numerous subgrains in quartz and feldspars (XPL).

4.4 Eastern Wabigoon subprovince

4.4.1 Croll Lake Stock

Fifty-four structural orientations and ten hand samples were collected from four outcrops of the Croll Lake Stock exposed on highway 11 around the town of Longlac, ON (Figure 77). This is the only pluton studied in the eastern Wabigoon subprovince.

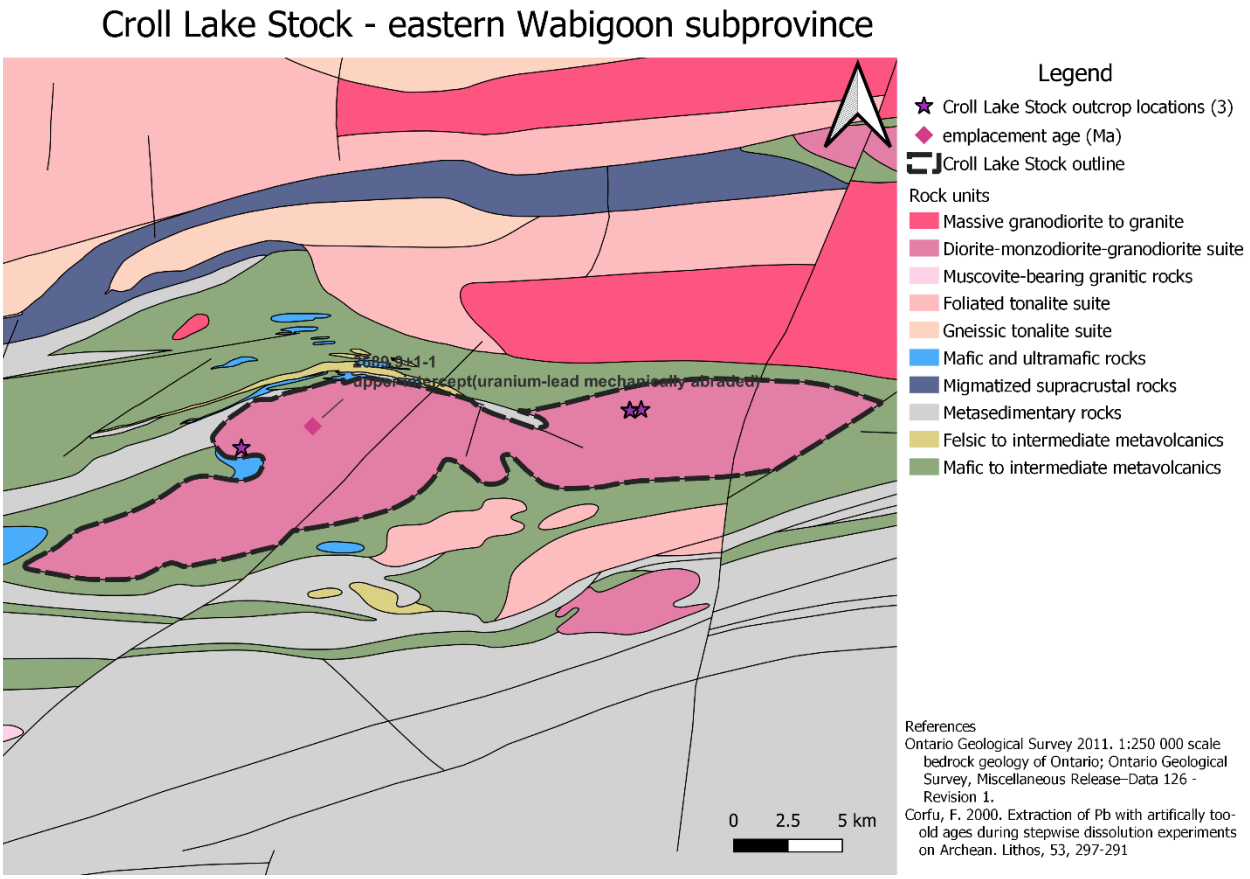

Figure 77. Map of the Croll Lake Stock showing outcrop locations and 1 available age date for the emplacement of the Croll Lake Stock (2689.9 Ma).

Mineralogy and alteration

The Croll Lake Stock is characterized by quartz, plagioclase feldspar and potassic feldspar that account for roughly 80% of the bulk rock mineralogy. Hornblende accounts for roughly 5 – 10% while the remaining 5 to 15% is accounted for by chlorite, epidote, white mica, biotite and sphene. White mica and epidote commonly replace feldspar (Figure 78), and chlorite is commonly replacing biotite (Figure 79). Both epidote and chlorite occur as shear fracture infilling and along microfractures within the host rock, typically associated with sphene.

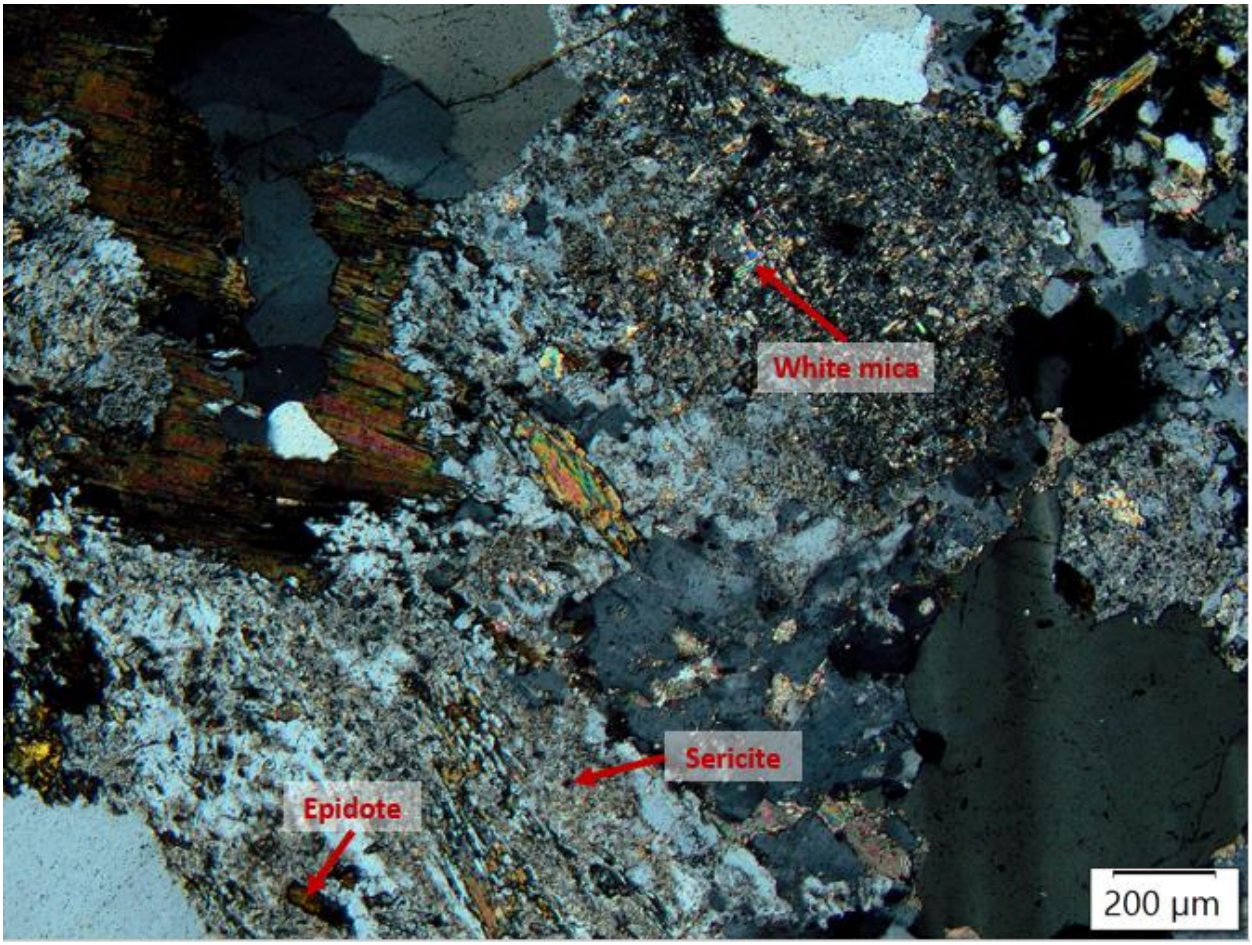

Figure 78. Photomicrograph showing white mica - epidote alteration within feldspars (XPL).

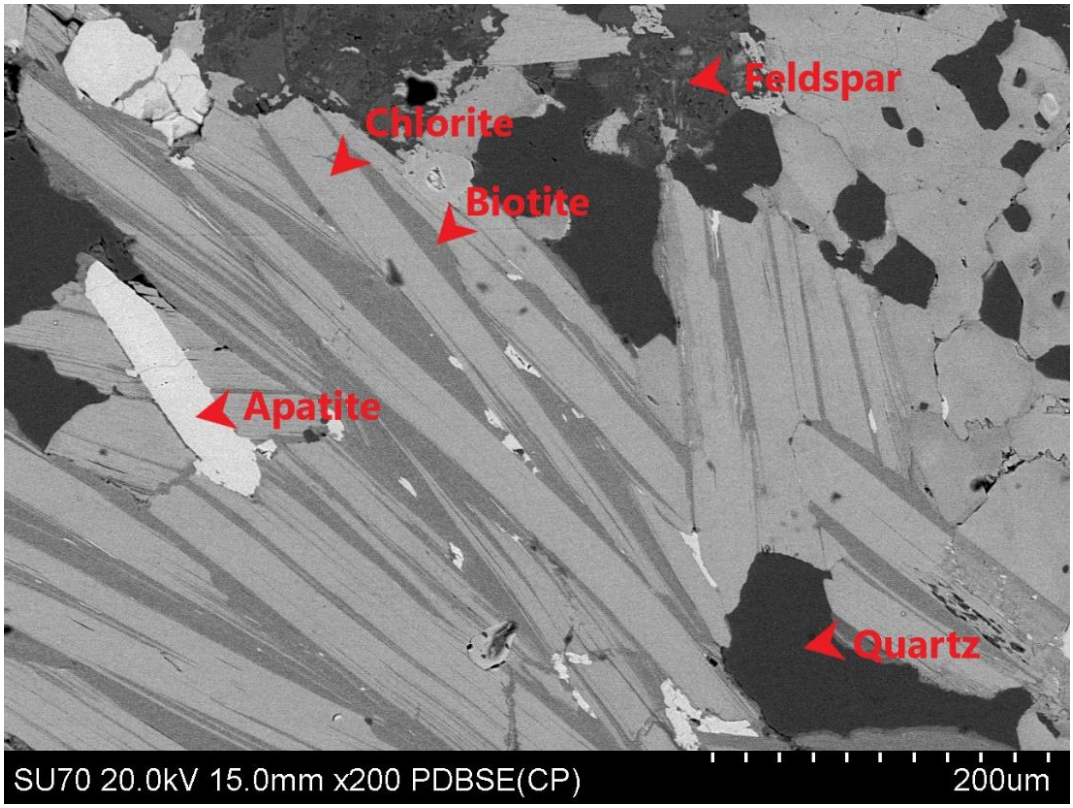

Figure 79. SEM-BSE image of chlorite (lighter color) replacing biotite laths (darker color).

Macrostructural alteration

Of the fifty-four structural orientations, twenty-five are chlorite infilled shear fractures, fifteen are unfilled fractures, eight are quartz veins and six are mixed infilled shear veins. The stereonet for all orientations is shown in Figure 80, while Figure 81 presents the individual stereonets and accompanying rose diagrams. Average and median dips of all shear veins is 64° and 72°, respectively. Although no slickenline orientations were measured in the field, slickenlines were noted to be sub-horizontal in nature (Figure 82). Chlorite infilled shear fractures have a dominant north-east to south-west strike with a second minor population that strike north-west to south-east. These two orientations may represent conjugate oblique strike-slip shear surfaces.

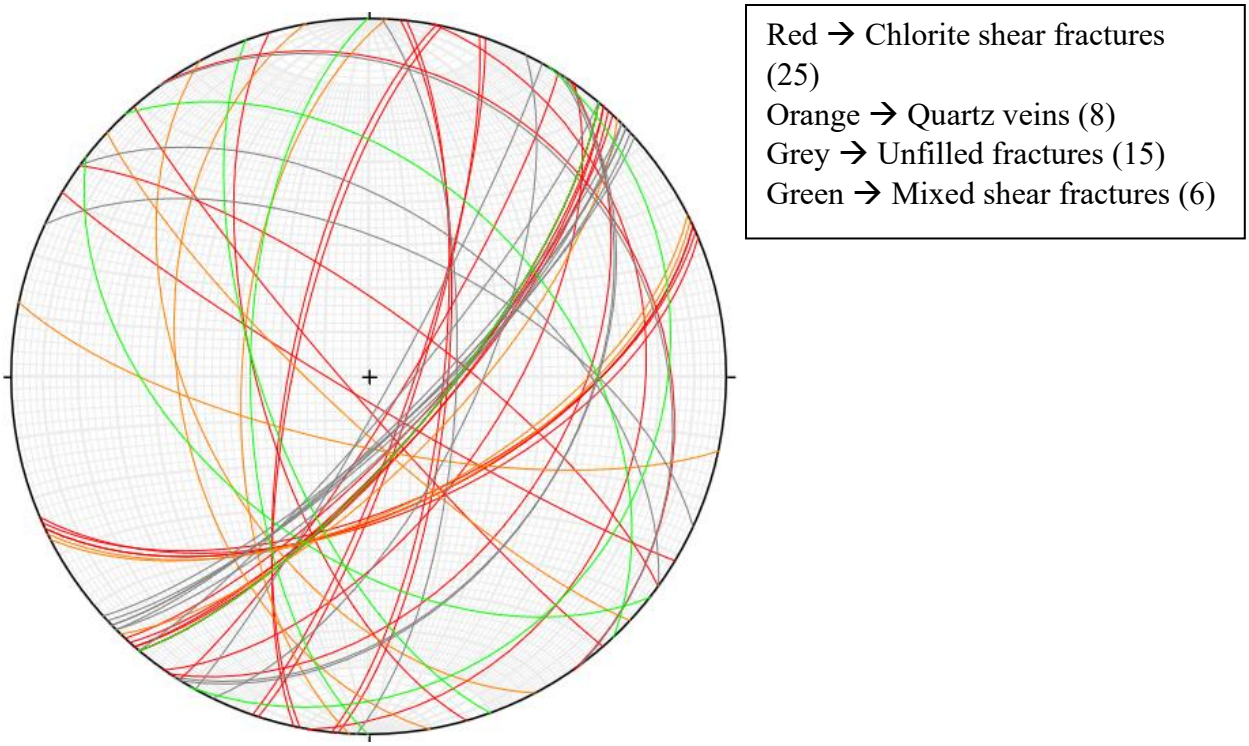

Figure 80. Stereonet of all measurements taken from the Croll Lake Stock outcrops. 54 measurements in total.

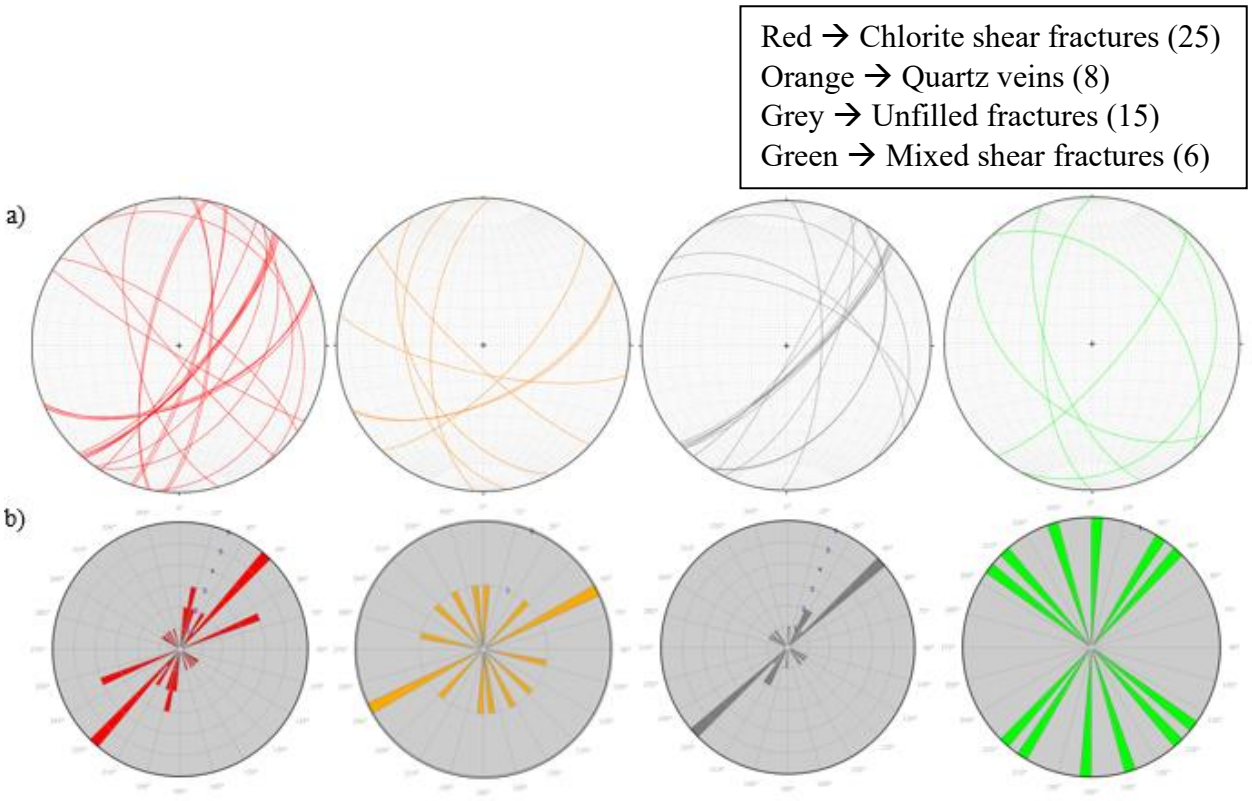

Figure 81. a) Stereonets of all measurements taken from the Croll Lake Stock outcrops. **b)** Rose diagrams for the Croll Lake Stock outcrops. Legend shown in Figure 70.

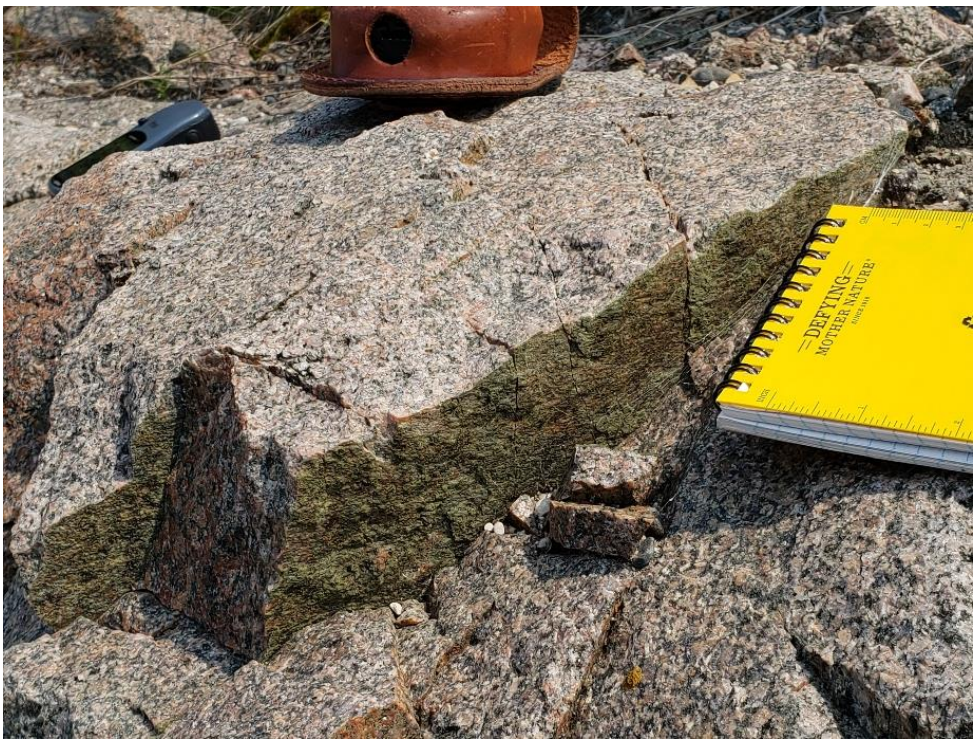

Figure 82. Outcrop photo of sub-horizontal slickenlines on chlorite infilled shear fractures.

Microstructural analysis

Quartz displays a bimodal grain size distribution with some crystals reaching up to 1.25mm. Most of the quartz is very fine grained (<0.5 mm). The coarsest grained quartz shows moderate to strong undulatory extinction, subgrains and weakly developed serrated grain boundaries. The finer grained quartz displays weak undulatory extinction, subgrains and weakly serrated to straight grain boundaries. Feldspar ranges from very fine- to medium-grained across the 4 plutons, with the small grain sizes <1 mm and the largest grain size reaching up to 6 mm. Feldspar has weak to strong undulose extinction, smooth to heavily serrated grain boundaries, subgrains (even in the largest crystals), deformation twins, intragranular microfractures and recrystallization along grain boundaries. Although strain is pervasive throughout all thin sections, the degree of the strain varies greatly (some thin sections show heavily serrated grain boundaries while others show smooth to weakly serrated grain boundaries).

A thin section of an infilled epidote shear fracture shows localized grain size reduction accompanied with an increase in alteration (sericite, muscovite, epidote and biotite – all very fine grained) in halos surrounding each side of the vein (Figure 83). Halos are approximately 3 mm thick.

A quartz vein within the Croll Lake stock demonstrates coeval brittle-ductile deformation. The vein is comprised of fine-grained quartz that is ductilely overprinted as shown through undulose extinction, serrated grain boundaries and subgrains (Figure 84).

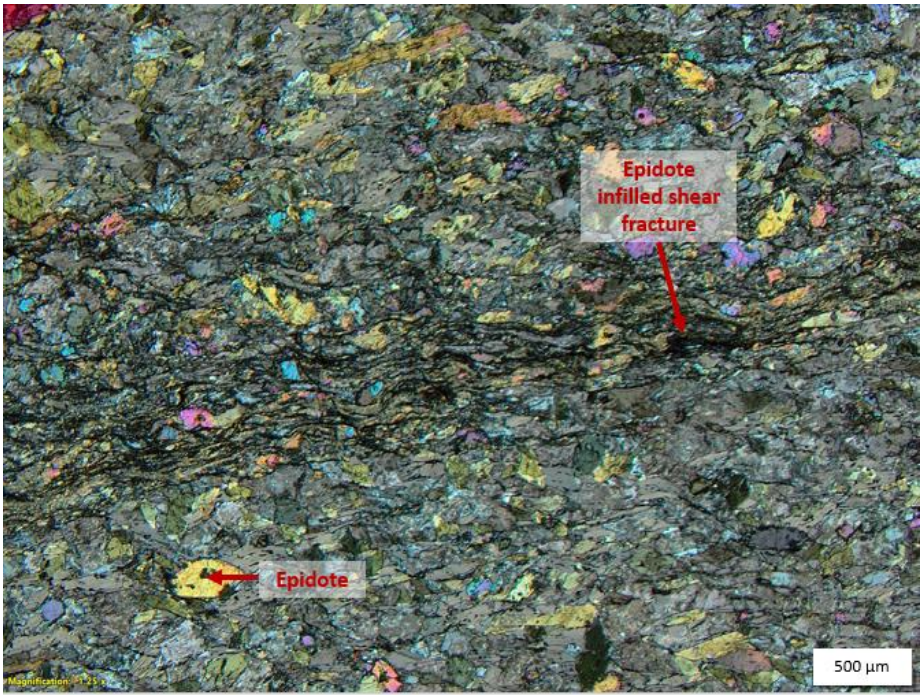

Figure 83. Photomicrograph of an epidote shear vein surrounded by a grain-size reduced halo with an increase in alteration minerals compared to the host granitoid (XPL). Alteration minerals are aligned roughly parallel to the shear vein walls. Scale bar is 500 µm.

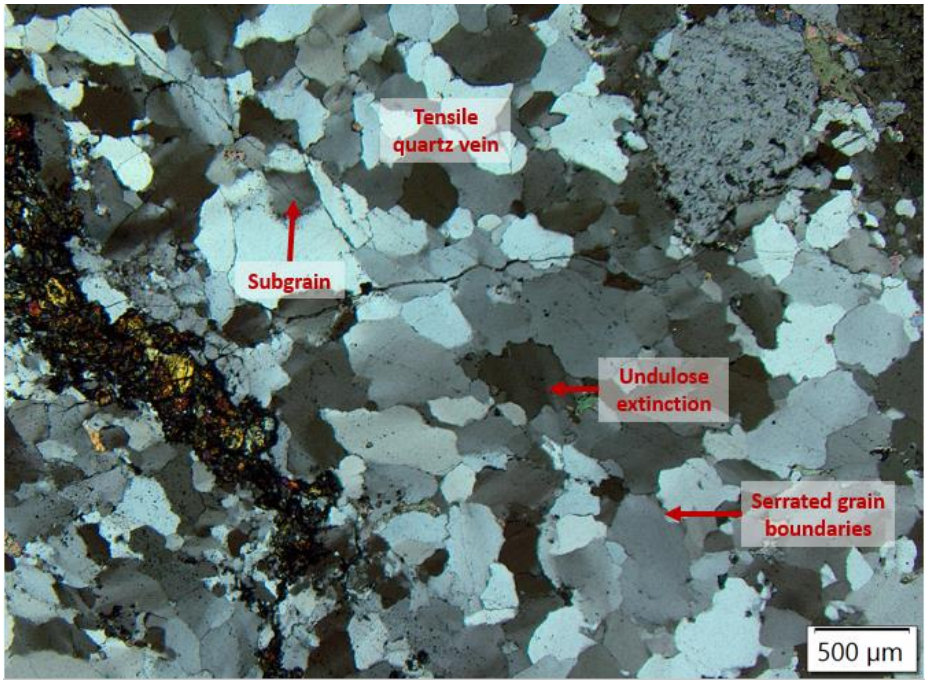

Figure 84. Photomicrograph of a ductilely deformed quartz vein (XPL). Scale bar is 500 µm.

Chapter 5: Mineralogy

The granitoid plutons of the Wabigoon subprovince are predominately composed of quartz, plagioclase feldspar and potassic feldspar that make up roughly 80% of the bulk mineralogy. Minor (2%-10%) occurrences of magmatic hornblende and biotite are noted within a few of the plutons. The remaining percentage consists of various hydrothermal/metasomatic minerals related to the brittle deformation of the plutons. Since granitoids are 'dry' rocks (they do not have an abundance of OH^- bearing minerals), the alteration of the plutons is directly related to fluids derived from outside sources that then circulate throughout the plutons via brittle pathways. Thus, understanding the hydrothermal/metasomatic mineral assemblages aids in understanding the chemistry of the fluid that circulated throughout the pluton.

The main hydrothermal/metasomatic minerals are chlorite (with varying Fe:Mg ratios), epidote and white mica (predominately phengite). Lesser amounts of calcite, sphene and hematite are also seen. Chlorite and epidote are the most abundant alteration minerals as they occur as both shear fracture infilling and as alteration products within the wall-rock, whereas white mica occurs almost exclusively as a replacement of feldspar. The occurrence styles of each of the alteration minerals will be discussed in their respective section.

This chapter will present the mineral composition of the magmatic feldspar and biotite phases along with the hydrothermal/metasomatic mineral phases, as well as provide insight into the different occurrence styles of the alteration minerals.

5.1 Chlorite

Chlorite is represented by four different types of occurrences: 1) as fracture infilling both within (Figure 19) and outside of shear zones, 2) as laths within the granitoid typically seen associated with microcracks (Figure 62), 3) as partially metamorphosed replacements of biotite laths (intermingled chlorite-biotite laths, Figure 79), and 4) in the matrix of cataclasites (Figure 65). The mineral chemistry of chlorite was analyzed from hand samples taken from seven granitoid plutons (Appendix III). Average chlorite mineral formulas were calculated for each pluton studied, and the results are shown in Table 2. Mineral formulas were calculated on the basis of 14 oxygens with a general formula of:

$$(Fe,Mg,Mn,Al)_{\sum 3.00}(Si,Al)_{\sum 4.00}O_{10}(OH)_2 \cdot (Fe,Mg,Mn,Al)_{\sum 3.00}(OH)_6$$

In addition to hand samples, mineral chemistry of chlorite along fracture planes was also analyzed in drill core samples taken from 4 plutons – 2 unnamed plutons located just north of the

Wabigoon-Quetico subprovince boundary (one in western Wabigoon, the other in the eastern Wabigoon), the Atikwa batholith and the Marmion batholith. The mineral chemistry for these samples is discussed in chapter 6.

Figure 85 shows a chlorite discrimination diagram from Hey (1954) which plots Fe/ (Fe + Mg) against Si per formula unit (henceforth abbreviated pfu). The different colors represent different plutons, while the different shapes within the color scheme represent the different occurrences of chlorite analyzed. The majority of chlorite analyses plot within the pycnochlorite field with a few occurrences of ripidolite and one occurrence of brunsvigite. All chlorite analyzed have Si (pfu) values between 2.7 and 3.1 and Fe/(Fe + Mg) values between 0.35 and 0.65. Analyses plotted on this diagram represent chlorite analyses of each occurrence type mentioned previously. Overall, each pluton appears to have some consistency in the type of chlorite present. Some exceptions to this are seen in the Sowden Wabakimi Lakes batholithic complex where each chlorite analysis plots in a different field (ripidolite, brunsvigite and pycnochlorite) although the occurrence type of chlorite analyzed is the same across the three points (chlorite laths in the host rock seen along microcracks). The Sabaskong batholith also displays some scatter in its chlorite analyses – one of the five analyses represents chlorite along fracture planes seen in a brittle-ductile shear zone (pycnochlorite) while the other four represent chlorite laths seen in the host rock of a ductile shear zone (ripidolite). The Dryberry batholith shows the largest degree of scatter, with three analyses plotting in the ripidolite field and one plotting in the pycnochlorite field. The three points within the ripidolite field come from a ductile shear zone within the Dryberry seen directly along Highway 71, while the point in the pycnochlorite field represents a chlorite lath seen in an outcrop located near the contact of the pluton with the host greenstone belt near Kenora, Ontario.

Each chlorite analysis within the Revell batholith, the White Otter pluton and the Marmion batholith show consistent values in their Fe/(Fe + Mg) ratio and Si (pfu) values.

A major limitation of this chlorite discrimination diagram (Hey, 1954) stems from the substitutions of Fe and Mg for Mn in the octahedral site of the chlorite. Mn impurities, which are common but minor in the granitoid plutons, are not accounted for in this chlorite discrimination diagram.

Chlorite can also be classified based on their Fe:Mg ratio, with values above 1 called chamosite (Fe-rich endmember) and values below 1 called clinochlore (Mg-rich endmember). This naming scheme also does not consider the substitution of Mn for Mg or Fe in the octahedral sites

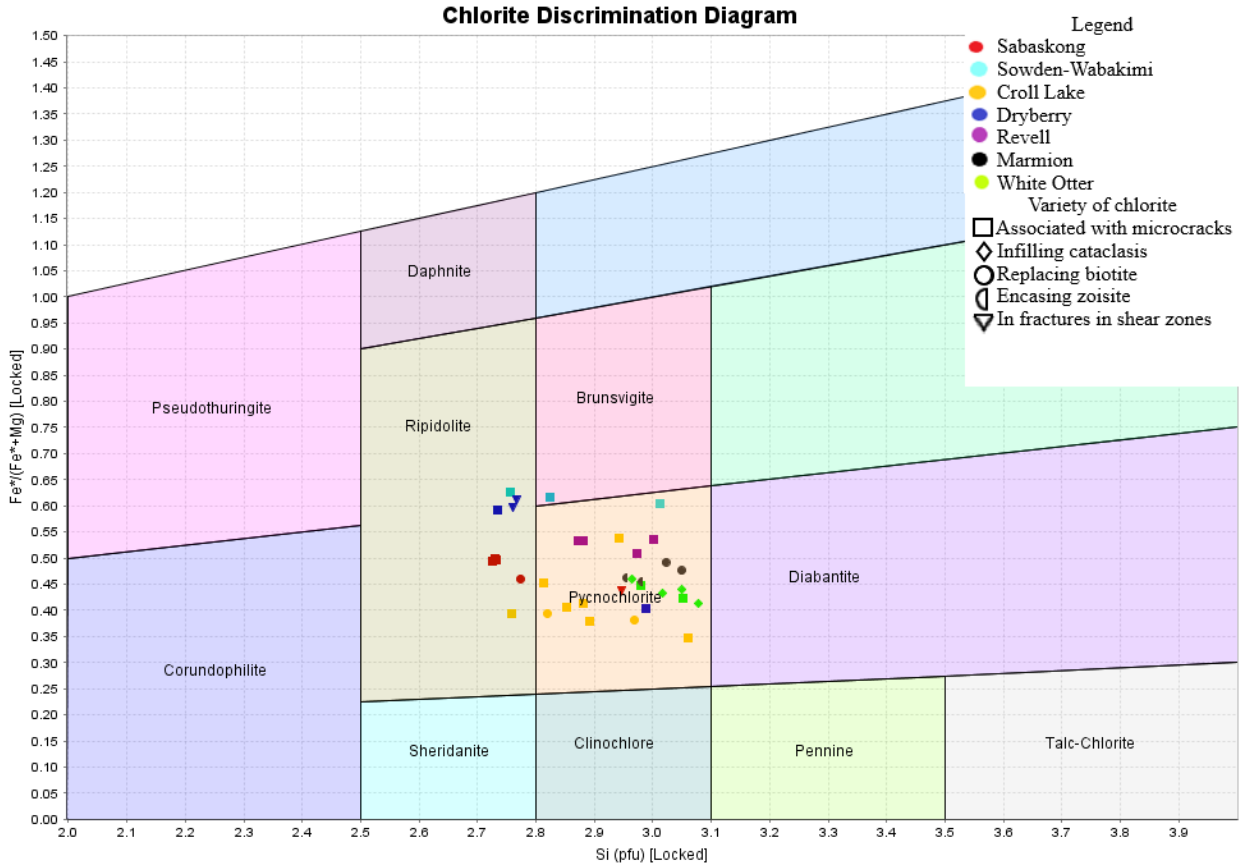

Figure 85. A chlorite discrimination diagram from Hey (1954) showing the mineral chemistry of chlorites analyzed within 7 plutons of the Wabigoon subprovince. Most analyses plot within the pycnochlorite field, with a few exceptions. Different shapes within color groups represent different occurrence types.

of the chlorites. The Croll Lake stock, Sabaskong batholith, White Otter Lake batholithic complex and the Marmion batholith each have average chlorite compositions characterized as clinochlore (Fe:Mg ratios < 1). The Dryberry batholith, Sowden-Wabakimi Lakes batholithic complex and the

Revell batholith have average chlorite compositions that fall into the chamosite field (Fe:Mg ratios > 1). It should be noted that some of the plutons have chlorite that fall into both the chamosite and clinochlore categories, represented in Table 2 (fourth column).

Table 2. Average chlorite mineral formulas for seven plutons across the Wabigoon subprovince.

Pluton Name	Chlorite mineral formulas (average)	Number of chlorites analyzed	clinochlore/ chamosite	Variety of chlorite
Croll Lake	$(Mg_{1.390}Fe_{0.977}Al_{0.595}Mn_{0.013}K_{0.002})_{\sum 2.977}(Si_{2.903}Al_{1.097})_{\sum 4.00}O_{10}(OH)_2 \cdot (Mg_{1.390}Fe_{0.977}Al_{0.595}Mn_{0.013}K_{0.002})_{\sum 2.977}(OH)_6$	8	7 clinochlore /1 chamosite	6 chlorite laths in host rock, 2 chlorite replacing biotite
Sabaskong	$(Mg_{1.197}Fe_{1.089}Al_{0.675}Mn_{0.006})_{\sum 2.967}(Si_{2.781}Al_{1.219})_{\sum 4.00}O_{10}(OH)_2 \cdot (Mg_{1.197}Fe_{1.089}Al_{0.675}Mn_{0.006})_{\sum 2.967}(OH)_6$	5	5 clinochlore / 0 chamosite	1 fracture infill, 3 chlorite laths in host rock, 1 chlorite replacing biotite
White Otter Lake	$(Mg_{1.375}Fe_{1.044}Al_{0.536}Mn_{0.019})_{\sum 2.974}(Si_{3.023}Al_{0.977})_{\sum 4.00}O_{10}(OH)_2 \cdot (Mg_{1.375}Fe_{1.044}Al_{0.536}Mn_{0.019})_{\sum 2.974}(OH)_6$	6	6 clinochlore / 0 chamosite	4 cataclasite infill, 2 chlorite laths in host rock
Dryberry	$(Fe_{1.283}Mg_{1.055}Al_{0.629}Mn_{0.015})_{\sum 2.982}(Si_{2.812}Al_{1.188})_{\sum 4.00}O_{10}(OH)_2 \cdot (Fe_{1.283}Mg_{1.055}Al_{0.629}Mn_{0.015})_{\sum 2.982}(OH)_6$	4	1 clinochlore / 3 chamosite	2 chlorite laths in host rock, 2 chlorite laths in close proximity to epidote shear vein
Sowden-Wabakimi	$(Fe_{1.419}Mg_{0.898}Al_{0.622}Mn_{0.030}K_{0.007})_{\sum 2.976}(Si_{2.865}Al_{1.135})_{\sum 4.00}O_{10}(OH)_2 \cdot (Fe_{1.419}Mg_{0.898}Al_{0.622}Mn_{0.030}K_{0.007})_{\sum 2.976}(OH)_6$	3	0 clinochlore / 3 chamosite	3 chlorite laths in host rock
Revell	$(Fe_{1.196}Mg_{1.105}Al_{0.609}Mn_{0.031}K_{0.013})_{\sum 2.954}(Si_{2.991}Al_{1.009})_{\sum 4.00}O_{10}(OH)_2 \cdot (Fe_{1.196}Mg_{1.105}Al_{0.609}Mn_{0.031}K_{0.013})_{\sum 2.954}(OH)_6$	5	0 clinochlore / 5 chamosite	5 chlorite laths in host rock
Marmion	$(Mg_{1.254}Fe_{1.119}Al_{0.556}Mn_{0.023}K_{0.010})_{\sum 2.962}(Si_{3.001}Al_{0.999})_{\sum 4.00}O_{10}(OH)_2 \cdot (Mg_{1.254}Fe_{1.119}Al_{0.556}Mn_{0.023}K_{0.010})_{\sum 2.962}(OH)_6$	4	4 clinochlore / 0 chamosite	2 chlorite replacing biotite, 2 chlorite encasing zoisite

5.2 Epidote

Epidote is a common alteration mineral occurring within the granitoid plutons. It occurs in clusters (typically along or at microcrack terminations), and is associated with biotite, chlorite and sphene, as inclusions within plagioclase feldspars (saussuritization – Figure 33), as fracture infilling with sub-horizontal slickenlines (Figure 30, Figure 45), and within shear zones (Figure 30). Mineral compositions of epidote were analyzed from ten granitoid plutons (Appendix III). All Fe^{2+} was converted to Fe^{3+}. Formulas were calculated on the basis of 12 oxygens and fit to the general formula of:

$$Ca_2Al_2(Al,Fe^{3+})_1OOH[Si_2O_7][SiO_4]$$

A ternary diagram which plots Fe%, Mn% and octahedral Al% was used to classify the type of epidote present. This ternary diagram is based on Nesse (2017) and is shown in Figure 86. Different colors represent different plutons, and different shapes represent the different varieties of epidote. Interestingly, the mineral chemistry of the epidote tends to cluster within the epidote composition field, regardless of the occurrence type of the epidote analyzed. There are 4 exceptions to this trend. The first 3 exceptions are all noted within the Marmion batholith where three of the epidotes analyzed plot within the zoisite composition field. In thin section, the zoisite is seen to be completely encased in chlorite ± sphene with very strong fan-like undulose extinction (Figure 87). The fourth analysis of epidote group minerals within the Marmion batholith plots as epidote and occurs in the host rock devoid of chlorite ± sphene. This highlights the presence of two epidote group minerals within the Marmion batholith – one that is not part of the stable metamorphic mineral assemblage (zoisite) and one that is (epidote). It is possible that the zoisite is not a metamorphic mineral but instead a primary magmatic mineral with a corona of chlorite ± sphene due to its unstable nature. Since the Marmiom batholith is older than the other plutons studies, another possibility is that the zoisite is a metamorphic mineral that represents an older metamorphic event than the late Archean metamorphism documented in the rest of the plutons. This variety of epidote is only noted in the Marmion batholith and is preserved in a low strain sample where potassic feldspar can reach up to 10 cm in length.

There is also a single epidote that plots outside of the main cluster seen in the Dryberry batholith. This epidote has a much lower octahedral Al% and a much higher Fe% than the rest of the epidote from that sample and the pluton in general. This epidote is identified in clusters with altered biotite (chloritization), much like the epidote analyzed in the rest of the pluton. The

explanation for this variance in octahedral Al% and Fe% is unknown. Average epidote group mineral formulas are shown in Table 3. Minor Mn impurities (0.27 – 0.73 MnO wt %) are noted within the Ottertail pluton, Sabaskong batholith, Dryberry batholith and the Revell batholith.

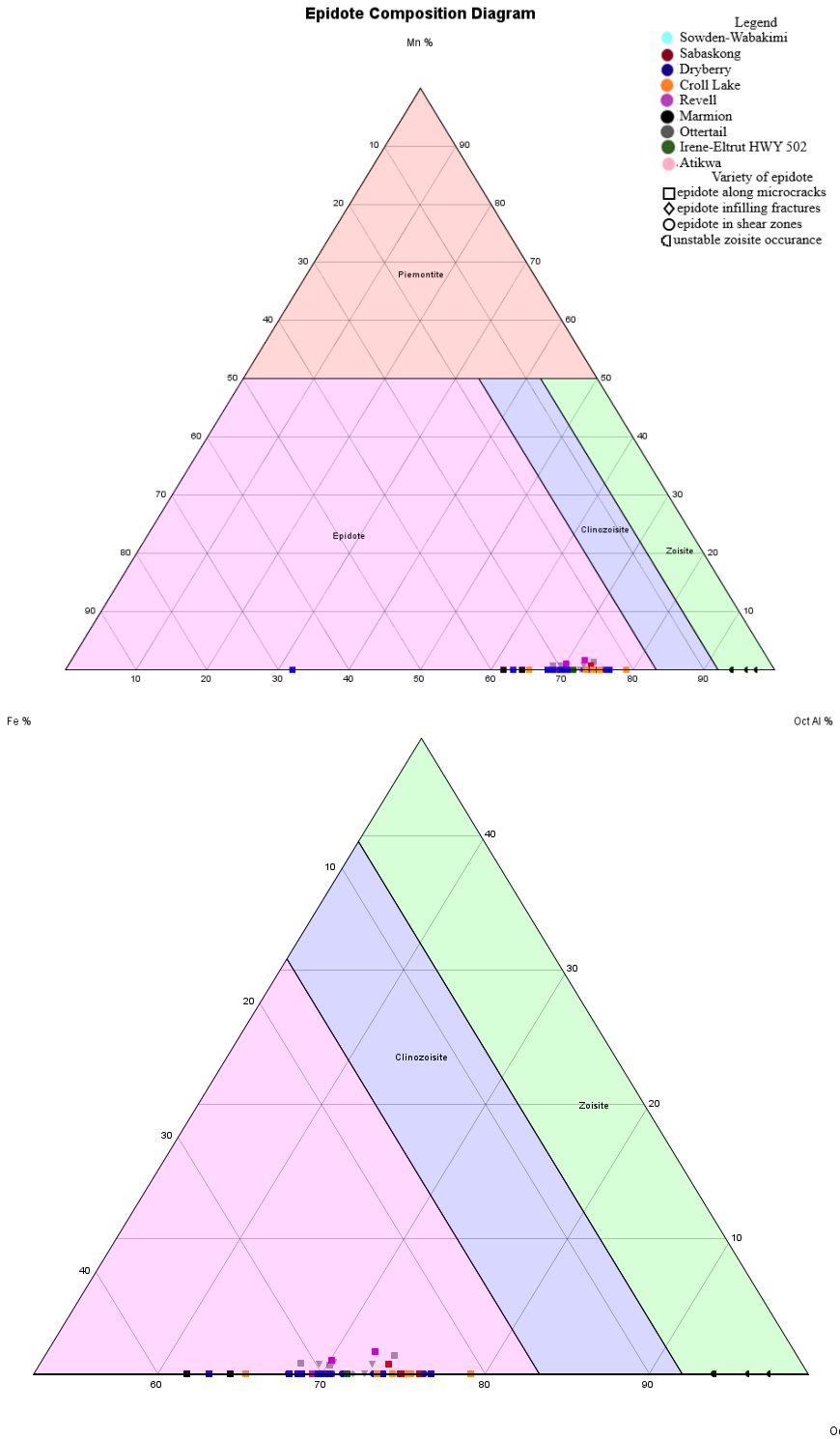

Figure 86. Top: Zoomed out. **Bottom:** Zoomed in. A ternary epidote composition diagram from Nesse (2017). Most analyses plot within the epidote composition field regardless of the variety type of epidote. Three points from the Marmion batholith plot within the zoisite field – in thin section the zoisite is seen to not be part of the stable metamorphic mineral assemblage and potentially represents primary magmatic epidote. Mn content of epidote group minerals within the plutons is minimal, reaching up to 3% Mn at maximum.

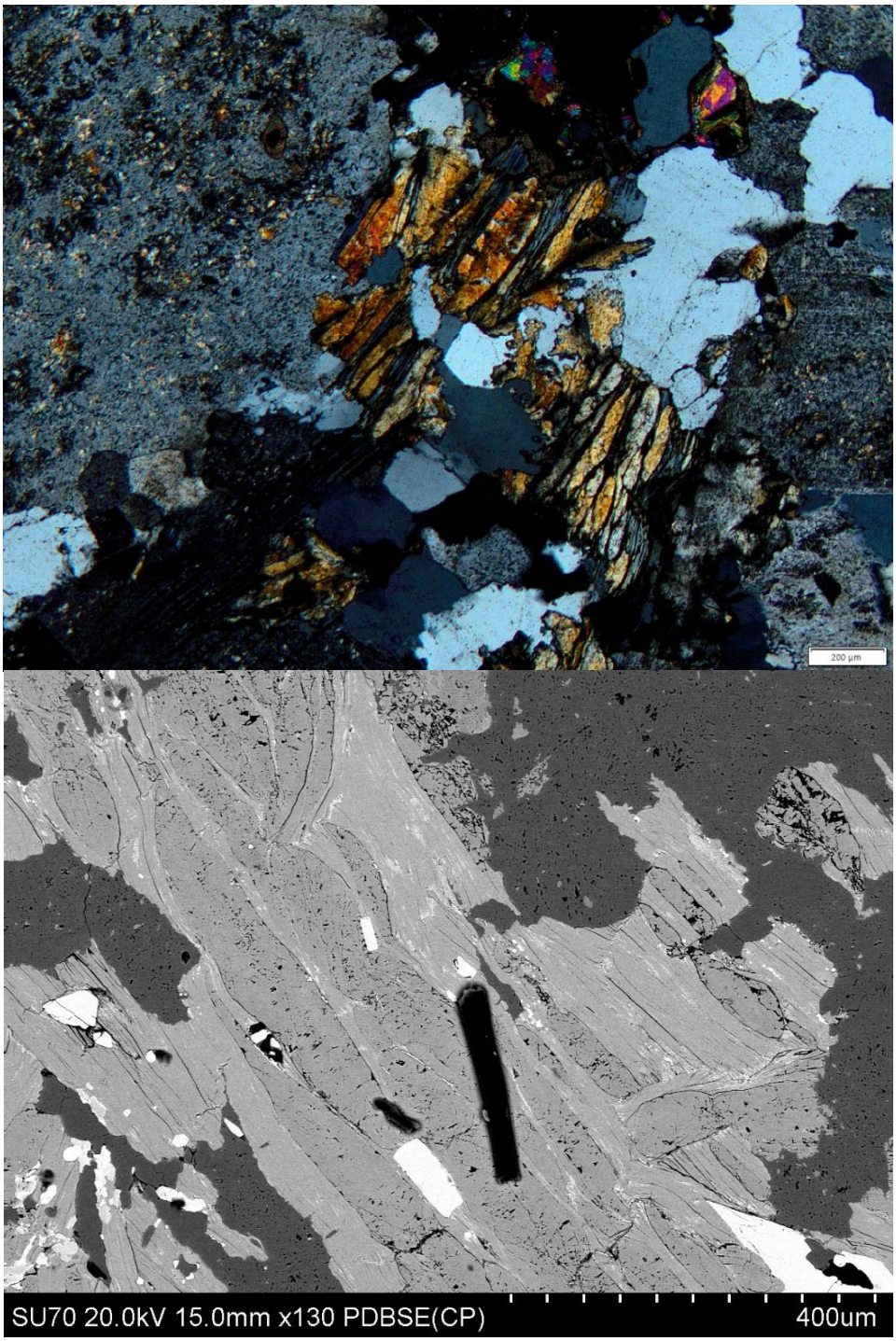

Figure 87. Top: Photomicrograph (XPL). Scale bar is 200 µm. **Bottom:** BSE image. Unstable zoisite crystals with strong fan-like undulose extinction encased in chlorite (clinochlore). Zoisite is preserved in a low strain sample of the Marmion batholith and could represent primary magmatic zoisite.

Table 3. Average epidote group mineral formulas in 9 granitoid plutons of the Wabigoon subprovince.

Pluton	Epidote mineral formulas (average)	n	Variety of epidote analyzed
Croll Lake	$Ca_{2.029}Al_{2.00}(Al_{0.181}Fe_{0.807})_{\sum 0.988}OOH[Si_{1.994}O_7][SiO_4]$	11	11 epidotes clustered along microcracks
Ottertail	$Ca_{1.981}Al_{2.00}(Al_{0.142}Fe_{0.856}Mn_{0.013})_{\sum 1.011}OOH[Si_{2.004}O_7][SiO_4]$	12	5 epidotes clustered along microcracks, 5 epidotes in shear zones, 2 epidote in fractures
Sabaskong	$Ca_{1.976}Al_{2.00}(Al_{0.248}Fe_{0.751}Mn_{0.006})_{\sum 1.005}OOH[Si_{2.011}O_7][SiO_4]$	4	4 epidotes clustered along microcracks
Dryberry	$Ca_{2.075}Al_{2.00}(Al_{0.041}Fe_{0.905}Mn_{0.0012})_{\sum 0.947}OOH[Si_{1.997}O_7][SiO_4]$	20	11 epidotes clustered along microcracks, 9 epidotes within shear zones
Revell	$Ca_{1.969}Al_{2.00}(Al_{0.146}Fe_{0.864}Mn_{0.0027})_{\sum 1.013}OOH[Si_{1.995}O_7][SiO_4]$	3	3 epidotes clustered along microcracks
Sowden-Wabakimi	$Ca_{2.018}Al_{2.00}(Al_{0.095}Fe_{0.884})_{\sum 0.979}OOH[Si_{2.007}O_7][SiO_4]$	1	1 epidote along microcrack
Irene-Eltrut 502	$Ca_{2.001}Al_{2.00}(Al_{0.148}Fe_{0.854})_{\sum 1.002}OOH[Si_{1.998}O_7][SiO_4]$	1	1 epidote along microcrack
Marmion (epidote)	$Ca_{1.982}Al_{1.909}(Fe_{1.117})_{\sum 1.117}OOH[Si_{1.991}O_7][SiO_4]$	2	2 epidotes along microcracks
Marmion (zoisite)	$Ca_{2.000}(Al_{2.141}Fe_{0.106}Si_{0.412}Ca_{0.306})_{\sum 2.965}OOH[Si_{2.000}O_7][SiO_4]$	4	4 epidotes encased in chlorite (not part of stable metamorphic mineral assemblage)
Atikwa (Drill core)	$Ca_{2.014}Al_{2.00}(Al_{0.213}Fe_{0.768})_{\sum 0.981}OOH[Si_{2.007}O_7][SiO_4]$	1	1 epidote in fracture

5.3 White mica

White mica commonly occurs as an alteration product of feldspar in the form of sericite, and as coarse-grained white mica. Sericite/white mica alteration may be present in only the cores of feldspar (Figure 46), the rims of feldspar, or both (Figure 69). White mica has a higher prevalence in samples taken near the margins of plutons rather than samples taken near the middle of plutons – likely due to the necessity of brittle fracturing to provide pathways for hydrothermal fluid flow. Mineral compositional analysis focused on the coarser grained white mica and analyses were conducted in eleven plutons (Appendix III). Mineral formulas were calculated on the basis of 11 oxygens and fit to the general formula of:

$$KAl_2(AlSi_3O_{10})(OH)_2$$

A ternary diagram from Tappert et al. (2013) plots Si (pfu) on one corner and Fe% and Mg% on the other two to classify the type of white mica present. Figure 88 shows the discrimination ternary diagram for the analyses conducted in eleven granitoid plutons. The ternary diagram shows that three analysis points plot in the muscovite field while all remaining points (78) plot within the phengite series. The phengite series is differentiated from the muscovite series as having 3.1 to 3.5 Si cations pfu based on 11 oxygens (Tappert et al, 2013). Most points have Fe values that are slightly higher than their Mg values, with a few points having slightly higher Mg values. Table 4 displays the average mineral formulas for muscovite by pluton. Only one pluton, the Marmion batholith, demonstrated substitution of K^+ for Na^+.

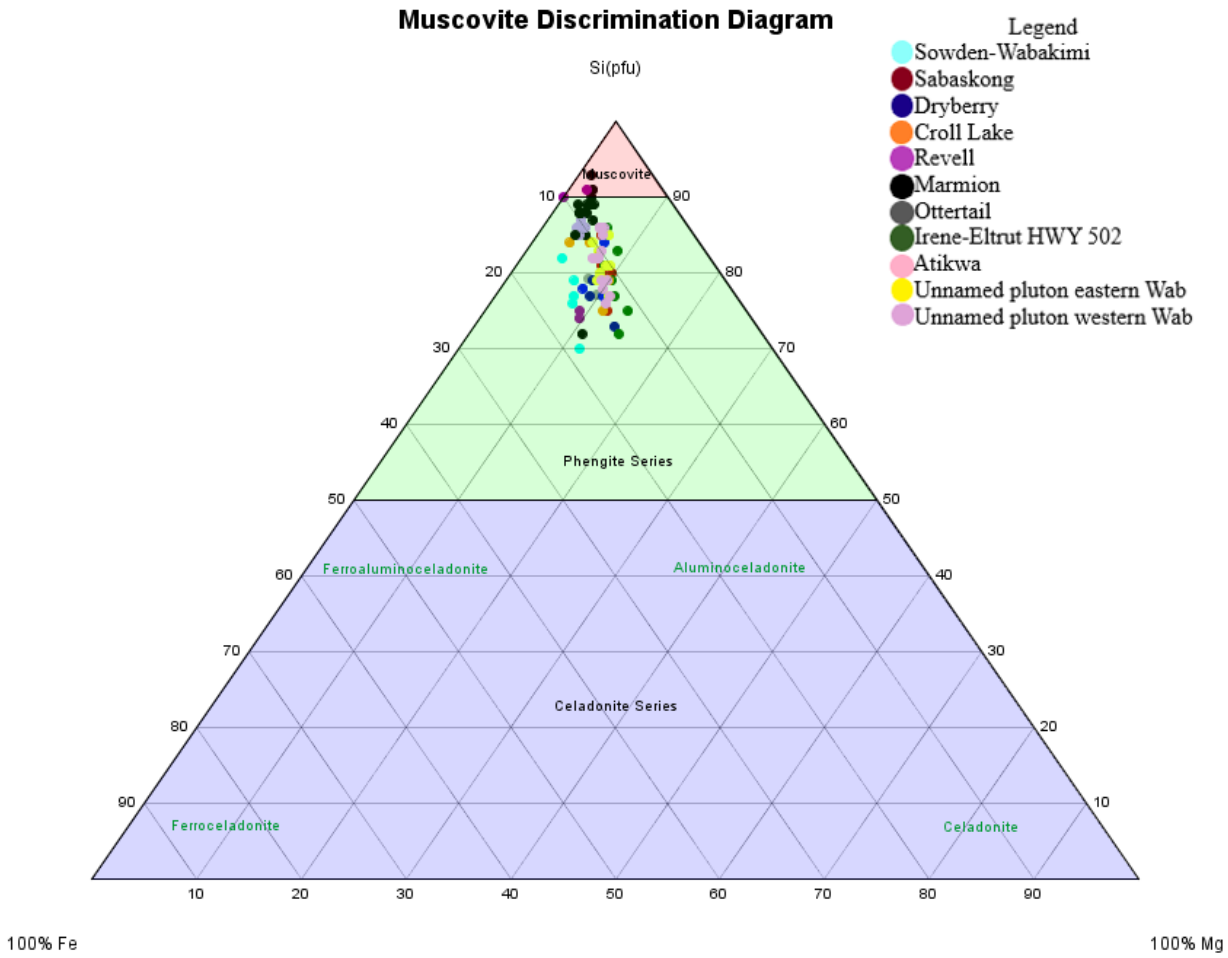

Figure 88. A ternary muscovite discrimination diagram from Tappert et al., (2013). Three points plot within the muscovite field while the remaining seventy-eight plot within the phengite series, which is differentiated from muscovite as having 3.1 – 3.5 Si cations per formula unit. There are no analyses which plot in the celadonite series.

Table 4. Average white mica (phengite) mineral formulas for eleven plutons across the Wabigoon subprovince.

Pluton	White mica mineral formulas (average)	n
Sabaskong	$K_{0.997}(Al_{1.611}Fe_{0.247}Mg_{0.191}Ti_{0.027})_{\sum 2.076}(Al_{0.816}Si_{3.184})_{\sum 4.00}O_{10}(OH)_2$	7
Croll Lake	$K_{1.032}(Al_{1.655}Fe_{0.233}Mg_{0.154}Ti_{0.009})_{\sum 2.051}(Al_{0.804}Si_{3.196})_{\sum 4.00}O_{10}(OH)_2$	3
Revell	$K_{1.005}(Al_{1.683}Fe_{0.254}Mg_{0.116}Ti_{0.009})_{\sum 2.062}(Al_{0.825}Si_{3.175})_{\sum 4.00}O_{10}(OH)_2$	4
Sowden-Wabakimi	$K_{1.029}(Al_{1.463}Fe_{0.394}Mg_{0.182}Ti_{0.049})_{\sum 2.088}(Al_{0.767}Si_{3.233})_{\sum 4.00}O_{10}(OH)_2$	5
Ottertail	$K_{1.023}(Al_{1.524}Fe_{0.310}Mg_{0.217}Ti_{0.032})_{\sum 2.083}(Al_{0.778}Si_{3.222})_{\sum 4.00}O_{10}(OH)_2$	3
Dryberry	$K_{1.021}(Al_{1.620}Fe_{0.253}Mg_{0.185}Ti_{0.006})_{\sum 2.064}(Al_{0.781}Si_{3.219})_{\sum 4.00}O_{10}(OH)_2$	6
Irene Eltrut HWY 502	$K_{1.009}(Al_{1.578}Fe_{0.252}Mg_{0.248}Ti_{0.011})_{\sum 2.089}(Al_{0.790}Si_{3.210})_{\sum 4.00}O_{10}(OH)_2$	7
Marmion (all drill core)	$(K_{0.984}Na_{0.038})_{\sum 1.022}(Al_{1.775}Fe_{0.176}Mg_{0.067}Ti_{0.011})_{\sum 2.029}(Al_{0.874}Si_{3.126})_{\sum 4.00}O_{10}(OH)_2$	18
Atikwa (all drill core)	$K_{1.019}(Al_{1.652}Fe_{0.222}Mg_{0.165}Ti_{0.016})_{\sum 2.055}(Al_{0.815}Si_{3.185})_{\sum 4.00}O_{10}(OH)_2$	13
Small pluton - eastern Wabigoon (all drill core)	$K_{1.020}(Al_{1.551}Fe_{0.291}Mg_{0.226}Ti_{0.026})_{\sum 2.094}(Al_{0.810}Si_{3.190})_{\sum 4.00}O_{10}(OH)_2$	10
Small pluton – western Wabigoon (all drill core)	$K_{1.032}(Al_{1.785}Fe_{0.204}Mg_{0.073}Ti_{0.015})_{\sum 2.077}(Al_{0.858}Si_{3.142})_{\sum 4.00}O_{10}(OH)_2$	4

5.4 Biotite

Biotite typically occurs as laths associated with epidote and chlorite. It is present in the form of pure laths or as laths partially replaced by chlorite (Figure 79) within all granitoid plutons. Biotite formulas were calculated across eleven plutons based on eleven oxygens and fit to the general formula of:

$$K(Fe,Mg)_3AlSi_3O_{10}(OH)_2$$

A biotite discrimination diagram from Wlodek et al. (2015) plots the Fe/(Fe+Mg) ratios of the biotites against the Total Al to classify whether they plot within the annite, phlogopite, siderophyllite or eastonite fields (Figure 89). All biotite group minerals within the Sabaskong batholith, Atikwa batholith, Revell batholith, Marmion batholith, White Otter Lake and the Sowden-Wabakimi Lakes batholithic complex plot within the annite field while the biotite group minerals within the Ottertail pluton, Irene-Eltrut batholithic complex, Dryberry batholith, Unnamed pluton in the eastern Wabigoon subprovince and the Croll Lake stock plot within the phlogopite field.

A mica discrimination diagram from Foster (1960) and Dong et al. (2014) subdivides the biotite group into phlogopite, Fe-biotite, Mg-biotite and the siderophyllites and lepidomelanes. Using this diagram, the cluster that plots as slightly more Fe-rich biotite in Figure 89 is located directly at the cusp of the Mg-biotite and Fe-biotite members in Figure 90. Biotite within the Sowden-Wabakimi and the Atikwa batholith plot as Fe-biotite, while samples from the White Otter Lake batholith and the Sabaskong batholith plot as Mg-biotite. The samples from the Marmion batholith and the Revell batholith plot in both the Mg-biotite and the Fe-biotite fields. No biotite plots within the phlogopite or siderophyllite/ lepidomelane fields.

There is no variation in the mineral compositions of biotite compared to the biotite that has been partially replaced by chlorite. Average biotite mineral formulas for each of the 11 plutons studied are found in Table 5. The Sowden-Wabakimi batholith is the only pluton that has Na^+ substitution for K^+. Ti and Al are both present as substitutions for Fe and Mg in the biotite.

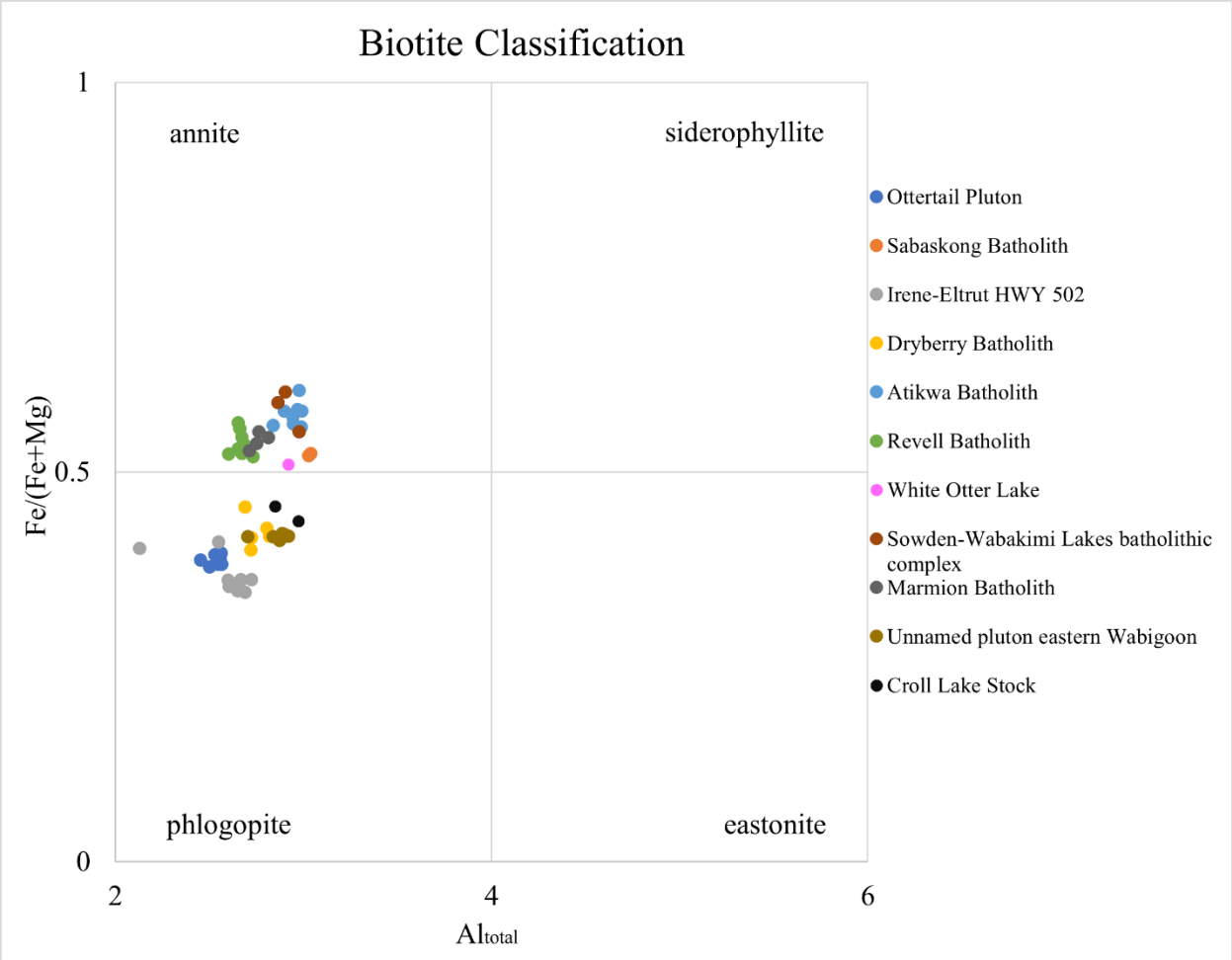

Figure 89. Biotite discrimination diagram from Wlodek et al. (2015) differentiating the four end-members of the biotite group. All plutons show consistency in their biotite end-members. Plutons (differentiated by color) tend to have biotite with similar total Al and Fe/(Fe+Mg) values that cluster together. Discrimination diagram is based on 22 oxygens.

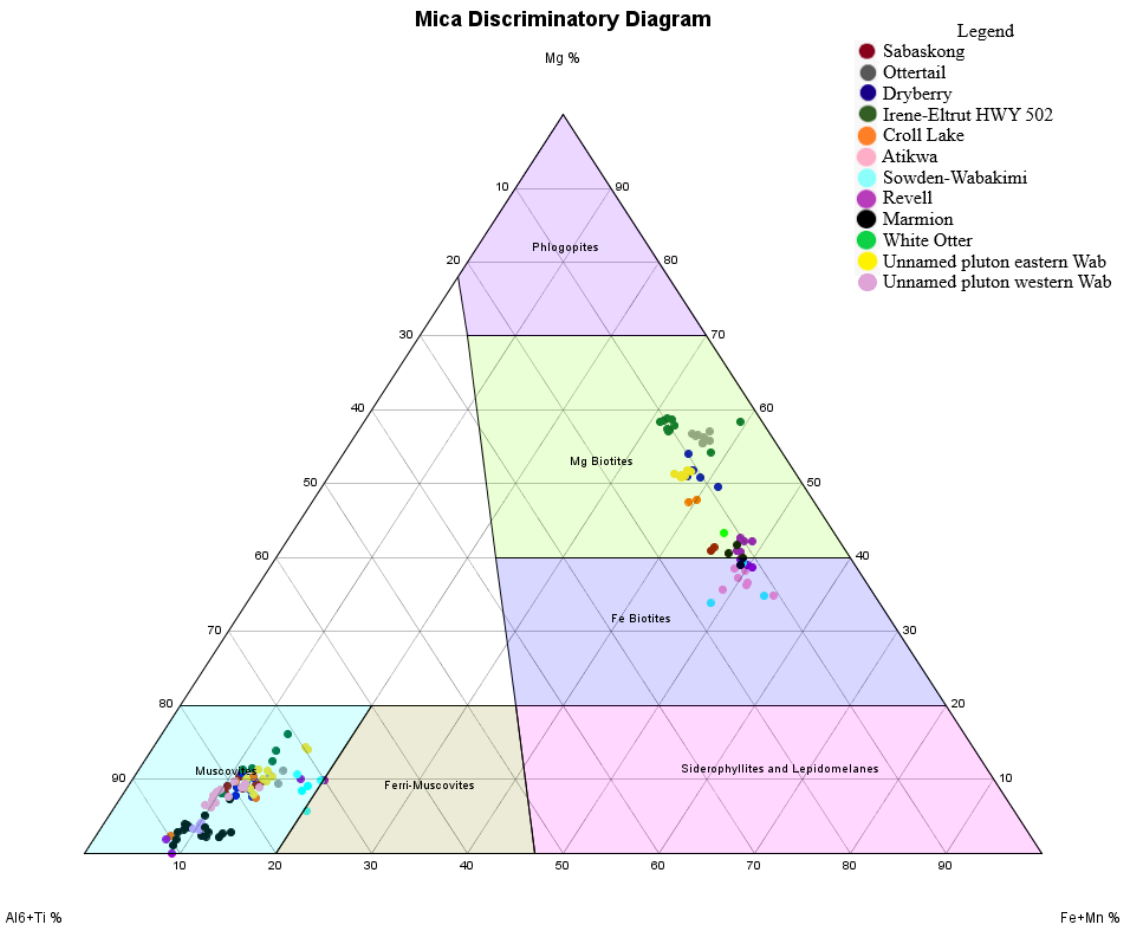

Figure 90. Mica discrimination diagram from Foster (1960) and Dong et al. (2014). 16 analyses from 4 plutons plot in the Fe-biotite field while the remaining 44 analyses from 9 plutons plot within the Mg-biotite field.

Table 5. Average biotite mineral formulas for eleven plutons across the Wabigoon subprovince.

Pluton	Biotite mineral formulas (average)	n
Sabaskong	$K_{1.018}(Fe_{1.286}Mg_{1.176}Al_{0.296}\ Ti_{0.099})_{\sum 2.857}Al_{1.221}Si_{2.779}O_{10}(OH)_2$	2
Ottertail	$K_{1.012}(Mg_{1.637}Fe_{1.039}Al_{0.163}\ Ti_{0.052})_{\sum 2.891}\ Al_{1.103}Si_{2.897}O_{10}(OH)_2$	9
Irene-Eltrut HWY 502	$K_{1.006}(Mg_{1.650}Fe_{0.950}Al_{0.175}Ti_{0.084})_{\sum 2.859}Al_{1.121}Si_{2.879}O_{10}(OH)_2$	10
Croll Lake	$K_{1.001}(Mg_{1.393}Fe_{1.124}\ Al_{0.249}Ti_{0.107})_{\sum 2.873}Al_{1.206}Si_{2.794}O_{10}(OH)_2$	2
Dryberry	$K_{1.017}(Mg_{1.484}Fe_{1.091}Al_{0.190}Ti_{0.105})_{\sum 2.870}Al_{1.186}Si_{2.814}O_{10}(OH)_2$	5
Atikwa (drill core)	$K_{0.997}(Fe_{1.437}Mg_{1.066}Al_{0.249}Ti_{0.113})_{\sum 2.863}Al_{1.223}Si_{2.777}O_{10}(OH)_2$	8
Sowden-Wabakimi	$(K_{0.771}Na_{0.190})_{\sum 0.916}(Fe_{1.466}Mg_{1.057}Al_{0.246}\ Ti_{0.150})_{\sum 2.919}Al_{1.211}Si_{2.789}O_{10}(OH)_2$	3
Revell	$K_{1.010}(Fe_{1.356}Mg_{1.171}Al_{0.186}Ti_{0.118})_{\sum 2.831}Al_{1.149}Si_{2.852}O_{10}(OH)_2$	9
Marmion (surface samples and drill core)	$K_{0.955}(Fe_{1.360}Mg_{1.159}Al_{0.198}Ti_{0.138})_{\sum 2.855}Al_{1.182}Si_{2.818}O_{10}(OH)_2$	4
White Otter	$K_{0.807}(Fe_{1.347}Mg_{1.294}Al_{0.208}Ti_{0.135})_{\sum 2.984}Al_{1.251}Si_{2.749}O_{10}(OH)_2$	1
Unnamed pluton eastern Wab (drill core)	$K_{1.012}(Mg_{1.472}Fe_{1.056}Al_{0.232}Ti_{0.108})_{\sum 2.868}Al_{1.199}Si_{2.801}O_{10}(OH)_2$	7

5.5 Feldspar

Feldspar-group minerals are the most common minerals of the granitoid plutons. Both perthite and myrmekyte are identified in the plutons, with myrmekyte the more dominant of the two. Mineral compositions of the cores of eighty-seven plagioclase feldspars and eighty-one potassic feldspars were analyzed from eleven granitoid plutons for plagioclase and eight granitoid plutons for potassic feldspars (Appendix III). Mineral formulas were calculated on the basis of eight oxygens and fit to the general formula of:

$$(K,Na,Ca)AlSi_3O_8$$

The analyses for both types of feldspar were plotted on a feldspar composition diagram (Figure 91). Most plutons have two types of plagioclase (albite and oligoclase or albite and andesine). The exceptions to this are the Atikwa batholith, White Otter Lake batholith and the unnamed pluton in the eastern Wabigoon, which had only albite, oligoclase and albite, respectively. Average mineral formulas as well as the amount of albite/oligoclase/andesine present for each pluton are shown in Table 6.

All potassium feldspar plot as orthoclase. No anorthoclase is present in the 81 potassic feldspars analyzed. Most orthoclase has K% in the range of 85 – 100%, with three analyses having K% lower than 85% (one White Otter, one Ottertail, one Marmion). Average mineral formulas for the potassium feldspars of each pluton are shown in Table 7. Ba impurities are common in the potassic feldspars. Minor Fe and Mg impurities are seen in the Ottertail pluton (Mg only) and the Dryberry pluton (both Fe and Mg).

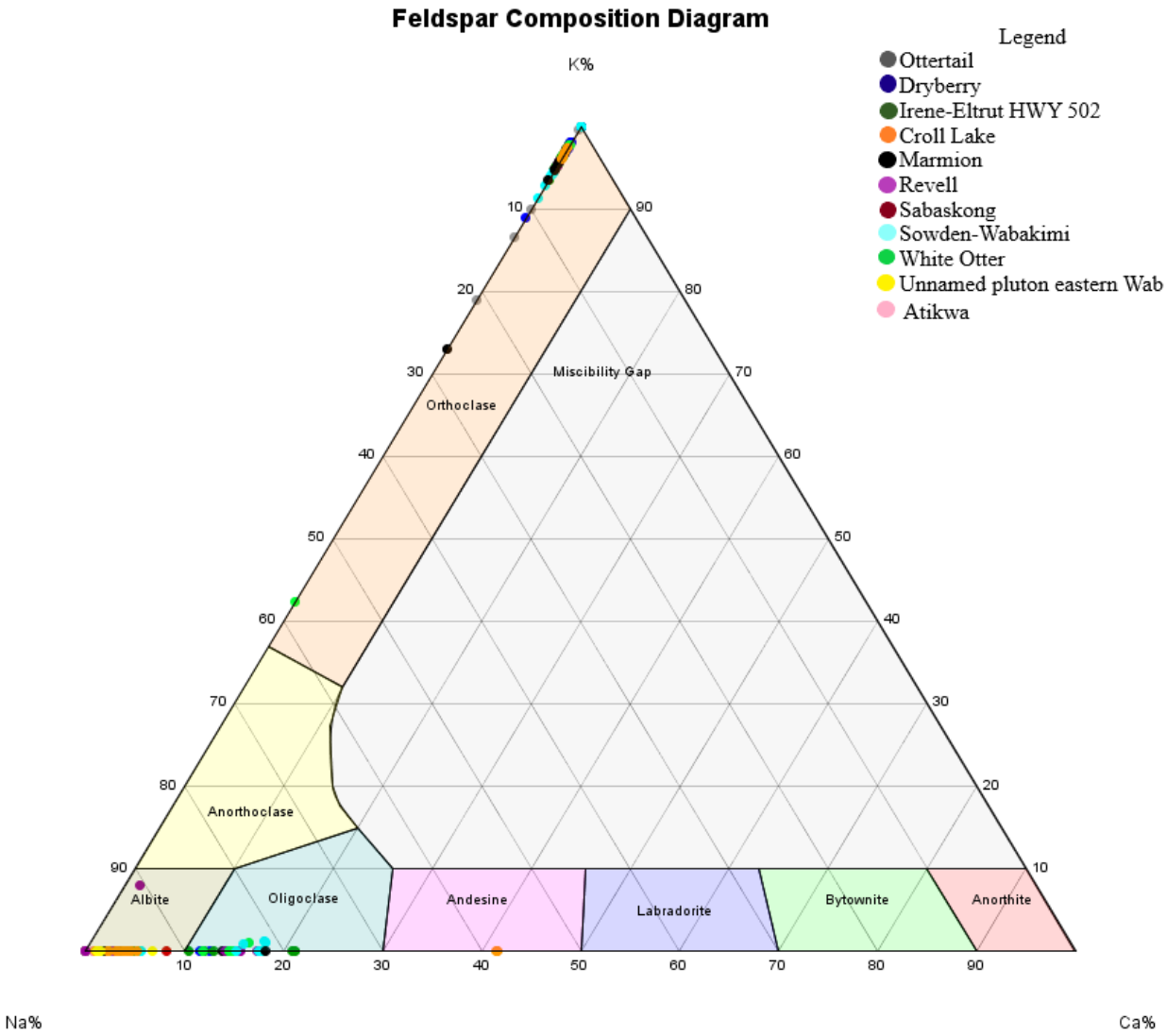

Figure 91. Feldspar composition diagram characterizing the types of plagioclase feldspar (87 analyses) and potassic feldspars (81 analyses) within the granitoid plutons of the Wabigoon subprovince. Albite and oligoclase are the most common plagioclase feldspars present, with only 2 plagioclase feldspars plotting as andesine. All potassic feldspars plots as orthoclase – with most analyses containing 85% or more K%. Three potassic feldspars have K% lower than 85%.

Table 6. Average plagioclase feldspar mineral formulas for eleven plutons in the Wabigoon subprovince. Also shown is the number of albite/oligoclase/andesine measurements for each of the plutons.

Pluton	Plagioclase mineral formulas (average)	Number of albite/oligoclase/andesine plagioclase feldspars present	n
Ottertail	$(Na_{0.969}Ca_{0.031})_{\sum 1.000}Al_{1.029}Si_{2.970}O_8$	7/0/0	7
Sabaskong	$(Na_{0.892}Ca_{0.121})_{\sum 1.013}Al_{1.113}Si_{2.884}O_8$	1/1/0	2
Irene-Eltrut HWY 502	$(Na_{0.929}Ca_{0.075})_{\sum 1.004}Al_{1.075}Si_{2.924}O_8$	8/5/0	13
Marmion	$(Na_{0.983}Ca_{0.040})_{\sum 1.023}Al_{1.017}Si_{2.983}O_8$	7/2/0	9
Dryberry	$(Na_{0.948}Ca_{0.046})_{\sum 0.994}Al_{1.037}Si_{2.962}O_8$	6/2/0	8
Revell	$(Na_{0.882}Ca_{0.102}K_{0.010})_{\sum 0.994}Al_{1.107}Si_{2.893}O_8$	3/5/0	8
Atikwa (all drill core)	$(Na_{0.970}Ca_{0.050})_{\sum 1.020}Al_{1.032}Si_{2.966}O_8$	10/0/0	10
White Otter	$(Na_{0.845}Ca_{0.149}K_{0.002})_{\sum 0.996}Al_{1.149}Si_{2.852}O_8$	0/6/0	6
Sowden-Wabakimi	$(Na_{0.808}Ca_{0.133}K_{0.004})_{\sum 0.945}Al_{1.130}Si_{2.868}O_8$	2/6/0	8
Croll Lake	$(Na_{0.903}Ca_{0.094})_{\sum 0.997}Al_{1.092}Si_{2.908}O_8$	10/0/2	12
Unnamed pluton eastern Wab (all drill core)	$(Na_{0.966}Ca_{0.026})_{\sum 0.992}Al_{1.017}Si_{2.982}O_8$	4/0/0	4

Table 7. Average potassic feldspar mineral formulas for eight plutons in the Wabigoon subprovince.

Pluton	K-feldspar mineral formulas (average)	n
Ottertail	$(K_{0.988}Na_{0.048}Mg_{0.036}Ba_{0.015})_{\sum 1.087}Al_{1.00}(Si_{2.952}Fe_{0.040})_{\sum 2.992}O_8$	16
Croll Lake	$(K_{0.997}Na_{0.034}Ba_{0.004})_{\sum 1.035}Al_{1.005}Si_{2.959}O_8$	4
Irene-Eltrut 502	$(K_{0.993}Na_{0.043}Ba_{0.007})_{\sum 1.043}Al_{0.996}Si_{2.961}O_8$	17
Dryberry	$(K_{0.998}Na_{0.020}Ba_{0.002}Fe_{0.005}Mg_{0.003})_{\sum 1.028}Al_{0.993}Si_{2.976}O_8$	14
Sowden-Wabakimi	$(K_{0.976}Na_{0.048}Mg_{0.006}Ba_{0.015})_{\sum 1.045}Al_{1.005}(Si_{2.949}Fe_{0.003})_{\sum 2.995}O_8$	9
White Otter	$(K_{0.912}Na_{0.119})_{\sum 1.031}Al_{0.992}Si_{2.977}O_8$	9
Revell	$(K_{0.987}Na_{0.049})_{\sum 1.036}Al_{0.993}Si_{2.969}O_8$	5
Marmion	$(K_{0.949}Na_{0.077}Ba_{0.123})_{\sum 1.149}Al_{1.004}Si_{2.952}O_8$	8

Chapter 6: Stable Isotope Analysis

Isotope fractionation is defined as a partitioning of stable isotopes between two coexisting phases (such as between hydrothermal fluid and a mineral). The hydrogen (δD) and oxygen (δO^{18}) stable isotope signature of hydrothermal/metasomatic chlorite occurring along infilled oblique strike-slip shear fractures in the granitoid plutons across the Wabigoon subprovince can be used to help constrain the source of the hydrothermal fluid that once circulated throughout them. This is based on: 1) the principal types of hydrothermal fluids have well defined isotopic compositions, 2) the temperature dependant fractionation factors between water-mineral pairs has been extensively studied, and 3) the isotopic signature of the hydrothermal/metasomatic mineral can be measured. The δD and $\delta^{18}O$ values of the hydrothermal fluid is calculated from the measured δD and $\delta^{18}O$ ratios of the hydrothermal chlorite, assuming isotopic equilibrium was reached between the fluid and the chlorite and no subsequent change in the isotopic ratios took place (Klein et al., 2007).

Seven chlorite shear veins from six drill core samples taken from three plutons (Marmion batholith, Atikwa batholith and a small unnamed pluton) of the Wabigoon subprovince were assessed for their δD and $\delta^{18}O$ isotopic signatures (Figure 92). Obtaining pure chlorite powders for analysis proved difficult due to the anastomosing and thin nature of the infilled chlorite shear fractures (Figure 93), resulting in trace contamination by quartz, muscovite, illite calcite and/or oligoclase. Nonetheless, isotopic compositions of the hydrothermal/metasomatic fluid were calculated for six of the seven chlorite veins (3 from the Marmion batholith and 3 from the Atikwa batholith). The chlorite vein from the small unnamed pluton in the western Wabigoon was excluded due to an anomalous $\delta^{18}O$ value of 2.9‰ relative to VSMOW. This anomalous value is likely due to higher degrees of sample impurities. This chapter will detail the difficulties in achieving stable isotope signatures of the infilled chlorite shear fractures, the suitability of the chlorite shear fractures with regards to the assumptions that must be made for stable isotope analysis to be meaningful as well as the results of the $\delta^{18}O$ and δD values of the hydrothermal/metasomatic fluid.

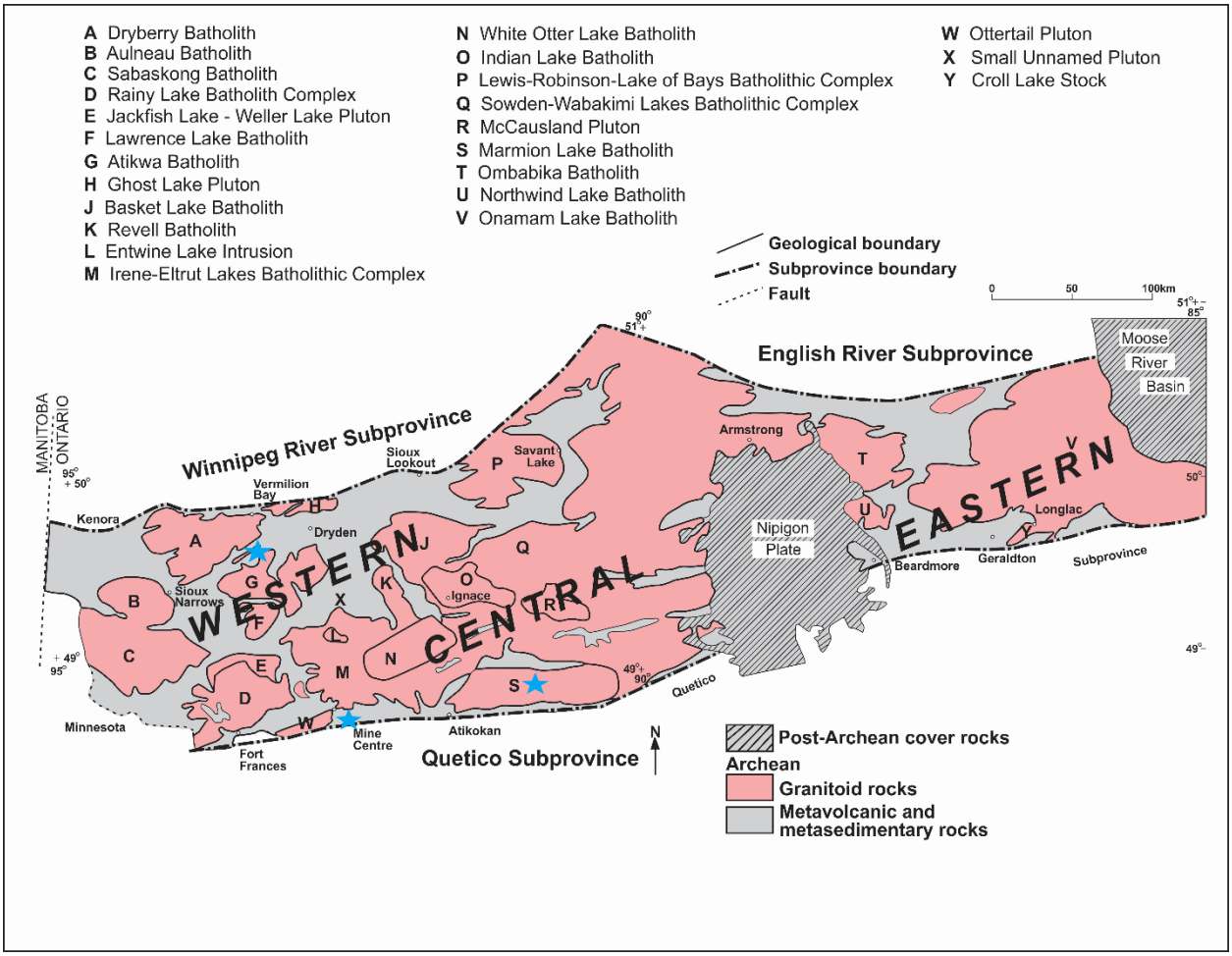

Figure 92. Map showing the approximate locations of drill core samples (blue stars) from the Atikwa batholith, the Marmion batholith and a small unnamed pluton in the western Wabigoon subprovince. Three chlorite shear fractures from 2 drill holes in the Atikwa batholith, 3 shear fractures from 2 drill holes in the Marmion batholith and 1 shear fracture taken from a small unnamed pluton.

Sample preparation difficulties stem from the need to analyze chlorite isotopic signatures via traditional mass spectrometer techniques which require a pure powdered sample of chlorite. In the case of infilled chlorite shear fractures, the primary challenge of sample preparation is obtaining a pure powder of the chlorite. The <1 to 3 mm thick chlorite shear fractures do not tend to have straight contacts with the host granitoid and anastomose around fragments of the host granitoid - predominately quartz and feldspar phases with lesser amounts of calcite and muscovite. Figure 93 shows a representative photograph, microphotograph and SEM-BSE image of the infilled chlorite shear fractures sampled for stable isotope analysis. Although dissolving the powder in acid is a helpful tool in getting rid of the calcite impurities, the quartz and feldspar impurities are more difficult to address. This obstacle was tackled by using a binocular microscope to remove any obvious impurities of quartz and feldspar within the powders – although trace impurities remain. Each of the six veins for which δD and $\delta^{18}O$ of the hydrothermal fluid has been calculated have sample impurities, which have the potential to skew the calculated hydrothermal fluid isotope signatures away from the true hydrothermal fluid isotope signatures. The XRD results of each sample are summarized in Table 8. XRD peaks are shown in Appendix IV. These veins would be better suited to recent techniques of stable isotope analysis such as Secondary Ion Mass Spectrometry (SIMS), which would allow for the chlorite to be analyzed in situ. Unfortunately, SIMS is not yet available for stable isotope analysis of chlorite due to the lack of chlorite standards necessary for the analysis to proceed.

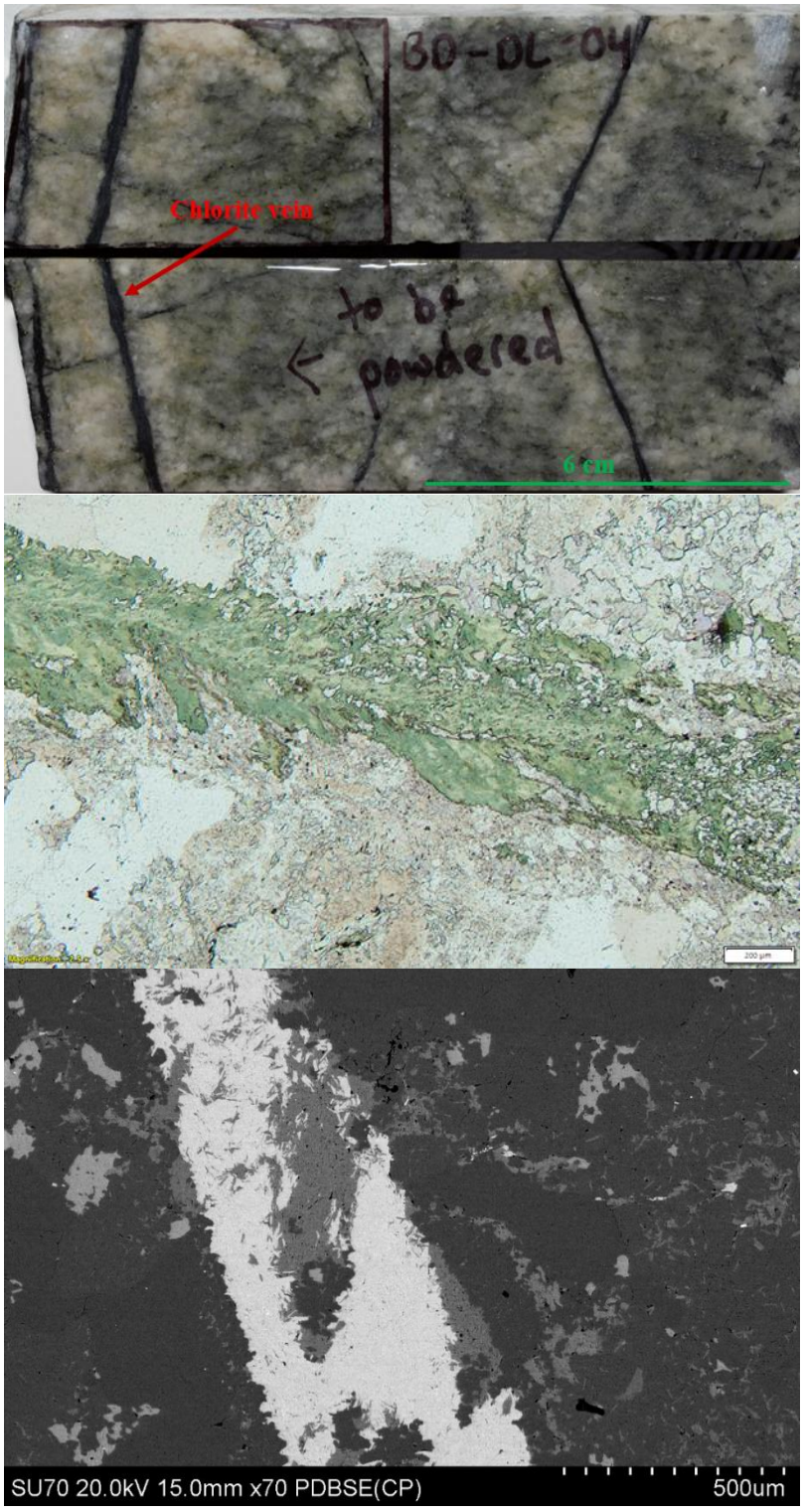

Figure 93. Top – Representative photograph of a mm-scale chlorite shear fracture (sample DL-04). **Middle –** Photomicrograph of the DL-04 chlorite shear fracture showing the anastomosing nature of the vein around the host granitoid (PPL). **Bottom –** SEM-BSE image of the chlorite shear fracture in DL-04, again showing the difficulty of obtaining a pure powder of chlorite for analysis.

Table 8. XRD qualitative results of each infilled chlorite shear fracture sample. XRD results show sample impurities which have potential to skew the calculated hydrothermal/metasomatic fluid δD and δ18O values away from the true values.

Sample I.D	Mineral phases (XRD analysis)
BD-DL-04 (Marmion)	clinochlore, quartz, muscovite
BD-DL-04B (Marmion)	clinochlore, quartz, muscovite
BD-DL-05 (Atikwa)	clinochlore, quartz, calcite, muscovite, orthoclase
BD-DL-06 (Atikwa)	clinochlore, quartz, muscovite, albite
BD-DL-08 (Unnamed pluton in western Wabigoon)	clinochlore, muscovite, calcite
BD-DL-09 (Marmion)	clinochlore, quartz, illite 2M1
BD-DL-10 (Atikwa)	clinochlore, quartz, albite, illite 2M1

An assumption of stable isotope analysis is that isotopic equilibrium between the hydrothermal fluid and the hydrothermal chlorite had been reached. Since isotopic equilibrium is difficult to assess, SEM-EDX quantitative mineral composition analysis was completed on the infilled chlorite shear fractures in order to gauge whether or not chemical equilibrium had been reached. If chemical equilibrium seems to have been reached, isotopic equilibrium is assumed. Figure 94 shows the chlorite discrimination diagram from Hey (1954) for all the infilled chlorite shear fractures assessed for stable isotope analysis. Analyses for the individual shear fractures tend to cluster together, highlighting that chemical equilibrium of the chlorite had likely been achieved. All shear fractures plot as ripidolites with the exception of one sample from the Atikwa batholith that plots as a pycnochlorite. The lack of a large scatter of the Si (p.f.u) and Fe/(Fe+Mg) ratios of the individual veins suggest that chemical equilibrium between the hydrothermal fluid and the hydrothermal chlorite had been obtained, fulfilling the assumption of isotopic equilibrium. The average chlorite mineral formulas calculated for each of the samples can be found in Table 9.

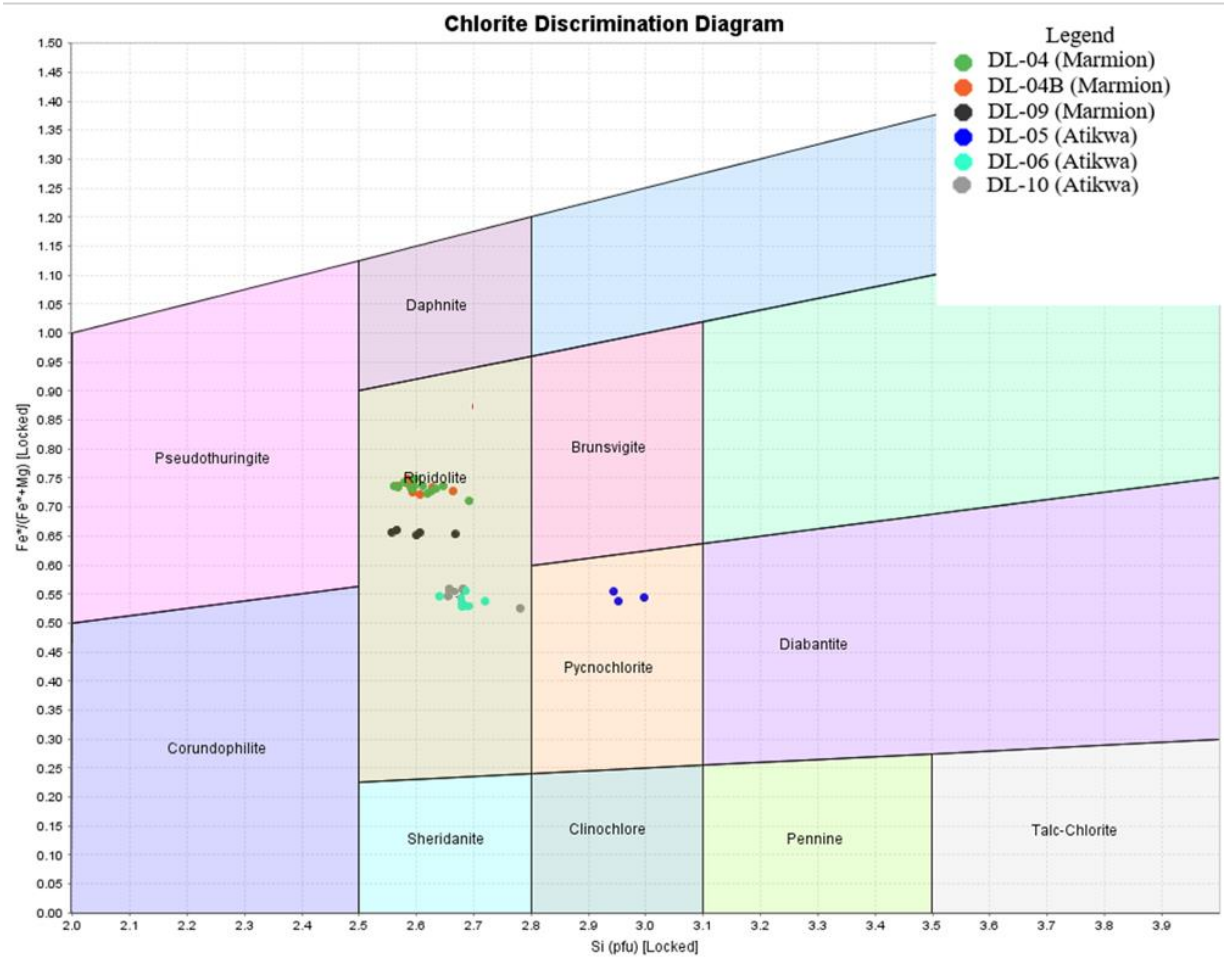

Figure 94. Chlorite discrimination diagram from Hey (1954) showing the chlorite classification for each of the chlorite infilled shear fractures assessed for stable isotope analysis.

Table 9. Chlorite mineral formulas (average) for each of the infilled chlorite shear fractures chosen for stable isotope analysis.

Pluton	Chlorite mineral formulas (average)	n
Marmion BD-DL-04B	$(Fe_{1.702}Mg_{0.616}Al_{0.686}Mn_{0.003})_{\sum 3.007}(Si_{2.602}Al_{1.398})_{\sum 4.00}O_{10}(OH)_2 \cdot (Fe_{1.702}Mg_{0.616}Al_{0.686}Mn_{0.003})_{\sum 3.007}(OH)_6$	8
Marmion BD-DL-04	$(Fe_{1.685}Mg_{0.614}Al_{0.699}Mn_{0.001})_{\sum 2.999}(Si_{2.607}Al_{1.393})_{\sum 4.00}O_{10}(OH)_2 \cdot (Fe_{1.685}Mg_{0.614}Al_{0.699}Mn_{0.001})_{\sum 2.999}(OH)_6$	14
Marmion BD-DL-09	$(Fe_{1.505}Mg_{0.790}Al_{0.704})_{\sum 2.999}(Si_{2.599}Al_{1.401})_{\sum 4.00}O_{10}(OH)_2 \cdot (Fe_{1.505}Mg_{0.790}Al_{0.704})_{\sum 2.999}(OH)_6$	5
Atikwa BD-DL-05	$(Fe_{1.346}Mg_{1.122}Al_{0.517}Mn_{0.015})_{\sum 3.000}(Si_{2.964}Al_{1.036})_{\sum 4.00}O_{10}(OH)_2 \cdot (Fe_{1.346}Mg_{1.122}Al_{0.517}Mn_{0.015})_{\sum 3.000}(OH)_6$	3
Atikwa BD-DL-06	$(Fe_{1.259}Mg_{1.073}Al_{0.664}Mn_{0.002})_{\sum 2.998}(Si_{2.681}Al_{1.319})_{\sum 4.00}O_{10}(OH)_2 \cdot (Fe_{1.259}Mg_{1.073}Al_{0.664}Mn_{0.002})_{\sum 2.998}(OH)_6$	8
Atikwa BD-DL-10	$(Fe_{1.277}Mg_{1.060}Al_{0.661})_{\sum 2.998}(Si_{2.684}Al_{1.316})_{\sum 4.00}O_{10}(OH)_2 \cdot (Fe_{1.277}Mg_{1.060}Al_{0.661})_{\sum 2.998}(OH)_6$	9
Unnamed pluton western Wabigoon BD-DL-08	$(Fe_{1.925}Mg_{0.316}Al_{0.726})_{\sum 2.970}(Si_{2.680}Al_{1.320})_{\sum 4.00}O_{10}(OH)_2 \cdot (Fe_{1.925}Mg_{0.316}Al_{0.726})_{\sum 2.970}(OH)_6$	5

6.1 Chlorite Geothermometry

Chlorite geothermometry is a widely used technique in assessing the formation temperature of chlorite (Klein et al., 2007). Chlorite geothermometry has been completed on each of the six veins for which the δD and $\delta^{18}O$ values of the hydrothermal fluid has been calculated. Temperature estimates of chlorite formation are essential to understanding the fractionation of the hydrogen and oxygen isotopes between the chlorite-water system, as fractionation is temperature dependant.

The variation in Al^{IV} content and the Fe/(Fe+Mg) ratios seen in hydrothermal/metasomatic chlorites as a function of temperature have been used to constrain three widely used empirical chlorite geothermometry formulas (Kranidiotis and MacLean, 1987; Cathelineau, 1988; Zang and Fyfe, 1995). Two issues regarding empirical chlorite geothermometry include: 1) the contamination of chlorite by inclusions or interlayers (Klein et al., 2007; Schiffman and Fridleifsson, 1991; Jiang et al., 1994), 2) the commonly unknown influence of the fluid to rock ratio, $f\,O_2$, $f\,S_2$, pH and the composition of the fluid and host rock on the Fe/(Fe+Mg) ratios and formation temperatures of the hydrothermal/metasomatic fluids. Additionally, a few criteria must be met for chlorite geothermometry to be an effective tool in estimating formation temperatures (Klein et al., 2007). These criteria include:

1) The chemical analysis of the chlorite being studied needs to be similar to the chemical analysis of the chlorite used to calibrate the geothermometer.

2) Results are independently compared with other temperature estimates.

3) A correlation between the Al^{IV} content and the Fe/(Fe+Mg) ratios exist.

The three empirical chlorite geothermometry formulas are as follows:

1) $T°C = -61.9229 + 321.9772(Al^{IV})$ (Cathelineau, 1988). Based on $(Si, Al)_4$.

2) $T°C = 106*Al_{Corrected}^{IV} + 18$ where $Al_{corrected}^{IV} = Al_{measured}^{IV} \pm 0.7(Fe/(Fe+Mg))$ (Kranidiotis and MacLean, 1987). Based on $(Si, Al)_8$.

3) $T°C = 106.2*Al_{Corrected}^{IV} + 17.5$ where $Al_{Corrected}^{IV} = Al_{measured}^{IV} - 0.88(Fe/(Fe+Mg) - 0.34)$ (Zang and Fyfe, 1995). Based on $(Si, Al)_8$.

The second two geothermometers have corrected Al^{IV} values because the temperatures calculated for chlorite with higher Fe/(Fe+Mg) ratios will be notably higher if the calculation is made without any corrections to the Al^{IV} content (Kranidiotis and MacLean, 1987; Zang and Fyfe,

1995). The substitution of Al^{IV} for Si in the tetrahedral site allows for the larger Fe ions to substitute for Mg in the octahedral site, resulting in an enrichment of Al in the tetrahedral site when compared to the Al content in the octahedral site (Zang and Fyfe, 1995).

Figure 95 shows a plot of Al^{IV} against the Fe/(Fe+Mg) ratios for each of the six infilled shear fractures to assess whether there is a correlation between them. Although data points are limited, there does seem to be a correlation, satisfying the third criteria needed for chlorite geothermometry to be effective.

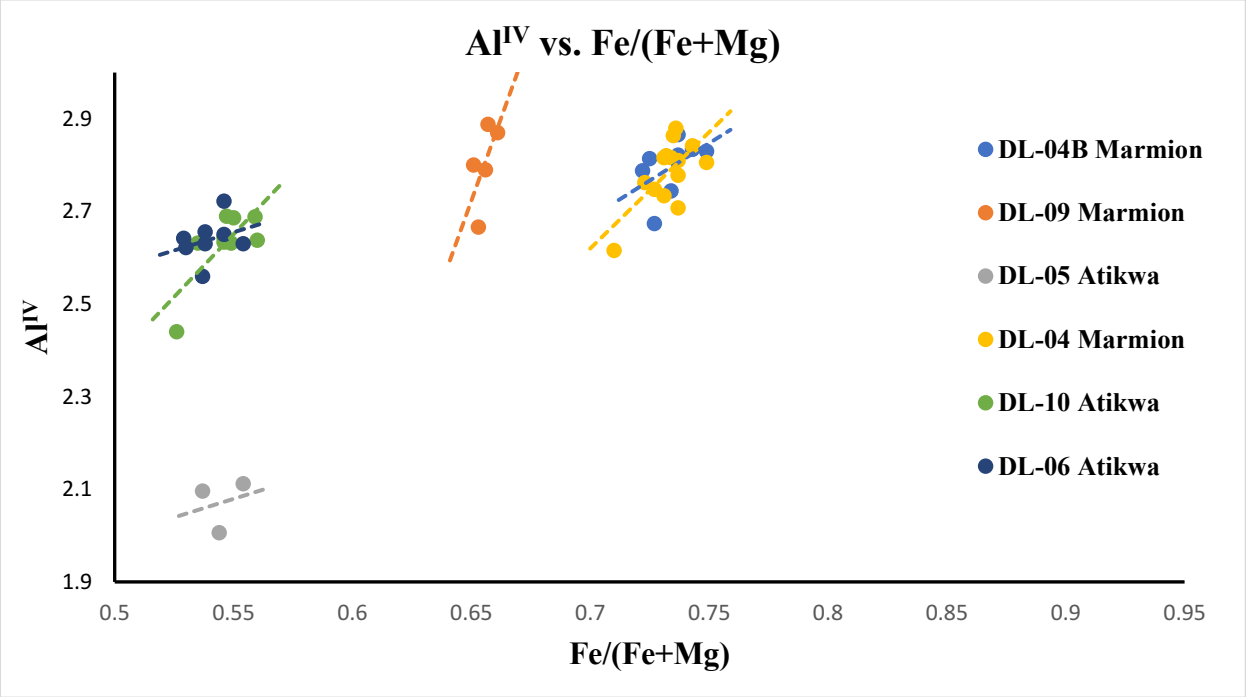

Figure 95. A plot of Al^{IV} against Fe/(Fe+Mg). Although data points are limited, there does seem to be a correlation between Al^{IV} and Fe/(Fe+Mg) ratios, suggesting that the 3rd criteria for chlorite geothermometry (see text) is satisfied.

After assessing the Al^{IV} and Fe/(Fe+Mg) correlations for each of the samples, each of the three geothermometers were used to assess the formation temperature of the chlorite, the results of which are shown in Table 3. After comparing the chemical compositions of the chlorites analyzed in this work to the chlorites used to calibrate each of the three geothermometers, it was decided that the appropriate geothermometer to use for the Atikwa batholith chlorite samples is that of Kranidiotis and MacLean (1987), while the appropriate geothermometer for the Marmion batholith samples was deemed to be that of Zang and Fyfe (1995). It should be noted that one of

the criteria for chlorite geothermometry to be most successful (as discussed earlier) was not met for any of the samples. Based on correlations between the brittle and ductile deformation seen in the 12 plutons studied in this research, it seems likely that these chlorite shear fractures formed at temperatures near 450°C, corresponding to peak metamorphism. However, it is quite probable that the brittle deformation was ongoing not just during peak metamorphism but also during exhumation, cooling and retrograde metamorphism as evidenced by the presence of chlorite infilled cataclasites found within the White Otter Lake batholithic complex. The cataclasites suggest lower temperature brittle deformation, so a temperature of formation around 270°C - 360°C is not unlikely considering the wide stability field of chlorite. The presence of illite within the chlorite powders (Table 8) also provides evidence for lower temperature hydrothermal/metasomatic alteration, as the stability field of illite is constrained to roughly 200°C to 300°C (Merriman and Frey, 1999). For these reasons, isotope fractionation factors for both oxygen and hydrogen were based on the calculated temperatures shown in Table 10.

Table 10. Chlorite geothermometry temperatures of chlorite formation for the geothermometer used in the calculation of fractionation factors.

Sample I.D	Fe/(Fe+Mg) (Average)	Kranidiotis and MacLean (1987) T°C (Average)	Cathelineau (1988) T°C (Average)	Zang and Fyfe (1995) T°C (Average)	Geothermometer to use based on Fe/(Fe+Mg)	Does the temperature calculated fit the temperate estimated?	Does a correlation between Al^{IV} and Fe/(Fe+Mg) exist?
DL-04 (Marmion)	0.733	368	387	277	Zang and Fyfe (1995)	No	Yes
DL-04B (Marmion)	0.734	369	388	278	Zang and Fyfe (1995)	No	Yes
DL-09 (Marmion)	0.656	364	389	286	Zang and Fyfe (1995)	No	Yes
DL-05 (Atikwa)	0.545	278	272	218	Kranidiotis and MacLean (1987)	No	Yes
DL-06 (Atikwa)	0.540	338	363	279	Kranidiotis and MacLean (1987)	No	Yes
DL-10 (Atikwa)	0.546	337	362	278	Kranidiotis and MacLean (1987)	No	Yes

6.2 Chlorite-Water fractionation factors and the isotopic signature of the hydrothermal fluid

The oxygen exchange chlorite-water fractionation factor from Cole and Ripley (1998) was used in this study. The fraction factor ($\alpha_{chl\text{-}water}$) is as follows:

$$1000\ln\alpha_{chl\text{-}water} = 2.693(10^9/T^3) - 6.342(10^6/T^2) + 2.969(10^3/T)$$

where T is the temperature estimated through chlorite geothermometry in Kelvin (K). For the hydrogen exchange chlorite-water fractionation factor, the work of Graham et al (1987) was used. Graham et al. (1987) note that there is no appreciable temperature dependence for the chlorite-water hydrogen isotope fractionation factor over the temperature range of 200°C-500°C, with $10^3\ln\alpha_{chl\text{-}water}$ laying in the range of -30 to -40. However, they note that with decreasing temperatures, the $10^3\ln\alpha_{chl\text{-}water}$ value also decreases. Furthermore, the $1000\ln\alpha_{chl\text{-}water}$ values used for the hydrogen isotope values is estimated at between -30 to -40, with lower values of the range used for lower temperatures. Table 11 shows the measured isotopic composition of chlorite veins, the formation temperature of the chlorite for each sample based on chlorite geothermometry, the calculated oxygen fractionation factors, the estimated $10^3\ln\alpha_{chl\text{-}water}$ values for the hydrogen isotope chlorite-water exchange system and finally, the calculated δD and $\delta^{18}O$ values of the hydrothermal fluid. The $\delta^{18}O$ and δD values of the hydrothermal fluid were calculated using the formulas:

$$\delta D_{chl} - \delta D_{water} \approx 10^3\ln(\alpha_{chl\text{-}water})$$

and

$$\delta^{18}O_{chl} - \delta^{18}O_{water} \approx 10^3\ln(\alpha_{chl\text{-}water})$$

The calculated δD and $\delta^{18}O$ ratios of the hydrothermal fluid were then plotted against each other in Figure 96 to assess the potential source(s) of the hydrothermal fluid (Hoefs, 2015). Although sample purity was not achieved with the chlorite powders, each of the six veins plot together in the metamorphic water domain. It seems likely that the source of the hydrothermal fluid would be fluids derived from the surrounding hydrous greenstone, particularly fluids sourced from devolatilization reactions of the hydrous mineral phases during regional metamorphism. The clustering of the veins together within a source that seemingly makes sense could possibly mean that the influence of the non-chlorite mineral phases within the chlorite powders was negligible, not enough to skew the isotopic signature of the hydrothermal fluid itself. However, the fluid source should be assessed carefully, as the influence of the non-chlorite mineral phases on the isotopic signature of the hydrothermal fluid remains unknown.

Table 11. Table showing the measured isotopic signatures of the chlorite powders, the temperature of formation for each of the chlorite samples, as well as the calculated oxygen and hydrogen fractionation factors. Finally, the calculated isotopic signature of the hydrothermal fluid for each chlorite powder is shown.

Sample ID	**δ^2H_{chl}(‰) vs VSMOW**	**$\delta^{18}O_{chl}$ (‰) vs VSMOW**	**Temp (°C)**	**$\alpha_{chl\text{-}water}$ for Oxygen**	**$1000ln\alpha_{chl\text{-}water}$ for oxygen**	**$1000ln\alpha_{chl\text{-}water}$ for hydrogen**	**δ^2H_{water}(‰)**	**$\delta^{18}O_{water}$ (‰)**
BD_DL_04 (Marmion)	-79 ± 3.0	6.5 ± 0.4	277	1.0006	0.599	-38	-41 ± 3.0	5.9 ± 0.4
BD_DL_04B (Marmion)	-72 ± 3.0	6.2 ± 0.4	278	1.0006	0.599	-38	-34 ± 3.0	5.6 ± 0.4
BD_DL_05 (Atikwa)	-68 ± 3.0	6.7 ± 0.4	278	1.0006	0.599	-38	-30 ± 3.0	6.1 ± 0.4
BD_DL_06 (Atikwa)	-70 ± 3.0	6.1 ± 0.4	338	0.9997	-0.300	-35	-35 ± 3.0	6.4 ± 0.4
BD_DL_09 (Marmion)	-71 ± 3.0	6.1 ± 0.4	286	1.0004	0.399	-38	-33 ± 3.0	5.7 ± 0.4
BD_DL_10 (Atikwa)	-70 ± 3.0	6.8 ± 0.4	337	0.9997	-0.300	-35	-35 ± 3.0	7.1 ± 0.4

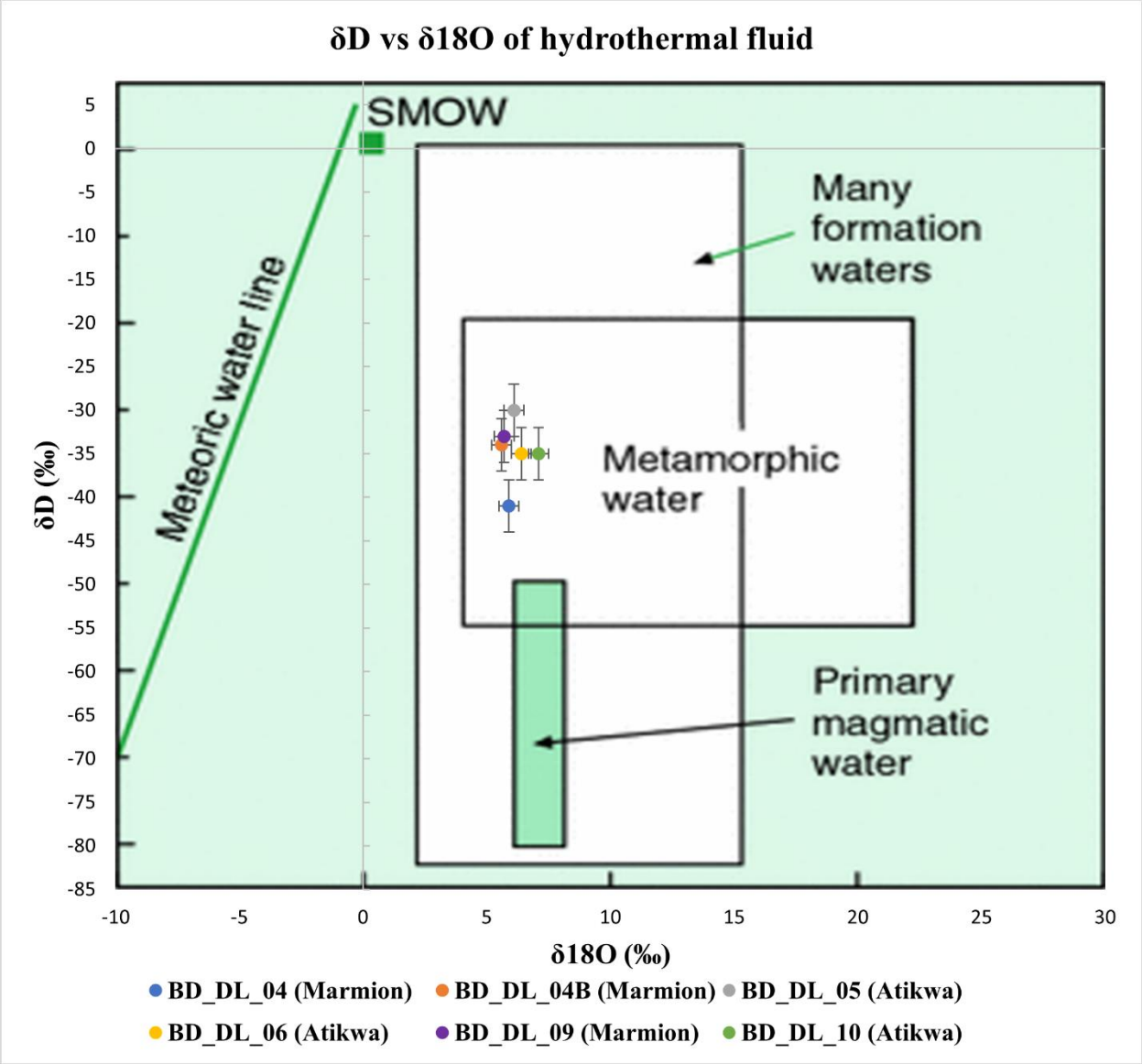

Figure 96. A plot of δD^{fluid} and $\delta^{18}O^{fluid}$ showing a metamorphic water origin for the hydrothermal fluid. Water domains are from Hoefs (2015).

Chapter 7: Cathodoluminescence Imaging

Cathodoluminescence (henceforth abbreviated CL) is a luminescence technique that is best described as the excitation of various mineral phases via an electron beam. When the electron beam contacts the mineral phases, the ions with an unfilled shell pass from the ground state to the excited state, releasing light in the visible spectrum. CL imaging allows for the visualization of alteration, trace element incorporation, zoning and deformation that may not always be visible using standard microscopy techniques. The CL activation of various minerals such as silicates, carbonates and phosphates can be related to substitutional trace activators (Mn^{2+}, Fe^{3+}, Cr^{3+}, Eu^{2+} and REE^{3+}) and/or electron centers associated with lattice defects. This chapter aims to explore the potential of using CL imaging as a tool in assessing the degree of alteration/trace element incorporation and the deformation seen in feldspar and quartz mineral phases throughout the granitoid plutons of the Wabigoon subprovince. Eighteen thin sections from 10 plutons had CL imaging completed to analyze the cathodoluminescence properties of the quartz and feldspar mineral phases. Additional CL images are shown in Appendix V. The thin sections selected for CL imaging range from low strain samples to intermediate strain samples and high strain samples in order to assess the degree of alteration, trace element and REE incorporation in the mineral phases with varying degrees of deformation. Samples chosen lacked an abundant degree of chlorite-epidote alteration as these mineral phases do not luminesce.

The CL was run with a 9 kV accelerating voltage and a 480 µA beam current. Felspar CL images were taken at 4s exposure time and 2x gain. All potassic feldspars show a bright blue CL color while all plagioclase feldspars show a dark purple/red CL color at this operating setting. Quartz images taken at 4s exposure time and 2x gain do not luminesce, appearing black. For quartz, the CL was still run with a 9 KV accelerating voltage and a 480 µA beam current, but images were taken with longer exposure times (30s) and a higher gain set (48x). Even with the longer exposure time and higher gain set, the quartz has only a faint red/blue luminescence that tends to be washed out from the nearby highly luminescent feldspars and carbonates, making the quartz CL properties difficult to assess in most cases. Nonetheless, feldspars (specifically potassic) show variations in the blue CL colors along microcracks and grain boundaries, with increasing color variations in higher strain samples, demonstrating an increase in trace elements and/or REEs along hydrothermal fluid pathways. Note that all CL images shown are edited with higher levels of light to pick out the dark red CL colors of the plagioclase feldspars, which are typically dampened by

the intense blue luminescence of the potassic feldspar in the original images. The field of view for all CL images is approximately 2.5mm, unless stated otherwise.

7.1 High strain samples

High strain samples are characterized by a high intensity of brittle and/or ductile deformation. These samples include shear zones, cataclasites, potential pseudotachylyte and highly ductiley deformed and boudinaged quartz veins typically associated with shear zones. A wide variety of the blue CL color hues are seen within potassic feldspars in and directly adjacent to brittle-ductile shear zones (Figure 97). Variations of the blue CL colors can be seen in the K-feldspars primarily along grain boundaries and microcracks, corresponding to variations in the degree of trace element and REE contents. The plagioclase feldspar also show variations in the intensity of their red CL colors, although the color changes are not as pronounced as for the potassic feldspar. When comparing the CL images to transmitted cross polarized light photomicrographs, the CL color changes cannot always be correlated to a visible presence of alteration, suggesting that the CL images have potential to provide new insight into the alteration and trace element incorporation of the feldspars (Figure 98).

The blue CL color hues seen in feldspar porphyroclasts within a ductile shear zone in the Sabaskong batholith also vary substantially (Figure 99). The distinct CL properties of the feldspars and quartz also allow for the rapid distinction between very fine-grained quartz and feldspars within the grain-size reduced matrix material as the feldspars have a blue CL color while the quartz is black (Figure 99). The porphyroclasts show strong alteration in their cores, appearing as brown. The brown alteration can also be seen in the grain-size reduced matrix material. In the non-altered portions of the porphyroclast, variation in the blue hue of the CL colors can be seen that likely correlate to trace element incorporation or REE incorporation. Note that the feldspar porphyroclasts within this ductile shear zone display zoning in cross polarized transmitted light but not in the CL images, suggesting that the zonation is a function of the major element constituents as opposed to trace elements or REE constituents.

Two CL images of ductilely deformed hydrothermal quartz veins were taken. The first vein, taken from the Sabaskong batholith, shows only a faint red to purple luminescence with an apparent lack of zoning, notable trace element and/or REE incorporation and/or defects (Figure 100). The second quartz vein, taken from the Dryberry batholith, shows more variation in the CL colors of the quartz, with some grains giving a blue luminescence in the center and a redder

luminescence near the grain boundaries (Figure 101). Other grains show primarily blue CL colors with some faint red luminescence near the centers of the grains. This quartz vein appears to have some combination of trace element impurities, REE impurities of accumulated defects which cause the change in the luminescence properties. No growth zoning can be seen within either of the quartz veins.

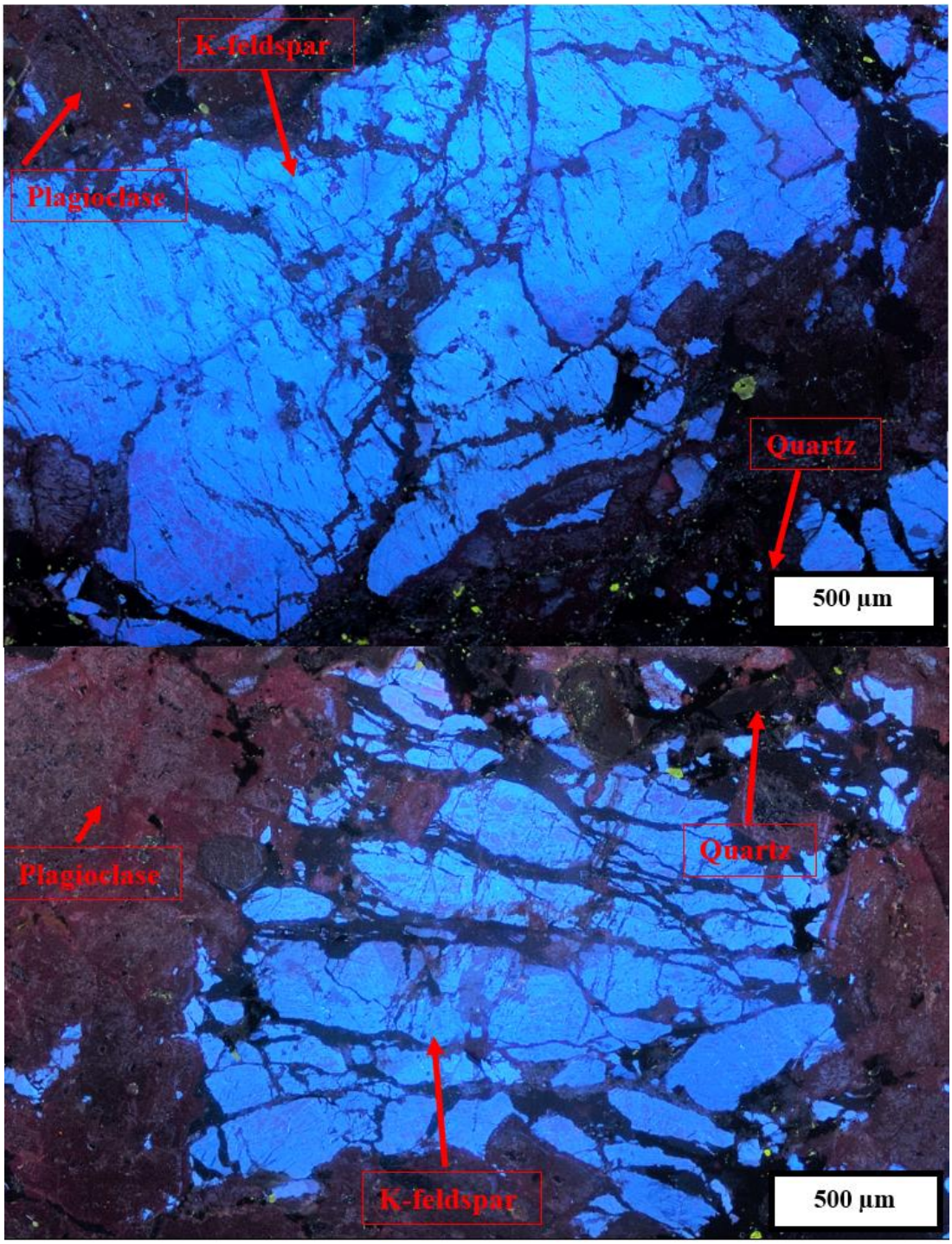

Figure 97. CL images of fractured K-feldspar (blue), plagioclase feldspar (red) and quartz (black) from the Ottertail pluton in the western Wabigoon subprovince. Variations in the blue CL colors and red CL colors are seen in both feldspar phases, corresponding to variations in the trace element and REE contents.

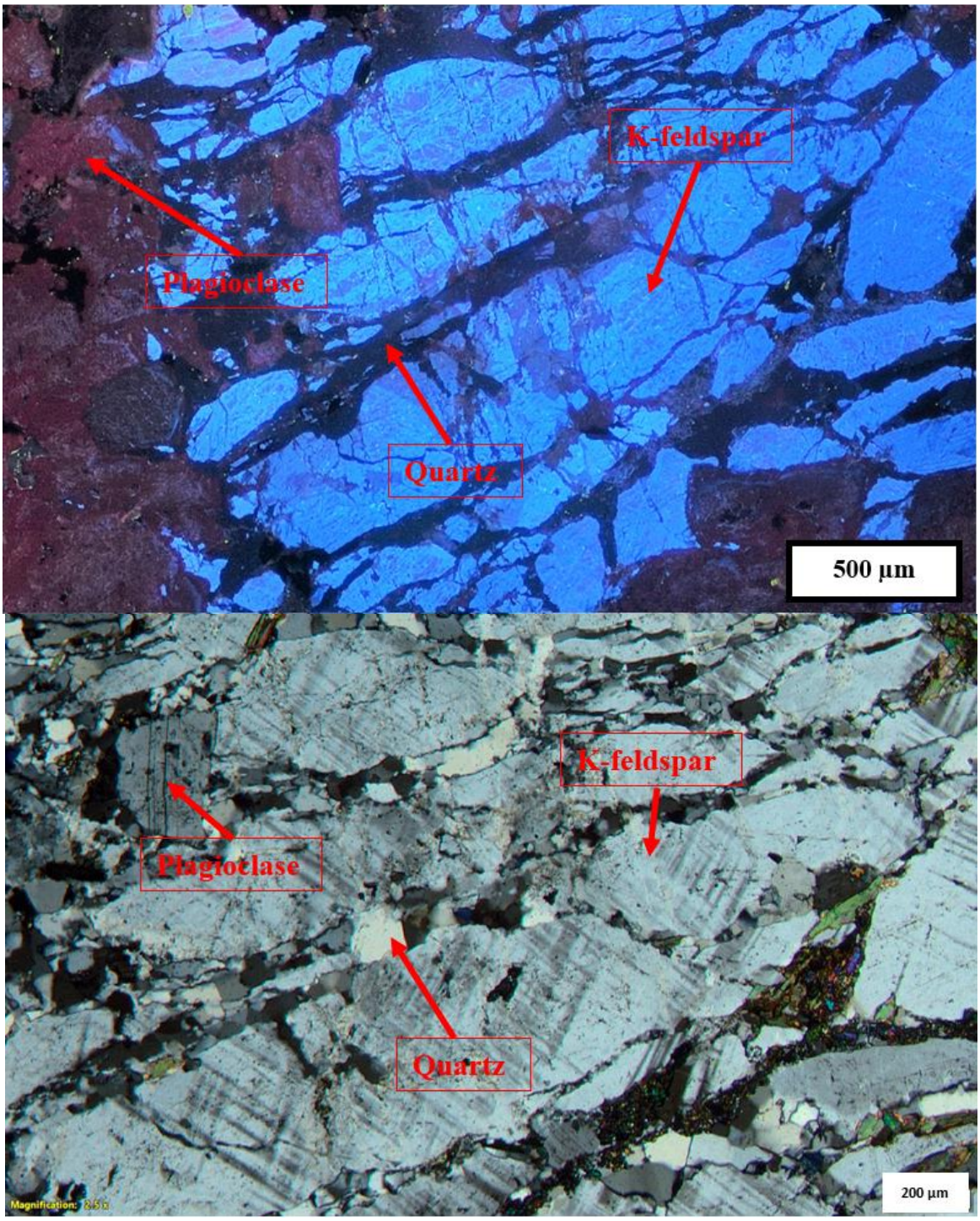

Figure 98. A comparison of the CL image (top) and its corresponding cross polarized transmitted light image (bottom – slightly more zoomed in).

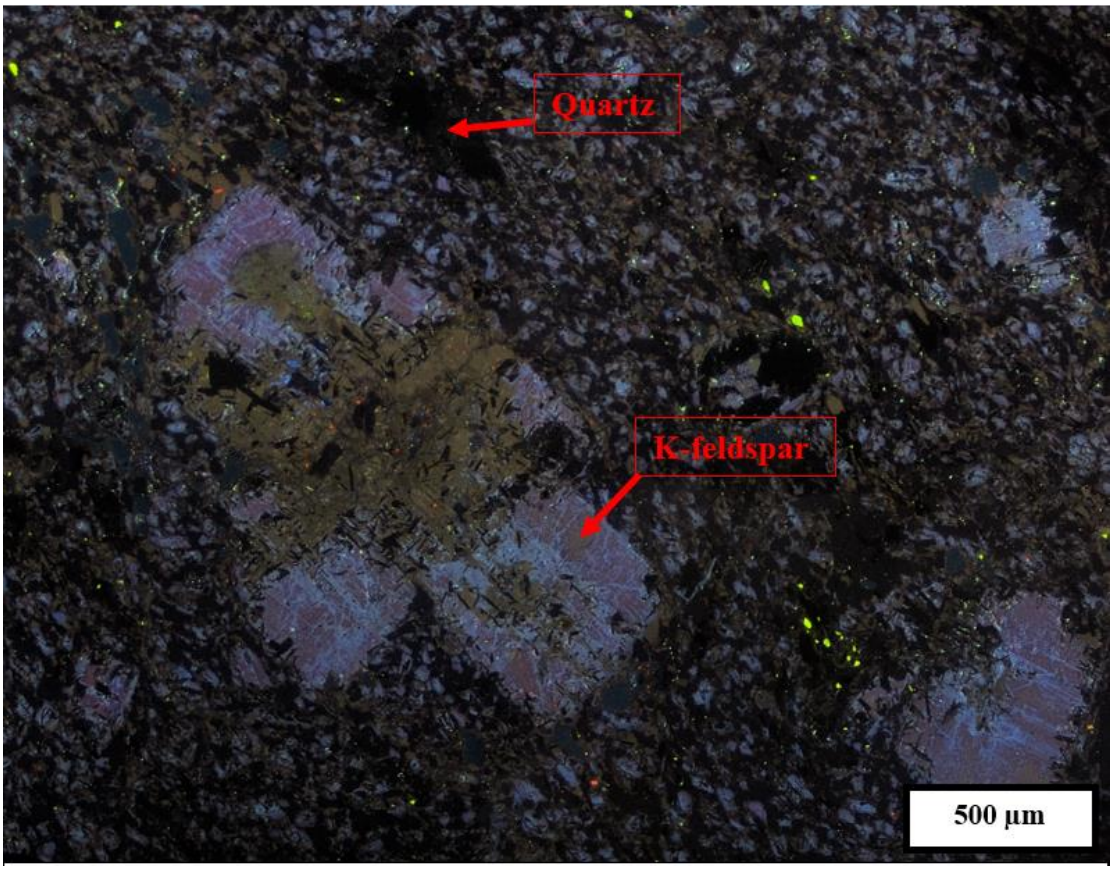

Figure 99. CL image of a ductile shear zone in the Sabaskong batholith. Feldspar porphyroclasts appear with blue CL colors. Strong alteration (brown) can be seen in the core of one of the porphyroclasts. The distinction between matrix material is easily viewable.

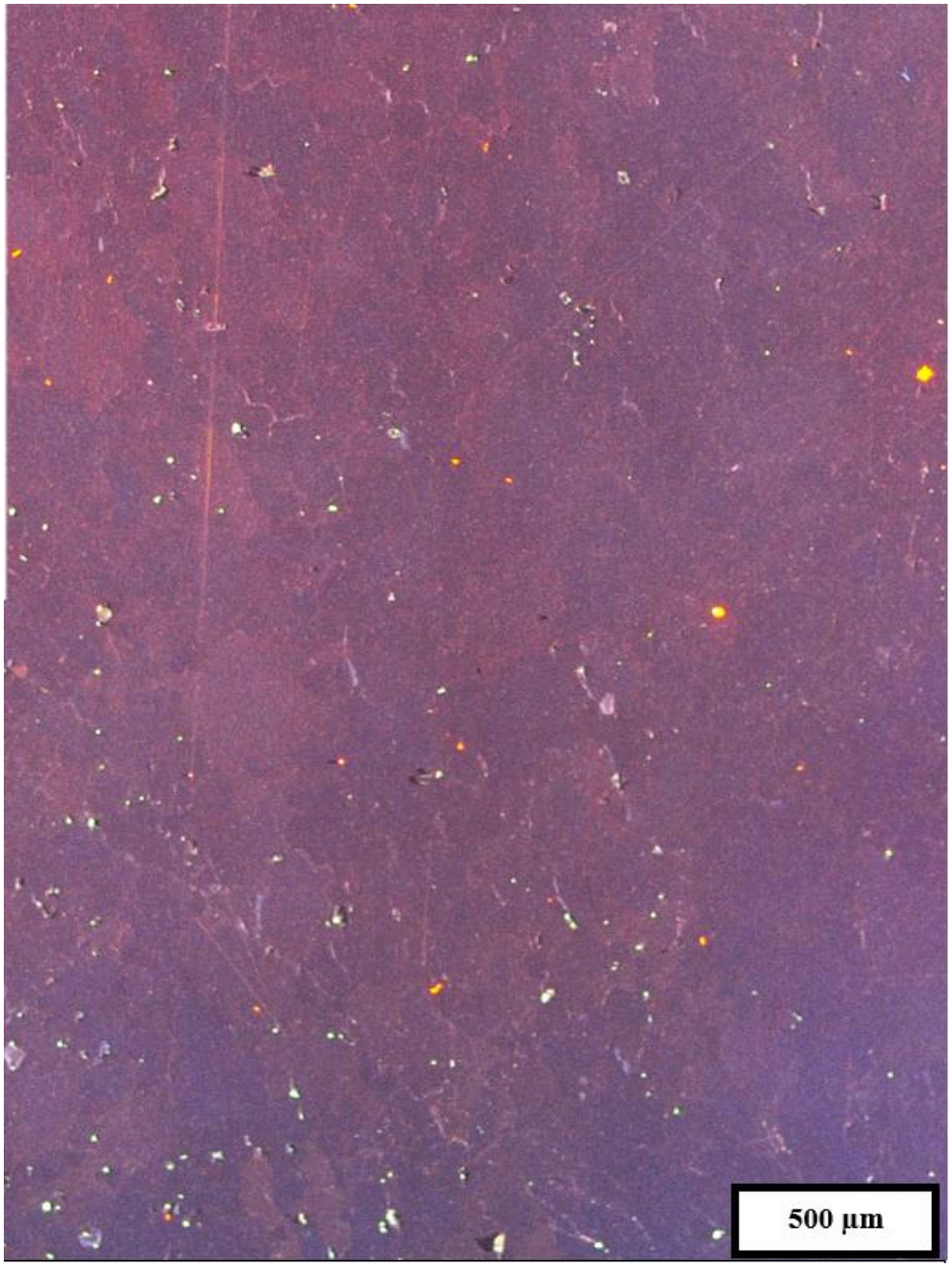

Figure 100. CL image of a ductilely deformed hydrothermal quartz vein showing a faint red-purple luminescence. No growth zoning or lattice defects are visible with CL imaging.

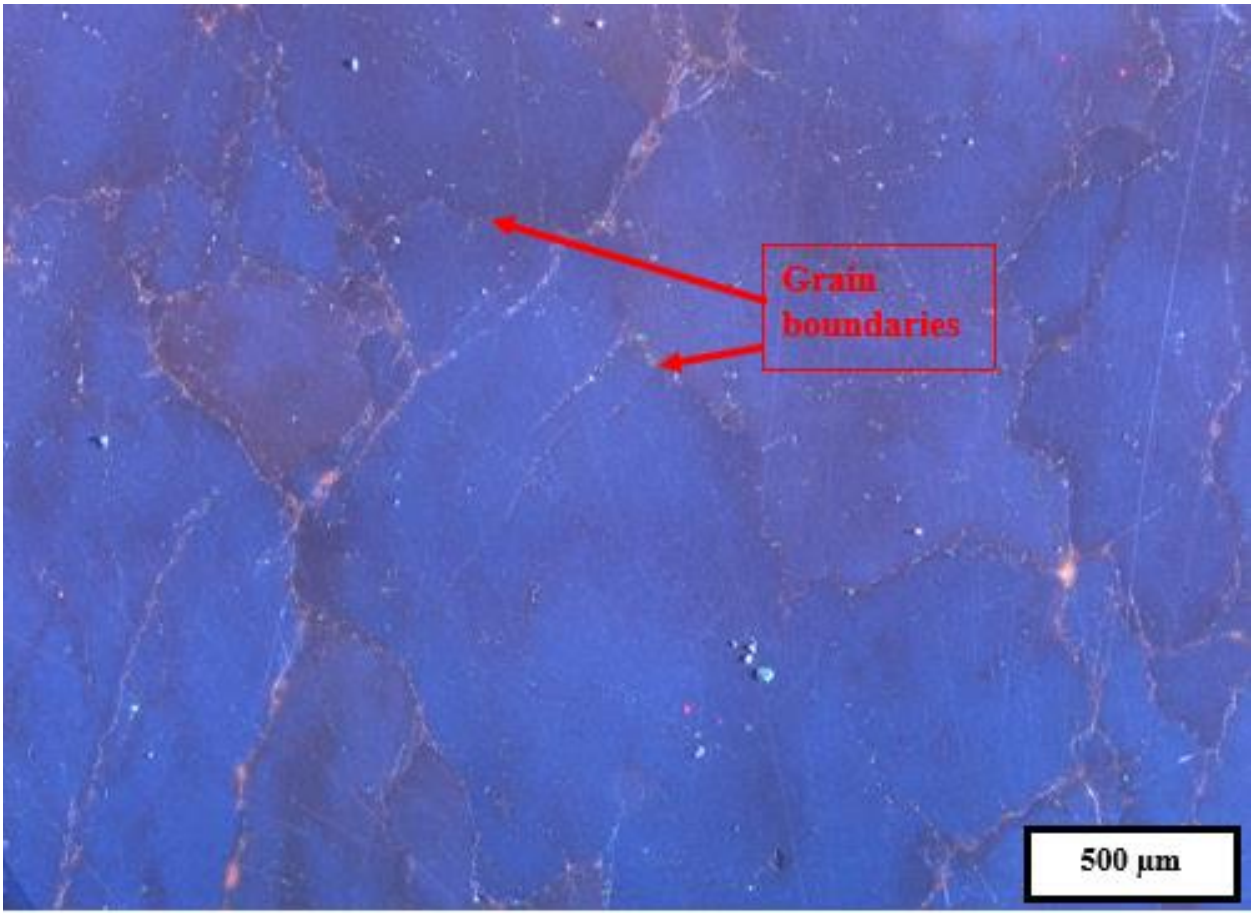

Figure 101. A ductilely deformed quartz vein from the Dryberry batholith showing variation in CL colors from blue to red. The shift from blue to red is likely a combination of substitutional trace element activators and/or defects. Color variations are strongest along apparent grain boundaries.

7.2 Medium strain samples

Medium strain samples are samples that are intermediate between low strain and high strain. Many of the medium strain samples show variation in CL color hues, particularly in the potassic feldspar. A CL image from the Sowden-Wabakimi batholithic complex shows a wide variety of the blue CL color hue in the potassic feldspar primarily along the grain boundary and microcracks (Figure 102). Another interesting CL image comes from the Revell batholith, which shows a potassic feldspar crystal with strong blue color variations (Figure 103). Color variation can also be seen in the red-purple plagioclase feldspar, along with core and rim alteration present as brown patches.

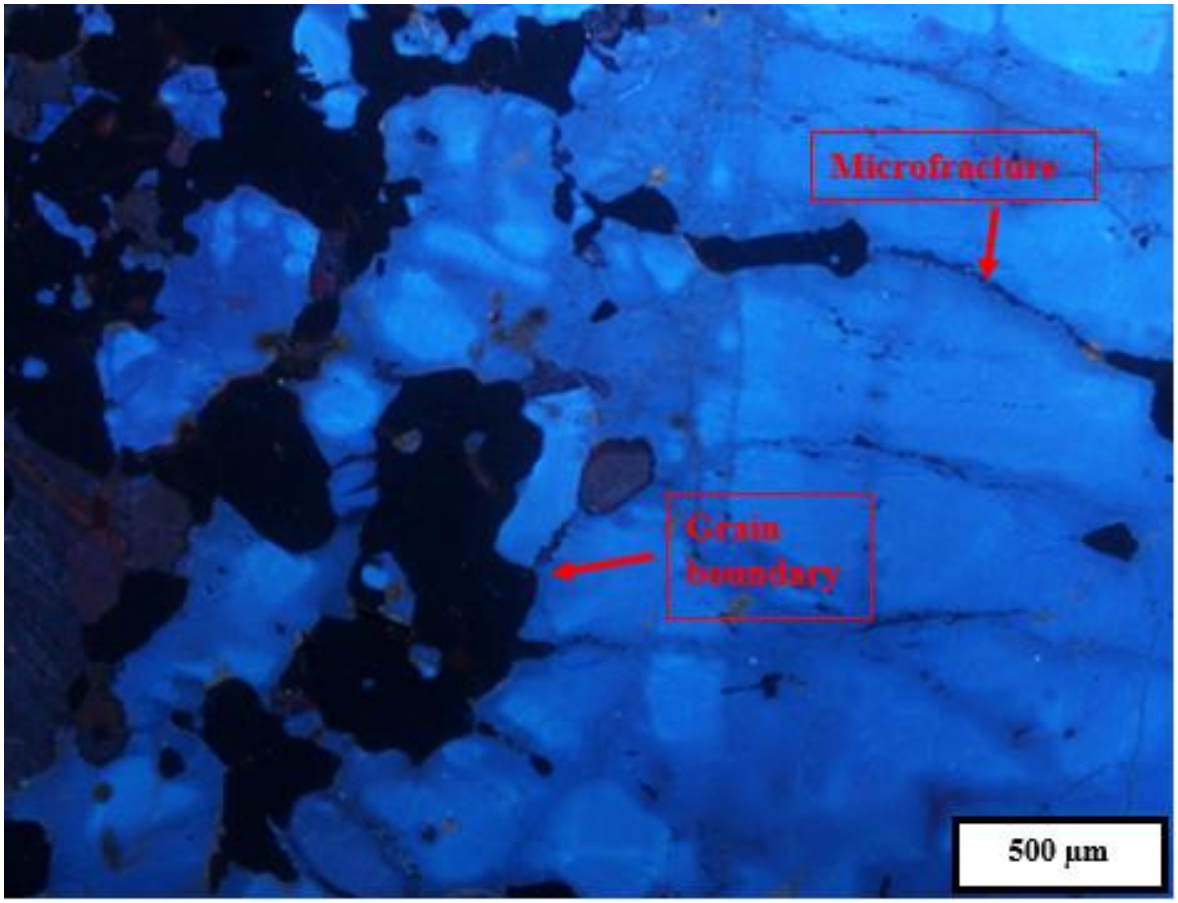

Figure 102. Potassic feldspar (blue) from the Sowden-Wabakimi Lakes batholithic complex showing a wide variety of its blue CL color primarily along the grain boundaries.

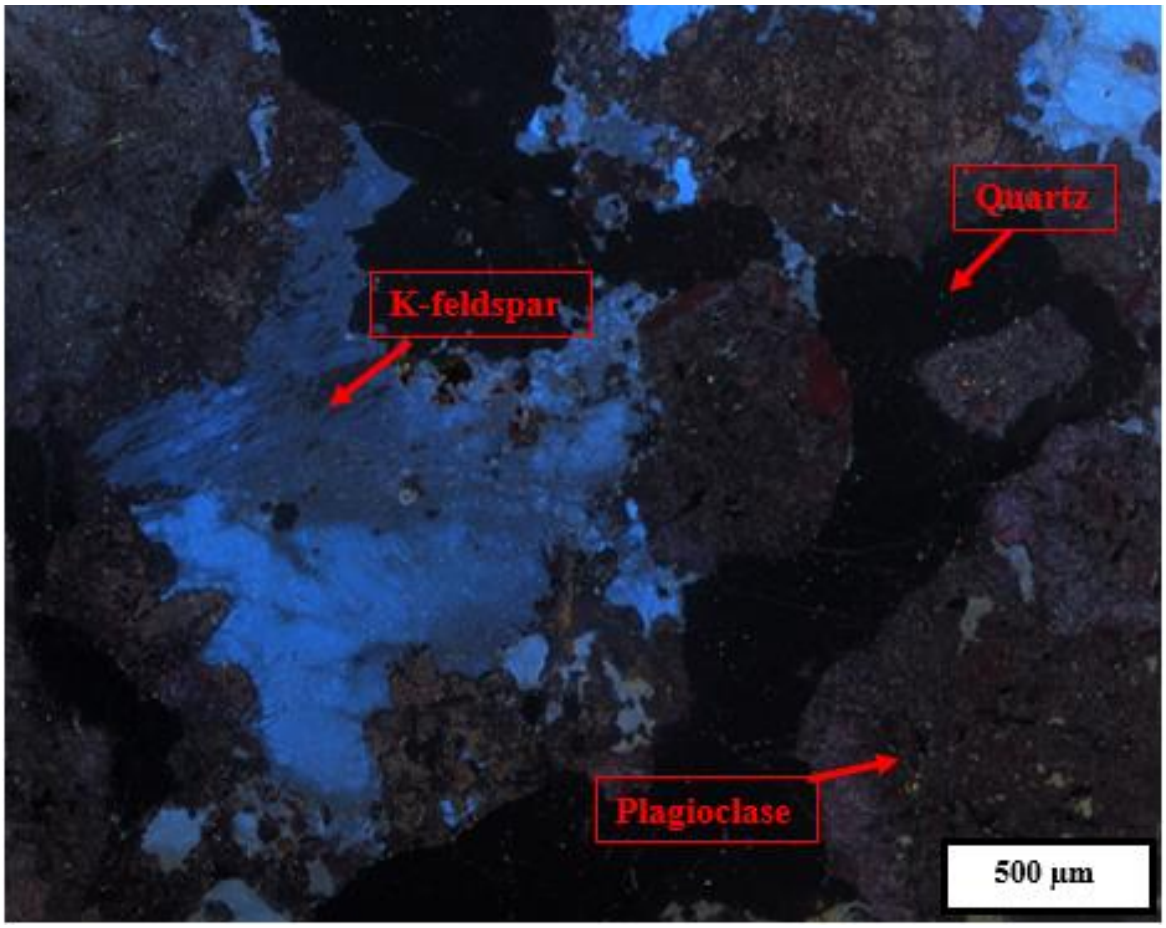

Figure 103. A medium strained sample from the Revell batholith showing strong variation in the blue CL colors of a potassic feldspar crystal. The red-purple plagioclase feldspar also shows some CL color variations. Alteration, appearing as brown, can be seen in the plagioclase feldspar.

7.3 Low strain samples

Low strain samples are defined as those samples with only minimal evidence for brittle and ductile deformation. These samples typically have feldspar crystals that can reach up to 5 cm in length. Although chlorite and/or epidote coated shear fractures are present in the outcrop, the thin section sample itself does not show much in terms of brittle deformation. A low strain sample taken from the Indian Lake batholith in the central Wabigoon subprovince shows minimal variation in the CL colors of potassic feldspars (Figure 104).

Two samples from the Marmion batholith show CL color zoning in the core of coarse-grained feldspars that are reflective of trace element and/or REE variations rather than variations in the major element concentrations, as the zonation is not viewable in cross polarized transmitted light. Along the margins of the coarse grained potassic feldspar, the zonation becomes less notable and more patchy in CL color zonation (Figure 105).

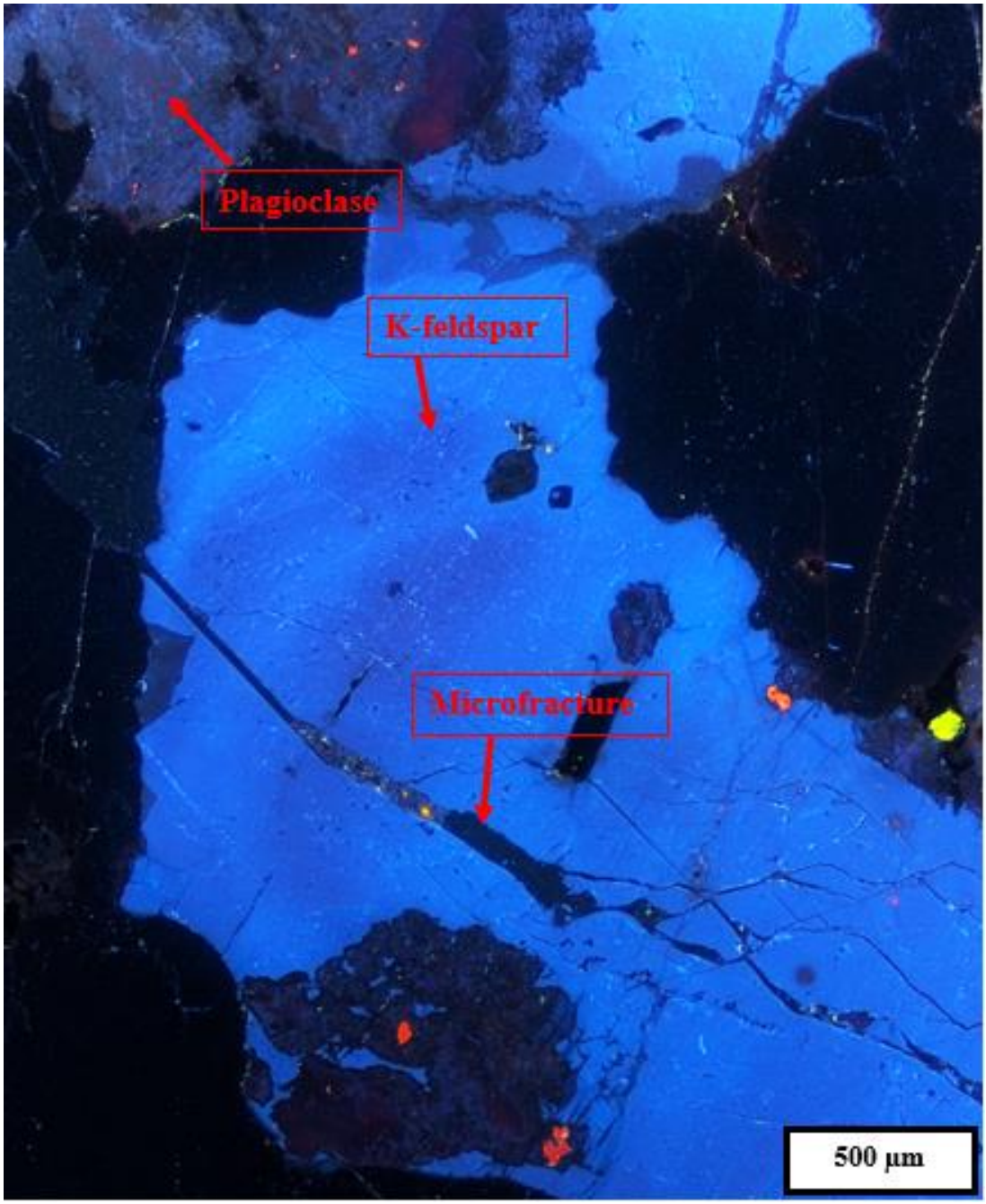

Figure 104. CL image of a feldspars (potassic is blue, plagioclase is red-blue) and quartz (black) taken from a low strain sample in the Indian Lake batholith. Slight variations of the blue CL color can be seen in the potassic feldspar, primarily along the grain boundaries and a microfracture. Slight color changes can be seen in the core of the feldspar. The plagioclase in the upper left-hand corner also shows some variation in CL color hues.

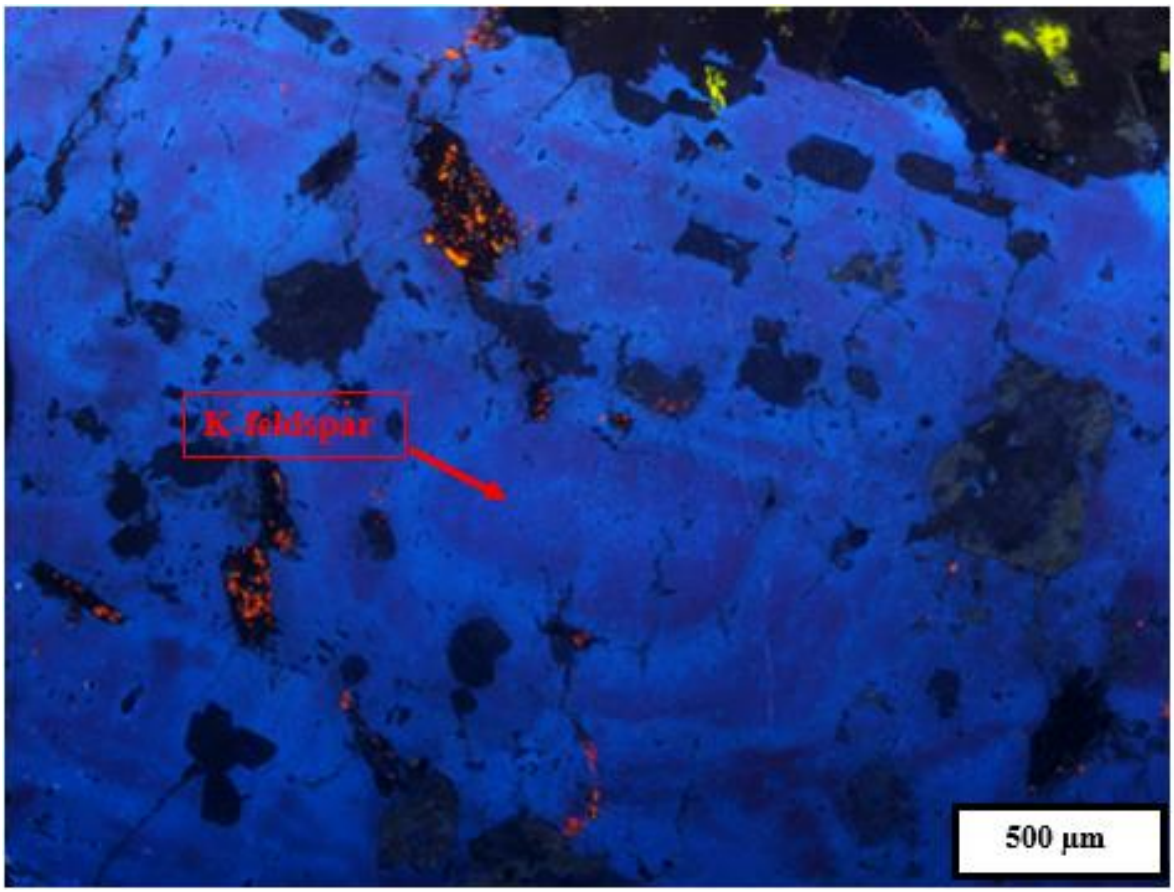

Figure 105. CL image of a coarse-grained feldspar crystal (blue) showing zonation caused by trace element/REE variations in its core. Zoning is not visible in cross polarized transmitted light. CL color variations become more patchy towards the rims of the crystal.

7.4 Summary of results

Based on the samples selected for CL imaging, the low strain samples show the least variation in CL color hues and are also the only samples to show any form of zoning, while the medium and high strain samples show a higher degree of CL color hue variation. It is possible that the variation in CL color hues is directly related to the Archean-aged hydrothermal fluid flow during regional scale transpression (and accompanying brittle-ductile deformation). If so, CL imaging clearly shows textures related to the trace element and REE incorporation into the feldspar crystal lattice that is not identifiable in traditional transmitted light microscopy, highlighting the potential to provide new insight into understanding the interactions of the hydrothermal fluid and the host granitoids.

Future work should focus on high strain and medium strain zones, for the purpose of understanding the influence of hydrothermal fluid flow on the trace element incorporation within quartz and feldspar mineral phases. CL imaging in low strain samples (such as samples taken in the center of the pluton) would be most beneficial for looking into potential magmatic zonation and other potentially preserved magmatic textures. In all cases, CL imaging should be accompanied with spectroscopy to accurately depict the cause the shift in the mineral luminescence properties. CL images can also be used as maps that clearly represent the hydrothermal fluid pathways. Using these maps alongside SEM-EDX spot analysis can provide valuable insight into the trace element incorporation associated with the fluid flow, allowing for grain-scale insight into the migration of the fluid that is not identifiable in traditional transmitted light spectroscopy.

Chapter 8: Discussion

The granitoid plutons of the Wabigoon subprovince are highly competent plutonic bodies that are more difficult to deform compared to the surrounding host greenstone belts – leading to a more cryptic deformation and alteration history. The dry nature of the granitoids coupled with the wide stability field of their main mineral constituents (quartz and feldspar) means that there is no characteristic metamorphic mineral assemblage at any of the grades of metamorphism. In addition, granitoids lack an abundance of platy minerals, meaning that they do not tend to display obvious signs of deformation such as foliation. The dry and crystalline nature of the plutons also means that the hydrothermal alteration/ metasomatism of the plutons is heavily linked to the presence of brittle fractures which would allow for the circulation of the fluid throughout the low permeability plutons. This research aimed to characterize and assess the relationship between the brittle deformation, the hydrothermal/metasomatic alteration and the ductile deformation of the granitoid plutons of the Wabigoon subprovince in order to provide insight into regional Archean tectonics and hydrothermal fluid flow. Techniques used include macrostructural analysis, microstructural analysis, petrography, SEM-EDX compositional analysis of the alteration minerals, stable isotope (δD and $\delta^{18}O$) analysis of chlorite infilled shear fractures, and cathodoluminescence imaging.

The brittle deformation of the twelve granitoid plutons studied consists of (on average) steeply dipping chlorite and/or epidote infilled shear fractures with shallowly plunging slickenlines (Chapter 4) indicative of oblique strike-slip displacement, a hallmark of transpression-related tectonics (Chetty, 2017; Storti et al., 2003). The presence of chlorite and/or epidote along the shear surfaces coupled with the conjugate strike-slip nature of some of the shear surfaces (Figure 6) means that the brittle deformation did not occur at or near Earths surface, as neither chlorite nor epidote are stable there. The wide stability field of chlorite ranges from 80°C to up to 700°C (Bourdelle, 2021), while epidote's stability field ranges from <200°C to 700°C (Apted et al., 1983; Franz and Liebscher, 2004). There is also a variability in the strikes of the shear fractures within plutons that appears more notable when studying more than one outcrop. For example, only one outcrop of the Sabaskong batholith was studied, and within this outcrop, there is a dominant north-south striking population and a north-west to south-east striking population (Figure 16b) that roughly conforms to a conjugate strike-slip population. For the seven outcrops studied from the Dryberry batholith, the shear fractures have a dominant north-west to south-east striking population, but many other non-negligible strikes are also noted (Figure 27b). This variation in

strike can be explained through the concept of non-coaxial strain in which the rigid and competent plutons themselves have undergone a component of rigid body rotation during transpression. This concept is similar to the concept of a rigid garnet porphyroblast undergoing rigid body rotation within a shear zone. Although the direction of the maximum principal stress (σ_1) remains stationary during oblique convergence (transpression), the rigid body rotation of the plutons results in a shifting trend of the maximum elongation direction (strain). Since transpression within the Wabigoon subprovince is believed to be dextral (Percival et al., 2003), the rotation of the plutons would be clockwise. However, the degree of rotation that each pluton has undergone should vary based on the size and shape of the pluton themselves. For example, the smaller and rounded plutons such as the Ottertail pluton should theoretically have a larger degree of rotation when compared to the more elongated plutons such as the Revell batholith. When looking at the stereonets for the Ottertail pluton (Figures 7 and 8), there is notable variation in the strikes of the infilled shear fractures across the two outcrops studied. This is also reflected in the rounded Dryberry batholith – the strikes of the shear fractures vary widely as seen in Figures 26 and 27. However, the Revell batholith (Figures 53 and 54) records much more consistency to the strikes of the shear fractures with a dominant north-west strike, suggesting a lesser degree of rotation for this pluton. The Indian Lake batholith also shows great consistency in the strike of the shear fractures, with a dominant south-east and south striking population conforming to a conjugate strike-slip relationship (Figure 58 and 59). This batholith is located within a larger batholithic complex in the central Wabigoon subprovince (Figure 1) which likely resulted in a lesser degree of rotation as the large batholithic complexes may be harder to rotate. Furthermore, the shape, size and location of each pluton during Archean transpression likely resulted in variations of the degree of rotation each pluton underwent, and an analysis of the shear fracture orientations can be used to provide insight into a pluton's degree of rotation. However, it's important to note that the factors controlling the rotation of rigid bodies is complex and still being studied. Zhang and Fossen (2020) note that over the past two decades, numerous studies have been completed on whether rigid clasts rotate (eg., Johnson, 2008; Johnson, 2009; Bell and Fay, 2016) and how matrix properties influence the rotational behaviour of rigid clasts in noncoaxial flow (eg., Stahr and Law, 2014; Mulchrone and Meere, 2015). This work was pioneered by Jeffrey (1922), who isolated a rigid clast immersed in an isotropic linear viscous matrix. In this model, Jeffrey (1922) concluded that the more circular clasts rotate at a constant rate of half the strain rate under simple shear. However, the elliptical clast rotations have minimum and maximum rotation rates that can be predicted at the flow-parallel and flow-normal

orientations, respectively. Based on the Jeffrey model, the degree of rotation of the Revell batholith in specific depends on its original emplacement orientation. If the Revell batholith was emplaced with a northwest-southeast orientation (as it is now), then the batholith would not have undergone a significant degree of rotation as it was oriented parallel to the northwest directed oblique compression event. However, if the Revell batholith was emplaced oblique to the northwest-southeast oblique compression, it would have undergone at least a component of rigid body rotation. Based on the consistency of the infilled shear fracture orientations collected in this work, it appears that it is most probable that the Revell batholith was emplaced in a northwest-southeast directed orientation and did not undergo a significant degree of rigid body rotation. However, more orientation data should be collected within the Revell batholith to test this hypothesis. Also of note within the brittle deformation of the plutons is the presence of a single (yet important) cataclasite documented within the White Otter Lake pluton that has a chlorite infilled matrix (Figure 65). The importance of this chlorite infilled cataclasite will be discussed later in this chapter. A high temperate ultracataclasite / potentially recrystallized pseudotachylyte (Figure 11) is also very important and will be discussed later in the chapter.

The hydrothermal/metasomatic alteration documented within the twelve granitoid plutons show remarkable consistency. Shear fractures are infilled with chlorite (Figure 19) and epidote (Figure 45) throughout all twelve plutons studied. In the wall rock adjacent to brittle shear fractures, common alteration styles include sericitization (Figure 25) and/or sausseritization (white mica + epidote ± calcite – Figure 33) of the feldspars and chloritization of biotite laths (Figure 79). Additional chlorite, epidote and minor sphene are seen along microcracks within the wall rock (chlorite along microcracks is seen in Figure 62). Minor occurrences of calcite are noted as a replacement of feldspar or associated with epidote along microfractures. Chlorite, epidote and white mica (predominately phengite) are the most common alteration minerals within the plutons. Although chlorite, epidote and phengite are all considered to be low grade metamorphic minerals, it is important to note that all three of these minerals have wide stability fields and do not inherently reflect low temperature metasomatism. The alteration of the plutons is greatest near the shear fractures and where shear fractures are concentrated, which is near the margins of the plutons where the competency contrast of the plutons and the surrounding host greenstone results in a localization of strain. Towards the centers of the plutons where brittle deformation is lowest, alteration is less notable. For example, Figure 14 shows a representative photomicrograph of the alteration seen within a low strain sample from near the margin of the Sabaskong batholith,

whereas Figure 62 shows a photomicrograph of the typical alteration documented within the White Otter Lake pluton, which is in the center of a large batholithic complex. It is noted that the marginal Sabaskong batholith sample has a much higher degree of alteration when compared to the central White Otter Lake pluton sample.

The ductile deformation of the plutons, which is used to constrain the recorded peak metamorphic conditions of the plutons, also shows remarkable consistency across all twelve plutons studied. Each pluton records solid-state deformation microstructures which include undulose extinction, subgrains and serrated grain boundaries within quartz and undulose extinction, subgrains, serrated grain boundaries, minor recrystallization and microcracks within feldspar (Figure 17). The solid-state dislocation creep textures within quartz and feldspar are most notable within shear zones and samples taken near the margins of the plutons as opposed to samples taken from outcrops located in the center of the plutons. Centrally located samples have dislocation creep textures such as undulose extinction, minor subgrains and minor serrated grain boundaries within feldspars. The presence of undulose extinction, subgrains and serrated grain boundaries within quartz and feldspars is particularly important as it confirms that dislocation creep was active in both mineral phases. Dislocation creep is a temperature dependent process that does not become effective within the crystalline lattice of feldspar until temperatures reach ~450°C (Passchier and Trouw, 2005), corresponding to the onset of amphibolite facies metamorphism. The presence of two dykes within the Taylor Lake Stock and the Sowden-Wabakimi batholithic lakes complex (Figure 67) can also be used to constrain the metamorphic conditions of the plutons. The dyke within the Taylor Lake Stock is composed of clinopyroxene + plagioclase + amphibole + apatite + biotite (Figure 32) and is interpreted to represent a mafic dyke partially metamorphosed to the amphibolite facies of metamorphism. The dike within the Sowden-Wabakimi Lakes batholithic complex is composed of amphibole + plagioclase + quartz and is interpreted to represent a mafic dyke metamorphosed to the amphibolite facies. Both dykes are consistent with the amphibolite facies temperatures inferred from deformation microstructures noted across the twelve plutons. Although both dykes are metamorphosed to the amphibolite facies, it should be noted that the metamorphic conditions recorded by the dykes only represents the metamorphic conditions after the emplacement of dykes and does not necessarily correlate to peak metamorphic conditions of the granitoid plutons in which they are hosted. The same case can also be made for the microstructures that record amphibolite facies conditions within all twelve granitoid plutons. It's possible that at least some of the plutons were emplaced in higher temperature conditions (such

as granulite facies) but either cooled past those temperatures quickly or have had their higher temperature deformation features overprinted. Furthermore, the amphibolite facies metamorphic temperatures recorded within the twelve granitoid plutons and the two dykes represent recorded peak metamorphic conditions, but do not necessarily correlate to actual peak metamorphic conditions.

Six of the plutons (Ottertail, Sabaskong, Dryberry, Irene-Eltrut, Sowden-Wabakimi and Croll Lake) record high strain zones (shear zones) that are marked by the presence of grain-size reduced quartzo-feldspathic matrix, the importance of some of the shear zones will be discussed later within this chapter. The presence of unstable zoisite within the Marmion batholith is also interesting as this zoisite could possibly be reflective of 1) an older metamorphic event not seen in the younger granitoid plutons (since the Marmion batholith is older than the other granitoid plutons) or 2) a potential magmatic zoisite.

The plutons also record evidence for both brittle and ductile deformation in the amphibolite facies of metamorphism. Evidence stems from the presence of the oblique strike-slip infilled shear fractures defining fabric within narrow shear zones in the Sabaskong batholith (Figure 18 and 19), the Ottertail pluton, the Irene-Eltrut batholithic complex and the Dryberry batholith (Figure 30). Further evidence for ongoing brittle deformation during regional amphibolite facies ductile deformation stems from the presence of ductilely deformed quartz veins within the Sabaskong batholith (Figure 21), Irene-Eltrut batholithic complex, Dryberry batholith (Figure 29), Revell batholith (Figure 55), Ottertail pluton (Figure 10) and the Croll Lake Stock (Figure 84). These ductilely deformed quartz veins can be seen boudinaged within shear zones, directly adjacent to shear zones or not associated with shear zones at all. The quartz vein themselves represents a brittle feature where opening of the wall rock perpendicular to the maximum elongation direction resulted in the precipitation of quartz within the vein. The subsequent boudinaging of the vein coupled with the formation of undulose extinction, subgrains and serrated grain boundaries provide evidence for a ductile deformation overprint to the brittle quartz vein. The Dryberry batholith has an exposed outcrop along Highway 71 that shows the presence of potential boudinaged quartz veins that appear as quartz ‘eyes’ that define the fabric of the outcrop. These features highlight the presence of brittle deformation during ductile deformation of the plutons. The Ottertail pluton is also host to an ultracataclasite/ potential psuedotachylyte unit (Figure 11), both of which are markers for high temperature brittle deformation. Furthermore, the plutons of the Wabigoon subprovince

contain structures that highlight the presence of ongoing brittle deformation during ductile deformation in the amphibolite facies of metamorphism.

The mineral compositions of the main hydrothermal/metasomatic mineral phases (chlorite, epidote and white mica) show consistency across the plutons with the exception of the chlorite. For white mica, most analyses (n=81) classify as the phengite series while three are classified as muscovite (Figure 88). White mica occurs predominately as a replacement of feldspar with minor occurrences noted along shear fractures with chlorite. Epidote has four different occurrence types including: 1) in clusters associated with biotite (Figure 24), chlorite and sphene 2) as replacements of feldspars (Figure 33), 3) as shear fracture infilling (Figure 45) and 4) within shear zones (Figure 30). All epidote analyzed (apart from one unstable zoisite occurrence in the Marmion batholith) show great consistency in their Mn%, Fe% and octahedral Al% (Figure 86) regardless of occurrence type, providing some evidence that all occurrence types and epidote alteration styles occurred during a single tectonic event. Chlorite is present as: 1) infilling shear fractures (Figure 19), 2) within microcracks (Figure 62) and 3) as a replacement of magmatic biotite (Figure 79). The mineral chemistry of the chlorite varies across the occurrence type, outcrop locations and plutons and could be a function of the mineral chemistry of the lithology the fluid was derived from, a function of the temperature of the system during fluid formation and migration, or a combination of the various factors. Overall, chlorite shows the highest degree of scatter with regards to its mineral chemistry (Figure 85). Although the chlorite shows scatter across occurrence type, outcrops and plutons, there is evidence to support localized chemical equilibrium within the oblique shear fractures based on the consistency of the mineral chemistry within individual veins as seen in the mineral chemistry of the chlorite infilled shear fractures (Figure 94).

The δD and $\delta^{18}O$ signatures of six chlorite infilled shear fractures from the Marmion batholith and Atikwa batholith record metamorphic water signatures as the source of the hydrothermal/metasomatic fluid (Figure 96). Although the chlorite samples analyzed have minor impurities (Table 8, Appendix III), each of the six veins show great consistency in the type of hydrothermal/metasomatic fluid source, highlighting the possibility that the impurities were not great enough to skew the chlorite isotopic signature. Furthermore, it is possible that the hydrothermal/metasomatic fluid is sourced from the surrounding hydrous greenstone belt during regional transpression and accompanying devolatilization reactions – which would have been ongoing during Archean regional transpression, metamorphism and exhumation. Chlorite geothermometry completed on the six chlorite infilled shear fractures suggest formation

temperatures between 277°C and 338°C (Table 10 and 11), which is lower than the peak metamorphic/deformation conditions of 450°C to 550°C. Although there is evidence to suggest that at least a component of the chlorite metasomatism/hydrothermal alteration occurred during peak metamorphism (based on the presence of chlorite infilled shear fractures within shear zones), there is also evidence to support ongoing oblique strike-slip shear fracturing into lower temperature conditions and potentially through exhumation. XRD analyses of the six chlorite shear fractures for stable isotope analysis shows the presence of the illite 2M1 polytype (Table 8, Appendix III) within two of the shear veins. However, since illite crystallinity was not completed, it is important to note that distinction between the illite 2M1 and 1D6 polytypes was not made, so although Table 8 shows the 2M1 polytype, the true polytype could be illite 1D6. Either way, the presence of illite is significant as it likely stems from the same metasomatic/hydrothermal event the chlorite formed from. The transition of smectite to illite occurs at temperatures between 25°C to 200°C while the transition from illite to muscovite occurs at temperatures between 200°C and 300°C (Merriman and Frey, 1999), quite a bit lower than the peak metamorphic temperature of around 500°C. This suggests either ongoing brittle deformation and fluid flow after the cessation of peak metamorphism (likely during exhumation) or possible reactivation and fluid flow through the shear fractures. This coupled with the presence of a chlorite infilled cataclasite documented within the White Otter Lake pluton and the chlorite geothermometry formation temperatures suggests that brittle deformation and associated hydrothermal/metasomatic alteration of the plutons continued after peak metamorphism and likely into exhumation.

Cathodoluminescence also provides valuable insight into the alteration and deformation of the plutons. CL images of the potassic feldspars taken in high strain areas show a large degree of scatter in the color hues, indicating REE or trace element incorporation into the feldspar crystal lattice (Figure 97, 98 and 99). The low strain samples show the least variation in color hues in both the potassic feldspar and plagioclase feldspars, consistent with the notion of less alteration in lower strain areas (Figure 104). CL imaging may therefore provide a fast and effective method for determining alteration styles and variations within the plutons. This technique can also be used as effective maps for studying the trace element and REE incorporation into the feldspar crystalline lattice.

Furthermore, the brittle deformation, ductile deformation, stable isotope analysis and alteration study of the twelve granitoid plutons across the Wabigoon subprovince support regional-scale Archean brittle-ductile deformation and associated hydrothermal/metasomatic alteration

associated with transpression that affected all plutons studied. Steeply dipping planar shear structures with shallowly plunging oblique strike-slip lineations are a common feature of transpressional environments and are noted in the transpressional Rosy Finch shear zone that extends through the plutons of the Mono Pass Intrusive Suite in the Sierra Nevada Magmatic Arc (Tikoff and Saint Blanquat, 1997) and the Archean-aged North Caribou Greenstone belt within the Superior Province (Gagnon et al., 2016). The variation in orientation of chlorite and/or epidote infilled shear fractures across the plutons could be the result of non-coaxial strain in which the direction of the maximum elongation direction is shifting in response to the rigid body rotation of the competent granitoid plutons during Archean transpression. This concept is the same as a garnet porphyroblast undergoing rigid body rotation within a shear zone and is in part supported by the shape of the Ottertail pluton in the western Wabigoon subprovince. Czeck et al. (2006) note that the pluton resembles a porphyroclast caught within a dextral shear zone (Figure 2). The foliation of the surrounding less competent greenstone belt is also seen to wrap around the pluton, similar to foliation wrapping around a garnet porphyroblast within a shear zone. This hypothesis of rigid body rotation of the plutons agrees with the regional tectonic framework of transpression.

The finding of transpression related structures within all plutons is important as the 2695.0 ± 3.6 Ma age for the Taylor Lake stock in the western Wabigoon subprovince has historically been used to represent the cessation of regional tectonics within the area (Davis et al., 1982). This research demonstrates that the Taylor Lake Stock was not actually emplaced post-tectonically, but rather pre- to syn-tectonically. The date of 2695.0 ± 3.6 Ma (Davis et al., 1982) should not be used to represent the cessation of Archean transpression within the Western Wabigoon subprovince.

A major take-away from this study is that the structure and alteration within the granitoid plutons points to a late Archean tectonic history of transpression.

Future work recommended for understanding the deformation and alteration of the plutons within the Wabigoon subprovince includes the following:

1. Additional U-Pb geochronology of zircon rims and cores to provide insight into deformation ages (rim analysis) and potential crystallization ages (core analysis) of the plutons.
2. $^{40}Ar/^{39}Ar$ dating of feldspars within cataclasites to constrain timing of cataclastic deformation.
3. Potential U-Pb dating of infilled epidote shear fractures to constrain timing of oblique strike-slip shear fracturing.
4. More stable isotope analysis (δD and $\delta^{18}O$) of chlorite shear fractures and chlorite-infilled cataclasites to learn more about the water-rock interactions that have occurred within the plutons

– although it is recommended that a SIMS in-situ analysis is completed once standards become available.

5. An in-depth alteration study extending outwards of individual chlorite and/or epidote infilled shear fractures including detailed SEM-EDX analysis and BSE imaging and CL imaging.

6. CL imaging along with spectroscopy to assess the incorporation of trace element and REE activators within feldspar and quartz crystal lattices. CL spectroscopy can also be used to study the lattice defects present within the luminescent mineral phases.

7. A kinematic analysis and paleomagnetic study of the plutons to assess the direction of rotation of the granitoid plutons during Archean transpression in more detail and to provide insight into the Archean transpression model.

8. The distribution of the infilled shear fractures across the pluton margins should be studied in more detail. Since Archean transpression of the Wabigoon subprovince is believed to be northwest directed, then there should theoretically be a higher degree of strain along the northwest and southeast margins of the plutons. However, since the formation of the brittle fractures could be a result of fluid pressure buildup along the competency contrast of the plutons and the host greenstone, it is also possible that the distribution of the infilled shear fractures across the margins of the plutons could be more uniform.

Chapter 9: Conclusions

The data presented from this study permits the following interpretations:

1. The brittle deformation documented within all twelve plutons studied across the Wabigoon subprovince consists of (on average) steeply dipping chlorite and/or epidote infilled shear fractures that record conjugate strike-slip relationships with sub-horizontal lineations. This is indicative of transpression, which likely had a dextral sense of displacement.
2. The shift in strikes of the shear fractures could be due to non-coaxial strain in which the rigid and competent granitoid plutons have undergone a component of rigid body rotation, resulting in the rotation of the maximum elongation direction. Since transpression is believed to have been dextral, plutons would have undergone a clockwise sense of rotation. The degree of rotation of a pluton is likely to be controlled by its size and shape.
3. Microstructural analysis conducted on all twelve plutons shows evidence for dislocation creep textures within quartz and feldspar that would indicate deformation temperatures corresponding to the onset of amphibolite facies metamorphism (>450°C). This metamorphic grade is consistent with two metamorphosed mafic dykes documented within the Sowden-Wabakimi Lakes batholithic complex and the Taylor Lake Stock (both metamorphosed to the amphibolite facies, although one is only partially metamorphosed). The twelve plutons have a *recorded* peak metamorphism condition of amphibolite facies metamorphism.
4. The presence of infilled shear fractures within shear zones coupled with ductilely deformed quartz veins supports coeval brittle-ductile deformation in the amphibolite facies of metamorphism. This lends to the finding that the plutons of the Wabigoon subprovince were emplaced pre- to syn-tectonically and have undergone Archean brittle-ductile transpression in the amphibolite facies of metamorphism.
5. The Taylor Lake stock age date of 2695.0 ± 3.6 Ma (Davis et al., 1982) should not be used to constrain the cessation of regional Archean orogenesis in the western Wabigoon subprovince.
6. Hydrothermal/metasomatic alteration mineral assemblages documented within the plutons are represented by chlorite, epidote and white mica with lesser amounts of hematite, calcite and sphene. Alteration is directly associated with the brittle fracturing and appears greatest near the margins of the plutons when compared to the center of the plutons.
7. White mica and epidote mineral analysis show great consistency across the subprovince, regardless of occurrence type. Chlorite shows scatter likely related to the composition of the host rock from which the fluid was derived and/or temperature conditions.

8. The δD_{fluid} and $\delta^{18}O_{fluid}$ values of the hydrothermal fluid calculated from measured δD and $\delta^{18}O$ values of chlorite infilled shear fractures from six samples in two plutons range from -30 to -45‰ and 5.6 to 7.1‰, respectively, recording a metamorphic water signature that likely stems from the devolatilization of the surrounding host greenstone during regional Archean metamorphism.

9. The presence of the illite 2M1 polytype associated with the chlorite infilled shear fractures, the chlorite infilled cataclasite documented in the White Otter Lake pluton and the chlorite geothermometry formation temperatures of 277°C to 338°C for six chlorite veins supports continual brittle deformation and associated alteration post peak metamorphism, likely into exhumation.

References

Allmendinger, R. W., Cardozo, N., and Fisher, D., 2012. Structural geology algorithms: Vectors and tensors in structural geology: Cambridge University Press.

Apted, M. J., and Liou, J. G., 1983. Phase relations among greenschist, epidote-amphibolite, and amphibolite in a basaltic system. American Journal of Science, 283(A), 328 – 354.

Beakhouse, G.P., 2013. Western Wabigoon Subprovince Synthesis Project; *In* Summary of Field Work and Other Activities, Ontario Geological Survey, Open File Report 6290, 5-1 – 5 7.

Beakhouse, G.P., Blackburn, C.E., Breaks, F.W., Ayer, J., Stone, D., and Stott, G.M., 1995. Precambrian ’95 western Superior Province field trip guidebook; Ontario Geological Survey, Open File Report 5924, 1-94.

Bell, T.H., and Fay, C., 2016. Holistic microstructural techniques reveal synchronous alternating andalusite and staurolite growth during three tectonic events resulted from shifting partitioning of growth vs deformation. Lithos 262. 699 – 712.

Blackburn, C.E., Johns, G.W., Ayer, J.A. and Davis, D.W., 1991. Wabigoon Subprovince; *in* Geology of Ontario, Ontario Geological Survey, Special Volume 4, Part 1, 303-382.

Borradaile, G.J., and Kehlenbeck, M.M., 1996. Possible cryptic tectono-magnetic fabrics in “post tectonic” granitoid plutons of the Canadian Shield. Earth and Planetary Science Letters, 137, 119-127.

Bourdelle, F., 2021. Low-temperature chlorite geothermometry and related recent analytical advances: a review. Minerals 11, 130.

Cathelineau, M., 1988. Cation site occupancy in chlorites and illites as a function of temperature. Clay Minerals 23, 471–485.

Card, K.D., Ciesielski, A., 1986. DNAG subdivisions of the superior province of the Canadian shield. Geoscience Canada, 13, 5-13.

Cardozo, N., and Allmendinger, R.W., 2013. Spherical projections with OSXStereonet: Computers & Geosciences, 51, 193 – 205.

Cavalcante, C., Lagoeiro, L., Fossen, H., Egydio-Silva, M., Morales, L.F.G., Ferreira, F., Conte, T., 2018. Temperature constraints on microfabric patterns in quartzofeldsphatic mylonites, Ribeira belt (SE Brazil). Journal of Structural Geology, 115, 243-262.

Chetty, T.R.K., 2017. Proterozoic Orogens of India. Elsevier, p. 1-426.

Clayton, R.N. and Mayeda, T.K., 1963. The use of Bromine Pentafluoride in the extraction of oxygen from oxides and silicates for isotopic analysis. Geochimica et Cosmochimica Acta, 27, 43-52.

Cole, D. R., and Ripley, E. M., 1998. Oxygen isotope fractionation between chlorite and water from 170 to 350C: a preliminary assessment based on partial exchange and fluid/rock experiments. Geochim Cosmochim Acta, 63 (3–4), 449.

Corfu, F., 2000. Extraction of Pb with artificially too-old ages during stepwise dissolution experiments on Archean zircon. Lithos, 53, 279–291.

Czeck, D.M., Maes, S.M., Sturm, C.L., and Fein, E.M., 2006. Assessment of the relationship between emplacement of the Algoman plutons and regional deformation in the Rainy Lake region, Ontario. Canadian Journal of Earth Sciences, 43, 1653-1671.

Davis, D.W. 1990. Geological study of the Winnipeg River-Wabigoon subprovince boundary. EMR Research Agreement No.[unpublished].

Davis, D.W., 1993. Report on U-Pb geochronology in the Atikokan area, Wabigoon Subprovince, Ontario; unpublished report of the Earth Sciences Department, Royal Ontario Museum, 100 Queen's Park, Toronto, Ontario.

Davis, D.W. 2006. Geochronology of rocks from the Marmion Terrane and Hudson Bay Lowland basement, western Superior Province, unpublished report to the Ontario Geological Survey by the Jack Satterly Geochronology Laboratory, Department of Geology, University of Toronto, Toronto, Ontario.

Davis, D. W.; Blackburn, C. E.; Krogh, T. E., 1982. Zircon U–Pb ages from the Wabigoon Manitou Lakes region, Wabigoon Subprovince, northwest Ontario. Canadian Journal of Earth Sciences, 19(2), 254–266.

Davis, D.W., and Edwards, G.R., 1982. Zircon U–Pb ages from the Kakagi Lake area, Wabigoon Subprovince, northwest Ontario. Canadian Journal of Earth Sciences, 19, 1235–1245.

Davis, D.W. and Edwards, G.R., 1986. Crustal evolution of Archean rocks in the Kakagi Lake area, Wabigoon Subprovince, Ontario, as interpreted from high-precision U–Pb geochronology; Canadian Journal of Earth Sciences, 23, 182-192.

Davis, D.W. and Jackson, M.C., 1988. Geochronology of the Lumby Lake Greenstone Belt: a 3 Ga complex within the Wabigoon Subprovince, northwest Ontario; Geological Society of America Bulletin, 100, 818-824.

Davis, D.W., Poulsen, K.H., and Kamo, S.L., 1989. New insights into Archean crustal development from geochronology in the Rainy Lake area, Superior Province, Canada Journal of Geology, 97, 379-398.

Davis, D.W., Sutcliffe, R.H., Trowell, N.F., 1988. Geochronological constraints on the tectonic evolution of a late Archean greenstone belt, Wabigoon Subprovince, northwestern Ontario, Canada Precambrian Research 39, 171–191.

Dong, Y. P., Yang, Z., Liu, X. M., Zhang, X. N., He, D. F., Li, W., Zhang, F. F., Sun, S. S., Zhang, H. F., & Zhang, G. W., 2014. Neoproterozoic amalgamation of the northern Qinling terrain to the North China Craton: Constraints from geochemistry of the Kuanping ophiolite. Precambrian Research, 255, 77– 95.

Droop, G.T.R., 1987. A general equation for estimating Fe^{3+} concentrations in ferromagnesian silicates and oxides from microprobe analyses, using stoichiometric criteria. Mineralogical Magazine, 51, 431 – 435.

Faleiros, F.M., Campanha, G.A.C., Bello, R.M.S. , Fuzikawa, K., 2010. Quartz recrystallization regimes, c-axis texture transitions and fluid inclusion reequilibration in a prograde greenschist to amphibolite facies mylonite zone (Ribeira Shear Zone, SE Brazil). Tectonophysics, 485, 193-214.

Foster, M.D., 1960. Interpretation of the composition of lithium micas. U.S. Geologic Survey Professional Paper, 354 p.

Franz, G., and Liebscher, A.. 2004. Physical and chemical properties of the epidote minerals – an introduction. Reviews in Mineralogy and Geochemistry, 56(1), 1-81.

Gagnon, E., Schneider, D., Kalbfleisch, T., Habler, G., 2016. Characterization of transpressive deformation in shear zones of the Archean North Caribou greenstone belt (NW Superior Province) and the relationship with regional metamorphism. Tectonophysics, 693.

Goldich, S.S. and Fischer, L.B. 1986, Air-abrasion experiments in U-Pb dating of zircon. Journal of Chemical Geology 58, 195-215.

Graham, C.M., Viglino, J.A., and Harmon, R.S., 1987. Experimental study of hydrogen-isotope exchange between aluminous chlorite and water and of hydrogen diffusion in chlorite. American Mineralogist. 72(5), 566-579.

Hey, M.H., 1954. A new review of the chlorites. Mineralogical Magazine, 30, 277–292.

Hoefs, J., 2015. Stable Isotope Geochemistry. Springer, Cham. 359 p.

Hunter, N.J.R., Weinberg, R.F., Wilson, C.J.L., Law, R.D., 2018. A new technique for quantifying symmetry and opening angles in quartz c-axis pole figures: Implications for interpreting the kinematic and thermal properties of rocks. Journal of Structural Geology, 112, 1-6.

Jeffrey, G.B., 1922. The motion of ellipsoidal particles immersed in a viscous fluid. Proceedings of the Royal Society of London. A102, 161-179.

Jiang, W.T., Peacor, D.R., Buseck, P.R., 1994. Chlorite geothermometry? – contamination and apparent octahedral vacancies. Clays and Clay Minerals, 42, 593–605.

Johnson, S.E., 2008. The effects of strain localisation and rigid–object kinematics. In: Bons, P.D., Koehn, D., Jessell, M.W. (Eds.), Microdynamics Simulation, Lecture Notes in Earth Sciences, 106, 247–253.

Johnson, S.E., 2009. Porphyroblast rotation and strain localization: debate settled! Geology 37, 663-666.

Kirkpatrick, J.D., and Rowe, C.D., 2013. Disappearing ink: How pseudotachylytes are lost from the rock record. Journal of Structural Geology, 52, 183-198.

Klein, E.L., Harris, C., Giret, A., and Moura, C.A.V., 2007. The Cipoeiro gold deposit, Gurupi Belt, Brazil: Geology, chlorite geochemistry, and stable isotope study. Journal of South American Earth Sciences, 23, 242-255.

Kranidiotis, P., MacLean, W.H., 1987. Systematics of chlorite alteration at the Phelps Dodge massive sulfide deposit, Matagami, Quebec. Economic Geology 82, 1898–1911.

Larti, Y., Stevenson, R., Machado, N., Breaks, F. and Gariepy, C. 1995. The generation of Late Archean leucogranite and continental collision in the western Superior Province. Western Superior Transect, second annual workshop, Lithoprobe Report, 53, 47-53.

Lin, A., 1999. Roundness of clasts in pseudotachylytes and cataclastic rocks as an indicator of frictional melting. Journal of Structural Geology 21, 473-478.

Melnyk, M., Davis, D., Cruden, A. and Stern, R.A. 2006. U-Pb ages constraining development of an Archean terrane boundary in the Lake of the Woods area, western Superior Province, Canada. Canadian Journal of Earth Sciences, 43, 967-993.

Melnyk, M.J., Scott, D., and Cruden, A.R., 1999. Structure and relative timing of deformation in the Lake of the Woods greenstone belt, western Wabigoon subprovince. *in* 1999 Western Superior Transect 5th Annual Workshop, Ottawa, Ont., Feb. 1-3, 1999. Lithoprobe

Secretariat, The University of British Columbia, Vancouver, B.C., Lithoprobe Report 70, 40-47.

Merriman, R. J., and Frey, M., 1999. Patterns of very low-grade metamorphism in metapelitic rocks. *in*: Frey, M and Robinson, D. (eds) Low-Grade Metamorphism. Blackwell Sciences Ltd., Oxford., 61-107.

Mulchrone, K.F., Meere, P.A., 2015. Shape fabric development in rigid clast populations under pure shear: the influence of no-slip versus slip boundary conditions. Tectonophysics 659, 63-69.

Nesse, W.D., 2017. Introduction to Mineralogy. Oxford University Press, 495 p.

Park, R.G., 1981. Shear-zone deformation and bulk strain in granite-greenstone terrain of the western Superior Province, Canada; Precambrian Research, 14, 31-47.

Ontario Geological Survey 2011. 1:250 000 scale bedrock geology of Ontario; Ontario Geological Survey, Miscellaneous Release – Data 126 – Revision 1.

Passchier, C.W., and Trouw R.A.J., 2005. Microtectonics. Springer, Berlin, 366 p.

Percival, J.A., McNicoll, V., Brown, J.L and Whalen., J.B., 2003. Convergent margin tectonics, central Wabigoon subprovince, Superior Province, Canada. Precambrian Research, 132, 213-244.

Percival, J.A., Sanborn-Barrie, M., Skulski, T., White, D.J., Stott, G.M., and Helmstaedt, H. 2006. Tectonic evolution of the western superior province from NATMAP and Lithoprobe studies. Canadian Journal of Earth Sciences, 43, 1085-1117.

Poulsen, K.H., 2000. Archean metallogeny of the Mine Centre – Fort Frances area. Ontario Geological Survey, Report 266.

Ribeiro, B.V., Faleiros, F.M., Campanha, G.A.C., Lagoeiro, L., Weinberg, R.F., Hunter, N.J.R., 2019. Kinematics, nature of deformation and tectonic setting of the Taxaquara Shear Zone, a major transpressional zone of the Ribeira Belt (SE Brazil). Tectonophysics, 751, 83-108.

Schiffman, P., Fridleifsson, G.O., 1991. The smectite–chlorite transition in drillhole NJ-15, Nesjavellir geothermal field, Iceland: XRD, BSE and electron microprobe investigations. Journal of Metamorphic Geology 9, 679–696.

Schwerdtner, W.M., Stone, D., Osadetz, K., Morgan, J. and Stott, G.M., 1979. Granitoid complexes and the Archean tectonic record in the southern part of northwestern Ontario; Canadian Journal of Earth Sciences, 16, 1965-1977.

Scott, D., 1999. Anisotropy of magnetic susceptibility of the Viola Lake Stock, Lake of the Woods Area, Wabigoon Subprovince, Ontario, Canada. B.Sc. Thesis, University of Toronto, Toronto, Ont.

Stahr III, D.W., and Law, R.D., 2014. Strain memory of 2D and 3D rigid inclusion populations in viscous flows – What is clast SPO telling us? Journal of Structural Geology 68, 347-363.

Stone, D., 2010. Precambrian geology of the central Wabigoon Subprovince area, northwestern Ontario; Ontario Geological Survey, Open File Report 5422.

Stone, D., Davis, D.W., Hamilton, M.A and Falcon, A. 2010. Interpretation of 2009 geochronology in the central Wabigoon subprovince and the Bending Lake areas, northwestern Ontario. In Summary of Field Work and Other Activities 2010, Ontario Geological Survey Open File Report 6260, 6260, 14-1 – 14-13.

Storti, F., Holdsworth, R.E., and Salvini, F. Intraplate strike-slip deformation belts; Geologic Society of London Special Publications, 210, 1-14.

Tappert, M.C., Rivard, B., Giles, D., Tappert, R., and Mauger, A., 2013. The mineral chemistry, near-infrared, and mid-infrared reflectance spectroscopy of phengite from the Olympic Dam IOCG deposit, South Australia: Ore Geology Reviews, 53, 26-38.

Tikoff, B., de Saint Blanquat, M., 1997.Transpressional shearing and strike-slip partitioning in the Late Cretaceous Sierra Nevada magmatic arc, California. Tectonics 16 (3), 442–459.

Tomlinson, K.Y., Davis, D.W., Stone, D, and Hart, T.R. 2001. New U-Pb and Nd geochronology from volcanic and granitoid rocks of the central Wabigoon Subprovince. Western Superior Transect, 7th annual Meeting, 80, 10-16.

Tomlinson, K.Y., Davis, D.W., Stone, D. and Hart, T.R., 2003. U-Pb age and Nd isotopic evidence for Archean terrane development and crustal recycling in the south-central Wabigoon Subprovince, Canada; Contributions to Mineralogy and Petrology, 144, 684-702.

Tomlinson, K.Y., Stott, G.M., Percival, J.A. and Stone, D., 2004. Basement terrane correlations and crustal recycling in the western Superior Province: Nd isotopic character of granitoid and felsic volcanic rocks in the Wabigoon Subprovince, N. Ontario, Canada; Precambrian Research, 132, 245-274.

Wilks, M.E. and Nisbet E., 1988. Stratigraphy of the Steep Rock Group, northwest Ontario: a major Archean unconformity and Archean stromatolites; Canadian Journal of Earth Sciences, 25, 370-391.

Wlodek A., Grochowina, A., Golebiowska, B., Pieczka, A. 2015. A phosphate-bearing pegmatite from Lutomia and its relationships to other pegmatites of the Góry Sowie Block, southwestern Poland. Journal of Geosciences, 60, 45-72.

Wu, T., Polat, A., Fire, R., Fryer, B.J., Yang, K-G. and Kusky, T. 2019. Geochemistry, Nd, Pb and Sr isotope systematics, and U-Pb zircon ages of the Neoarchean Bad Vermillion Lake greenstone belt and spatially associated granitic rocks, western Superior Province, Canada. Precambrian Research 282, 21-51.

Young Technology Inc., 2014. Georose. Edmonton, Canada.

Zang, W., and Fyfe, W.S., 1995. Chloritization of the hydrothermally altered bedrock at the Igarape´Bahia gold deposit, Caraja´s, Brazil. Mineralium Deposita 30, 30–38.

Zhang, Q., and Fossen, H. 2020. The dilemma of asymmetric porphyroclast systems and sense of shear. Journal of Structural Geology, 130, 1-11.

Appendix I
Outcrop locations

Pluton	GPS coordinates of outcrops (NAD 83)	Structural orientations measured?	Hand samples collected
Ottertail pluton	15 U 508947.02 m E 5396927.79 m N	Yes	Yes
	15 U 516557.09 m E 5399255.70 m N	No	Yes
	15 U 513108.07 m E 5398640.75 m N	Yes	Yes
Sabaskong batholith	15 U 431936.00 m E 5422224.00 m N	Yes	Yes
Dryberry batholith	15 U 425083.00 m E 5480596.00 m N	Yes	Yes
	15 U 405738.00 m E 5509323.00 m N	Yes	Yes
	15 U 404912.00 m E 5509135.00 m N	Yes	Yes
	15 U 403470.00 m E 5509211.00 m N	No	Yes
	15 U 443563.00 m E 5517357.00 m N	No	Yes
	15 U 443584.00 m E 5518060.00 m N	Yes	Yes
	15 U 445551.00 m E 5520498.00 m N	No	Yes
	15 U 445398.00 m E 5520547.00 m N	Yes	Yes
	15 U 448585.00 m E 5520489.00 m N	Yes	Yes
	15 U 464171.00 m E 5519310.00 m N	Yes	Yes
	15 U 464171.00 m E 5519310.00 m N	No	Yes
	15 U 482335.00 m E 5517701.00 m N	No	Yes
Taylor Lake Stock	15 U 526449.00 m E 5469929.00 m N	Yes	Yes
	15 U 526030.00 m E 5469294.00 m N	Yes	Yes
	15 U 525220.00 m E 5466990.00 m N	No	Yes
Atikwa batholith	15 U 511832.00 m E 5501027.00 m N	Yes	Yes

Irene-Eltrut batholithic complex	15 U 514462.00 m E 5451616.00 m N	Yes	Yes
	15 U 506913.00 m E 5446399.00 m N	No	Yes
	15 U 501408.00 m E 5438326.00 m N	Yes	Yes
Revell Batholith	15 U 563714.04 m E 5487200.07 m N	Yes	Yes
	15 U 566399.10 m E 5480751.03 m N	Yes	Yes
Indian Lake Batholith	15 U 621273. 00 m E 5499819.00 m N	Yes	Yes
	15 U 613526.00 m E 5488452.00 m N	Yes	Yes
	15 U 599604.00 m E 5477134.00 m N	Yes	Yes
	15 U 599672.00 5476197	Yes	Yes
White Otter Pluton	15 U 560337.00 m E 5436226.92 m N	Yes	Yes
Sowden-Wabakimi Batholithic complex	15 U 666910.00 m E 5442868.14 m N	Yes	Yes
	15 U 654302.00 m E 5452950.11 m N	Yes	Yes
	15 U 626712.00 m E 5458654.00 m N	Yes	Yes
	15 U 623239.00 m E 5461490.00 m N	Yes	Yes
Marmion Batholith	15 U 708711 m E 5424572 m N	Yes	Yes
Croll Lake Stock	16 U 0543184.00 m E 5514266.00 m N	Yes	Yes
	16 U 0542653.00 m E 5514217.00 m N	Yes	Yes
	16 U 0524956.00 m E 5511462.00 m N	Yes	Yes
	16 U 0542676.00 m E 5514193.00 m N	Yes	Yes
TOTAL:		31 outcrops across 12 plutons	39 outcrops across 12 plutons

Appendix II

Structural Orientations for each outcrop

Pluton	Outcrop location (NAD 83)	Infilled chlorite shear fractures strike/dip (plunge/trend)	Infilled epidote shear fractures	Infilled mix mineral shear fractures	Tensile quartz veins	Unfilled fractures	Shear zones	Foliation
Ottertail Pluton (29 structural orientations)	15 U 508947.02 m E 5396927.79 m N	220/77 273/70 146/86 (33/149) 256/62 220/76 225/79 (10/043) 152/90 (20/152) 241/72	194/80	255/68	NA	271/71 266/60 227/78 262/81 235/81 261/75 263/74 261/72	248/67	NA
	15 U 513108.07 m E 5398640.75 m N	150/83 179/90 175/67 174/88 265/75 318/79 (134/19) 175/66	079/68 (66/196)	189/74	221/90	NA	NA	NA
Sabaskong Batholith (35 structural orientations)	15 U 431936.00 m E 5422224.00 mN	277/53 254/69 126/88 311/84 310/83 139/90 056/67 316/86 108/40 110/41 294/32 093/15 003/89 002/90 177/82 010/83 184/74 131/76 (13/308)	NA	NA	194/71	059/69 071/43 099/02 072/15 062/64 060/40 129/81 169/90	023/65 200/50	NA

		106/67 (14/280) 149/87 (00/329) 178/62 (22/346) 121/80 (08/300) 120/72 (10/297) 009/89 (10/009)						
Dryberry Batholith (87 structural orientations)	15 U 425083.00 m E 5480596.00 m N	NA	074/82	NA	084/87 305/22	085/84 283/31 115/80 074/90 074/90 074/90 324/72 324/72 329/75 331/73 085/90 083/89 089/81 082/85 076/85 079/90 009/54 009/54 009/54 009/54 009/54 009/54	NA	084/87
	15 U 405738.00 m E 5509323.00 m N	011/76 252/52 266/76 055/61 233/89 291/62 252/58 259/80 258/86	160/40 314/78 106/80	NA	NA	NA	145/43	NA
	15 U 404912.00 m E	144/42	159/90 141/50	NA	NA	NA	NA	NA

	5509135.00 m N		135/42 156/86 156/86 156/86 156/86 156/86 156/86 156/86 156/86 156/86					
	15 U 443584.00 m E 5518060.00 m N	NA	NA	NA	NA	329/81 315/87 011/88	NA	NA
	15 U 445398.00 m E 5520547.00 m N	343/81 (13/345) 339/72 (19/345) 341/69 (17/348) 337/73 (27/346) 339/66 (24/350) 338/69 (18/345) 341/70 (16/347) 003/86 003/86 332/64 344/76 096/76	NA	001/65 (11/006) 078/70	NA	082/74	NA	NA
	15 U 448585.00 m E 5520489.00 m N	188/62 (25/354) 183/70 (24/354)	NA	NA	NA	NA	NA	NA
	15 U 464171.00 m E 5519310.00 m N	204/90 120/90 124/90 126/82 188/90 200/88 132/79 130/85	NA	NA	NA	NA	NA	NA

		140/76 115/74 179/90 117/88 205/77 146/80						
Taylor Lake Stock (11 structural orientations)	15 U 526449.00 m E 5469929.00 m N	034/83 (09/035) 169/87 (06/169) 163/88 (04/342)	074/46	039/80 176/89 (04/176) 079/47 (14/092)	NA	NA	NA	NA
	15 U 526030.00 m E 5469294.00 m N	339/75 (06/341) 158/75 (16/334) 148/80 (45/158)	NA	149/77	NA	NA	NA	NA
Atikwa Batholith (29 structural orientations)	15 U 511832.00 m E 5501027.00 m N	349/55 012/75 326/59 354/74 004/78 004/78 004/78 003/46 354/56 (03/172) 322/70 (08/325)	NA	000/51	140/60 328/59	281/86 322/72 269/62 002/86 270/11 004/84 322/44 322/44 355/89 355/89 355/89 355/89 355/89 355/89 230/86	000/45	NA
Irene-Eltrut batholithic complex (13 structural orientations)	15 U 514462.00 m E 5451616.00 m N	NA	026/72 045/46 355/61 331/53 003/56 (15/013) 356/60 (10/002)	044/67 (22/054)	NA	NA	NA	NA
	15 U 501408.00 m E 5438326.00 m N	024/80 (19/027)	NA	214/58 (19/021) 024/74 282/74	NA	NA	325/80 124/74	NA

Revell Batholith (42 structural orientations)	15 U 563714.04 m E 5487200.07 m N	321/90 318/85 318/76 320/77 311/88 131/74 038/88 334/79	NA	102/64 328/71	NA	325/65 282/83 261/88 311/86 260/87 263/88 318/68 291/10 331/81 328/86 331/74 297/16	NA	NA
	15 U 566399.10 m E 5480751.03 m N	316/89 043/77 325/79 005/81 314/83 (10/315) 305/84 (08/306)	NA	NA	NA	312/83 348/03 165/71 311/84 005/05 308/82 132/90 146/86 185/13 319/88 314/81 312/75 144/69 324/81	NA	NA
Indian Lake Batholith (58 structural orientations)	15 U 621273. 00 m E 5499819.00 m N	132/69 149/58 153/79 136/82 139/80 129/72 148/75 135/63 140/75 170/85 (04/170) 139/67 (03/140) 131/81 (04/132) 141/66 (07/144)	NA	NA	NA	144/64 173/73 121/88 322/80 129/72 149/66 278/21 321/21 329/28	NA	NA

		145/65 (06/148) 196/76 (01/196) 139/78 (01/139) 144/72 (01/144) 132/67 (15/138)						
	15 U 613526.00 m E 5488452.00 m N	131/66	NA	NA	NA	139/77 137/77 314/86 302/86 289/86 322/88 320/88 214/89 146/86 141/89 144/86 138/85 121/65	NA	NA
	15 U 599604.00 m E 5477134.00 m N					275/88 350/88 014/30 358/81		
	15 U 599672.00 m E 5476197.00	168/80	NA	NA	NA	184/88 006/83 180/83 010/89 185/81 168/74 324/41 008/90 005/90 002/89 174/76 004/74	NA	NA
White Otter Lake (17 structural orientations)	15 U 560337.00 m E 5436226.92 m N	NA	NA	253/89 058/90 310/89 289/88 296/90	NA	090/88 247/87 066/90 094/89 271/87	NA	NA

				270/88 183/71 284/77 126/82 135/90 (12/135)		081/90 086/90		
Sowden Wabakimi Lakes Batholithic Complex (44 structural orientations)	15 U 666910.00 m E 5442868.14 m N	074/78 031/54 061/61 014/76 032/85 210/83 035/82 009/86 041/56 047/55	NA	NA	NA	178/60 243/82 076/84 073/83 187/79 142/85 285/85 041/90 032/90 034/83 274/81 068/46 042/53 037/59 008/62	NA	NA
	15 U 654302.00 m E 5452950.11 m N	316/81 312/85 095/65	NA	NA	NA	094/75 314/83 314/81 314/81 316/81	195/71	NA
	15 U 626712.00 m E 5458654.00 m N	122/83	NA	NA	NA	NA	NA	065/49
	15 U 623239.00 m E 5461490.00 m N	324/74 132/86 009/85 (21/011) 005/66 (10/010)	NA	NA	NA	120/80 117/87 143/85	NA	282/81
Marmion Batholith (9 structural orientations)	15 U 708711 m E 5424572 m N	068/65 258/84 152/69 054/84 (21/231)	NA	054/39 080/36	NA	052/68 109/67	NA	173/72
	16 U 0543184.00 m E	NA	NA	NA	152/50	NA	NA	NA

Croll Lake Stock (54 structural orientations)	5514266.00 m N							
	16 U 0542653.00 m E 5514217.00 m N	139/85 164/65 306/75 040/74 042/73 041/74 043/75 040/74 041/73	NA	040/74 317/45	NA	NA	NA	NA
	16 U 0524956.00 m E 5511462.00 m N	121/85 032/82 128/50	NA	180/63 160/66 128/50	183/61 133/80 102/74	046/77 047/76 045/75 048/77 046/77 045/78	NA	NA
	16 U 0542676.00 m E 5514193.00 m N	018/79 019/80 005/72 006/73 325/20 010/24 191/72 192/72 065/59 067/58 066/60 065/59 035/60	NA	030/20	170/46 044/70 064/59 063/60	032/41 033/41 002/70 324/21 029/85 026/66 040/82 295/60 306/53	NA	NA

Appendix III

SEM-EDX point analyses (raw data)

BD-20-07A Ottertail Pluton										
Mineral Phase	**Biotite**	**Biotite**	**Biotite**	**Biotite**	**Biotite**	**Biotite**	**Biotite**	**Biotite**	**Epidote**	**Epidote**
SiO_2	37.77	38.80	38.83	37.35	38.14	38.51	38.28	38.34	37.02	36.87
Al_2O_3	14.22	14.44	14.31	13.82	14.37	14.45	14.52	13.73	21.55	23.43
TiO_2	0.86	0.92	0.86	0.93	1.01	1.03	0.99	0.88	-	-
FeO	15.89	16.25	16.76	15.99	16.62	16.85	17.29	16.53	13.75	11.15
MnO	0.32	0.28	0.34	0.36	0.34	0.33	0.37	0.34	0.34	0.59
CaO	-	-	-	-	-	-	-	-	23.05	22.30
MgO	14.41	14.72	14.44	13.85	14.63	14.64	14.77	14.71	-	-
Na_2O	-	-	-	-	-	-	-	-	-	-
K_2O	10.54	10.60	10.40	10.44	10.44	10.59	10.18	10.83	-	-
P_2O_5	-	-	-	-	-	-	-	-	-	-
BaO	-	-	-	-	-	-	-	-	-	-
Total	94.01	96.00	95.93	92.73	95.33	96.41	96.39	95.36	95.71	94.34
Cation Sum	4.33	4.32	4.31	4.32	4.33	4.33	4.32	4.34	3.99	3.96

BD-20-07A Ottertail Pluton										
Mineral Phase	**Epidote**	**Epidote**	**Epidote**	**Sphene**	**Sphene**	**Sphene**	**Kspar**	**Kspar**	**Kspar**	**Kspar**
SiO_2	38.36	37.23	37.67	29.57	29.00	29.85	64.61	65.25	64.87	64.91
Al_2O_3	22.72	22.31	22.44	1.42	1.28	1.28	18.47	18.05	18.42	18.22
TiO_2	-	-	-	37.20	36.33	37.93	-	-	-	-
FeO	13.32	13.33	13.15	1.49	1.95	2.12	-	-	-	-
MnO	0.27	-	-	-	-	-	-	-	-	-
CaO	23.70	23.24	23.60	27.60	26.70	27.74	-	-	-	-
MgO	-	-	-	-	-	-	-	-	-	-
Na_2O	-	-	-	-	-	-	0.40	0.24	0.27	0.58
K_2O	-	-	-	-	-	-	17.29	17.56	17.39	17.13
P_2O_5	-	-	-	-	-	-	-	-	-	-
BaO	-	-	-	-	-	-	-	-	-	-
Total	98.38	96.11	96.86	97.28	95.26	98.92	100.78	101.09	100.95	100.83
Cation Sum	3.98	3.98	3.98	3.64	3.64	3.64	3.78	3.78	3.78	3.78

BD-20-07A Ottertail Pluton										
Mineral Phase	**Kspar**	**Kspar**	**Kspar**	**Kspar**	**Kspar**	**Kspar**	**Kspar**	**Plagioclase**	**Plagioclase**	**Plagioclase**
SiO_2	64.59	63.80	63.80	61.94	65.13	64.44	63.24	66.89	67.26	67.21
Al_2O_3	18.78	18.42	18.25	17.57	18.33	18.55	18.31	19.73	19.57	19.53
TiO_2	-	-	-	-	-	-	-	-	-	-
FeO	-	-	-	-	-	-	-	-	-	-
MnO	-	-	-	-	-	-	-	-	-	-
CaO	-	-	-	-	-	-	-	0.48	0.62	0.48
MgO	-	-	-	-	-	-	-	-	-	-
Na_2O	0.40	-	-	-	-	0.59	0.59	11.15	11.44	11.61
K_2O	17.41	-	17.45	16.65	17.69	16.48	16.53	-	-	-
P_2O_5	-	-	-	-	-	-	-	-	-	-
BaO	-	0.95	-	-	-	0.92	1.01	-	-	-
Total	101.20	100.47	99.51	96.16	101.15	100.98	99.69	98.26	98.89	98.84
Cation Sum	3.79	3.78	3.77	3.76	3.77	3.77	3.78	3.74	3.75	3.76

BD-20-07A Ottertail Pluton										
Mineral Phase	**Plagioclase**	**Plagioclase**	**Plagioclase**	**Quartz**						
SiO_2	66.53	66.71	66.56	101.33						
Al_2O_3	19.90	19.89	19.23	-						
TiO_2	-	-	-	-						
FeO	-	-	-	-						
MnO	-	-	-	-						
CaO	0.86	0.86	0.41	-						
MgO	-	-	-	-						
Na_2O	11.25	11.25	11.13	-						
K_2O	-	-	-	-						
P_2O_5	-	-	-	-						
BaO	-	-	-	-						
Total	98.55	98.71	97.33	101.33						
Cation Sum	3.76	3.75	3.74	3.00						

BD-20-10A Ottertail Pluton										
Mineral Phase	**Epidote**	**Epidote**	**Epidote**	**Epidote**	**Epidote**	**Muscovite**	**Apatite**	**Kspar**	**Kspar**	**Kspar**
SiO_2	37.41	36.32	36.73	36.36	37.05	77.71	2.53	64.06	62.64	66.03
Al_2O_3	22.65	22.93	21.74	22.67	22.40	11.63	1.15	18.11	18.28	19.42
TiO_2	-	-	-	-	-	-	-	-	-	-
FeO	11.64	11.80	13.16	12.05	12.96	0.68	1.64	-	0.69	0.35
MnO	-	0.32	0.31	-	0.36	-	-	-	-	-
CaO	23.02	22.48	22.08	22.87	22.83	-	51.88	-	-	-
MgO	-	-	-	-	-	0.41	1.46	-	0.32	-
Na_2O	-	-	-	-	-	-	-	-	1.49	8.09
K_2O	-	-	-	-	-	10.02	-	17.26	14.63	6.84
P_2O_5	-	-	-	-	-	-	39.07	-	-	-
BaO	-	-	-	-	-	-	-	-	-	-
Total	94.72	93.85	94.02	93.96	95.60	100.46	97.73	99.42	98.05	100.73
Cation Sum	3.96	3.97	3.98	3.98	3.98	3.44	3.53	3.77	3.78	3.81

BD-20-10A Ottertail Pluton										
Mineral phase	**Kspar**	**Kspar**	**Kspar**	**Plagioclase**	**Plagioclase**	**Plagioclase**	**Plagioclase**	**Quartz**	**Quartz**	**Quartz**
SiO_2	63.08	63.87	60.64	65.09	63.21	67.04	67.44	101.26	100.37	101.27
Al_2O_3	18.70	18.54	18.42	18.13	17.90	19.77	19.93	-	-	-
TiO_2	-	-	-	-	-	-	-	-	-	-
FeO	-	0.39	3.04	-	-	-	-	-	-	-
MnO	-	-	-	-	-	-	-	-	-	-
CaO	-	-	-	-	-	0.62	0.67	-	-	-
MgO	-	-	1.73	-	-	-	-	-	-	-
Na_2O	-	0.35	1.06	0.27	0.27	11.20	11.06	-	-	-
K_2O	16.60	16.72	14.26	17.06	17.08	0.16	-	-	-	-
P_2O_5	-	-	-	-	-	-	-	-	-	-
BaO	2.45	0.66	-	-	-	-	-	-	-	-
Total	100.82	100.52	99.14	100.55	98.46	98.79	99.11	101.26	100.37	101.27
Cation Sum	3.77	3.78	3.82	3.76	3.78	3.75	3.74	3.00	3.00	3.00

BD-20-10B Ottertail Pluton										
Mineral Phase	**Muscovite**	**Muscovite**	**Muscovite**	**Biotite**	**Epidote**	**Epidote**	**Kspar**	**Quartz**	**Quartz**	
SiO_2	45.75	45.79	47.78	39.48	37.57	36.77	64.46	102.33	101.12	
Al_2O_3	27.27	28.21	29.00	14.23	22.47	22.08	18.55	-	-	
TiO_2	0.72	0.52	0.62	0.78	-	-	-	-	-	
FeO	5.36	5.50	5.18	15.98	12.39	13.12	-	-	-	
MnO	-	-	-	0.30	-	-	-	-	-	
CaO	-	-	-	-	22.22	22.78	-	-	-	
MgO	2.22	1.88	2.18	14.75	-	-	-	-	-	
Na_2O	-	-	-	-	-	-	0.31	-	-	
K_2O	11.38	11.61	11.68	10.57	0.48	-	16.94	-	-	
P_2O_5	-	-	-	-	-	-	-	-	-	
BaO	-	-	-	-	-	-	0.74	-	-	
Total	92.70	93.52	96.44	96.09	95.13	94.76	101.01	102.33	101.12	
Cation Sum	5.17	5.18	5.16	5.74	5.29	5.31	5.03	4.00	4.00	

BD-WB-18 Sabaskong Batholith brittle-ductile shear zone										
Mineral Phase	**Chlorite**	**Muscovite**	**Muscovite**	**Muscovite**	**Muscovite**	**Epidote**	**Epidote**	**Epidote**	**Apatite**	**Plagioclase**
SiO_2	27.28	45.24	45.62	44.36	46.33	37.73	37.36	37.48	0.78	66.43
Al_2O_3	19.53	30.12	29.21	28.88	29.16	23.56	23.46	24.04	-	20.95
TiO_2	-	0.67	0.85	0.39	-	-	-	-	-	-
FeO	21.23	4.33	4.33	3.60	3.62	11.19	11.12	10.71	-	-
MnO	-	-	-	-	-	-	-	-	-	-
CaO	-	-	-	-	-	22.82	22.84	22.69	48.95	1.74
MgO	15.29	1.76	1.84	1.56	1.79	-	-	-	-	-
Na_2O	-	-	-	-	-	-	-	-	-	10.78
K_2O	-	11.26	10.98	10.84	11.05	-	-	-	-	-
P_2O_5	-	-	-	-	-	-	-	-	40.22	-
BaO	-	-	-	-	-	-	-	-	-	-
Total	83.32	93.39	92.83	89.63	91.95	95.26	94.79	94.91	89.96	99.91
Cation Sum	2.80	2.58	2.57	2.56	2.56	2.63	2.63	2.63	2.21	2.50

BD-WB-18 Sabaskong Batholith brittle-ductile shear zone										
Mineral Phase	**Quartz**	**Quartz**	**Quartz**	**Quartz**						
SiO_2	100.49	99.75	99.52	95.12						
Al_2O_3	-	-	-	-						
TiO_2	-	-	-	-						
FeO	-	-	-	-						
MnO	-	-	-	-						
CaO	-	-	-	-						
MgO	-	-	-	-						
Na_2O	-	-	-	-						
K_2O	-	-	-	-						
P_2O_5	-	-	-	-						
BaO	-	-	-	-						
Total	100.49	99.75	99.52	95.12						
Cation Sum	2.00	2.00	2.00	2.00						

BD-WB-19 Sabaskong Batholith ductile shear zone										
Mineral Phase	**Chlorite**	**Chlorite**	**Chlorite**	**Chlorite**	**Muscovite**	**Muscovite**	**Muscovite**	**Biotite**	**Biotite**	**Epidote**
SiO_2	25.75	25.75	26.26	25.03	44.30	45.21	46.40	35.14	36.18	37.29
Al_2O_3	20.52	20.66	21.56	19.69	28.92	28.94	30.01	16.34	16.69	23.87
TiO_2	-	-	-	-	0.92	0.79	-	1.83	1.54	-
FeO	26.21	26.11	22.81	25.44	4.68	4.89	3.97	19.44	20.01	11.65
MnO	-	-	0.25	0.45	-	-	-	-	-	0.32
CaO	-	-	-	-	-	-	-	-	-	23.46
MgO	14.90	15.04	15.21	14.64	1.81	1.93	2.09	9.92	10.32	-
Na_2O	-	-	-	-	-	-	0.26	-	-	-
K_2O	-	-	-	-	11.10	11.19	11.52	10.06	10.41	-
P_2O_5	-	-	-	-	-	-	-	-	-	-
BaO	-	-	-	-	-	-	-	-	-	-
Total	87.37	87.57	86.09	85.22	91.71	92.95	94.24	92.73	95.16	96.58
Cation Sum	2.85	2.85	2.82	2.86	2.58	2.58	2.59	2.86	2.87	2.65

BD-WB-19 Sabaskong Batholith ductile shear zone										
Mineral Phase	**Plagioclase**	**Plagioclase**	**Apatite**	**Quartz**	**Quartz**					
SiO_2	65.54	64.10	-	101.26	101.47					
Al_2O_3	20.43	21.80	-	-	-					
TiO_2	-	-	-	-	-					
FeO	0.58	-	-	-	-					
MnO	-	-	-	-	-					
CaO	1.50	3.34	55.98	-	-					
MgO	-	-	-	-	-					
Na_2O	10.58	10.06	-	-	-					
K_2O	-	-	-	-	-					
P_2O_5	-	-	42.18	-	-					
BaO	-	-	-	-	-					
Total	98.63	99.30	98.17	101.26	101.47					
Cation Sum	2.50	2.51	2.41	2.00	2.00					

BD-WB-21 Dryberry Batholith										
Mineral Phase	**Chlorite**	**Chlorite**	**Muscovite**	**Muscovite**	**Muscovite**	**Epidote**	**Epidote**	**Sphene**	**Kspar**	**Kspar**
SiO_2	26.45	25.60	44.49	46.32	48.20	38.27	38.83	30.70	64.85	65.12
Al_2O_3	20.71	19.80	28.47	29.29	29.31	24.44	24.94	4.12	18.36	18.12
TiO_2	-	-	-	-	-	-	-	33.50	-	-
FeO	31.54	31.26	4.48	4.16	3.96	10.47	10.95	1.46	-	-
MnO	0.34	0.44	-	-	-	-	-	-	-	-
CaO	-	-	-	-	-	23.61	24.18	29.18	-	-
MgO	12.01	11.28	1.66	1.53	2.20	-	-	-	-	-
Na_2O	-	-	-	-	-	-	-	-	-	-
K_2O	-	-	10.98	11.60	11.70	-	-	-	16.91	17.04
P_2O_5	-	-	-	-	-	-	-	-	-	-
BaO	-	-	-	-	-	-	-	-	-	-
Total	91.04	88.38	90.08	92.91	95.37	96.79	98.91	98.92	100.12	100.28
Cation Sum	5.69	5.70	5.15	5.15	5.14	5.26	5.27	4.92	5.00	5.00

BD-WB-21 Dryberry Batholith										
Mineral Phase	**Kspar**	**Kspar**	**Kspar**	**Quartz**	**Quartz**	**Quartz**	**Quartz**			
SiO_2	65.57	66.31	62.16	102.19	103.14	102.28	103.59			
Al_2O_3	18.33	18.61	17.76	-	-	-	-			
TiO_2	-	-	1.31	-	-	-	-			
FeO	-	-	-	-	-	-	-			
MnO	-	-	-	-	-	-	-			
CaO	-	-	1.35	-	-	-	-			
MgO	-	-	-	-	-	-	-			
Na_2O	-	0.24	1.18	-	-	-	-			
K_2O	17.27	17.86	14.26	-	-	-	-			
P_2O_5	-	-	-	-	-	-	-			
BaO	-	-	-	-	-	-	-			
Total	101.17	103.02	98.02	102.19	103.14	102.28	103.59			
Cation Sum	5.00	5.04	5.01	3.00	3.00	3.00	3.00			

BD-CL-01 – Croll Lake Stock										
Mineral Phase	**Chlorite**	**Chlorite**	**Muscovite**	**Muscovite**	**Muscovite**	**Epidote**	**Epidote**	**Epidote**	**Calcite**	**Calcite**
SiO_2	26.90	29.88	46.39	46.11	44.95	38.51	37.27	37.44	-	-
Al_2O_3	19.41	17.41	29.71	32.69	29.49	25.63	20.32	22.06	-	-
TiO_2	-	-	-	-	0.40	-	-	-	-	-
FeO	21.03	18.73	3.89	2.75	4.99	9.55	15.18	14.10	-	-
MnO	0.35	0.37	-	-	-	-	-	-	0.39	0.53
CaO	-	-	-	-	-	24.12	23.41	23.85	53.29	53.27
MgO	17.49	20.13	1.95	0.46	1.48	-	-	-	-	-
Na_2O	-	-	-	-	-	-	-	-	-	-
K_2O	-	0.28	11.91	11.55	11.56	-	-	-	-	-
P_2O_5	-	-	-	-	-	-	-	-	-	-
BaO	-	-	-	-	-	-	-	-	-	-
Total	85.17	86.80	93.84	93.56	92.88	97.83	96.17	97.45	53.69	53.80
Cation Sum	4.26	4.25	3.88	3.83	3.88	3.94	4.01	4.00	6.00	6.00

BD-CL-01 – Croll Lake Stock										
Mineral Phase	**Calcite**	**Calcite**	**Apatite**	**Kspar**	**Kspar**	**Kspar**	**Plagioclase**	**Plagioclase**	**Plagioclase**	**Plagioclase**
SiO_2	-	-	-	64.75	64.22	63.96	67.31	68.26	67.35	67.55
Al_2O_3	-	-	-	18.76	18.31	18.62	19.65	19.97	20.25	19.57
TiO_2	-	-	-	-	-	-	-	-	-	-
FeO	-	-	-	-	-	-	-	-	-	-
MnO	-	0.30	-	-	-	-	-	-	-	-
CaO	53.02	53.80	57.43	-	-	-	0.64	0.72	1.11	0.48
MgO	-	-	-	-	-	-	-	-	-	-
Na_2O	-	-	-	0.42	0.37	0.45	11.18	11.38	11.18	11.41
K_2O	-	-	-	17.01	17.18	16.68	-	-	-	-
P_2O_5	-	-	42.81	-	-	-	-	-	-	-
BaO	-	-	-	-	-	0.95	-	-	-	-
Total	53.02	54.10	100.24	100.94	100.08	100.65	98.78	100.34	99.89	99.00
Cation Sum	6.00	6.00	3.61	3.78	3.78	3.78	3.74	3.75	3.75	3.75

BD-CL-01 – Croll Lake Stock										
Mineral Phase	**Plagioclase**	**Plagioclase**								
SiO_2	64.70	68.10								
Al_2O_3	18.79	19.40								
TiO_2	-	-								
FeO	-	-								
MnO	-	-								
CaO	0.23	0.45								
MgO	-	-								
Na_2O	11.94	11.22								
K_2O	-	-								
P_2O_5	-	-								
BaO	-	-								
Total	95.66	99.16								
Cation Sum	3.79	3.73								

BD-CL-02 – Croll Lake Stock										
Mineral Phase	**Chlorite**	**Chlorite**	**Chlorite**	**Biotite**	**Muscovite**	**Epidote**	**Epidote**	**Epidote**	**Sphene**	**Sphene**
SiO_2	27.08	27.84	27.11	36.57	46.84	37.31	37.24	37.53	30.03	30.12
Al_2O_3	19.89	17.20	16.89	16.60	28.44	23.98	23.35	23.69	1.38	1.40
TiO_2	-	-	-	1.77	0.27	-	-	-	38.53	38.26
FeO	21.14	20.49	28.67	17.31	4.42	11.10	11.95	11.54	0.75	0.81
MnO	0.39	0.31	0.43	-	-	-	-	-	-	-
CaO	-	-	-	-	-	23.72	23.78	23.72	28.53	28.36
MgO	18.23	18.68	13.80	12.49	2.05	-	-	-	-	-
Na_2O	-	-	-	-	-	-	-	-	-	-
K_2O	-	-	-	10.26	11.62	-	-	-	-	-
P_2O_5	-	-	-	-	-	-	-	-	-	-
BaO	-	-	-	-	-	-	-	-	-	-
Total	86.73	84.51	86.90	94.99	93.64	96.11	96.33	96.48	99.32	98.94
Cation Sum	15.65	5.69	5.70	5.73	5.15	5.29	5.30	5.29	4.85	4.84

BD-CL-02 – Croll Lake Stock										
Mineral Phase	**Plagioclase**	**Plagioclase**								
SiO_2	67.13	66.72								
Al_2O_3	20.21	20.14								
TiO_2	-	-								
FeO	-	-								
MnO	-	-								
CaO	0.89	0.98								
MgO	-	-								
Na_2O	11.21	10.94								
K_2O	-	-								
P_2O_5	-	-								
BaO	-	-								
Total	99.45	98.79								
Cation Sum	5.00	4.99								

BD-CL-03 – Croll Lake Stock										
Mineral Phase	**Chlorite**	**Chlorite**	**Chlorite**	**Chlorite**	**Biotite**	**Epidote**	**Epidote**	**Epidote**	**Epidote**	**Epidote**
SiO_2	27.00	27.89	26.54	27.38	36.61	37.51	37.80	37.38	37.45	37.88
Al_2O_3	21.41	18.83	19.64	18.23	15.74	23.72	24.22	23.84	24.01	23.93
TiO_2	-	-	-	-	1.94	-	-	-	-	-
FeO	19.86	20.79	23.59	22.72	17.87	10.95	11.34	11.14	10.60	10.97
MnO	-	-	0.45	-	-	-	-	-	-	-
CaO	2.93	-	-	-	-	24.02	23.94	23.81	23.80	23.41
MgO	17.08	19.18	16.25	18.14	11.97	-	-	-	-	-
Na_2O	-	-	-	-	-	-	-	-	-	-
K_2O	-	-	-	-	10.30	-	-	-	-	-
P_2O_5	-	-	-	-	-	-	-	-	-	-
BaO	-	-	-	-	-	-	-	-	-	-
Total	88.29	86.68	86.47	86.48	94.43	96.20	97.30	96.16	95.86	96.19
Cation Sum	4.27	4.27	4.27	4.28	4.29	3.97	3.97	3.97	3.96	3.95

BD-CL-03 – Croll Lake Stock										
Mineral Phase	**Sphene**	**Sphene**	**Kspar**	**Plagioclase**	**Plagioclase**	**Plagioclase**	**Plagioclase**	**Quartz**	**Quartz**	**Quartz**
SiO_2	30.61	31.20	64.53	68.06	67.72	57.61	57.78	101.46	101.77	101.43
Al_2O_3	1.05	1.53	18.50	19.21	20.44	26.81	26.41	-	-	-
TiO_2	40.88	37.94	-	-	-	-	-	-	-	-
FeO	0.51	1.63	-	0.30	-	-	-	-	-	-
MnO	-	-	-	-	-	-	-	-	-	-
CaO	29.18	28.65	-	0.19	0.80	8.70	8.51	-	-	-
MgO	-	-	-	-	-	-	-	-	-	-
Na_2O	-	-	0.30	11.32	11.23	6.74	6.64	-	-	-
K_2O	-	-	17.11	-	-	-	-	-	-	-
P_2O_5	-	-	-	-	-	-	-	-	-	-
BaO	-	-	-	-	-	-	-	-	-	-
Total	102.23	100.95	100.44	99.07	100.18	99.87	99.34	101.46	101.77	101.43
Cation Sum	3.62	3.64	3.77	3.74	3.75	3.75	3.74	3.00	3.00	3.00

BD-DL-04B Hammond Reef Marmion Batholith										
Mineral Phase	**Chlorite**	**Chlorite**	**Chlorite**	**Chlorite**	**Chlorite**	**Chlorite**	**Chlorite**	**Chlorite**	**Chlorite**	**Muscovite**
SiO_2	23.31	24.01	23.34	22.69	21.94	23.35	22.70	24.21	23.9	43.51
Al_2O_3	21.43	21.9	21.71	20.83	19.56	20.82	20.59	19.69	20.52	31.47
TiO_2	-	-	-	-	-	-	-	0.4	-	-
FeO	35.82	36.28	37.04	36.22	36.17	35.91	36.03	35.22	36.16	2.96
MnO	-	0.3	0.26	-	-	-	-	-	-	-
CaO	-	-	-	-	-	-	-	-	-	-
MgO	7.63	7.82	7.41	7.04	6.79	7.28	7.23	8.34	7.61	0.61
Na_2O	-	-	-	-	-	-	-	-	-	-
K_2O	-	-	-	-	-	-	-	-	-	11.26
P_2O_5	-	-	-	-	-	-	-	-	-	-
BaO	-	-	-	-	-	-	-	-	-	-
Total	88.19	90.31	89.76	86.78	84.46	87.35	86.56	87.86	88.19	89.91
Cation Sum	4.29	4.28	4.30	4.29	4.31	4.28	4.30	4.28	4.28	3.85

BD-DL-04B Hammond Reef Marmion Batholith										
Mineral Phase	**Muscovite**	**Muscovite**	**Muscovite**	**Muscovite**	**Muscovite**	**Calcite**	**Calcite**	**Plagioclase**	**Plagioclase**	**Plagioclase**
SiO_2	44.54	45.09	47.86	46.82	44.06	-	-	66.81	67.23	66.51
Al_2O_3	32.5	32.79	33.78	34.58	34.13	-	-	19.64	19.73	19.51
TiO_2	0.32	-	0.32	0.28	-	-	-	-	-	-
FeO	2.88	3.14	3.17	1.98	1.72	2.17	1.94	-	-	-
MnO	-	-	-	-	-	1.11	1.08	-	-	-
CaO	-	-	-	-	-	47.97	48.82	0.72	0.45	0.62
MgO	0.56	0.74	0.81	0.5	0.21	0.44	0.41	-	-	-
Na_2O	-	-	-	0.96	0.6	-	-	11.53	11.48	11.21
K_2O	11.11	11.60	11.61	10.84	10.85	-	-	-	-	-
P_2O_5	-	-	-	-	-	-	-	-	-	-
BaO	-	0.68	-	-	-	-	-	-	-	-
Total	91.92	94.04	97.54	95.97	91.57	51.69	52.25	98.69	98.89	97.86
Cation Sum	3.83	3.86	3.82	3.84	3.84	6.00	6.00	3.76	3.75	3.75

BD-DL-04B Hammond Reef Marmion Batholith										
Mineral Phase	**Quartz**	**Quartz**	**Quartz**	**Quartz**	**Quartz**	**Quartz**	**Quartz**			
SiO_2	100.33	101.36	97.66	99.42	97.26	100.67	99.78			
Al_2O_3	-	-	-	-	-	-	-			
TiO_2	-	-	-	-	-	-	-			
FeO	-	-	-	-	-	-	-			
MnO	-	-	-	-	-	-	-			
CaO	-	-	-	-	-	-	-			
MgO	-	-	-	-	-	-	-			
Na_2O	-	-	-	-	-	-	-			
K_2O	-	-	-	-	-	-	-			
P_2O_5	-	-	-	-	-	-	-			
BaO	-	-	-	-	-	-	-			
Total	100.33	101.36	97.66	99.42	97.26	100.67	99.78			
Cation Sum	3.00	3.00	3.00	3.00	3.00	3.00	3.00			

BD-20-37 Irene – Eltrut Batholith western contact										
Mineral Phase	**Muscovite**	**Muscovite**	**Muscovite**	**Muscovite**	**Muscovite**	**Muscovite**	**Muscovite**	**Muscovite**	**Muscovite**	**Muscovite**
SiO_2	45.09	44.52	45.34	46.07	44.69	45.41	45.6	46.33	45.19	45.91
Al_2O_3	29.42	30.84	28.19	27.09	27.96	27.56	27.42	26.47	29.50	29.76
TiO_2	-	-	-	-	0.59	0.64	-	0.88	-	-
FeO	3.95	3.61	4.10	4.37	4.66	4.64	3.69	4.72	4.57	4.30
MnO	-	-	-	-	-	-	-	-	-	-
CaO	-	-	-	-	-	-	-	-	-	-
MgO	1.78	1.60	2.26	2.55	2.76	2.40	2.17	3.22	2.04	1.96
Na_2O	-	-	-	-	-	-	-	-	-	-
K_2O	10.96	11.02	10.9	11.4	11.4	11.23	11.00	11.53	11.23	11.44
P_2O_5	-	-	-	-	-	-	-	-	-	-
BaO	1.65	1.37	1.09	-	0.86	0.79	0.98	-	1.12	1.25
Total	92.85	92.96	91.88	91.48	92.92	92.67	90.87	93.14	93.89	94.61
Cation Sum	3.86	3.87	3.87	3.88	3.90	3.88	3.86	3.89	3.89	3.88

BD-20-37 Irene – Eltrut Batholith western contact										
Mineral Phase	**Muscovite**	**Plagioclase**	**Plagioclase**	**Plagioclase**	**Plagioclase**	**Calcite**	**Calcite**	**Calcite**	**Calcite**	**Biotite**
SiO_2	45.06	68.18	66.56	65.65	68.37	-	-	-	-	37.00
Al_2O_3	28.07	19.18	18.97	19.64	19.96	-	-	-	-	14.94
TiO_2	-	-	-	-	-	-	-	-	-	1.39
FeO	4.75	-	-	-	-	0.36	-	0.35	0.35	13.46
MnO	-	-	-	-	-	0.46	0.51	0.48	0.50	-
CaO	-	0.21	0.25	0.88	0.39	51.38	51.41	50.78	49.20	-
MgO	2.49	-	-	-	-	0.43	-	0.52	0.51	14.68
Na_2O	-	11.69	11.42	11.00	11.62	-	-	-	-	-
K_2O	10.95	-	-	-	-	-	-	-	-	10.06
P_2O_5	-	-	-	-	-	-	-	-	-	-
BaO	1.32	-	-	-	-	-	-	-	-	0.57
Total	92.63	99.26	97.19	97.17	100.34	52.63	51.92	52.13	50.56	92.10
Cation Sum	3.88	3.75	3.75	3.75	3.75	6.00	6.00	6.00	6.00	4.29

BD-20-37 Irene – Eltrut Batholith western contact										
Mineral Phase	**Biotite**	**Biotite**	**Biotite**	**Biotite**	**Quartz**	**Quartz**	**Quartz**	**Quartz**	**Quartz**	**Quartz**
SiO_2	38.42	37.80	37.54	38.08	101.80	99.49	100.72	99.72	100.51	100.69
Al_2O_3	15.24	15.02	14.88	14.87	-	-	-	-	-	-
TiO_2	1.52	2.16	1.96	1.62	-	-	-	-	-	-
FeO	14.17	14.68	14.64	14.09	-	-	-	-	-	-
MnO	-	-	-	-	-	-	-	-	-	-
CaO	-	-	-	-	-	-	-	-	-	-
MgO	15.01	14.67	14.46	14.84	-	-	-	-	-	-
Na_2O	-	-	-	-	-	-	-	-	-	-
K_2O	10.43	10.36	10.20	10.71	-	-	-	-	-	-
P_2O_5	-	-	-	-	-	-	-	-	-	-
BaO	-	-	-	-	-	-	-	-	-	-
Total	94.79	94.69	93.68	94.20	101.80	99.49	100.70	99.70	100.51	100.69
Cation Sum	4.29	4.29	4.29	4.30	3.00	3.00	3.00	3.00	3.00	3.00

BD-20-37 Irene – Eltrut Batholith western contact										
Mineral Phase	**Apatite**	**Apatite**								
SiO_2	-	-								
Al_2O_3	-	-								
TiO_2	-	-								
FeO	-	-								
MnO	-	-								
CaO	54.86	53.97								
MgO	-	-								
Na_2O	-	-								
K_2O	-	-								
P_2O_5	41.28	40.28								
BaO	-	-								
Total	96.14	94.25								
Cation Sum	3.60	3.57								

BD-DL-09 Hammond Reef Marmion Batholith										
Mineral Phase	**Chlorite**	**Chlorite**	**Chlorite**	**Chlorite**	**Chlorite**	**Chlorite**	**Muscovite**	**Muscovite**	**Muscovite**	**Muscovite**
SiO_2	23.76	23.93	23.81	31.67	23.57	24.36	46.12	44.18	47.29	46.08
Al_2O_3	21.99	22.70	21.60	20.45	22.26	21.00	32.95	31.03	34.59	34.12
TiO_2	-	-	-	-	-	-	0.36	-	0.26	0.36
FeO	32.32	33.72	33.06	32.38	33.5	32.83	3.26	3.73	3.02	3.14
MnO	-	-	-	-	-	-	-	-	-	-
CaO	-	-	-	2.37	-	-	-	-	-	-
MgO	9.73	9.68	9.73	9.66	9.79	9.78	0.54	0.68	0.46	0.38
Na_2O	-	-	-	-	-	-	0.68	-	0.87	-
K_2O	-	-	-	-	-	-	11.37	10.86	10.49	10.68
P_2O_5	-	-	-	-	-	-	-	-	-	-
BaO	-	-	-	-	-	-	-	-	-	-
Total	87.80	90.02	88.20	86.53	89.12	87.97	95.29	90.48	96.99	94.75
Cation Sum	4.28	4.29	4.29	4.36	4.29	4.28	3.86		3.83	3.80

BD-DL-09 Hammond Reef Marmion Batholith										
Mineral Phase	**Muscovite**	**Calcite**	**Calcite**	**Plagioclase**						
SiO_2	47.54	-	-	68.53						
Al_2O_3	34.58	-	-	19.50						
TiO_2	0.30	-	-	-						
FeO	3.10	15.77	19.85	-						
MnO	-	0.60	0.53	-						
CaO	-	29.23	28.30	-						
MgO	0.48	9.36	7.54	-						
Na_2O	0.56	-	-	11.71						
K_2O	11.26	-	-	-						
P_2O_5	-	-	-	-						
BaO	-	-	-	-						
Total	97.83	54.96	56.22	99.74						
Cation Sum	3.84	6.00	6.00	3.75						

Rev 5 Revell Batholith										
Mineral Phase	**Chlorite**	**Chlorite**	**Chlorite**	**Chlorite**	**Muscovite**	**Muscovite**	**Epidote**	**Epidote**	**Apatite**	**Plagioclase**
SiO_2	30.77	26.77	27.05	28.21	45.77	45.27	37.26	36.82	-	66.82
Al_2O_3	16.32	16.95	18.58	16.85	34.68	34.22	22.36	23.21	-	19.54
TiO_2	-	-	-	-	-	-	-	-	-	-
FeO	25.44	25.34	27.77	28.21	2.17	2.71	12.97	11.71	0.40	0.46
MnO	0.51	0.64	0.88	0.78	-	-	0.44	0.73	-	-
CaO	-	-	-	-	-	-	23.22	22.53	56.20	0.60
MgO	13.85	14.01	14.06	14.14	-	0.37	-	-	-	-
Na_2O	-	-	-	-	0.49	-	-	-	-	10.95
K_2O	0.98	-	-	-	11.34	11.47	-	-	-	-
P_2O_5	-	-	-	-	-	-	-	-	40.11	-
BaO	-	-	-	-	-	-	-	-	-	-
IrO_2	-	-	-	-	-	-	-	-	4.13	-
Total	87.88	83.71	88.34	88.19	94.45	94.03	96.26	95.01	100.82	98.38
Cation Sum	4.21	4.25	4.27	4.26	3.84	3.84	3.98	3.97	3.59	3.74

Rev 5 Revell Batholith										
Mineral Phase	**Plagioclase**	**Kspar**	**Kspar**	**Quartz**						
SiO_2	68.61	63.39	64.55	101.15						
Al_2O_3	19.39	17.83	18.51	-						
TiO_2	-	-	-	-						
FeO	0.26	-	-	-						
MnO	-	-	-	-						
CaO	-	-	-	-						
MgO	-	-	-	-						
Na_2O	11.52	0.54	0.50	-						
K_2O	-	16.63	16.81	-						
P_2O_5	-	-	-	-						
BaO	-	-	0.59	-						
Total	99.78	98.39	100.96	101.15						
Cation Sum	3.74	3.78	3.77	3.00						

Rev 8 Revell Batholith										
Mineral Phase	**Biotite**	**Biotite**	**Biotite**	**Biotite**	**Biotite**	**Biotite**	**Biotite**	**Biotite**	**Biotite**	**Chlorite**
SiO_2	36.43	37.05	35.70	36.14	36.55	36.73	36.20	36.59	36.36	27.64
Al_2O_3	14.54	14.98	14.20	14.38	14.10	14.58	14.46	14.45	14.45	20.06
TiO_2	1.88	1.06	1.83	2.07	2.18	2.32	1.86	2.21	2.56	-
FeO	20.59	20.61	20.73	20.49	20.23	20.71	20.08	21.15	21.72	27.49
MnO	0.51	0.46	0.40	0.39	0.35	0.40	0.46	0.43	0.32	0.59
CaO	-	-	-	-	-	-	-	-	-	-
MgO	10.49	10.68	10.30	9.90	10.34	9.69	9.88	9.48	9.47	13.49
Na_2O	-	-	-	-	-	-	-	-	-	-
K_2O	10.00	10.09	10.21	9.78	10.35	10.40	9.93	10.15	10.13	-
P_2O_5	-	-	-	-	-	-	-	-	-	-
BaO	-	-	-	1.10	-	-	-	-	-	-
Total	94.44	94.93	93.36	94.26	94.10	94.83	92.88	94.46	95.01	89.28
Cation Sum	4.30	4.30	4.32	4.29	4.30	4.28	4.28	4.28	4.29	4.24

Rev 8 Revell Batholith										
Mineral Phase	**Muscovite**	**Muscovite**	**Epidote**	**Sphene**	**Sphene**	**Apatite**	**Kspar**	**Kspar**	**Kspar**	**Plagioclase**
SiO_2	47.60	46.25	37.71	30.25	30.27	1.72	64.56	64.07	63.62	63.10
Al_2O_3	28.02	27.15	22.38	2.67	5.73	0.36	18.36	18.11	18.02	21.22
TiO_2	-	0.35	-	36.98	30.77	-	-	-	-	-
FeO	6.47	6.24	13.90	1.28	1.55	-	-	-	-	-
MnO	-	-	-	-	0.29	-	-	-	-	-
CaO	-	-	22.86	28.7	27.74	54.28	-	-	-	2.98
MgO	2.11	2.00	-	-	-	-	-	-	-	-
Na_2O	-	-	-	-	-	-	0.51	0.64	0.54	9.98
K_2O	11.65	11.40	-	-	-	-	16.88	16.77	16.40	-
P_2O_5	-	-	-	-	-	40.50	-	-	-	-
BaO	-	-	-	-	-	-	-	-	-	-
Total	95.86	93.39	96.85	99.88	96.36	96.86	100.32	99.59	98.59	97.28
Cation Sum	3.88	3.88	3.98	3.66	3.52	3.54	3.77	3.78	3.77	3.76

Rev 8 Revell Batholith										
Mineral Phase	**Plagioclase**	**Plagioclase**	**Plagioclase**	**Plagioclase**	**Quartz**	**Quartz**	**Quartz**	**Quartz**	**Quartz**	
SiO_2	64.41	63.76	63.86	63.76	96.91	101.71	99.55	100.66	100.77	
Al_2O_3	22.18	21.12	22.01	22.35	-	-	-	-	-	
TiO_2	-	-	-	-	-	-	-	-	-	
FeO	-	-	-	-	-	-	-	-	-	
MnO	-	-	-	-	-	-	-	-	-	
CaO	3.25	2.92	3.34	3.65	-	-	-	-	-	
MgO	-	-	-	-	-	-	-	-	-	
Na_2O	9.92	9.79	9.92	9.64	-	-	-	-	-	
K_2O	-	-	-	-	-	-	-	-	-	
P_2O_5	-	-	-	-	-	-	-	-	-	
BaO	-	-	-	-	-	-	-	-	-	
Total	99.77	97.58	99.14	99.40	96.91	101.71	99.55	100.66	100.77	
Cation Sum	3.75	3.74	3.76	3.75	3.00	3.00	3.00	3.00	3.00	

BD-WB-50 White Otter Lake Batholith										
Mineral Phase	**Chlorite**	**Chlorite**	**Chlorite**	**Chlorite**	**Chlorite**	**Chlorite**	**Chlorite**	**Biotite**	**Sphene**	**Sphene**
SiO_2	28.14	28.07	27.99	29.15	25.67	29.59	28.93	34.54	31.03	31.03
Al_2O_3	17.56	15.91	16.56	16.13	15.94	16.06	16.56	15.55	3.85	5.78
TiO_2	-	-	-	-	-	-	-	2.25	32.51	30.23
FeO	23.57	23.41	25.37	24.10	24.44	22.74	22.67	20.23	2.91	3.58
MnO	0.43	0.41	0.42	0.47	0.48	0.45	0.43	-	-	-
CaO	-	-	-	-	-	-	-	-	26.47	25.13
MgO	16.63	17.52	16.99	17.58	15.00	18.53	17.62	10.91	0.68	1.85
Na_2O	-	-	-	-	-	-	-	-	-	-
K_2O	-	-	-	0.35	-	-	-	7.95	-	-
P_2O_5	-	-	-	-	-	-	-	-	-	-
BaO	-	-	-	-	-	-	-	-	-	-
Total	86.32	85.33	87.33	88.14	81.53	87.37	86.22	91.44	97.45	97.60
Cation Sum	4.25	4.28	4.29	2.85	2.86	2.84	2.83	2.83	2.37	2.39

BD-WB-50 White Otter Lake Batholith										
Mineral Phase	**Sphene**	**Kspar**	**Kspar**	**Kspar**	**Kspar**	**Kspar**	**Kspar**	**Plagioclase**	**Plagioclase**	**Plagioclase**
SiO_2	30.16	64.62	64.25	68.54	63.62	64.23	64.10	63.15	63.17	63.28
Al_2O_3	6.01	17.96	18.36	19.27	18.23	18.21	18.01	21.04	21.46	21.68
TiO_2	28.05	-	-	-	-	-	-	-	-	-
FeO	5.31	-	-	-	-	-	-	-	-	-
MnO	-	-	-	-	-	-	-	-	-	-
CaO	23.80	-	-	-	-	-	-	2.28	3.02	3.37
MgO	3.31	-	-	-	-	-	-	-	-	-
Na_2O	-	-	0.40	6.92	0.41	0.33	0.25	9.41	9.87	9.62
K_2O	-	17.18	17.04	7.74	16.58	17.33	17.15	-	-	0.17
P_2O_5	-	-	-	-	-	-	-	-	-	-
BaO	-	-	-	-	-	-	-	-	-	-
Total	96.64	99.76	100.05	102.48	98.83	100.11	99.51	95.88	97.51	98.13
Cation Sum	2.52	3.76	7.55	2.51	2.51	2.52	2.52	3.72	3.76	7.51

BD-WB-50 White Otter Lake Batholith										
Mineral Phase	**Plagioclase**	**Plagioclase**	**Plagioclase**	**Apatite**	**Quartz**	**Quartz**	**Quartz**	**Quartz**	**Quartz**	**Hematite**
SiO_2	64.76	62.87	64.40	-	101.35	101.22	101.76	100.21	100.61	0.53
Al_2O_3	22.22	22.20	21.87	-	-	-	-	-	-	-
TiO_2	-	-	-	-	-	-	-	-	-	-
FeO	-	-	-	-	-	-	-	-	-	91.66
MnO	-	-	-	-	-	-	-	-	-	-
CaO	3.10	3.75	3.12	56.14	-	-	-	-	-	-
MgO	-	-	-	-	-	-	-	-	-	-
Na_2O	10.06	9.44	9.84	-	-	-	-	-	-	-
K_2O	-	-	-	-	-	-	-	-	-	-
P_2O_5	-	-	-	41.66	-	-	-	-	-	-
BaO	-	-	-	-	-	-	-	-	-	-
Total	100.15	98.26	99.24	97.81	101.35	101.22	101.76	100.21	100.61	92.19
Cation Sum	2.50	2.50	2.50	2.38	3.00	3.00	3.00	3.00	3.00	11.92

BD-WB-38B Sowden Wabakimi Batholithic Complex										
Mineral Phase	**Chlorite**	**Chlorite**	**Muscovite**	**Muscovite**	**Biotite**	**Kspar**	**Kspar**	**Kspar**	**Kspar**	**Kspar**
SiO_2	25.12	25.77	45.53	45.56	35.51	62.79	63.82	62.68	65.17	61.03
Al_2O_3	18.65	18.43	26.85	25.90	16.17	18.50	18.92	17.94	18.78	17.36
TiO_2	-	-	1.40	1.72	1.54	-	-	-	-	-
FeO	32.57	31.45	6.50	6.53	22.81	-	-	-	-	0.65
MnO	0.60	0.70	-	-	0.32	-	-	-	-	-
CaO	-	-	-	-	-	-	-	-	-	-
MgO	11.14	11.20	1.67	1.79	10.36	-	-	-	-	0.75
Na_2O	-	-	-	-	0.57	0.97	0.82	0.63	-	-
K_2O	-	-	11.52	11.49	5.52	15.50	16.26	16.28	17.28	17.11
P_2O_5	-	-	-	-	-	-	-	-	-	-
BaO	-	-	-	-	-	1.51	1.10	0.70	0.89	-
Total	88.07	87.55	93.48	93.00	92.79	99.27	100.92	98.23	102.13	96.90
Cation Sum	11.47	11.41	15.52	15.51	5.61	5.04	5.04	5.04	5.02	5.08

BD-WB-38B Sowden Wabakimi Batholithic Complex										
Mineral Phase	**Kspar**	**Plagioclase**	**Plagioclase**	**Plagioclase**	**Plagioclase**	**Quartz**	**Quartz**	**Quartz**		
SiO_2	64.52	69.47	63.09	63.00	63.57	102.32	102.17	102.81		
Al_2O_3	18.50	20.46	22.06	21.84	22.74	-	-	-		
TiO_2	-	-	-	-	-	-	-	-		
FeO	-	-	-	-	-	-	-	-		
MnO	-	-	-	-	-	-	-	-		
CaO	-	0.42	3.71	3.28	3.64	-	-	-		
MgO	-	-	-	-	-	-	-	-		
Na_2O	0.67	12.19	9.57	9.74	9.25	-	-	-		
K_2O	16.38	-	0.22	0.16	0.19	-	-	-		
P_2O_5	-	-	-	-	-	-	-	-		
BaO	0.57	-	-	-	-	-	-	-		
Total	100.64	102.53	98.65	98.02	99.39	102.32	102.17	102.81		
Cation Sum	5.03	5.02	5.01	5.01	4.99	3.00	3.00	3.00		

BD-WB-38A Sowden Wabakimi Batholithic Complex										
Mineral Phase	**Chlorite**	**Muscovite**	**Muscovite**	**Muscovite**	**Biotite**	**Biotite**	**Epidote**	**Apatite**	**Apatite**	**Kspar**
SiO_2	27.48	47.34	44.72	47.35	36.70	34.79	37.97	-	0.69	65.05
Al_2O_3	18.13	27.58	27.98	26.52	15.49	15.77	22.45	-	-	18.58
TiO_2	-	0.54	0.51	0.46	3.08	3.02	-	-	-	-
FeO	28.84	7.32	7.19	5.99	20.37	24.10	13.35	1.40	-	-
MnO	0.64	-	-	-	-	0.31	-	-	-	-
CaO	-	-	-	-	-	-	23.79	55.18	55.60	-
MgO	10.62	2.04	1.12	2.11	7.96	8.89	-	-	-	-
Na_2O	-	-	-	-	-	-	-	-	-	0.69
K_2O	0.32	11.38	11.32	11.77	9.58	8.10	-	-	-	16.51
P_2O_5	-	-	-	-	-	-	-	41.11	41.77	-
BaO	-	-	-	-	-	-	-	-	-	-
Total	86.04	96.21	92.83	94.20	93.19	94.98	97.55	97.69	98.06	100.83
Cation Sum	4.22	3.88	3.89	3.88	4.20	4.25	3.98	3.59	3.58	3.77

BD-WB-38A Sowden Wabakimi Lakes Batholithic Complex										
Mineral Phase	**Kspar**	**Kspar**	**Plagioclase**	**Plagioclase**	**Plagioclase**	**Plagioclase**	**Plagioclase**	**Quartz**	**Quartz**	
SiO_2	63.59	63.85	63.32	65.83	64.07	63.39	63.19	101.79	101.63	
Al_2O_3	18.41	18.49	22.20	22.29	22.50	22.44	21.82	-	-	
TiO_2	-	-	-	-	-	-	-	-	-	
FeO	-	-	-	-	-	-	-	-	-	
MnO	-	-	-	-	-	-	-	-	-	
CaO	-	-	3.56	3.26	3.64	3.73	3.68	-	-	
MgO	-	-	-	-	-	-	-	-	-	
Na_2O	0.35	0.63	9.41	10.05	9.71	9.52	9.60	-	-	
K_2O	16.73	16.50	0.16	-	0.17	-	-	-	-	
P_2O_5	-	-	-	-	-	-	-	-	-	
BaO	1.02	0.73	-	-	-	-	-	-	-	
Total	100.10	100.19	98.65	101.43	100.09	99.09	98.29	101.79	101.63	
Cation Sum	3.78	3.78	3.75	3.75	3.76	3.75	3.75	3.00	3.00	

BD-WB-34 Marmion Batholith										
Mineral Phase	**Chlorite**	**Chlorite**	**Biotite**	**Biotite**	**Biotite**	**Biotite**	**Sphene**	**Sphene**	**Epidote**	**Apatite**
SiO_2	28.84	27.56	36.43	37.63	36.87	35.23	30.17	29.20	35.58	-
Al_2O_3	15.83	15.62	14.96	15.34	15.31	15.09	1.73	1.90	19.78	-
TiO_2	-	-	2.55	2.46	2.31	2.15	37.76	36.39	-	-
FeO	26.23	26.07	21.24	21.18	21.26	20.65	1.23	1.03	15.40	-
MnO	0.54	0.53	-	0.39	0.41	0.54	-	-	-	-
CaO	-	-	-	-	-	-	28.66	28.60	21.96	55.41
MgO	16.21	15.11	10.28	10.65	9.68	9.72	-	-	-	-
Na_2O	-	-	-	-	-	-	-	-	-	-
K_2O	0.31	0.28	7.45	10.66	10.63	10.10	-	-	-	-
P_2O_5	-	-	-	-	-	-	-	-	-	40.94
BaO	-	-	-	-	-	-	-	-	-	-
Total	87.96	85.17	92.92	98.31	96.46	93.49	99.54	97.11	92.73	96.34
Cation Sum	4.28	4.28	4.20	4.29	4.29	4.30	3.65	3.61	4.01	3.58

BD-WB-34 Marmion Batholith										
Mineral Phase	**Kspar**									
SiO_2	62.31									
Al_2O_3	18.10									
TiO_2	-									
FeO	-									
MnO	-									
CaO	-									
MgO	-									
Na_2O	0.32									
K_2O	16.45									
P_2O_5	-									
BaO	0.93									
Total	98.10									
Cation Sum	3.78									

BD-DL-04B Hammond Reef Marmion Batholith										
Mineral Phase	**Chlorite**	**Chlorite**	**Chlorite**	**Chlorite**	**Chlorite**	**Chlorite**	**Chlorite**	**Chlorite**	**Chlorite**	**Muscovite**
SiO_2	23.31	24.01	23.34	22.69	21.94	23.35	22.70	24.21	23.9	43.51
Al_2O_3	21.43	21.9	21.71	20.83	19.56	20.82	20.59	19.69	20.52	31.47
TiO_2	-	-	-	-	-	-	-	0.4	-	-
FeO	35.82	36.28	37.04	36.22	36.17	35.91	36.03	35.22	36.16	2.96
MnO	-	0.3	0.26	-	-	-	-	-	-	-
CaO	-	-	-	-	-	-	-	-	-	-
MgO	7.63	7.82	7.41	7.04	6.79	7.28	7.23	8.34	7.61	0.61
Na_2O	-	-	-	-	-	-	-	-	-	-
K_2O	-	-	-	-	-	-	-	-	-	11.26
P_2O_5	-	-	-	-	-	-	-	-	-	-
BaO	-	-	-	-	-	-	-	-	-	-
Total	88.19	90.31	89.76	86.78	84.46	87.35	86.56	87.86	88.19	89.91
Cation Sum	4.29	4.28	4.30	4.29	4.31	4.28	4.30	4.28	4.28	3.85

BD-DL-04B Hammond Reef Marmion Batholith										
Mineral Phase	**Muscovite**	**Muscovite**	**Muscovite**	**Muscovite**	**Muscovite**	**Calcite**	**Calcite**	**Plagioclase**	**Plagioclase**	**Plagioclase**
SiO_2	44.54	45.09	47.86	46.82	44.06	-	-	66.81	67.23	66.51
Al_2O_3	32.5	32.79	33.78	34.58	34.13	-	-	19.64	19.73	19.51
TiO_2	0.32	-	0.32	0.28	-	-	-	-	-	-
FeO	2.88	3.14	3.17	1.98	1.72	2.17	1.94	-	-	-
MnO	-	-	-	-	-	1.11	1.08	-	-	-
CaO	-	-	-	-	-	47.97	48.82	0.72	0.45	0.62
MgO	0.56	0.74	0.81	0.5	0.21	0.44	0.41	-	-	-
Na_2O	-	-	-	0.96	0.6	-	-	11.53	11.48	11.21
K_2O	11.11	11.60	11.61	10.84	10.85	-	-	-	-	-
P_2O_5	-	-	-	-	-	-	-	-	-	-
BaO	-	0.68	-	-	-	-	-	-	-	-
Total	91.92	94.04	97.54	95.97	91.57	51.69	52.25	98.69	98.89	97.86
Cation Sum	3.83	3.86	3.82	3.84	3.84	6.00	6.00	3.76	3.75	3.75

BD-DL-04B Hammond Reef Marmion Batholith										
Mineral Phase	**Quartz**	**Quartz**	**Quartz**	**Quartz**	**Quartz**	**Quartz**	**Quartz**			
SiO_2	100.33	101.36	97.66	99.42	97.26	100.67	99.78			
Al_2O_3	-	-	-	-	-	-	-			
TiO_2	-	-	-	-	-	-	-			
FeO	-	-	-	-	-	-	-			
MnO	-	-	-	-	-	-	-			
CaO	-	-	-	-	-	-	-			
MgO	-	-	-	-	-	-	-			
Na_2O	-	-	-	-	-	-	-			
K_2O	-	-	-	-	-	-	-			
P_2O_5	-	-	-	-	-	-	-			
BaO	-	-	-	-	-	-	-			
Total	100.33	101.36	97.66	99.42	97.26	100.67	99.78			
Cation Sum	3.00	3.00	3.00	3.00	3.00	3.00	3.00			

BD-DL-04 Hammond Reef Marmion Batholith										
Mineral Phase	**Chlorite**	**Chlorite**	**Chlorite**	**Chlorite**	**Chlorite**	**Chlorite**	**Chlorite**	**Chlorite**	**Chlorite**	**Chlorite**
SiO_2	22.61	23.30	23.42	23.20	24.06	23.37	22.78	23.27	22.94	23.03
Al_2O_3	20.89	21.49	22.07	20.51	21.24	21.12	20.88	21.27	20.78	21.12
TiO_2	-	-	-	-	-	-	-	-	-	-
FeO	36.57	35.99	36.79	35.54	37.07	36.86	36.61	34.84	36.25	35.96
MnO	-	0.31	-	-	-	-	-	-	-	-
CaO	-	-	-	-	-	-	-	-	-	-
MgO	7.37	7.32	7.43	7.35	7.79	7.61	7.09	7.47	7.27	7.39
Na_2O	-	-	-	-	-	-	-	-	-	-
K_2O	-	-	-	-	-	-	-	-	-	-
P_2O_5	-	-	-	-	-	-	-	-	-	-
BaO	-	-	-	-	-	-	-	-	-	-
Total	87.43	88.41	89.72	86.59	90.16	88.96	87.36	86.85	87.25	87.50
Cation Sum	4.31	4.29	4.29	4.28	4.29	4.30	4.30	4.27	4.29	4.29

BD-DL-04 Hammond Reef Marmion Batholith										
Mineral Phase	**Chlorite**	**Chlorite**	**Chlorite**	**Chlorite**	**Muscovite**	**Muscovite**	**Muscovite**	**Muscovite**	**Muscovite**	**Muscovite**
SiO_2	23.20	25.48	23.85	23.29	45.49	44.22	45.60	45.63	44.07	45.25
Al_2O_3	21.38	22.25	21.45	21.30	32.78	30.81	32.26	33.23	32.13	33.07
TiO_2	-	-	-	-	-	0.42	0.46	0.36	-	-
FeO	36.59	35.82	35.75	35.84	3.67	3.43	3.11	3.32	2.77	2.77
MnO	-	-	-	-	-	-	-	-	-	-
CaO	-	-	-	-	-	-	-	-	-	-
MgO	6.88	8.22	7.17	7.17	0.75	0.98	0.71	0.70	0.56	0.59
Na_2O	-	-	-	-	-	-	-	-	-	-
K_2O	-	-	-	-	11.63	11.54	11.44	11.72	11.43	11.36
P_2O_5	-	-	-	-	-	-	-	-	-	-
BaO	-	-	-	-	-	-	-	0.48	-	0.66
Total	88.05	91.77	88.23	87.59	94.33	91.40	93.58	95.44	90.95	93.71
Cation Sum	4.28	4.25	4.27	4.28	3.86	3.86	3.84	3.85	3.85	3.84

BD-DL-04 Hammond Reef Marmion Batholith										
Mineral Phase	**Muscovite**	**Calcite**	**Calcite**	**Calcite**	**Calcite**	**Calcite**	**Calcite**	**Calcite**	**Plagioclase**	**Plagioclase**
SiO_2	48.90	-	-	-	-	-	-	-	68.46	69.13
Al_2O_3	30.18	-	-	-	-	-	-	-	19.86	19.35
TiO_2	-	-	-	-	-	-	-	-	-	-
FeO	4.19	0.94	2.25	1.32	2.10	2.14	4.10	0.78	-	-
MnO	-	0.77	0.95	0.79	0.83	1.03	0.74	0.85	-	-
CaO	-	46.74	48.06	48.75	48.64	46.95	46.90	50.65	0.34	-
MgO	1.48	-	-	-	0.34	0.37	0.55	-	-	-
Na_2O	-	-	-	-	-	-	-	-	11.49	11.73
K_2O	11.57	-	-	-	-	-	-	-	-	-
P_2O_5	-	-	-	-	-	-	-	-	-	-
BaO	-	-	-	-	-	-	-	-	-	-
Total	96.32	48.45	51.27	50.86	51.90	50.48	52.29	52.28	100.16	100.22
Cation Sum	3.83	6.00	6.00	6.00	6.00	6.00	6.00	6.00	3.74	3.74

BD-DL-08 – Unnamed pluton western Wabigoon (drill core)										
Mineral Phase	**Chlorite**	**Chlorite**	**Chlorite**	**Chlorite**	**Chlorite**	**Muscovite**	**Muscovite**	**Muscovite**	**Muscovite**	**Calcite**
SiO_2	23.72	22.21	22.84	24.24	22.60	47.62	43.06	43.84	45.53	-
Al_2O_3	20.83	19.43	19.44	20.63	21.13	33.89	30.40	30.42	31.49	-
TiO_2	-	-	-	-	-	0.41	-	0.34	0.38	-
FeO	40.28	38.22	39.57	41.26	39.28	3.60	3.41	3.40	3.57	1.45
MnO	-	-	-	-	-	-	-	-	-	0.58
CaO	-	-	-	-	-	-	-	-	-	48.82
MgO	3.25	3.21	3.31	3.54	5.03	0.67	0.60	0.79	0.74	-
Na_2O	-	-	-	-	-	-	-	-	-	-
K_2O	-	-	-	-	-	11.56	11.49	11.64	11.57	-
P_2O_5	-	-	-	-	-	-	-	-	-	-
BaO	-	-	-	-	-	-	-	-	-	-
Total	88.09	83.07	85.17	89.66	88.04	97.76	88.96	90.44	93.27	50.85
Cation Sum	4.24	4.25	4.26	4.25	4.29	3.83	3.87	3.86	3.85	6.00

BD-DL-08 – Unnamed pluton western Wabigoon (drill core)										
Mineral Phase	**Calcite**	**Calcite**	**Calcite**	**Calcite**	**Calcite**	**Calcite**	**Quartz**	**Quartz**		
SiO_2	-	-	-	-	-	-	100.45	100.24		
Al_2O_3	-	-	-	-	-	-	-	-		
TiO_2	-	-	-	-	-	-	-	-		
FeO	1.62	0.52	2.14	1.96	1.75	1.79	-	-		
MnO	0.67	0.80	0.59	0.49	0.59	0.57	-	-		
CaO	48.07	51.20	49.60	46.71	51.08	50.58	-	-		
MgO	-	-	0.35	-	-	-	-	-		
Na_2O	-	-	-	-	-	-	-	-		
K_2O	-	-	-	-	-	-	-	-		
P_2O_5	-	-	-	-	-	-	-	-		
BaO	-	-	-	-	-	-	-	-		
Total	50.36	52.52	52.68	49.16	53.42	52.93	100.45	100.24		
Cation Sum	6.00	6.00	6.00	6.00	6.00	6.00	3.00	3.00		

BD-DL-10 – Atikwa batholith										
Mineral Phase	**Chlorite**	**Chlorite**	**Chlorite**	**Chlorite**	**Chlorite**	**Chlorite**	**Chlorite**	**Chlorite**	**Chlorite**	**Chlorite**
SiO_2	24.87	23.69	23.95	24.66	24.39	24.99	23.98	24.45	25.78	24.73
Al_2O_3	21.14	20.47	19.66	20.58	20.52	21.41	20.31	20.35	19.63	21.26
TiO_2	-	-	-	-	-	-	-	-	-	-
FeO	28.02	27.02	27.62	28.86	26.97	28.41	28.46	28.02	27.43	28.44
MnO	-	-	-	-	-	-	-	-	-	-
CaO	-	-	-	-	-	-	-	-	-	-
MgO	13.06	12.57	12.90	12.70	13.17	13.33	12.57	12.89	13.85	13.07
Na_2O	-	-	-	-	-	-	-	-	-	-
K_2O	-	-	-	-	-	-	-	-	-	-
P_2O_5	-	-	-	-	-	-	-	-	-	-
BaO	-	-	-	-	-	-	-	-	-	-
Total	87.09	83.75	84.14	86.80	85.05	88.15	85.31	85.71	86.69	87.50
Cation Sum	4.28	4.28	4.29	4.29	4.28	4.28	4.29	4.29	4.27	4.28

BD-DL-10 – Atikwa batholith										
Mineral Phase	**Biotite**	**Muscovite**	**Muscovite**	**Calcite**	**Plagioclase**	**Plagioclase**	**Plagioclase**	**Plagioclase**	**Plagioclase**	**Plagioclase**
SiO_2	34.97	46.68	44.53	-	67.51	67.30	69.09	66.81	67.75	67.11
Al_2O_3	16.12	29.94	30.51	-	19.42	18.94	19.45	19.83	19.16	20.25
TiO_2	2.16	0.42	0.61	-	-	-	-	-	-	-
FeO	21.27	3.49	3.56	0.77	-	-	-	-	-	-
MnO	-	-	-	0.43	-	-	-	-	-	-
CaO	-	-	-	48.10	0.39	-	0.16	0.61	0.20	0.86
MgO	9.45	1.71	1.32	0.52	-	-	-	-	-	-
Na_2O	-	-	-	-	11.55	11.88	11.80	11.41	11.39	11.14
K_2O	10.01	11.78	11.34	-	-	-	-	-	-	-
P_2O_5	-	-	-	-	-	-	-	-	-	-
BaO	-	-	-	-	-	-	-	-	-	-
Total	93.97	94.02	91.86	49.82	98.87	98.12	100.51	98.66	98.5	99.36
Cation Sum	4.30	3.86	3.86	6.00	3.75	3.76	3.75	3.76	3.74	3.75

BD-DL-06 – Atikwa batholith										
Mineral Phase	**Chlorite**	**Chlorite**	**Chlorite**	**Chlorite**	**Chlorite**	**Chlorite**	**Chlorite**	**Chlorite**	**Biotite**	**Muscovite**
SiO_2	24.90	25.16	24.97	24.66	24.43	23.69	24.48	24.04	36.53	42.51
Al_2O_3	20.84	20.98	20.02	20.77	20.44	20.56	20.57	20.38	15.65	28.19
TiO_2	-	-	-	-	-	-	-	-	2.01	0.52
FeO	27.54	27.63	27.70	27.61	28.05	27.42	27.24	27.24	20.89	4.11
MnO	-	-	-	0.27	-	-	-	-	-	-
CaO	-	-	-	-	-	-	-	-	-	-
MgO	13.73	13.73	13.42	13.31	12.69	12.77	13.10	12.70	8.57	1.67
Na_2O	-	-	-	-	-	-	-	-	-	-
K_2O	-	-	-	-	-	-	-	-	9.61	10.80
P_2O_5	-	-	-	-	-	-	-	-	-	-
BaO	-	-	-	-	-	-	-	-	-	-
Total	87.00	87.51	86.10	86.62	85.61	84.43	85.40	84.35	93.26	87.81
Cation Sum	4.29	4.28	4.28	4.29	4.28	4.29	4.28	4.28	4.24	3.87

BD-DL-05 – Atikwa batholith										
Mineral Phase	**Chlorite**	**Chlorite**	**Chlorite**	**Muscovite**	**Muscovite**	**Muscovite**	**Muscovite**	**Muscovite**	**Muscovite**	**Muscovite**
SiO_2	26.76	27.27	27.89	42.76	46.52	46.39	45.32	46.22	45.83	43.93
Al_2O_3	16.03	16.38	16.11	28.18	29.32	30.45	29.47	28.82	30.98	30.57
TiO_2	-	-	-	0.58	0.35	0.55	0.59	0.35	-	-
FeO	30.10	29.19	29.66	4.69	4.31	4.01	4.23	3.74	3.57	3.36
MnO	-	0.47	0.54	-	-	-	-	-	-	-
CaO	-	-	-	-	-	-	-	-	-	-
MgO	13.57	14.10	13.94	1.69	1.88	1.54	1.75	1.91	1.21	1.37
Na_2O	-	-	-	-	-	-	-	-	-	-
K_2O	-	-	-	11.08	11.65	11.48	11.45	11.64	11.44	11.30
P_2O_5	-	-	-	-	-	-	-	-	-	-
BaO	-	-	-	-	-	-	-	-	0.82	0.95
Total	86.46	87.41	88.14	88.97	94.04	94.42	92.79	92.67	93.85	91.47
Cation Sum	4.29	4.29	4.28	3.89	3.87	3.85	3.87	3.86	3.85	3.87

BD-DL-05 – Atikwa batholith										
Mineral Phase	**Biotite**	**Biotite**	**Biotite**	**Biotite**	**Epidote**	**Plagioclase**				
SiO_2	34.02	35.32	34.30	36.15	37.41	68.10				
Al_2O_3	15.44	16.18	15.88	16.35	23.36	19.23				
TiO_2	1.91	1.63	1.61	1.66	-	-				
FeO	20.87	22.07	23.82	22.40	11.43	-				
MnO	0.33	0.28	0.42	0.36	-	-				
CaO	-	-	-	-	23.38	-				
MgO	9.13	9.02	8.71	9.08	-	-				
Na_2O	-	-	-	-	-	11.72				
K_2O	9.98	10.29	9.25	10.22	-	-				
P_2O_5	-	-	-	-	-	-				
BaO	-	-	-	-	-	-				
Total	91.68	94.80	94.00	96.22	95.57	99.04				
Cation Sum	4.31	4.31	4.31	4.30	3.96	3.75				

BD-WB-33 Marmion Batholith										
Mineral Phase	**Epidote**	**Epidote**	**Epidote**	**Epidote**	**Epidote**	**Chlorite**	**Chlorite**	**Sphene**	**Plagioclase**	**Plagioclase**
SiO_2	42.74	36.63	42.64	43.04	42.03	27.89	27.63	28.03	68.71	67.29
Al_2O_3	23.24	19.31	22.31	22.47	22.72	18.20	17.81	1.40	19.59	19.32
TiO_2	-	-	-	-	-	-	-	35.67	-	-
FeO	0.91	16.84	2.07	2.03	1.35	24.22	23.28	1.89	-	-
MnO	-	-	-	-	-	0.51	0.43	-	-	-
CaO	27.02	22.70	27.03	26.80	26.65	-	-	25.80	0.25	0.40
MgO	-	-	-	-	-	15.85	15.60	-	-	-
Na_2O	-	-	-	-	-	-	-	-	11.91	11.62
K_2O	-	-	-	-	-	-	-	-	-	-
P_2O_5	-	-	-	-	-	-	-	-	-	-
BaO	-	-	-	-	-	-	-	-	-	-
Total	93.92	95.49	94.04	94.34	92.75	86.67	84.76	92.79	100.46	98.64
Cation Sum	3.83	4.02	3.85	3.84	3.84	4.25	4.24	3.64	3.76	3.76

BD-WB-33 Marmion Batholith										
Mineral Phase	**Kspar**	**Kspar**	**Kspar**	**Kspar**	**Kspar**	**Kspar**				
SiO_2	62.76	63.35	62.37	63.59	64.77	62.63				
Al_2O_3	17.84	18.37	17.99	18.30	18.61	18.33				
TiO_2	-	-	-	-	-	-				
FeO	-	-	-	-	-	-				
MnO	-	-	-	-	-	-				
CaO	-	-	-	-	-	-				
MgO	-	-	-	-	-	-				
Na_2O	0.57	0.73	0.49	0.36	3.24	0.51				
K_2O	15.91	15.83	16.52	16.47	13.27	16.15				
P_2O_5	-	-	-	-	-	-				
BaO	1.23	1.20	1.03	0.91	0.81	0.95				
Total	98.32	99.47	98.41	99.63	100.70	98.57				
Cation Sum	3.77	3.77	3.79	3.77	3.79	3.77				

Appendix IV
XRD Analysis Results

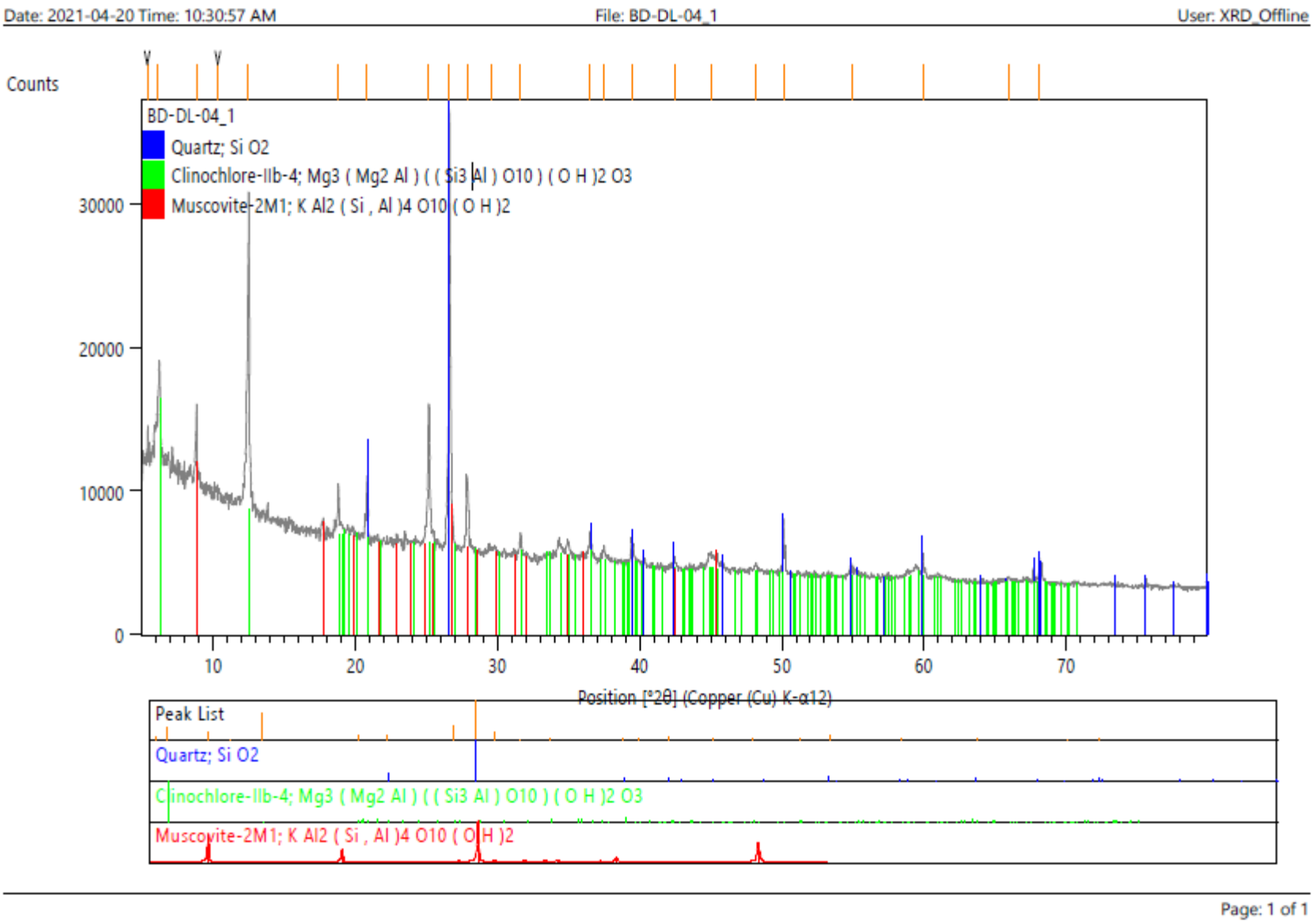
Date: 2021-04-20 Time: 10:30:57 AM
File: BD-DL-04_1
User: XRD_Offline
Counts
BD-DL-04_1
Quartz; Si O2
Clinochlore-IIb-4; Mg3 (Mg2 Al) ((Si3 Al) O10) (O H)2 O3
Muscovite-2M1; K Al2 (Si , Al)4 O10 (O H)2
30000
20000
10000
0
10
20
30
40
50
60
70
Position [°2θ] (Copper (Cu) K-α12)
Peak List
Quartz; Si O2
Clinochlore-IIb-4; Mg3 (Mg2 Al) ((Si3 Al) O10) (O H)2 O3
Muscovite-2M1; K Al2 (Si , Al)4 O10 (O H)2
Page: 1 of 1

Date: 2021-04-20 Time: 10:31:09 AM File: BD-DL-04B User: XRD_Offline

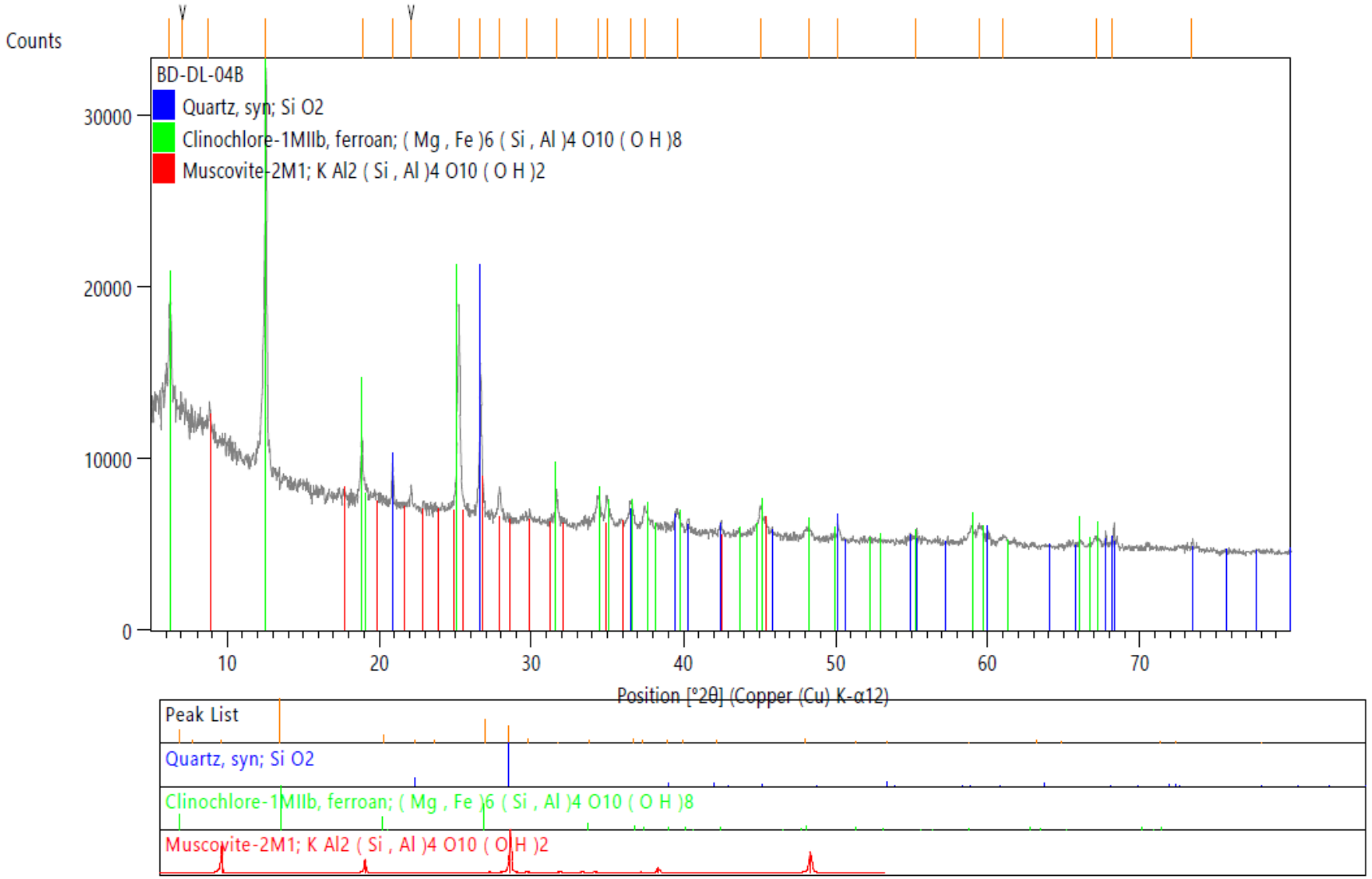

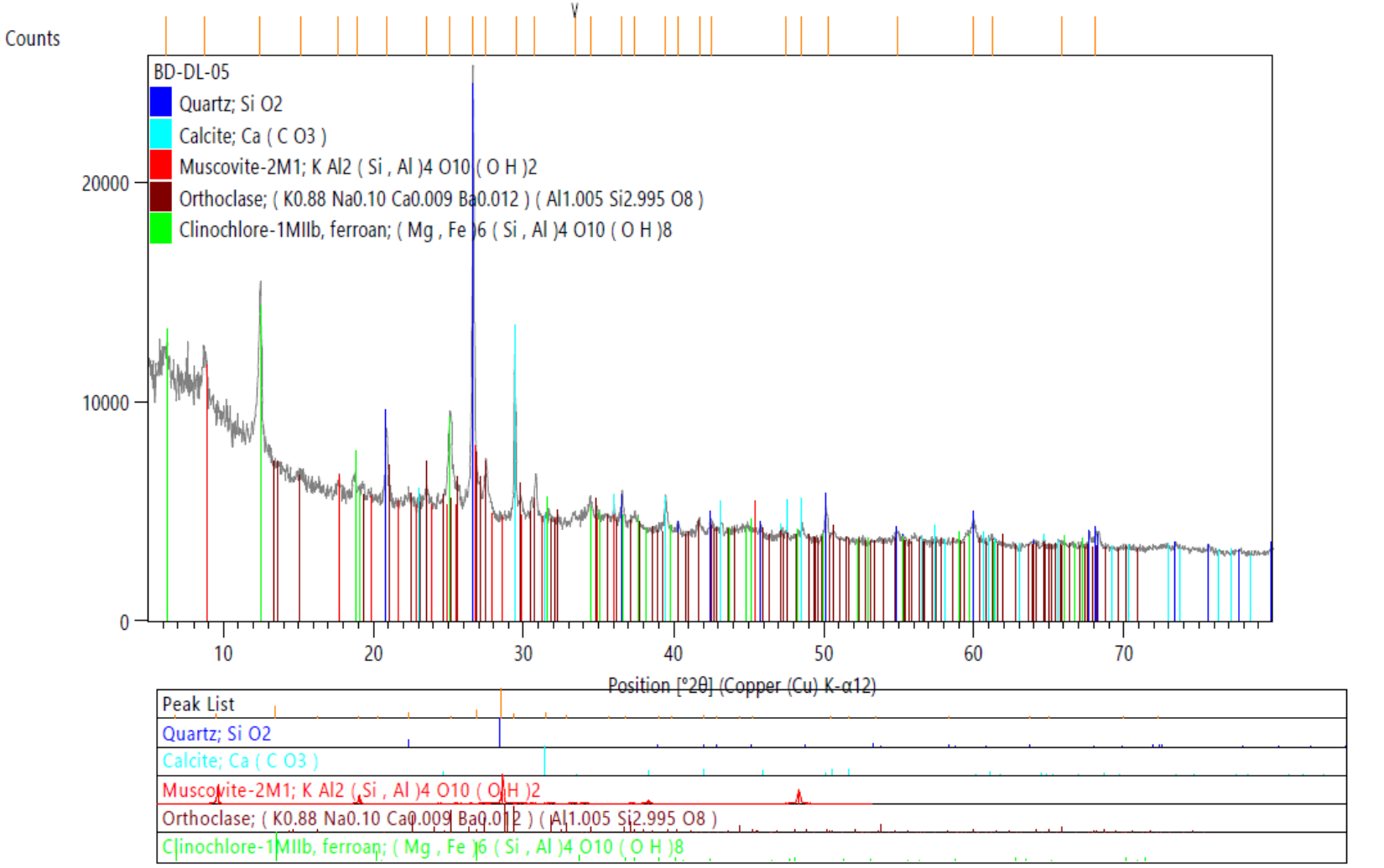
Counts
BD-DL-05
Quartz; Si O2
Calcite; Ca (C O3)
Muscovite-2M1; K Al2 (Si , Al)4 O10 (O H)2
Orthoclase; (K0.88 Na0.10 Ca0.009 Ba0.012) (Al1.005 Si2.995 O8)
Clinochlore-1MIIb, ferroan; (Mg , Fe)6 (Si , Al)4 O10 (O H)8
20000
10000
0
10
20
30
40
50
60
70
Position [°2θ] (Copper (Cu) K-α12)
Peak List
Quartz; Si O2
Calcite; Ca (C O3)
Muscovite-2M1; K Al2 (Si , Al)4 O10 (O H)2
Orthoclase; (K0.88 Na0.10 Ca0.009 Ba0.012) (Al1.005 Si2.995 O8)
Clinochlore-1MIIb, ferroan; (Mg , Fe)6 (Si , Al)4 O10 (O H)8

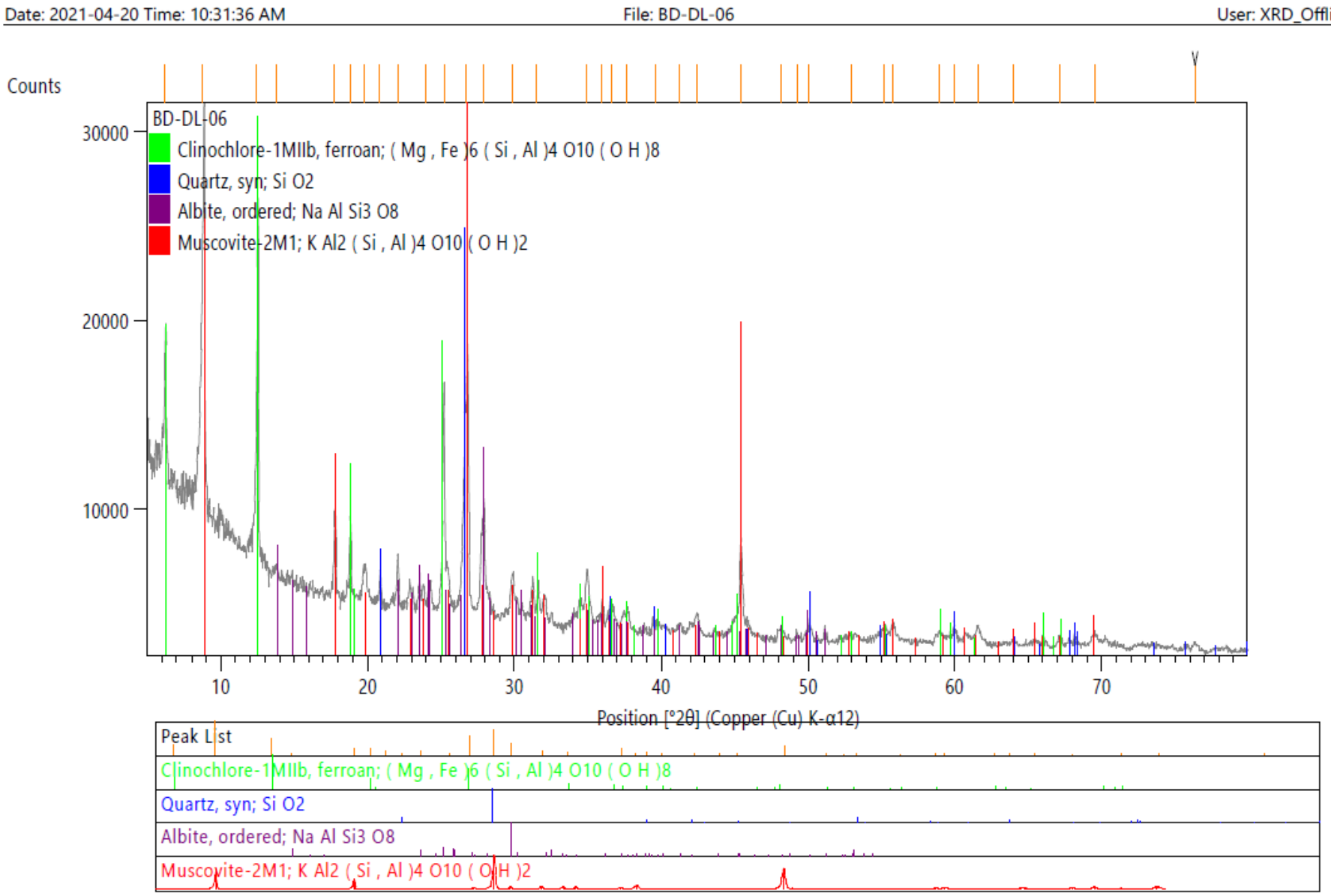
Date: 2021-04-20 Time: 10:31:36 AM
File: BD-DL-06
User: XRD_Offline
Counts
30000
20000
10000
BD-DL-06
Clinochlore-1MIIb, ferroan; (Mg , Fe)6 (Si , Al)4 O10 (O H)8
Quartz, syn; Si O2
Albite, ordered; Na Al Si3 O8
Muscovite-2M1; K Al2 (Si , Al)4 O10 (O H)2
10
20
30
40
50
60
70
Position [°2θ] (Copper (Cu) K-α12)
Peak List
Clinochlore-1MIIb, ferroan; (Mg , Fe)6 (Si , Al)4 O10 (O H)8
Quartz, syn; Si O2
Albite, ordered; Na Al Si3 O8
Muscovite-2M1; K Al2 (Si , Al)4 O10 (O H)2

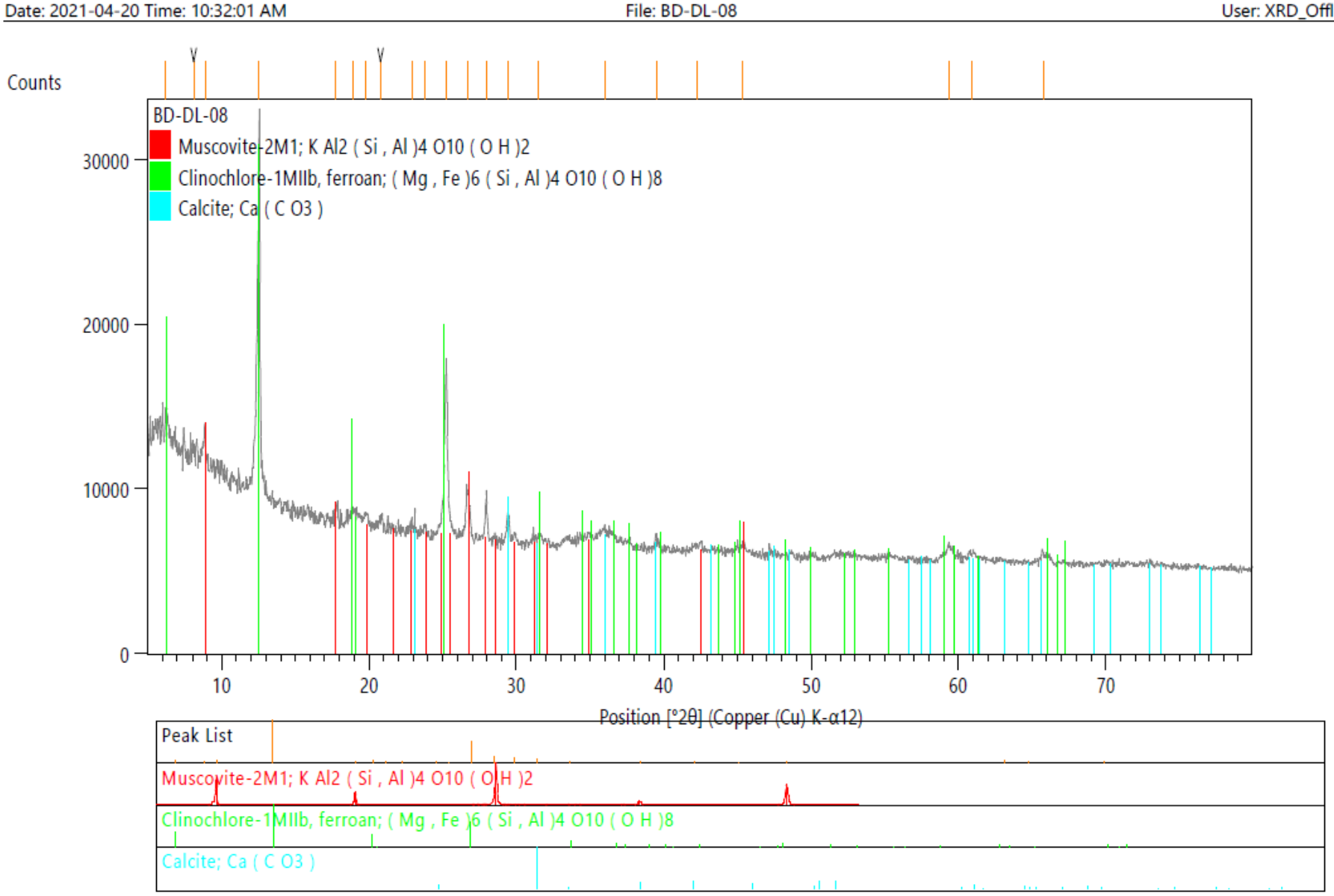
Date: 2021-04-20 Time: 10:32:01 AM
File: BD-DL-08
User: XRD_Offline
Counts
BD-DL-08
Muscovite-2M1; K Al2 (Si , Al)4 O10 (O H)2
Clinochlore-1MIIb, ferroan; (Mg , Fe)6 (Si , Al)4 O10 (O H)8
Calcite; Ca (C O3)
30000
20000
10000
0
10
20
30
40
50
60
70
Position [°2θ] (Copper (Cu) K-α12)
Peak List
Muscovite-2M1; K Al2 (Si , Al)4 O10 (O H)2
Clinochlore-1MIIb, ferroan; (Mg , Fe)6 (Si , Al)4 O10 (O H)8
Calcite; Ca (C O3)

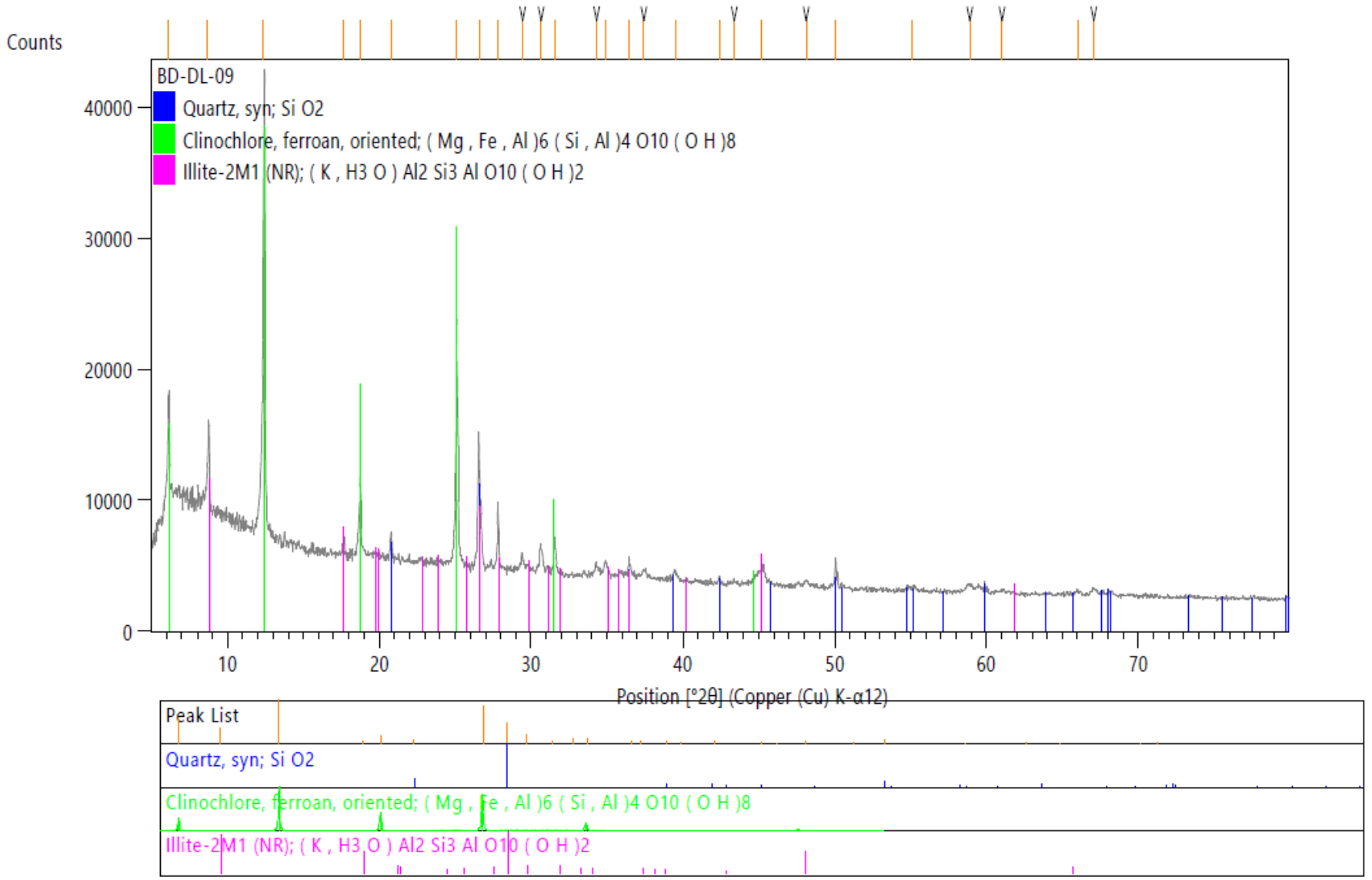
Date: 2021-04-20 Time: 10:32:19 AM
File: BD-DL-09
User: XRD_Offline
Counts
BD-DL-09
Quartz, syn; Si O2
Clinochlore, ferroan, oriented; (Mg , Fe , Al)6 (Si , Al)4 O10 (O H)8
Illite-2M1 (NR); (K , H3 O) Al2 Si3 Al O10 (O H)2
40000
30000
20000
10000
0
10
20
30
40
50
60
70
Position [°2θ] (Copper (Cu) K-α12)
Peak List
Quartz, syn; Si O2
Clinochlore, ferroan, oriented; (Mg , Fe , Al)6 (Si , Al)4 O10 (O H)8
Illite-2M1 (NR); (K , H3 O) Al2 Si3 Al O10 (O H)2

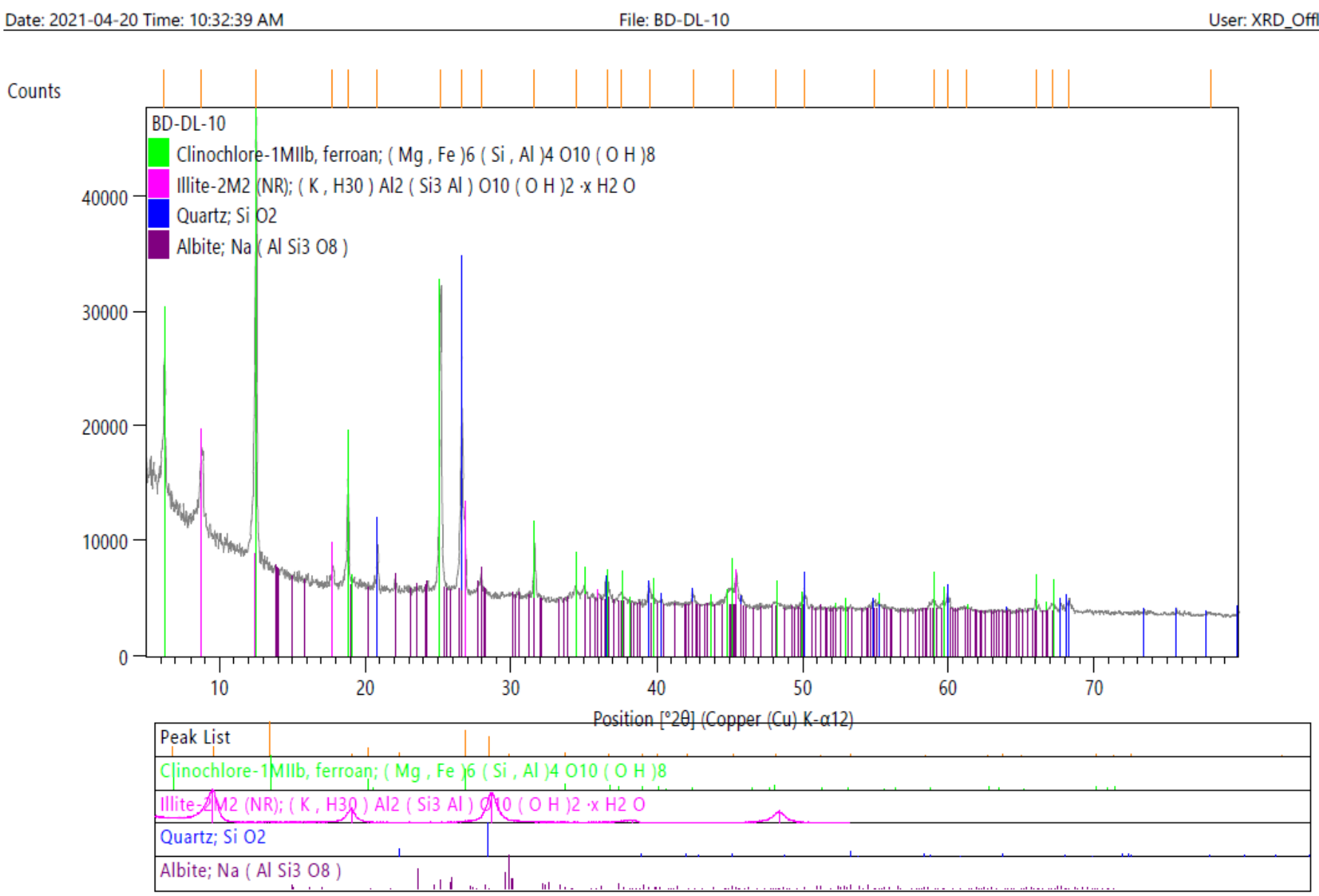
Date: 2021-04-20 Time: 10:32:39 AM
File: BD-DL-10
User: XRD_Offline
Counts
BD-DL-10
Clinochlore-1MIIb, ferroan; (Mg , Fe)6 (Si , Al)4 O10 (O H)8
Illite-2M2 (NR); (K , H30) Al2 (Si3 Al) O10 (O H)2 ·x H2 O
Quartz; Si O2
Albite; Na (Al Si3 O8)
40000
30000
20000
10000
0
10
20
30
40
50
60
70
Position [°2θ] (Copper (Cu) K-α12)
Peak List
Clinochlore-1MIIb, ferroan; (Mg , Fe)6 (Si , Al)4 O10 (O H)8
Illite-2M2 (NR); (K , H30) Al2 (Si3 Al) O10 (O H)2 ·x H2 O
Quartz; Si O2
Albite; Na (Al Si3 O8)

Appendix V

Cathodoluminescence images not used in Chapter 7

Field of view for all images is 2.5 mm unless otherwise stated

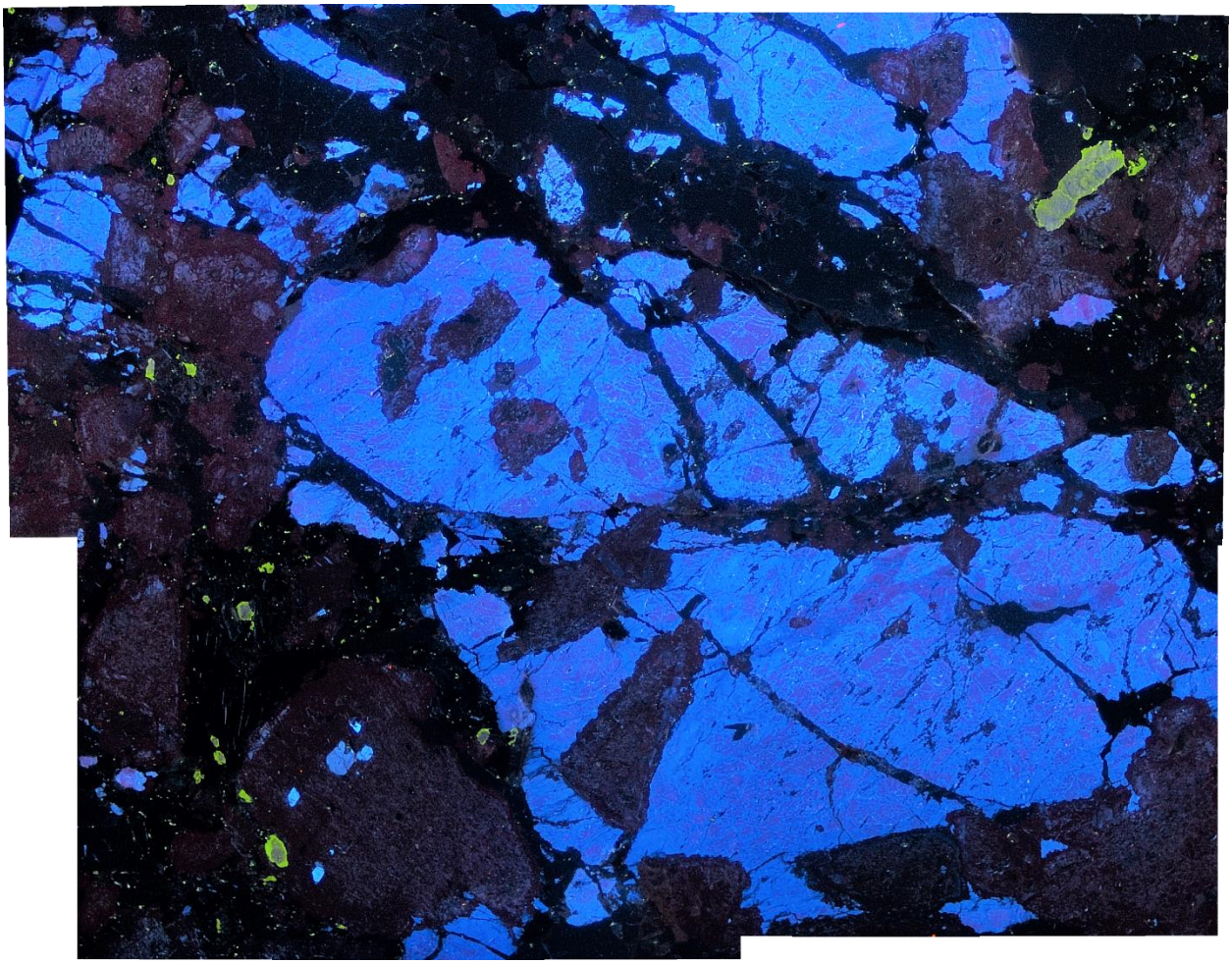

1. High strain sample from the Ottertail pluton. K-feldspar is blue, plagioclase is purple, quartz is black, and green is apatite.

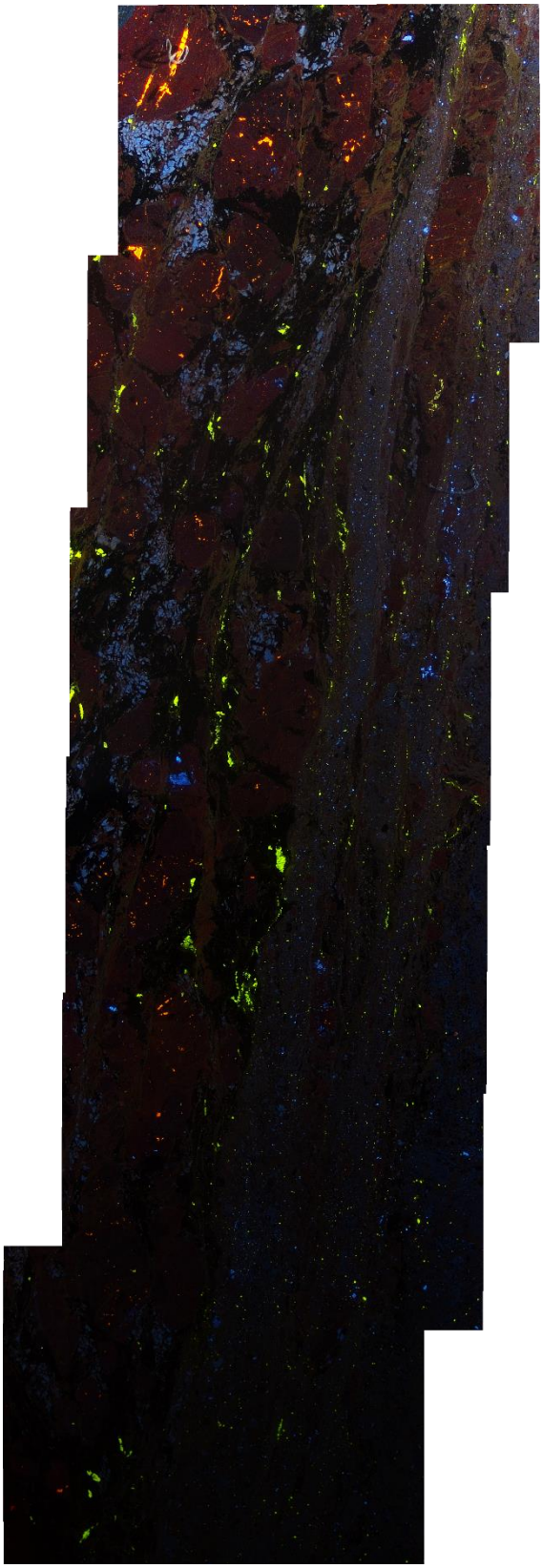

2. High strain sample from the Ottertail pluton. The fine grain size makes CL properties difficult to assess. Red/purple mineral is plagioclase, blue is likely K-feldspar, black is quartz, green is apatite and orange is calcite.

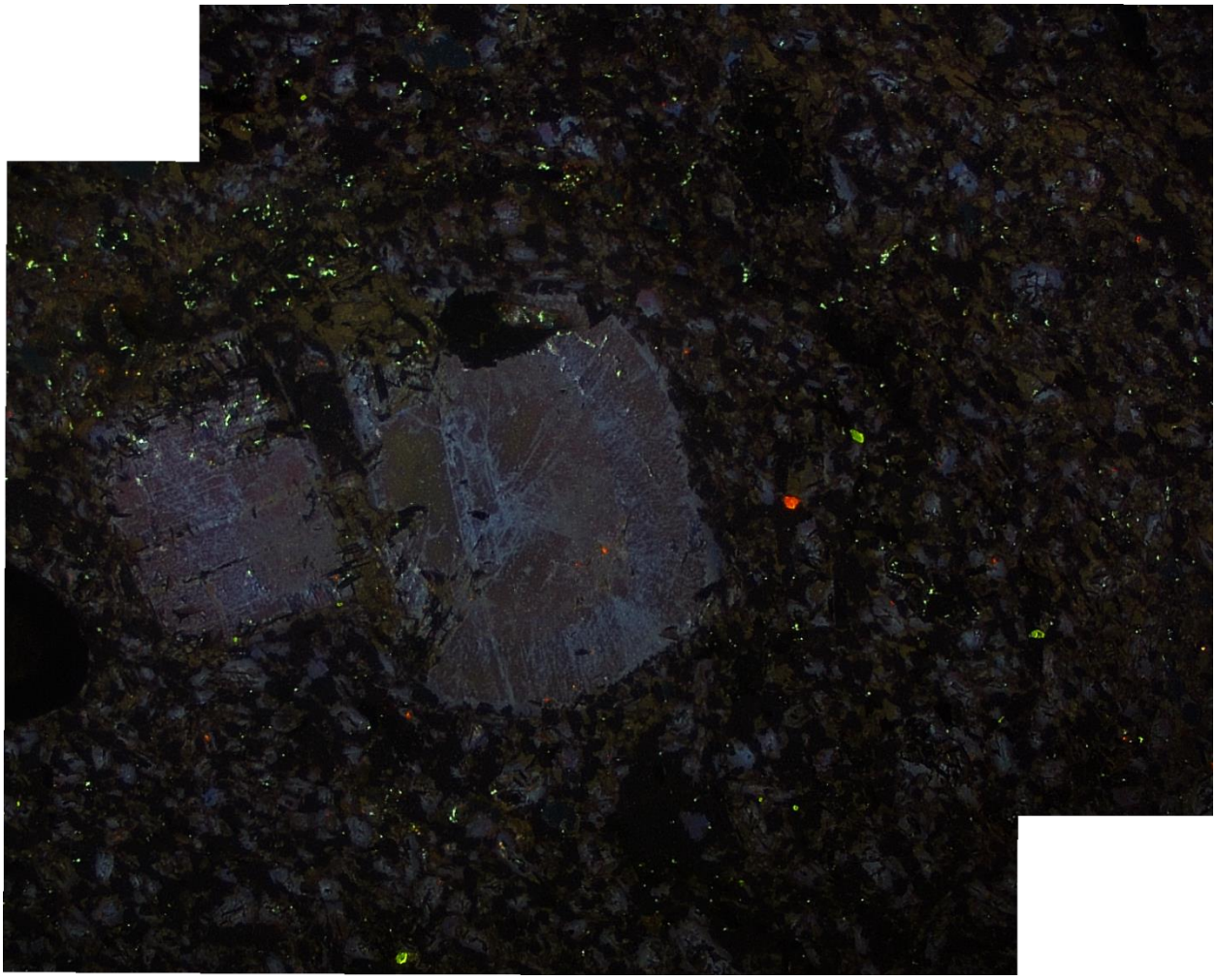

3. High strain sample from the Sabaskong batholith. Ductile shear zone. Blue is k-feldspar, black is quartz and brown is alteration.

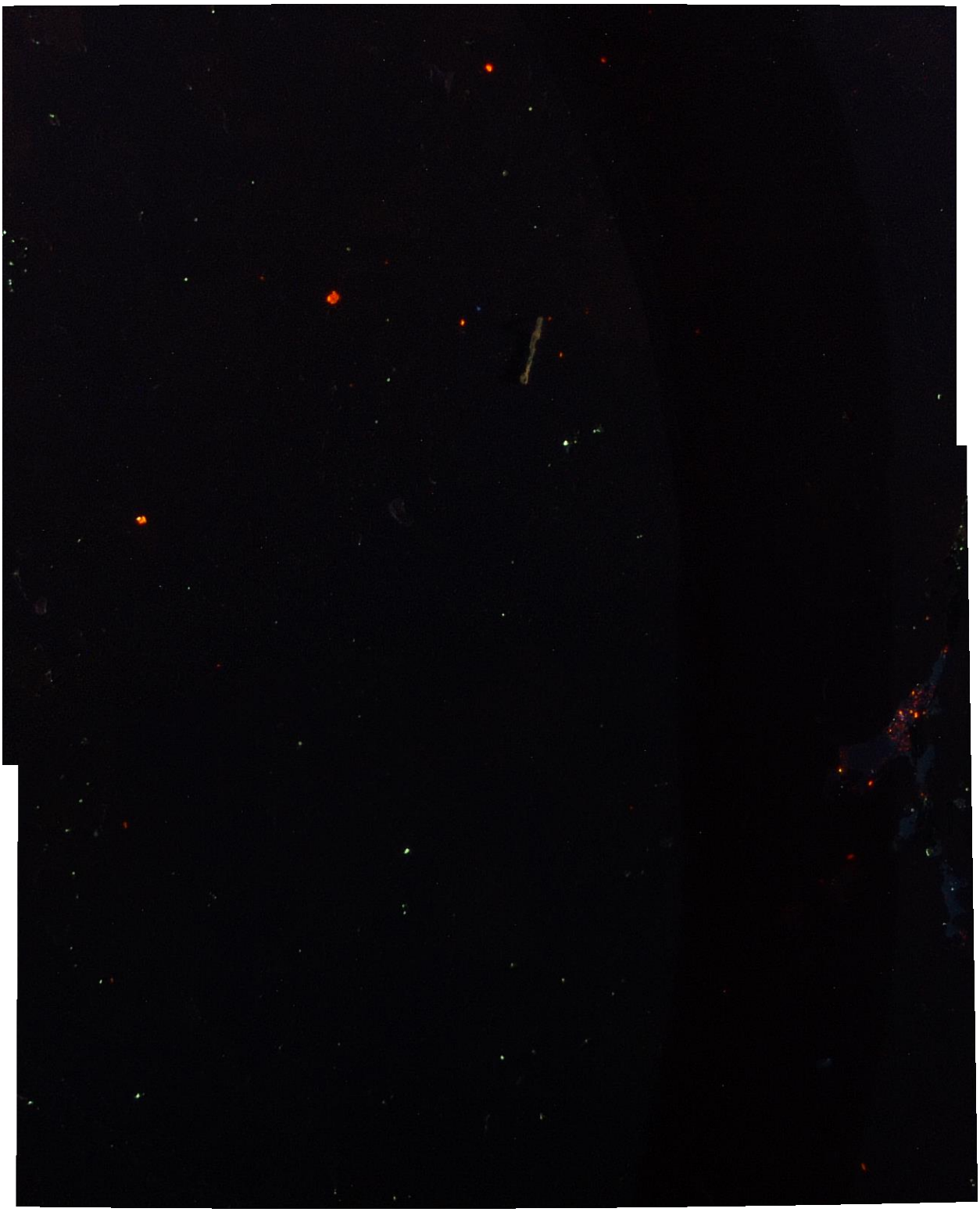

4. High strain sample of a ductilely deformed hydrothermal quart vein. Quartz does not display luminescence - likely due to CL operating settings.

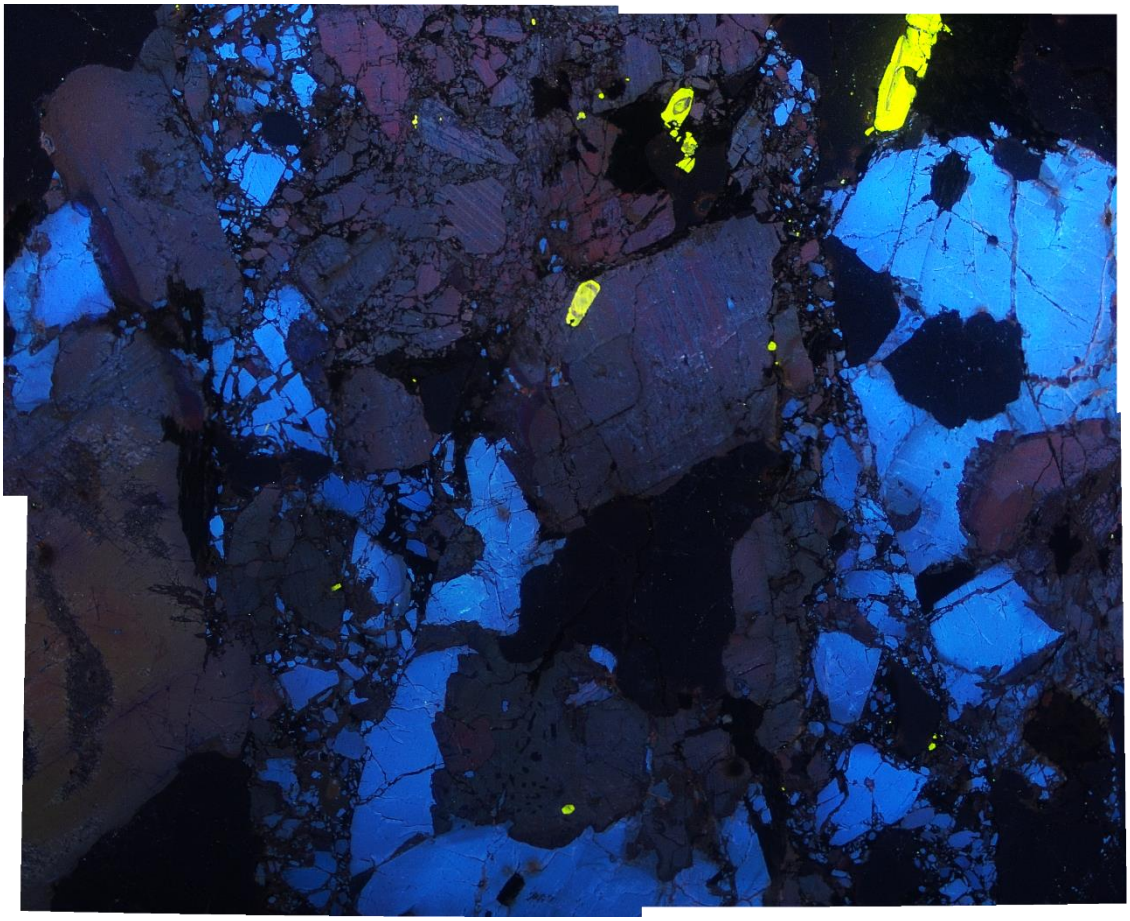

5. High strain sample of a cataclasite within the White Otter Lake batholith. Plagioclase feldspar is red, K-spar is blue, quartz is black and apatite is green.

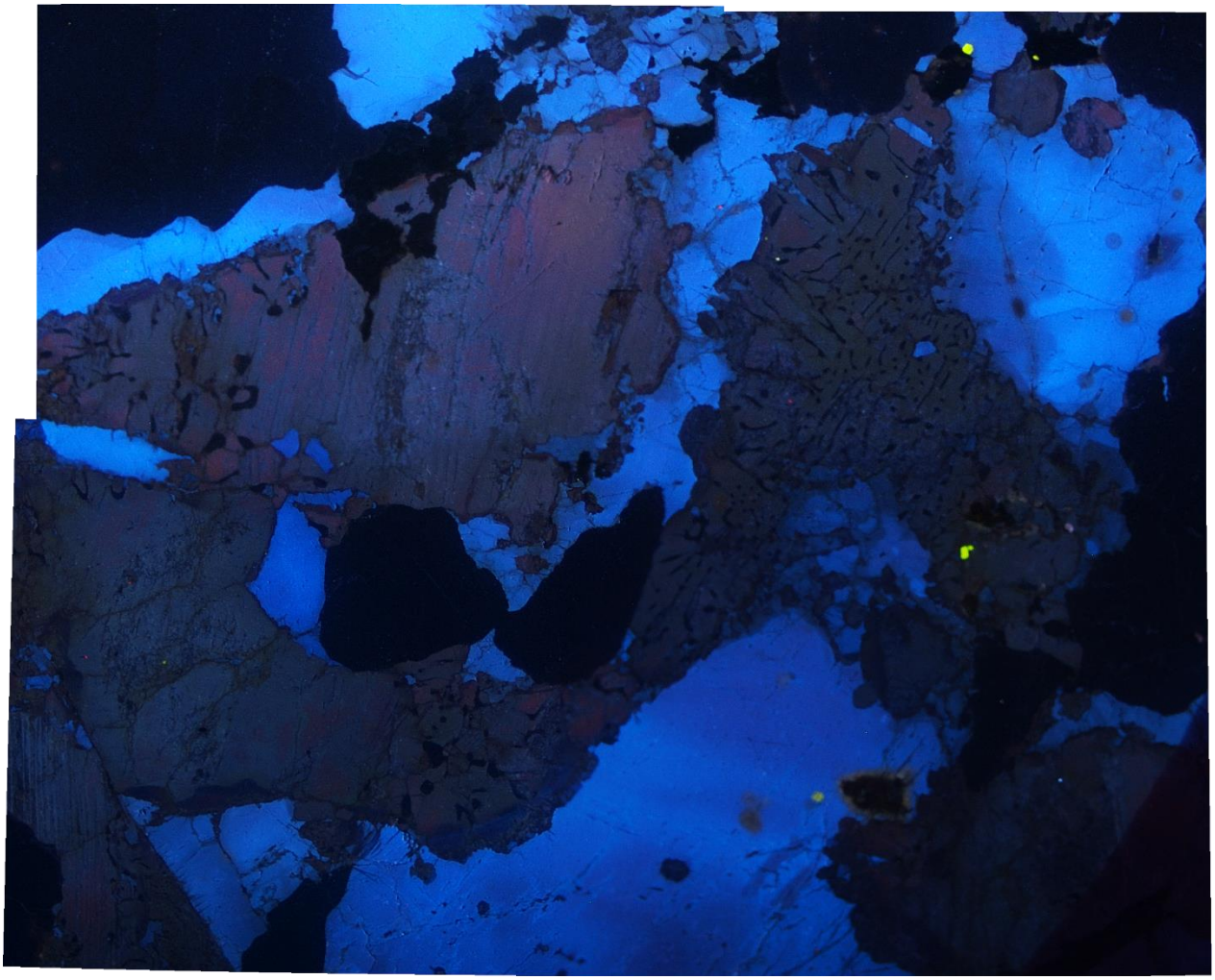

6. High strain sample of a cataclasis within the White Otter Lake batholith. Plagioclase is red, k-spar is blue, quartz is black. Myrmekyte is clearly visible within the plagioclase.

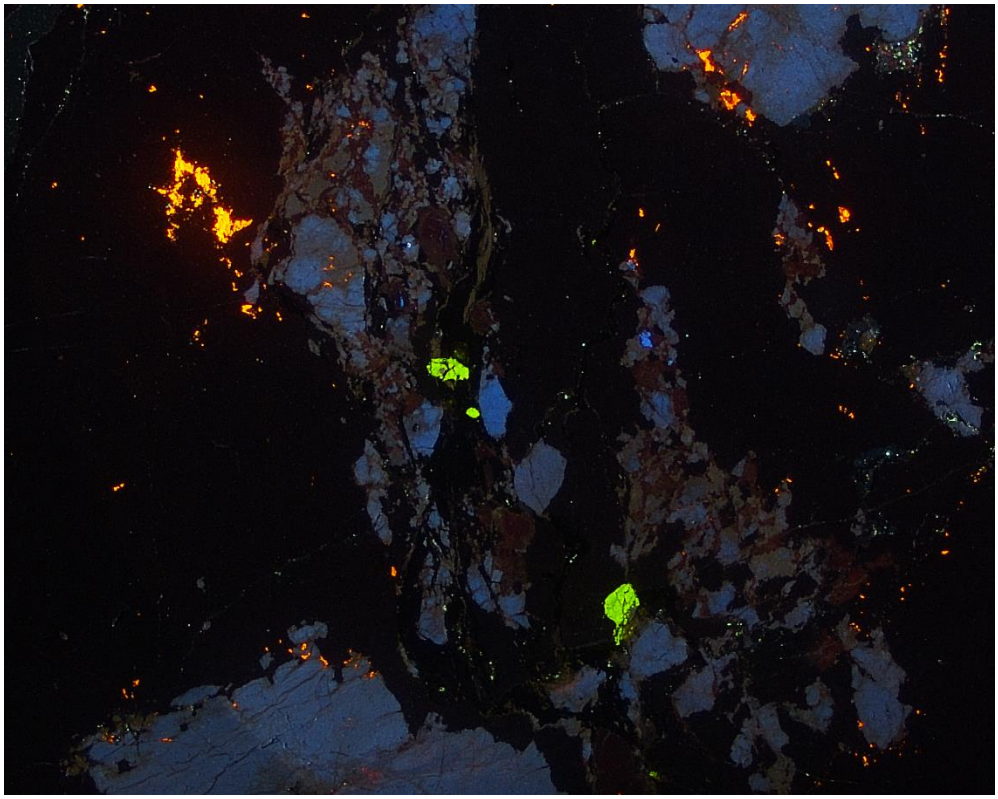

7. High strain sample from the Ottertail pluton. Blue is k-feldspar, plagioclase is red/purple, quartz is black, apatite is green, calcite is orange.

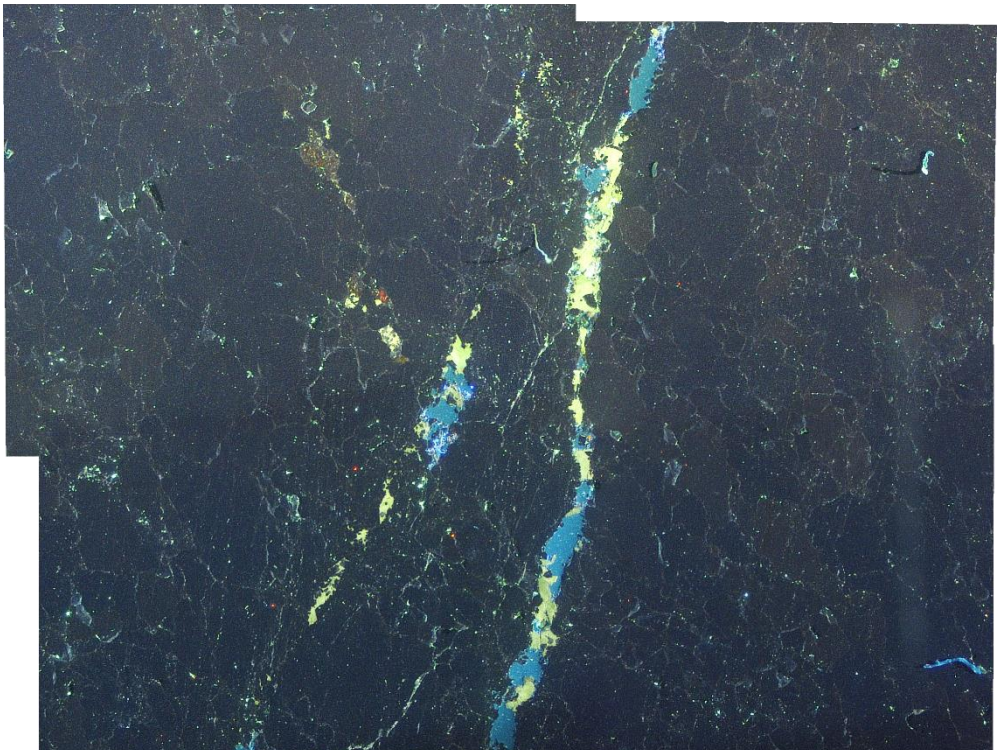

8. High strain sample (ductilely deformed quartz vein) from the Revell Batholith. High strain sample from the Ottertail pluton. Blue is k-feldspar, plagioclase is red/purple, quartz is black, apatite is green, calcite is orange.

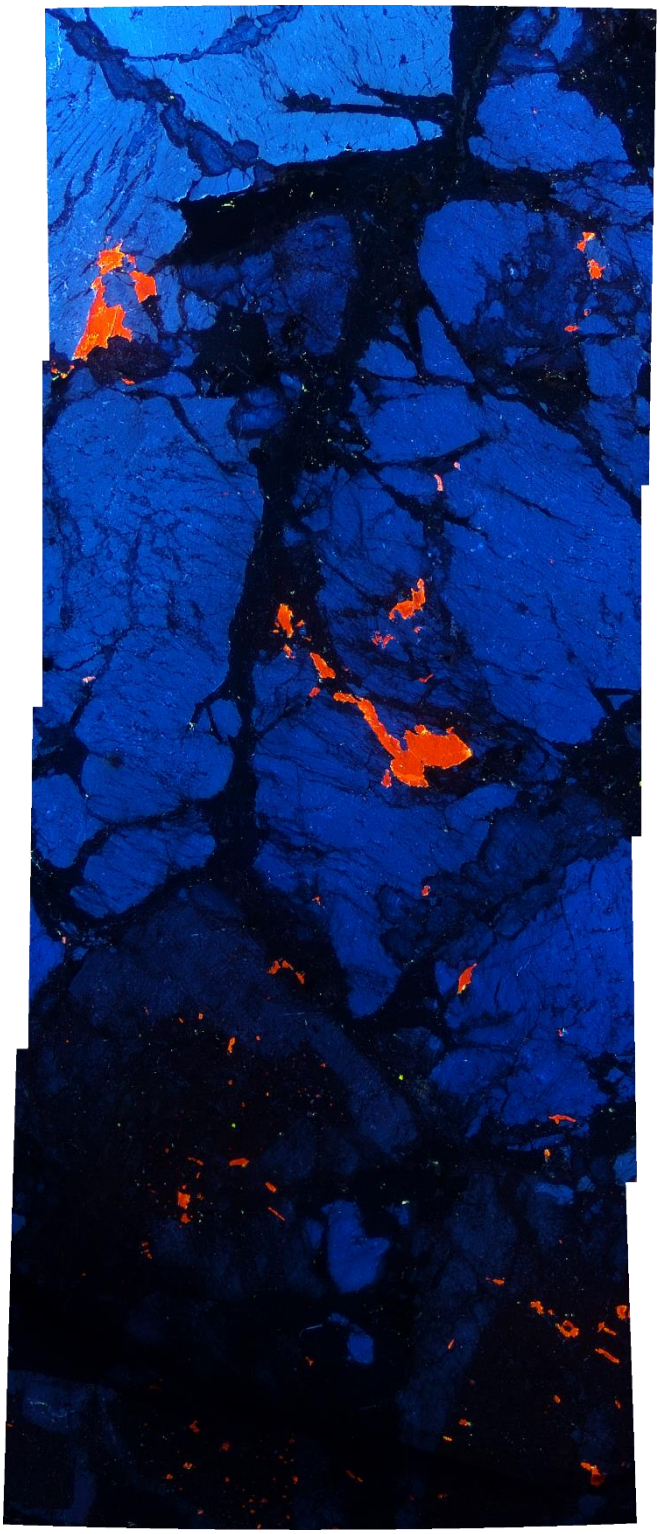

9. Medium strain sample from the Dryberry batholith. Blue is k-feldspar, black is quartz, orange is calcite.

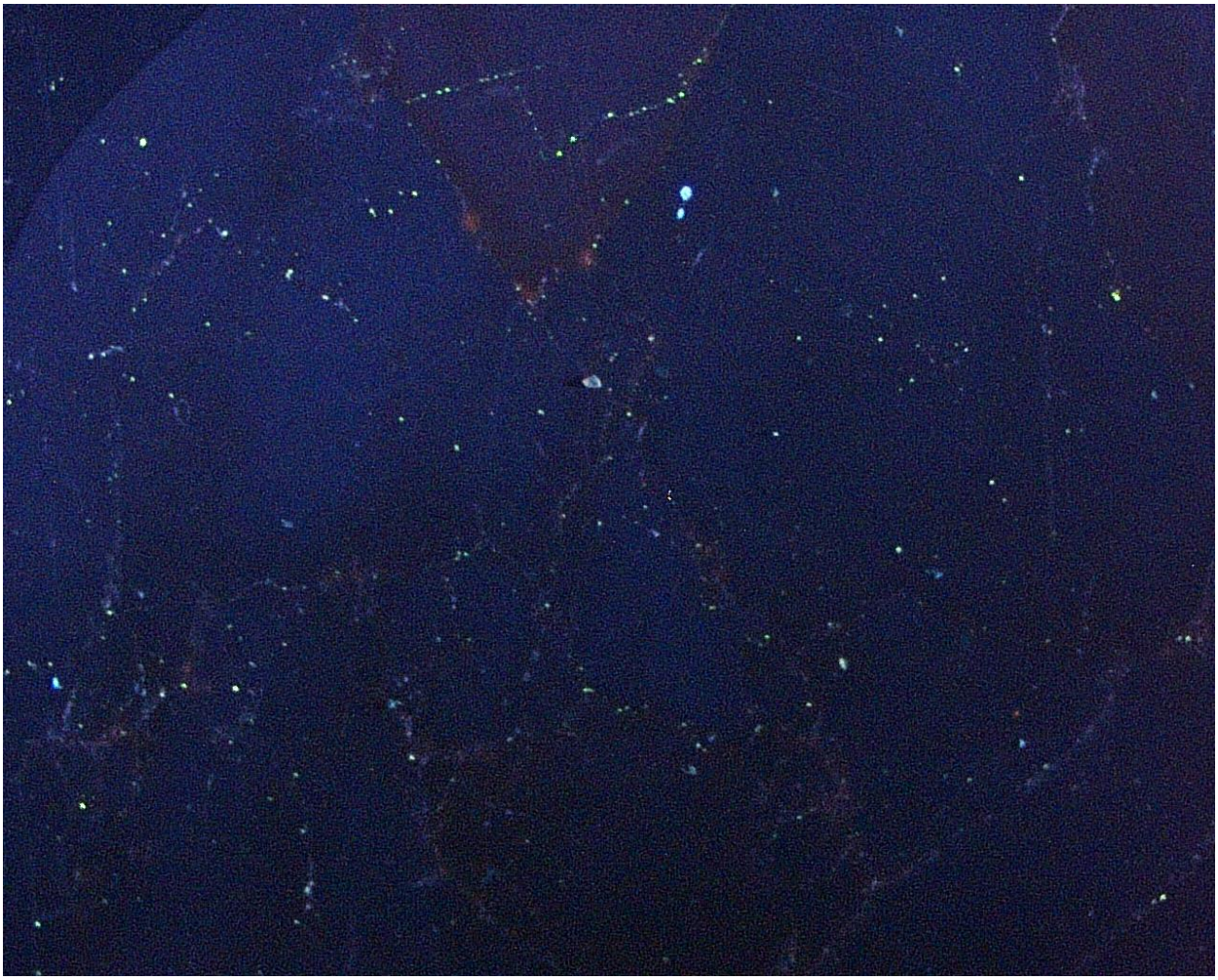

10. Hydrothermal quartz vein from the Dryberry batholith.

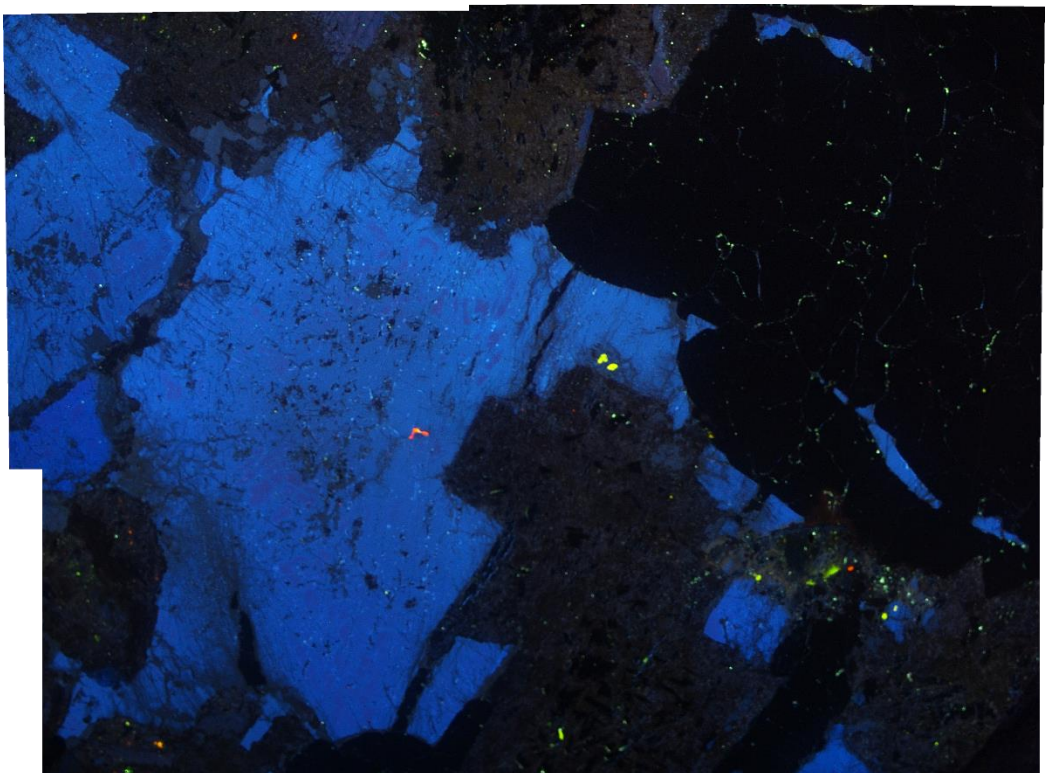

11. Medium strain sample from the Atikwa batholith. K-feldspar is blue, plagioclase is purple, quartz is black, and green is apatite.

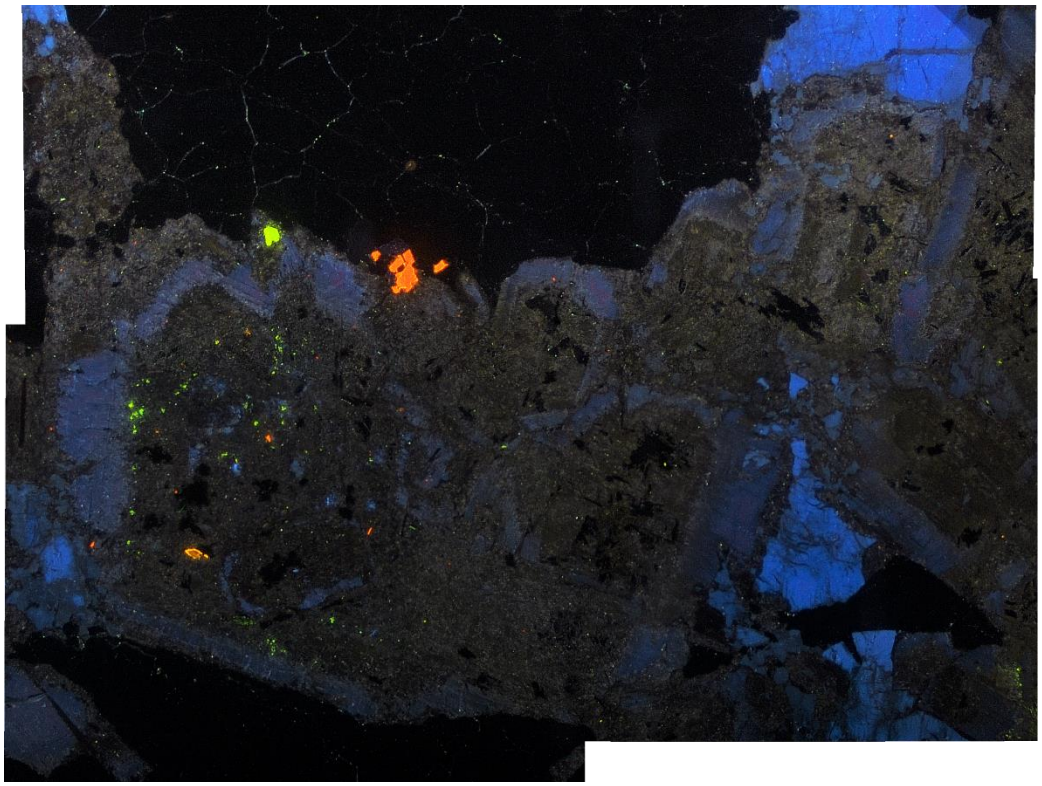

12. Medium strain sample from the Atikwa batholith. K-feldspar is blue, plagioclase is purple, quartz is black, and green is apatite.

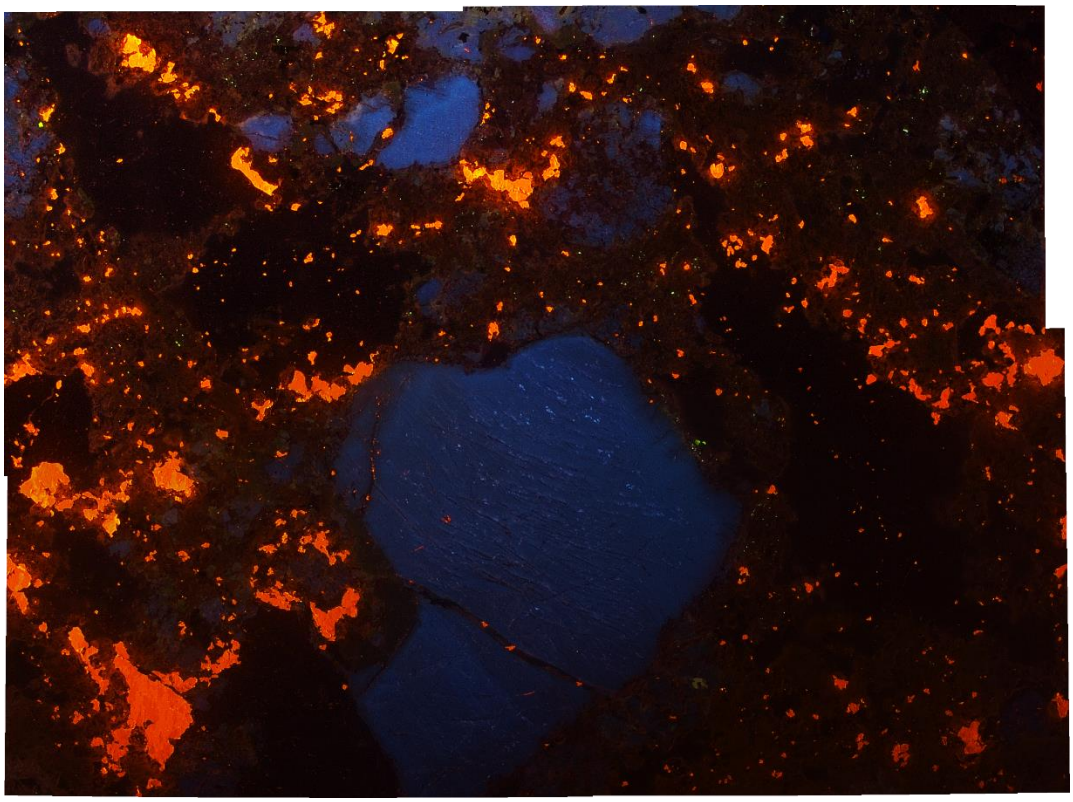

13. Medium strain sample from the Croll Lake Stock. Blue is K-feldspar, black is quartz, orange is calcite.

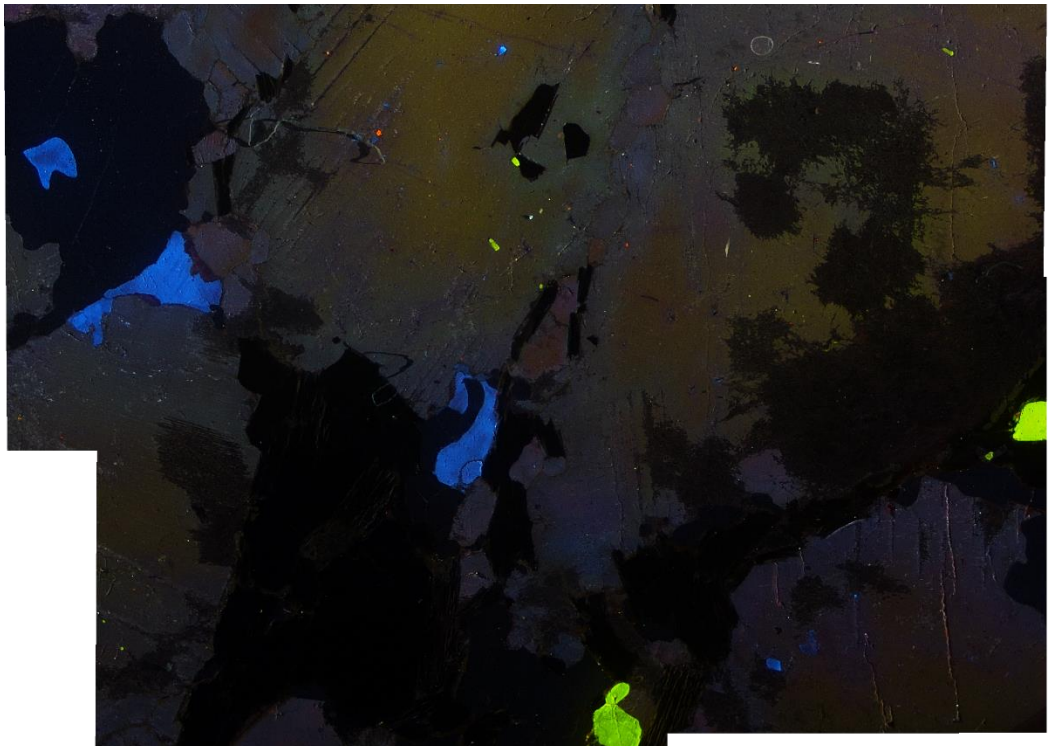

14. Medium strain sample from the Sowden-Wabakimi batholithic complex. Red is plagioclase, blue is k-feldspar, black is quartz. Brown is alteration within the plagioclase

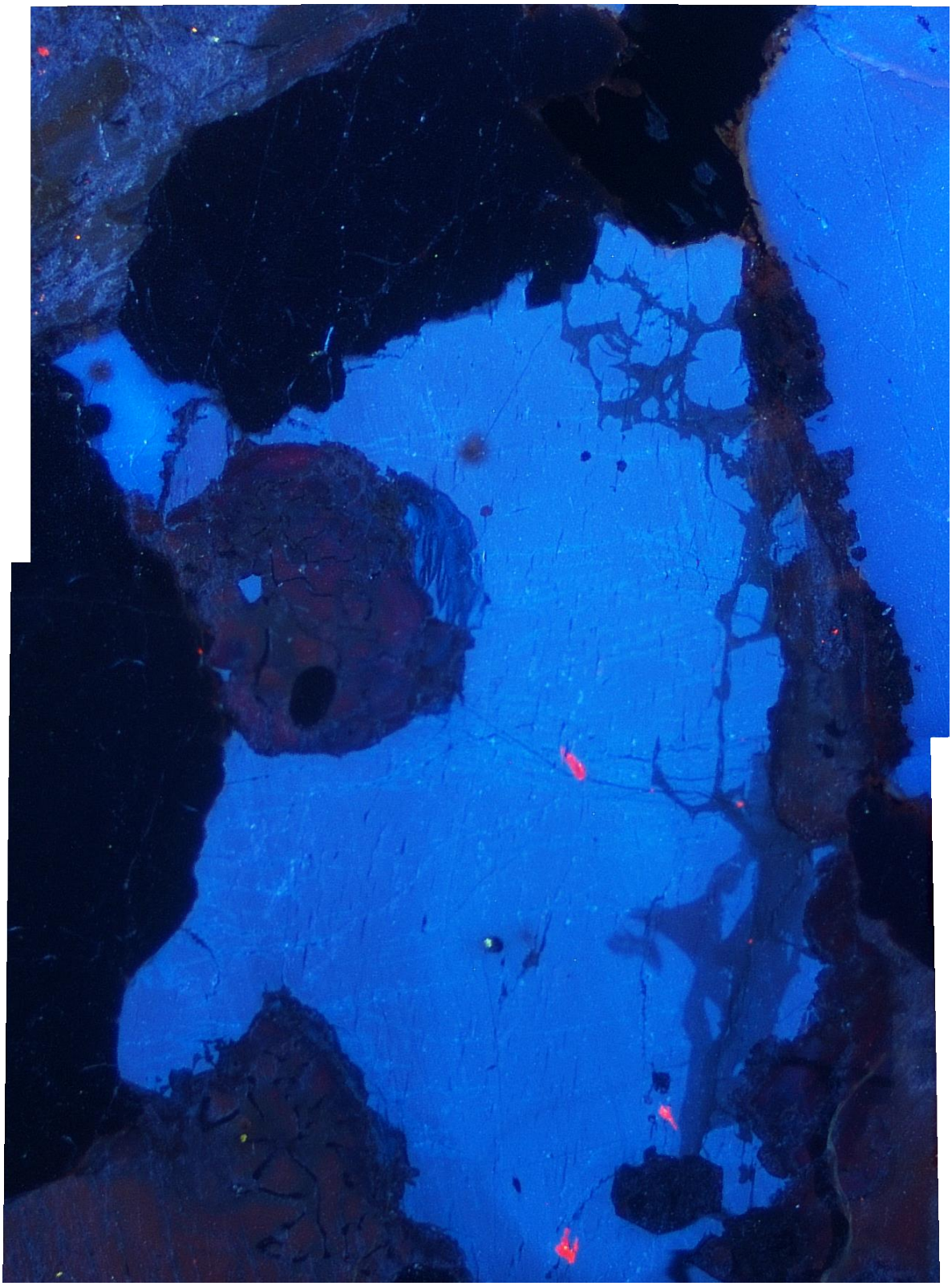

15. Low strain sample from the Indian Lake batholith. Blue is k-feldspar, red is plagioclase, black is quartz.

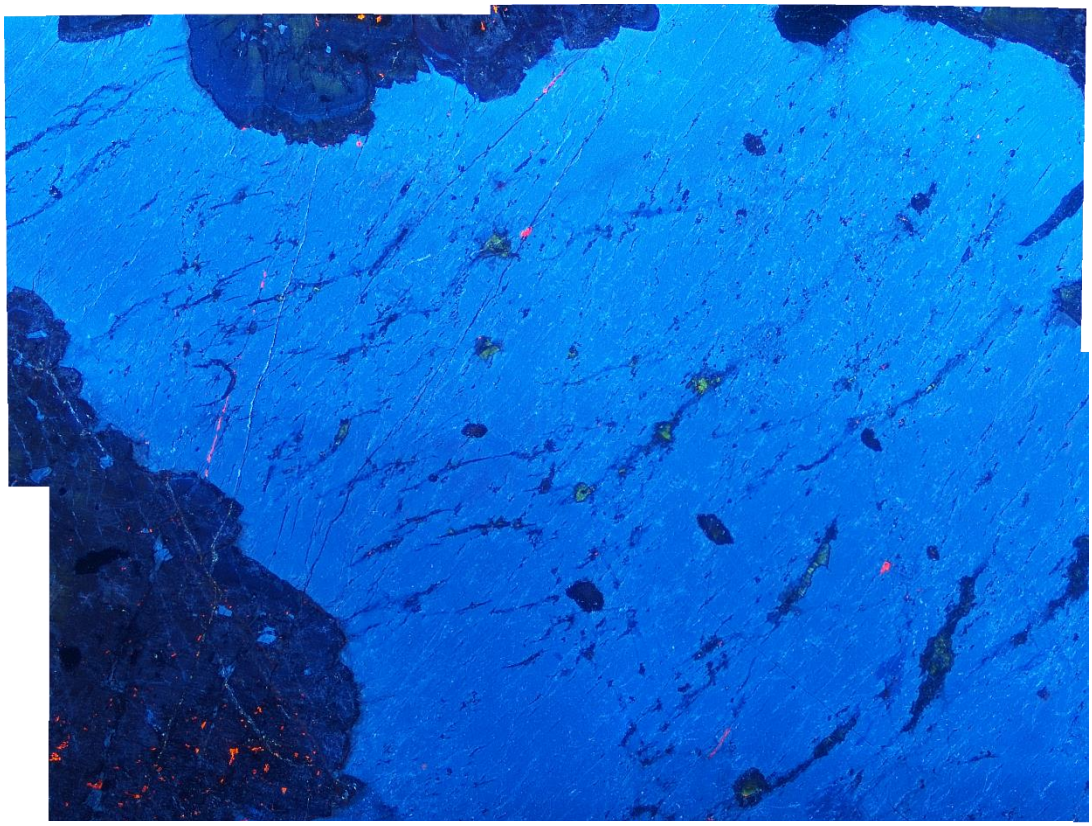

16. Low strain sample from the Dryberry batholith.

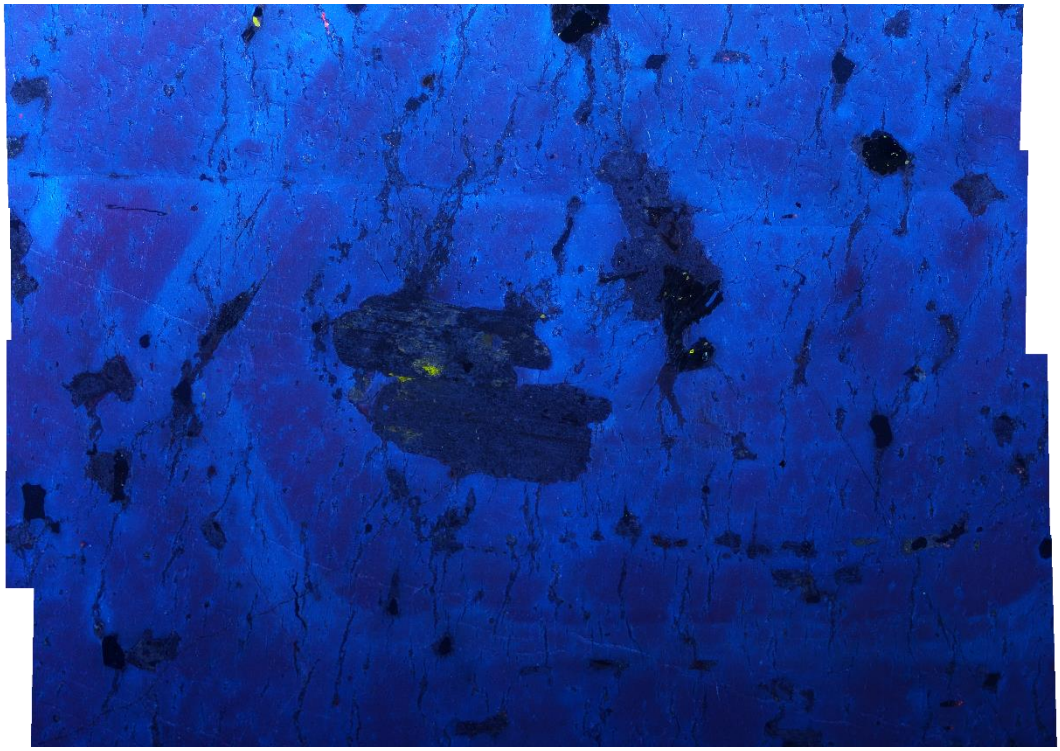

17. Low strain sample of k-feldspar from the Marmion batholith showing zoning.